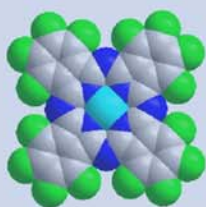
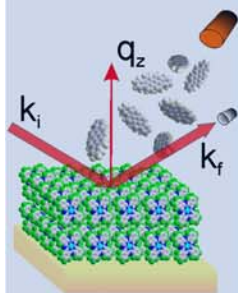


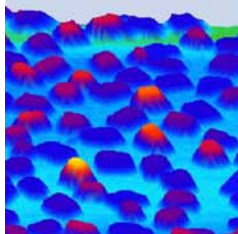
Fluorinated copper-phthalocyanines in organic thin-films, heterostructures and 2D supramolecular assemblies



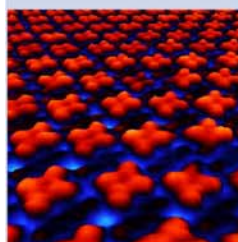
Dimas García de Oteyza
November 2006



Directed by Dr. Esther Barrena
and codirected by Prof. Helmut Dosch



Max-Planck-Institut
für Metallforschung



Departamento de Física
de la Materia Condensada,
Universidad Autónoma de Madrid.



A Luis y Ahlke.

La mayor parte de los hombres no quiere nadar antes de saber. ¿No es esto espiritual? ¡No quieren nadar, naturalmente! Han nacido para la tierra, no para el agua. Y, naturalmente, no quieren pensar; como que han sido creados para la vida, ¡no para pensar! Claro, y el que piensa, el que hace del pensar lo principal, ese podrá acaso llegar muy lejos en esto; pero ese precisamente ha confundido la tierra con el agua, y un día u otro se ahogará.

(Hermann Hesse, “El Lobo Estepario”)

Die meisten Menschen wollen nicht eher schwimmen, als bis sie es können. Ist das nicht witzig? Natürlich wollen sie nicht schwimmen! Sie sind ja für den Boden geboren, nicht fürs Wasser. Und natürlich wollen die nicht denken; sie sind ja fürs Leben geschaffen, nicht fürs Denken! Ja, und wer denkt, wer das Denken zur Hauptsache macht, der kann es darin zwar weit bringen, aber er hat doch eben den Boden mit dem Wasser vertauscht, und einmal wird er ersaufen.

(Hermann Hesse, “Der Steppenwolf”)

CONTENTS

RESUMEN	VI
1 MOTIVATION	1
2 INTRODUCTION	5
2.1 Organic semiconductors	5
2.1.1 General properties	5
2.1.2 Organic semiconducting molecules	6
2.1.3 Organic field-effect transistors (OFETs)	11
2.2 Thin film growth	16
2.2.1 Growth modes	16
2.2.2 Organic molecular beam deposition (OMBD)	18
2.2.3 Self-assembling monolayers (SAMs)	20
3 EXPERIMENTAL	30
3.1 Scanning probe microscopy	30
3.1.1 Scanning Tunneling Microscopy (STM)	31
3.1.2 Atomic Force Microscopy (AFM)	35
3.2 X-ray diffraction	44
3.2.1 Scattering	45
3.2.2 X-ray reflectivity	47
3.2.3 Grazing incidence X-ray diffraction (GIXD)	51
3.2.4 Real time measurements at the specular anti-Bragg point	52
3.2.5 Synchrotron beamlines	53
3.3 Sample preparation	56
3.3.1 Omicron system	56
3.3.2 JEOL system	57
3.3.3 Portable UHV chamber	58
3.3.4 Substrate preparation	59
4 TUNING THE GROWTH OF F₁₆CUPC ON SiO₂ BY USE OF A SELF-ASSEMBLED MONOLAYER (OTMS)	63
4.1 Experimental details	64
4.2 Study on the bare SiO ₂	64
4.2.1 Structure and morphology	64
4.2.2 Detailed focus on the first layers	70
4.2.3 Thermal expansion	77
4.2.4 Conclusions	79
4.3 Comparative study on SiO ₂ functionalized by OTMS	80
4.3.1 Morphology	81
4.3.2 Structure	84
4.3.3 Thermal desorption spectroscopy	86
4.3.4 Electrical characterization	87
4.3.5 Conclusions	89

5	P-N ORGANIC HETEROSTRUCTURES	93
5.1	Experimental details	94
5.2	F₁₆CuPc and pentacene	94
5.2.1	F ₁₆ CuPc on pentacene	95
5.2.2	Pentacene on F ₁₆ CuPc	110
5.2.3	Conclusions	116
5.3	F₁₆CuPc and DIP	117
5.3.1	DIP on F ₁₆ CuPc	118
5.3.2	F ₁₆ CuPc on DIP	129
5.3.3	Conclusions	134
6	SELF-ASSEMBLY OF MIXED TWO-DIMENSIONAL SUPRAMOLECULAR STRUCTURES	139
6.1	Experimental details	139
6.2	Deposition of pure DIP	140
6.2.1	Short-range ordered structure	142
6.2.2	Long-range ordered structure	147
6.3	Deposition of pure F₁₆CuPc	148
6.4	Binary molecular layers of DIP and F₁₆CuPc	149
6.4.1	DIP to F ₁₆ CuPc ratio 1:1	150
6.4.2	DIP to F ₁₆ CuPc ratio 2:1	152
6.4.3	DIP to F ₁₆ CuPc ratio 1:2	154
6.5	Conclusions and comparison to the results on Au(111)	155
7	SUMMARY	160
8	OUTLOOK	163
9	APPENDIX	164
A.	Fit parameters resulting from the study on the first F ₁₆ CuPc growth stages on SiO ₂	164
B.	Absorption effect of the F ₁₆ CuPc thin films.	165

Resumen

En los últimos años se están dedicando numerosos esfuerzos a la investigación de materiales semiconductores orgánicos. El interés que estos materiales suscitan proviene de sus propiedades innovadoras, que posibilitan el desarrollo de nuevas aplicaciones optoelectrónicas, así como de sus bajos costes de producción. Sin embargo, en comparación con los semiconductores convencionales, los semiconductores orgánicos presentan un menor rendimiento, siendo éste por tanto uno de los mayores obstáculos para su implementación en dispositivos optoelectrónicos.

Dos de los factores determinantes en su rendimiento son la inyección de cargas eléctricas procedente de los electrodos metálicos y el transporte de portadores de carga a través de la película, los cuales muestran a su vez una dependencia directa con la estructura y morfología de la película. A modo de ejemplo, cabe mencionar que el transporte de portadores de carga en los semiconductores orgánicos tiene lugar principalmente a lo largo de la dirección de solapamiento de los orbitales moleculares π . Dada la anisotropía propia de estos materiales, dicho solapamiento depende de la orientación relativa de las moléculas, y por tanto de la estructura cristalina. En consecuencia, son las propiedades estructurales de las películas orgánicas los parámetros clave que en última instancia determinan las propiedades optoelectrónicas de los dispositivos.

El crecimiento de películas orgánicas involucra procesos mucho más complejos que los conocidos para materiales inorgánicos. Sus propiedades intrínsecas, como son las grandes dimensiones moleculares, su anisotropía (con los nuevos grados de libertad rotacionales que implica), o las interacciones intermoleculares de Van der Waals (más débiles y menos direccionales que los enlaces covalentes), hacen que términos como epitaxia, tensión o interdifusión, adquieran un significado diferente al establecido y, en muchos casos, tengan menor relevancia que para el crecimiento de materiales inorgánicos. Por tanto, la extrapolación de los conocimientos ya establecidos para el crecimiento de materiales inorgánicos resulta en muchos casos

inadecuada. De hecho, no se ha conseguido todavía alcanzar el nivel de comprensión necesario para “diseñar” películas orgánicas con estructuras y morfologías específicas.

Este ha sido el punto de partida de esta tesis, cuyo objetivo es contribuir a alcanzar los conocimientos necesarios para dirigir y controlar el crecimiento de estructuras orgánicas en interfases de interés tecnológico, entre las que cuentan aquellas formadas entre el semiconductor y el dieléctrico o los contactos metálicos. Por otro lado, muchos de los dispositivos orgánicos, como es el caso en transistores ambipolares, células fotovoltaicas, o diodos orgánicos, se basan en heteroestructuras de semiconductores tipo p-semiconductores tipo n, lo cual a su vez genera una interfase adicional orgánico-orgánico. Sin embargo, a pesar de la importancia de estas intercaras, apenas hay estudios dedicados a su caracterización desde un punto de vista estructural, y se desconoce su influencia sobre la morfología de las películas, o el papel de aspectos tales como la interdifusión, la epitaxia, o las tensiones en la estabilidad o las propiedades de las heteroestructuras resultantes. En gran medida, la falta de estudios es debida a la dificultad de acceso a dichas interfases, una vez que quedan “enterradas” en el interior de la propia heteroestructura.

En el marco de esta tesis, combinando técnicas complementarias de microscopía de sonda de barrido (tanto microscopía de fuerza atómica como microscopía de efecto túnel) y medidas in-situ de difracción de rayos X (la cual posibilita el acceso a la estructura de intercaras enterradas), se han investigado las propiedades estructurales así como el propio crecimiento de diversos tipos de heteroestructuras relacionadas con las diferentes intercaras presentes en dispositivos optoelectrónicos.

Los estudios están centrados en la molécula ftalocianina de cobre fluorinada ($F_{16}CuPc$), cuyo principal interés reside en ser una de las pocas moléculas semiconductoras con comportamiento de tipo n que presenten estabilidad frente a su exposición al aire. A pesar de la importancia de su estructura cristalina para la eficiencia de los dispositivos, así como para la comprensión de las relaciones “propiedades optoelectrónicas-estructura”, aún se desconoce su estructura en películas delgadas.

Es en esta tesis la primera vez que se ha estudiado en detalle la estructura cristalina de películas de $F_{16}CuPc$ sobre SiO_2 , con especial énfasis en las primeras

capas, motivado por su especial relevancia en el transporte de carga en transistores. Además, se ha estudiado un nuevo método para la optimización de la estructura de las películas, mediante la manipulación controlada de las propiedades del sustrato al funcionalizar el SiO_2 con una monocapa autoensamblada de moléculas con un grupo terminal metilo. La nueva superficie, con una tensión superficial mucho menor, facilita la difusión de las ftalocianinas y promueve la formación de películas con la misma estructura pero dominios cristalinos mucho más extensos. Esto conlleva una reducción de las fronteras de grano y, en consecuencia, de la densidad de “trampas” para los portadores de carga. La movilidad efectiva de los portadores de carga en películas crecidas sobre las superficies funcionalizadas resulta por tanto un orden de magnitud mayor que en aquellas depositadas directamente sobre el SiO_2 .

Otra parte importante de esta tesis está dedicada al estudio de heteroestructuras orgánicas, en las cuales se han combinado F_{16}CuPc como semiconductor de tipo n con diindenoperileno (DIP) y pentaceno, ambos semiconductores de tipo p.

A pesar de las múltiples similitudes entre el DIP y el pentaceno, como por ejemplo su composición química, la morfología de sus películas o su hidrofobicidad, las heteroestructuras resultantes al combinarlas con F_{16}CuPc muestran procesos y modos de crecimiento, así como estructuras totalmente distintas, confirmando con ello la dificultad para establecer teorías de crecimiento generales aplicables a las heteroestructuras orgánicas. Por ejemplo, al depositar F_{16}CuPc sobre pentaceno, el entorno energéticamente y electrónicamente distinto en los escalones del pentaceno cataliza la formación de una nueva estructura de ftalocianinas, mientras que al depositarlo sobre DIP, los escalones del DIP no muestran ningún efecto sobre su crecimiento. Si bien esto podría sugerir una menor interacción de las F_{16}CuPc con el DIP, cuando el crecimiento de estas heteroestructuras (en ambas secuencias de deposición) tiene lugar a altas temperaturas, se observan unos procesos que sí sugieren también en este sistema interacciones importantes. Al depositar DIP sobre las ftalocianinas, se produce un crecimiento de Stranski-Krastanov del DIP (capa más islas), asociado a una reestructuración de las tres últimas capas de F_{16}CuPc , mientras que la estructura del DIP está relajada tanto en las islas como en la capa cerrada. En el orden de deposición inverso, el DIP actuando de sustrato no sufre ninguna reconstrucción, y las ftalocianinas forman una película cerrada, ordenada de principio a

fin con la nueva estructura. Esto contrasta con el escenario habitual en el crecimiento de materiales inorgánicos y muestra uno de aquellos casos en que los procesos de crecimiento en materiales orgánicos no están contemplados por las teorías establecidas (“inorgánicas”).

Por último, también se ha estudiado en esta tesis la autoorganización de nanoestructuras bidimensionales supramoleculares. Las interacciones entre el DIP y las $F_{16}CuPc$ han mostrado ser considerables, capaces de generar efectos como los descritos anteriormente en heteroestructuras. Por otro lado, esas interacciones posibilitan la síntesis de nanoestructuras altamente estables. La coevaporación de DIP y $F_{16}CuPc$ sobre una superficie de Cu(111) tiene como resultado la formación de distintas estructuras bidimensionales en función de las proporciones entre moléculas. Interesantemente, estas estructuras mixtas muestran dominios muy extensos (de hasta cientos de nm) y una estabilidad mayor que la de cada una de las moléculas por separado. Por tanto, además de poder aprovecharlas como patrones para el crecimiento de estructuras autoensambladas más complejas, la mayor sencillez del sistema, debido a su dimensionalidad reducida, puede facilitar la obtención de un mayor nivel de comprensión respecto a la naturaleza de las interacciones intermoleculares.

Con los estudios de esta tesis, dedicados a la caracterización estructural de las películas orgánicas, a la comprensión de las relaciones “propiedades optoelectrónicas-estructura”, así como de los procesos de crecimiento en películas orgánicas, y a la síntesis de nanoestructuras bidimensionales supramoleculares, se pretende contribuir (al margen de su interés para la física fundamental) al desarrollo y optimización de la electrónica orgánica, dando un paso más hacia el perseguido fin del crecimiento controlado de películas con la estructura deseada.

1 Motivation

The high application potential of the so-called “plastic electronics” has sparked a world-wide research activity in the field of organic semiconducting thin films. The weak Van der Waals forces between neighbouring organic molecules, along with the low processing temperatures, allow the organic films to be grown on a wide variety of novel substrates such as polymeric materials and enable the development of flexible devices.^{1, 2} However, the probably most appealing advantage of organic semiconductors that has attracted the interest of many major electronic firms is the potential low cost and ease of production of organic electronics, which might allow in a near future the production of e.g. large area electronics by printing methods.^{1,2,3,4,5} Up-to-date, organic-based devices have already been demonstrated, such as organic light-emitting devices (OLEDs),^{6,7,8} solar cells,^{9,10,11} organic field-effect transistors (OFETs),^{2,3,4,5} or gas sensors.^{12, 13}

Among the different explored materials, small aromatic molecules have emerged as promising candidates because they can be grown in films with high crystalline order, thus fulfilling one of the key requirements for high charge carrier mobility. The detailed knowledge of their film structure is a prerequisite to understand the optoelectronic properties. In particular, the structure and morphology of the first organic layers are known to have a large impact on the charge carrier mobility in OFETs.^{4,14} In addition, in those applications relying on heterojunctions of p- and n-type semiconductors, such as OLEDs, solar cells, or ambipolar transistors, the structure and morphology of the (additional) organic-organic interface are expected to play a crucial role in the final device performance. In general, the requirements in terms of film structure, morphology or interface properties vary somewhat for different applications. Thus, the goal is to find routes to control the organic film growth in order to tune their structural properties for the specific needs. A key milestone towards the success is the thorough understanding of the organic thin film growth mechanisms.

While the processes involved in the growth of inorganic materials are already well understood,^{15,16} thus allowing a certain control over the film growth to obtain desired structures and morphologies,^{17,18} a successful extrapolation of the current (inorganic)

growth theories to the organic materials is hindered by the increased complexity in their growth scenarios. The major differences with respect to the inorganic counterparts, which introduce quantitatively and qualitatively new growth behaviours, are the highly anisotropic molecular structures (thus with additional orientational degrees of freedom), the large dimensions of the organic molecules (generating lattice mismatches with the inorganic substrates of about one order of magnitude) or the weaker and less directional intermolecular and molecule-substrate interactions as compared to the covalent bonds.^{19, 20, 21} All these properties inherent to organic materials make that terms like “strain” or “epitaxy” lessen in significance with respect to their role in heteroepitaxy of inorganic semiconductors. Nevertheless, their role on the emerging film morphology, as well as other issues like molecular interdiffusion and structure at the organic-organic interface, remain largely unexplored. Consequently, the state-of-the-art of organic thin film growth is still far from being a well-established paradigm.

The studies performed in this thesis are centered on the molecule copper-hexadecafluorophthalocyanine ($F_{16}CuPc$). This molecule is receiving increasing attention for being one of the few air-stable n-type organic semiconductors. However, in spite of the importance of the crystal structure for the optoelectronic properties and thus for the understanding of its performance in devices, the $F_{16}CuPc$ thin film structure is still unknown. By combining multiple experimental techniques such as atomic force microscopy (AFM), scanning tunnelling microscopy (STM), and X-ray diffraction (XRD), we have devoted our studies to the structural characterization (and optimization) of $F_{16}CuPc$ thin films on SiO_2 , with a special emphasis on the first layers.^{22, 23} We show that changing the substrate properties by the use of self-assembling monolayers (SAMs) is a useful tool to modify the film morphology and therewith enhance the charge transport within the films.²⁴ In addition, we have studied the growth of organic heterostructures based on the combination of $F_{16}CuPc$ (as n-type semiconductor) with diindenoperylene (DIP) and pentacene (both of them p-type semiconductors). We have paid special attention to the underlying processes involved in the growth of these heterostructures, which, in spite of the similarities between DIP and pentacene, result in novel and largely different growth scenarios.^{25, 26, 27} Furthermore, in order to facilitate the understanding of the driving mechanisms in the

growth processes, we have studied the self-assembly of mixed DIP and F₁₆CuPc supramolecular structures in systems of reduced dimensionality (two-dimensional).

With the presented work, we try to take a step forward towards the controlled growth of desired organic architectures, and therewith contribute to the further development and optimization of organic electronics.

References

- ¹ S. R. Forrest, The path to ubiquitous and low cost organic electronic appliances on plastic, *Nature* **428**, 911 (2004)
- ² M. M. Ling, Z. Bao, Thin film deposition, patterning, and printing in organic thin film transistors, *Chem. Mater.* **16**, 4824 (2004)
- ³ C. D. Dimitrakopoulos, P. R. L. Malenfant, Organic thin film transistors for large area electronics, *Adv. Mater.* **14**, 99 (2002)
- ⁴ G. Horowitz, Organic thin film transistors: from theory to real devices, *J. Mater. Res.* **19**, 1946 (2004)
- ⁵ H. E. Katz, Recent advances in semiconductor performance and printing processes for organic transistor-based electronics, *Chem. Mater.* **16**, 4748 (2004)
- ⁶ C. W. Tang, S. A. Van Slyke, Organic electroluminescent diodes, *Appl. Phys. Lett.* **51**, 913 (1987)
- ⁷ Ed. J. Shinar, Organic light-emitting devices: a survey, Springer, Heidelberg (2004)
- ⁸ M. A. Baldo, D. F. O'Brien, Y. You, A. Shoustikov, S. Sibley, M. E. Thompson, S. R. Forrest, Highly efficient phosphorescent emission from organic electroluminescent devices, *Nature* **395**, 151 (1998)
- ⁹ P. Peumans, S. Uchida, S. R. Forrest, Efficient bulk heterojunction photovoltaic cells using small molecular-weight organic thin films, *Nature* **425**, 158 (2003)
- ¹⁰ H. Hoppe, N. S. Sariciftci, Organic solar cells: an overview, *J. Mater. Res.* **19**, 1924 (2004)
- ¹¹ K. M. Coakley, M. D. McGehee, Conjugated polymer photovoltaic cells, *Chem. Mater.* **16**, 4533 (2004)
- ¹² L. Wang, D. Fine, D. Sharma, L. Torsi, A. Dodabalapur, Nanoscale organic and polymeric field-effect transistors as chemical sensors, *Anal. Bioanal. Chem.* **384**, 310 (2006)
- ¹³ B. Crone, A. Dodabalapur, A. Gelperin, L. Torsi, H. E. Katz, A. J. Lovinger, Z. Bao, Electronic sensing of vapors with organic transistors, *Appl. Phys. Lett.* **78**, 2229 (2001)
- ¹⁴ A. Dodabalapur, L. Torsi, H. E. Katz, Organic transistors: two-dimensional transport and improved electrical characteristics, *Science* **268**, 270 (1995)
- ¹⁵ A. Pimpinelli, J. Villain, Physics of crystal growth, Cambridge University Press, Cambridge (1999)
- ¹⁶ J. A. Venables, G. D. T. Spiller, M. Hanbücken, Nucleation and growth of thin films, *Rep. Prog. Phys.* **47**, 399 (1984)
- ¹⁷ R. Nötzel, Self-organized growth of quantum dot structures, *Semicond. Sci. Tech.* **11**, 1365 (1996)
- ¹⁸ J. Stangl, V. Holý, G. Bauer, Structural properties of self-organized semiconductor nanostructures, *Rev. Mod. Phys.* **76**, 725 (2004)
- ¹⁹ Ed. W. Brütting, Physics of organic semiconductors, Wiley-VCH Verlag, Weinheim (2005)

-
- ²⁰ S. R. Forrest, Ultrathin organic films grown by molecular beam deposition and related techniques, *Chem. Rev.* **97**, 1793 (1997)
- ²¹ G. Witte, C. Wöll, Growth of aromatic molecules on solid substrates for applications in organic electronics, *J. Mater. Res.* **19**, 1889 (2004)
- ²² D. G. de Oteyza, E. Barrena, J. O. Ossó, S. Sellner, H. Dosch, *J. Am. Chem. Soc.* (in print)
- ²³ D. G. de Oteyza, E. Barrena, S. Sellner, J. O. Ossó, H. Dosch, Structural rearrangements during the initial growth stages of organic thin films of F₁₆CuPc on SiO₂, *J. Phys. Chem B* **110**, 16618 (2006)
- ²⁴ D. G. de Oteyza, E. Barrena, J. O. Ossó, H. Dosch, S. Meyer, J. Pflaum, Controlled enhancement of the electron field-effect mobility of F₁₆CuPc thin film transistors by use of functionalized SiO₂ substrates, *Appl. Phys. Lett.* **87**, 183504 (2005)
- ²⁵ E. Barrena, D. G. de Oteyza, S. Sellner, H. Dosch, J. O. Ossó, B. Struth, In situ study of the growth of organic nanodots in organic heteroepitaxy, *Phys. Rev. Lett.* **97**, 076102 (2006)
- ²⁶ D. G. de Oteyza, E. Barrena, J. O. Ossó, S. Sellner, H. Dosch, Site-selective molecular arrangement in organic heterostructures, *Chem. Mater.* **18**, 4212 (2006)
- ²⁷ D. G. de Oteyza, E. Barrena, S. Sellner, J. O. Ossó, H. Dosch, submitted.

2 Introduction

2.1 Organic semiconductors

2.1.1 General properties

Organic semiconductors owe their semiconducting properties to the presence of conjugated double bonds in their molecular structure. Carbon atoms forming conjugated double bonds are sp^2 hybridized and give rise to both σ - and π -bonds, whose energy levels are split into occupied bonding orbitals with a lower energy, and unoccupied anti-bonding orbitals of higher energy. This is shown schematically in Figure 2.1 with the example of two sp^2 hybridized C atoms forming an ethene molecule.¹ The main contribution to charge transfer or optical excitation processes results from the electronic states closest to the Fermi energy. This corresponds to the π -orbitals, which consequently are the most relevant orbitals for the optoelectronic properties of these organic materials. For molecules with a larger number of conjugated C atoms further splitting of the energy levels takes place.

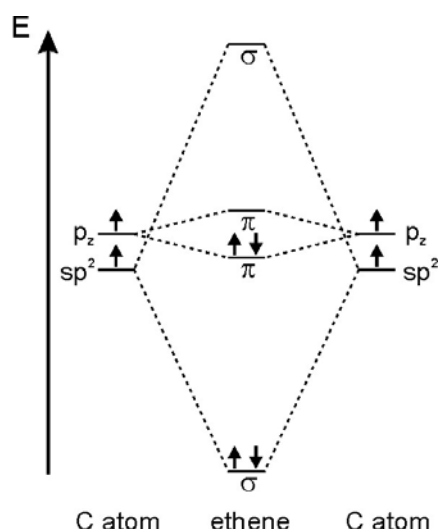


Figure 2.1. Schematic diagram showing the energy levels of two free carbon atoms and the change upon bond formation giving rise to an ethene molecule.

In this case the π -electrons are delocalized over the entire extent of conjugation (which might be the whole or only parts of the molecule), and the number of bonding and anti-bonding π -molecular orbitals increases. The highest occupied molecular orbital (HOMO) and the lowest unoccupied molecular orbital (LUMO) are for the organic semiconductors the analogous to the valence and conduction band edges of conventional inorganic semiconductors, respectively. Thus, the “band gap” of organic semiconductors corresponds to the HOMO-LUMO gap in their molecular orbitals. Organic chemistry offers virtually unlimited possibilities to synthesize different molecules by changing their size, atom arrangement, or including different atoms (“heteroatoms”) or functional groups at specific molecular positions. For any of these modified molecules the resulting molecular orbitals and, as a consequence their electronic properties, differ from each other, what can be used up to a certain extent to tailor the optoelectronic properties by the appropriate molecular synthesis. The structural anisotropy inherent to most organic semiconducting molecules gives rise to highly anisotropic optoelectronic properties, thus making of the molecular arrangement, i.e. the crystal structure, a key aspect for the physical properties of the films.^{2,3,4}

2.1.2 Organic semiconducting molecules

The immensely broad spectrum of organic semiconducting molecules can be classified into two major groups: polymers, and small weight molecules or oligomers. Polymers are long-chain molecules formed by the repetition of molecular units. The number of repetition units is indeterminate, thus leading to a variable molecular mass. On the contrary, small weight molecules have a well defined molecular weight. From the point of view of their electronic and optic properties both groups can be considered rather similar, being the main difference the thin-film deposition methods. In this sense, polymers show the advantage of being processable from solution e.g. by spin-coating, leading to lower production costs. Oligomers are in most of the cases insoluble and are thus deposited by technically more demanding methods with consequently higher associated costs. However, their major advantage with respect to

the polymers is that they can be grown in films of high purity and crystalline order, two important requirements to obtain high charge carrier mobility. In this thesis we have studied the growth of thin films formed by oligomers, purified twice by gradient sublimation before use, with complementary p- and n-type semiconducting behaviors. They are briefly presented in the following.

a. Copper-hexadecafluorophthalocyanine ($F_{16}CuPc$)

Phthalocyanines are porphyrin derivatives and cover a broad range of different molecules with similar structure. Since their first synthesis at the beginning of last century, phthalocyanines have established themselves as materials of high interest for the industry. Their interest relied initially on their intense coloring properties, motivating an extensive use as pigments. However, after the discovery of their semiconducting properties in 1948, the interest of the phthalocyanines has spread to a much wider range of industrial applications.

Among the different phthalocyanines, we have chosen for our studies copper-hexadecafluorophthalocyanine ($F_{16}CuPc$: $C_{32}F_{16}N_8Cu$), which is represented in Figure 2.2. It is a planar molecule belonging to the group of the metal-phthalocyanines, which are characterized by the presence of a metal atom in the molecular center. By simply changing this atom, a large number of similar phthalocyanines with different optoelectronic properties can be synthesized.^{5,6}

There are two different phthalocyanines with a central copper atom: $CuPc$ and $F_{16}CuPc$. They differ in the 16 atoms surrounding the molecule. For $CuPc$, one of the most studied phthalocyanines, these are hydrogen atoms, while for $F_{16}CuPc$ they are substituted by fluorines (Figure 2.2).

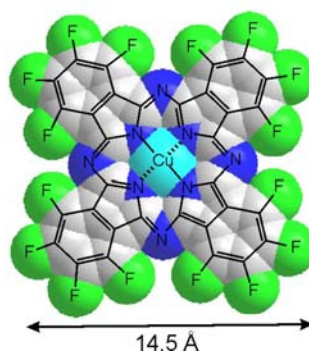


Figure 2.2 Molecular structure and dimension of $F_{16}CuPc$.

The fluorines increase the electron affinity of the molecules and favor an efficient electron injection into the empty LUMO states.⁷ As a consequence, the preferential p-type semiconducting behavior observed for CuPc when combined with typical contact materials such as Au (see section 2.1.3 for an understanding of the underlying principles), changes to n-type behavior in the case of F₁₆CuPc. The electric properties of F₁₆CuPc are stable upon air-exposure. Since there are only few air-stable n-type organic semiconductors,⁸ this makes of F₁₆CuPc an interesting candidate for all those applications in which both p- and n-type semiconductors are needed, such as organic solar cells, ambipolar transistors or OLEDs. As a matter of fact, the use of fluorinated copper-phthalocyanines has already been successfully demonstrated in unipolar transistors,^{8, 9, 10, 11, 12} ambipolar transistors,^{13, 14, 15, 16, 17} organic complementary circuits,^{18,19,20} organic photodetectors²¹ or gas sensors.^{22,23,24}

There are several studies focused on the bulk-structure of various phthalocyanines,^{25,26,27} including a recent study devoted to the characterization of F₁₆CuPc by X-ray powder diffraction,²⁸ for which the obtained cell parameters, volume and number of molecules per unit cell are shown in Table 2.1.

Two different structural phases have been reported for various phthalocyanines when grown in thin-films: a metastable α - and a stable β -phase.²⁹ The α -phase is obtained in thin films grown at substrate temperatures below a certain phase transition temperature.³⁰ An irreversible phase transformation to the β -phase can be induced by thermal treatment.^{31, 32} Up to now the detailed structure of F₁₆CuPc films was unknown and the β -phase of the analogous molecule CuPc²⁷ (cell parameters in Table 2.1) was often taken as reference.^{8,11,13,17,33} In the frame of this thesis the thin-film structure of F₁₆CuPc has been characterized, as reported in section 4.2.

	F ₁₆ CuPc	β -CuPc
a (Å)	20.018	19.407
b (Å)	5.106	4.79
c (Å)	15.326	14.628
α (deg.)	90	90
β (deg.)	111.83	120.56
γ (deg.)	90	90
V (Å ³)	1454	1166
Molec.	2	2

Table 2.1 Cell parameters reported for the bulk structure of F₁₆CuPc²⁸ and the CuPc β -phase.²⁷

b. Diindenoperylene (DIP)

Diindenoperylene (DIP) is an aromatic molecule with chemical formula $C_{32}H_{16}$. The molecular structure is shown in Figure 2.3a. It is a red dye and shows p-type semiconducting behavior in combination with Au contacts. There are several structural studies dealing with DIP single crystals³⁴ and thin films deposited on various surfaces, such as NaCl,³⁵ Perylene,³⁵ or SiO_2 .³⁶ (Parameters shown in Table 2.2). The growth of DIP thin films on SiO_2 results in a layered structure with the molecules in each of the layers standing upright and arranged in a herringbone pattern (Figure 2.3b).³⁶ The growth is characterized by an exceptionally high degree of order.³⁷ However, a strong increase in the film roughness is observed with increasing thickness³⁸ above a critical coverage.^{39,40}

The critical influence of the structural order on the performance of DIP-based organic thin-film transistors has been highlighted in a work by Karl et al., where a drastic enhancement of the field-effect mobility could be measured upon reduction of the mosaicity of the films.⁴¹

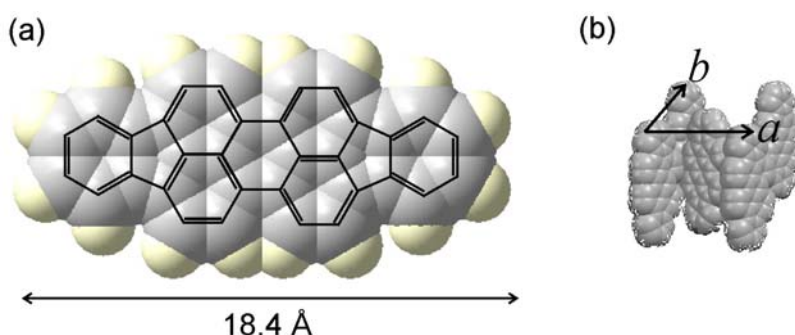


Figure 2.3 (a) Molecular structure and dimension of DIP. (b) Molecular arrangement within the thin-film unit cell.

	single cryst.	DIP/NaCl	DIP/Perylene	DIP/ SiO_2
a (Å)	11.59	8.67	11.0	8.55
b (Å)	12.97	6.96	10.6	7.09
c (Å)	14.88	18.55	17.5	16.6 (layer height)
α (deg.)	98.11	90	90	-
β (deg.)	98.10	93.5	106	-
γ (deg.)	114.43	90	90	90
Molec.	4	2	2	2

Table 2.2 Cell parameters reported for the DIP bulk structure³⁴ and thin-film structures on NaCl,³⁵ perylene,³⁵ and SiO_2 .³⁶

The optical properties of DIP have also shown to be very attractive, especially in combination with the previously mentioned $F_{16}\text{CuPc}$, since the respective absorption spectra complement each other covering most of the wavelengths in the visible range and thus resulting very interesting for their use in photovoltaic devices.⁴²

c. Pentacene

Pentacene is probably the most widely studied oligomer, whose main interest relies in its high charge carrier mobility. It shows preferentially p-type semiconducting behavior, though under specific conditions ambipolar behavior can also be obtained.^{43,44,45} The chemical formula is $\text{C}_{22}\text{H}_{14}$, and its molecular structure is shown in Figure 2.4.

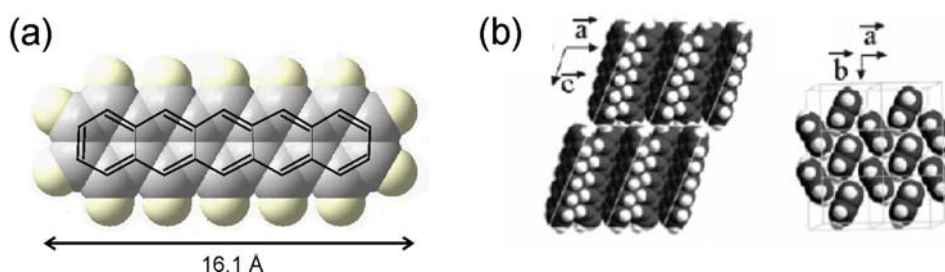


Figure 2.4 (a) Molecular structure and dimension of pentacene. (b) Molecular arrangement within the *bulk-structure* unit cell (From reference 46).

The structure and growth process of pentacene has been studied on a variety of surfaces.⁴⁶ Among them, the most common one is probably SiO_2 ^{46,47,48,49,50,51,52} because of its application as gate dielectric in field effect transistors. Pentacene thin films grow in a layered structure with a layer spacing of 15.5 Å. However, for coverages above a critical thickness which is inversely proportional to the substrate growth temperature, an additional structure forms with a layer spacing of 14.4 Å. The former is thus called *thin-film structure*, while the latter is generally called *bulk-structure*, since it seemed to be related to the bulk-structure determined by Campbell et al. in 1962.⁵³ Nevertheless, recent studies on the structure of pentacene films and single crystals by Mattheus et al.⁴⁹ have shown this name to be inappropriate, since also the structure with a layer spacing of 14.4 Å is apparently substrate induced. Furthermore, the cell parameters they have obtained for this structure are different

from those obtained by Campbell et al., and the layer spacing obtained in single crystals is 14.1 Å (also observed in films of extreme thickness, in the micrometer range).⁴⁹ There have also been efforts devoted to the characterization of the thin-film structure. Fritz et al. determined the unit cell for the first pentacene layer on the SiO₂,⁴⁷ and Ruiz et al. determined the structure in films with coverages ranging from the submonolayer to the multilayer regime.⁴⁸ The cell parameters for the various unit cells described above are given in Table 2.3.

	Single crystal ⁴⁹	“bulk” ⁴⁹	“bulk” ⁵³	“thin-film” multilayer ⁴⁸	“thin-film” 1 st layer ⁴⁸	“thin-film” 1 st layer ⁴⁷
Layer height (Å)	14.12	14.37	14.4	15.43	15.43	16±0.6
a (Å)	6.266	6.485	7.90	7.58	7.62	5.916
b (Å)	7.775	7.407	6.06	5.91	5.90	7.588
c (Å)	14.530	14.745	16.01	-	-	-
α (deg.)	76.475	77.25	101.9	-	-	-
β (deg.)	87.682	85.72	112.6	-	-	-
γ (deg.)	84.684	80.92	85.08	90±0.2	90±0.2	89.95
Molec.	2	2	2	2	2	2

Table 2.3 Reported cell parameters for the pentacene structures observed on SiO₂ as described in the text.

2.1.3 Organic field-effect transistors (OFETs)

The potential use of organic semiconductors in field-effect transistors was already demonstrated in the late eighties.^{54,55} Since then, tremendous efforts have been devoted to the development and optimization of these devices, which consequently lead to a rapid progress, to the level that the performance of good organic thin film transistors (OTFT) rivals that of commercial amorphous silicon transistors.

Thin film field-effect transistors consist on a semiconducting film contacted by metallic source and drain electrodes, and a third electrode (gate) separated from the semiconducting film by a dielectric layer. There are several different options to arrange the elements of the device, being the main difference the relative position of

the contacts with respect to the semiconductor (on top or below), as shown in Figure 2.5. The typical dimensions for the channel length (L) and width (W) are in the range of 1 to 50 μm and 100 μm to 1 mm respectively, though devices with channel lengths in the nanoscale have already been demonstrated.⁵⁶

The operation of OFETs depends on the applied gate and source-drain voltages.^{7,56} When a positive voltage is applied to the gate (V_G), negative charges are capacitively induced in the semiconducting layer (Figure 2.5) and vice-versa. Much of this charge is mobile and thus moves in response to an applied source-drain voltage (V_D).

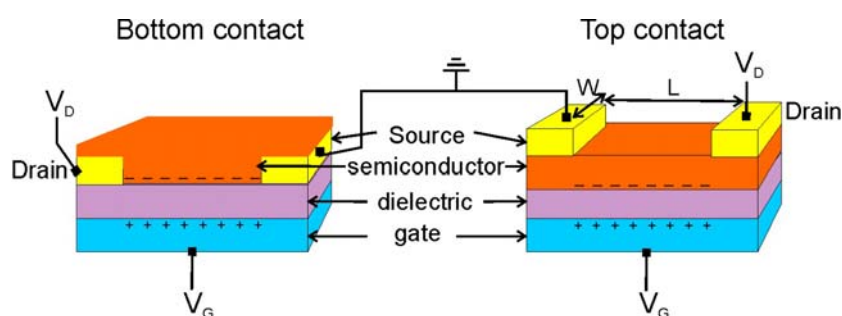


Figure 2.5. Schematic representation of OFETs in top contact and bottom contact geometries, together with the relevant voltages and dimensions.

Ideally, at $V_G=0$ there is an absence of mobile charge carriers and a consequently low conductance in the semiconducting film. The device is “off”. Upon gate voltage application, the charge injection increases the conductance and the device is turned “on”. In order to clarify the underlying concepts of the field effect transistor operation, Figure 2.6 shows, in a simplified way, a scheme of the evolution of the electronic energy levels in the device. The application of V_G shifts the semiconductor energy levels with respect to the Fermi levels of the contacts, until the HOMO ($V_G<0$, p-channel operation) or the LUMO ($V_G>0$, n-channel operation) reach the mentioned Fermi level. This leads to a charge injection into the semiconductor and to an electric current between source and drain upon application of a drain voltage. However, additional aspects not taken into account in this simple representation make that, with few exceptions, a given organic semiconductor acts only as hole or electron conductor and is consequently classified as n- or p-type semiconductor.

If we define the “threshold voltage” V_T as the voltage necessary to generate mobile charge carriers in the semiconductor, the current-voltage relationship in an OFET can be described, as for conventional semiconducting devices,^{57,58} by:

$$I_{D,lin} = \frac{W}{L} C \mu_{lin} \left[(V_G - V_T) V_D - \frac{V_D^2}{2} \right]. \quad (2.1)$$

This equation is called “linear regime” equation, and is valid when $V_D < (V_G - V_T)$. If $V_D = (V_G - V_T)$, the semiconductor region near the drain contact is completely depleted of free charge carriers. Once this point is reached, the current becomes independent of V_D and it follows:

$$I_{D,sat} = \frac{W}{2L} C \mu_{sat} (V_G - V_T)^2. \quad (2.2)$$

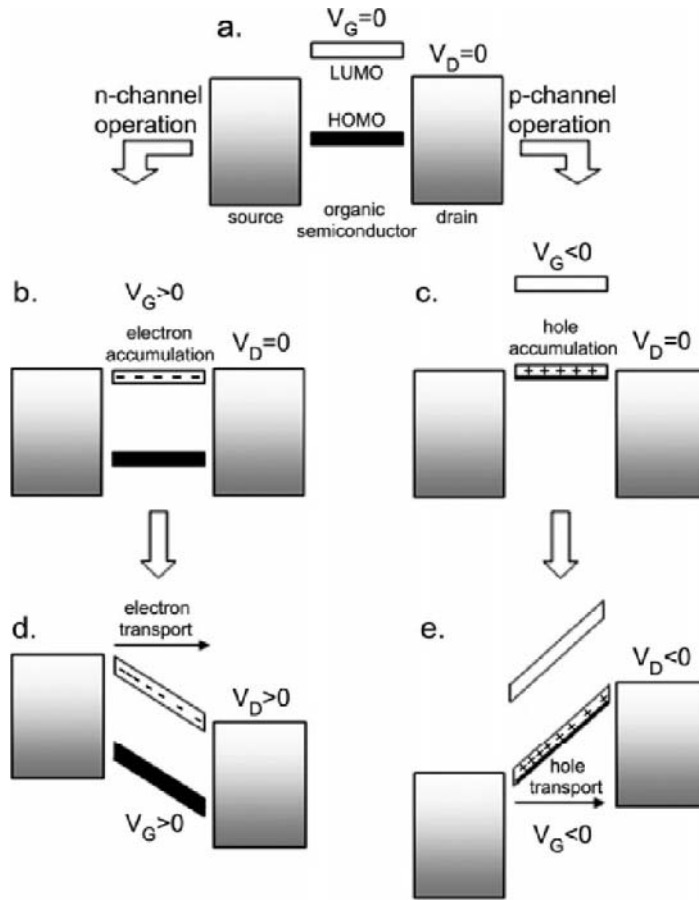


Figure 2.6. (a) Idealized energy level diagram of an organic TFT at $V_G = 0$ and $V_D = 0$. (b-e) demonstrate the principle of field effect transistor operation for the case of (b) electron accumulation and (c) transport and hole (d) accumulation and (e) transport. (from reference 7).

In general, the transistors are characterized either by sweeping V_D at a constant V_G (I_D - V_D or output curve), or by sweeping V_G at constant V_D (I_D - V_G or transfer curve). By adjusting the obtained curves in the linear or saturation regime to the equations (2.1) or (2.2), respectively, the mobilities μ_{lin} and μ_{sat} can be calculated (leading often to different values, usually with higher mobilities in the saturation regime), in addition to other important parameters such as V_T , I_{on}/I_{off} , and the subthreshold swing S (a measure of the switching speed from the on to the off state).

For a given molecular material, it is the charge carrier injection into the organic semiconducting layer and the charge carrier mobility within the organic film which mainly determine its electronic performance.

The charge carrier mobility depends crucially on the intermolecular overlap of the electronic π -orbitals of the molecules, which is in turn intimately related to the crystal structure.^{3,4,41,59,60,61} For an optimum electronic transport, the achievement of organic single crystalline films would be the ideal case, since the intrinsic charge carrier mobility obtained in single crystals actually represents an upper limit for the thin films.^{59, 62, 63, 64} In practice, the growth of TFT results in the formation of polycrystalline films, introducing charge traps at the grain boundaries,^{65,66,67,68} defects^{69,70} and interfaces,⁷¹ which reduce the effective carrier mobility in the films.

The charge carrier injection depends on the energy barrier at the semiconductor-metal interface and is strongly influenced by the structural and electronic properties of the organic films at the contacts.⁵⁶ The inherent contact resistance of a metal-semiconductor junction showing a potential barrier between the metal work function and the HOMO or LUMO level, is frequently further enhanced by additional dipole barriers generated at the interfaces.⁵⁶ In addition, in bottom contact devices the semiconductor usually shows different growth behaviors on the contacts and on the dielectric, giving rise to a large number of grain boundaries in the transition region close to the contacts.^{72,73} For these reasons, it is often the case that the contact resistances in the devices are large and limit their performance.^{56,74,75,76,77,78,79,80} Another important aspect for the device properties is the material purification,⁸¹ since the presence of impurities can have several negative effects on the device, as e.g.

generating traps or increasing the semiconductor conductivity with dopants and thereby reducing its $I_{\text{on}}/I_{\text{off}}$ ratio.^{7,70}

The challenge is to find a route to optimize the parameters of influence, i.e., increase the domain sizes,^{9,82} obtain structures of upright standing molecules in order to have the overlap of π -orbitals and thus the favoured direction of charge carrier transport in the surface plane,^{3,7,56} obtain highly aligned films,^{41,69} decrease defects or other charge carrier traps, or improve the charge injection. There is a number of accessible tools which have been explored to reach each of these goals.

For the optimization of the charge carrier mobility within the organic film, special attention has to be paid to the first layers in proximity to the dielectric, since it is already well established that the charge transfer takes place mainly along these very first layers of the semiconductor close to the dielectric interface.^{56,73,83,84,85,86,87} The functionalization by self-assembling monolayers of the dielectrics has been widely used to enhance the device performance.^{9,71,88,89,90,91,92,93,94,95,96,97,98,99,100,101,102,103} Some of the effects which have been proposed to lead to the improved performance are a reduction of the charge carrier traps at the dielectric interface,⁸⁹ an increased connectivity between the different grains,^{92,93,100,103} a reduction of domain boundaries,⁹ an enhanced delocalization of the molecular π -orbitals¹⁰¹ or a change in the surface charge carrier density.⁹⁸ However, often the concomitant occurrence of various changes in the film growth upon substrate functionalization (e.g. simultaneous changes of domain sizes and film structure) make the interpretation of surface treatment effects difficult, leading sometimes to different or even contradictory interpretations.⁷¹

Also for the improvement of the charge carrier injection several routes have been successfully applied. Among them we find the appropriate choice of contact metals (possibly asymmetric in drain and source electrodes) with their work functions fitting the semiconductor energy levels,^{77,78, 80,104} the functionalization of the contacts by self assembled monolayers in order to influence the film growth and reduce the grain boundaries at the contacts⁷² or to enhance the charge transfer,^{103, 105} and also the use of buffer layers at the contacts.^{10,106}

2.2 *Thin film growth*

2.2.1 Growth modes

Many of today's solid state devices are based on thin films, consequently making their growth a subject of high technological interest. The requirements for the film structure and morphology can vary from multilayers with layers of well defined thicknesses and sharp interfaces, for the use in e.g. quantum well structures; to three dimensional quantum dots for optoelectronic devices or single electron transistors. The control over the final film structures and morphologies is thus crucial for the device performance.

The theoretical background of film growth is very broad and has been studied under different approaches. Here, only a brief summary is presented focused on those aspects necessary for a basic understanding of the growth studies performed in the frame of this thesis. A thorough treatment of the underlying concepts can be found in references 107,108,109.

There are three basic scenarios that can describe the evolution of the film morphology upon film growth, as shown in Figure 2.7:

- i. One layer starts forming and the next layer never starts until the previous one is completed. This is called “layer-by-layer” or “Frank-Van der Merwe” growth.

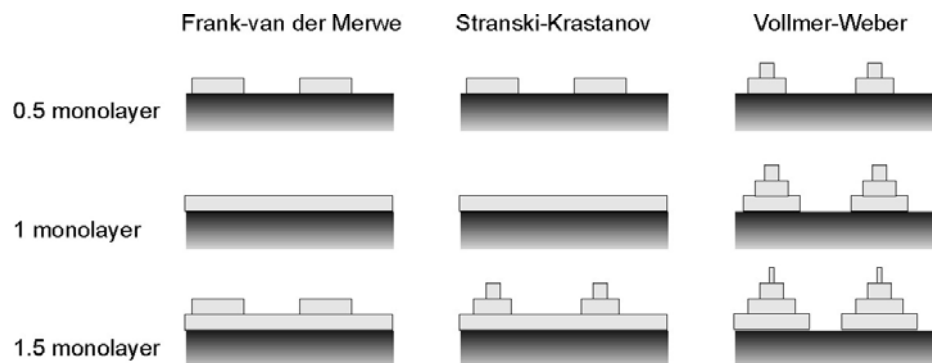


Figure 2.7. Schematic representation of the three different film growth scenarios.

ii. The deposited material assembles in islands. This is called “island” or “Vollmer-Weber” growth.

iii. Initially a layer-by-layer growth takes places, which switches to an island growth after a critical thickness. This is called “layer-plus-island” or “Stranski-Krastanov” growth.

One of the approaches to explain and predict the three different growth modes was derived by Bauer¹¹⁰ from the three macroscopic surface tensions of the involved interfaces, the overlayer-vacuum interface (γ_o), the overlayer-substrate interface (γ_i), and the substrate-vacuum interface (γ_s). If the surface tensions fulfill following condition:

$$\gamma_o + \gamma_i \leq \gamma_s \quad (2.3)$$

the system is energetically favored if the overlayer completely covers the surface, consequently leading to a layer-by-layer growth. If this is not the case, the substrate will be only partially covered, leading to an island growth. Stranski-Krastanov growth takes place if equation (2.3) is initially fulfilled below a critical thickness, thus following a layer-by-layer growth behavior, but only during the growth of the first layers. This growth scenario is often found in heteroepitaxial growth due to the formation of a strained overlayer. The strain accumulated in the overlayer can be considered to contribute to γ_i and shows a monotonic increase of energy with increasing film thickness. Thus, at a critical thickness an unstable situation is reached at which $\gamma_o + \gamma_i > \gamma_s$, and the system switches from layer-by-layer to island growth.

However, these considerations are only applicable in thermodynamic equilibrium, while film growth intrinsically implies being away from equilibrium. Consequently, only those systems which are close to equilibrium, i.e. high substrate temperature and low deposition flux, can be properly described by a thermodynamic approach. To account for growth scenarios arising from systems further from equilibrium (low substrate temperatures and high deposition rates), kinetic aspects have to be considered such as adsorption, desorption, diffusion or nucleation,^{107,108,109} as shown in Figure 2.8. Each of these processes has different activation barriers, and the final film morphology is determined by the hierarchy of their barriers together with the deposition rate and substrate temperature. By optimization of these two easily

controllable growth parameters, the kinetic aspects can be exploited to obtain desired metastable film morphologies.

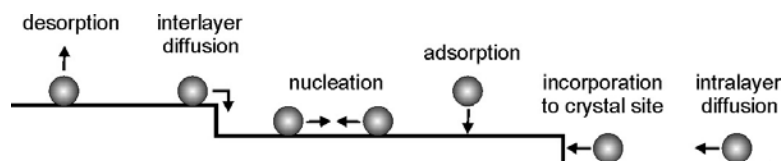


Figure 2.8. Kinetic processes occurring during film growth.

2.2.2 Organic molecular beam deposition (OMBD)

Among the various film growth techniques, molecular beam deposition (MBD) is widely used due to the good control it offers over the chemical purity, the atomically clean substrate and environment, film thickness, growth rate and substrate temperature. MBD consists on holding the substrate under ultra-high-vacuum (UHV) conditions, exposed to a beam of molecules in the vapor phase. The molecular beam is generated in so-called Knudsen cells, which typically consist on crucibles with a temperature sensor, surrounded by a heating filament and a thermal shielding. The material is put into the crucible and heated until sublimation (or evaporation, if it shows previously a liquid phase) takes place. The small opening of the crucible towards the UHV chamber generates a rather focused molecular beam, which can be blocked by a shutter and whose flux is controlled by the crucible temperature. The UHV environment allows the in-situ characterization of the substrate prior to deposition, or of the film during and/or after deposition, by techniques such as low energy electron diffraction (LEED), auger electron spectroscopy (AES), reflection high energy electron diffraction (RHEED), thermal desorption spectroscopy (TDS), UHV scanning tunneling microscopy (STM), etc.

When a film is grown on a crystalline substrate and the lattice mismatch between the structures of overlayer and substrate are small, the overlayer might adopt a strained structure in order to fit to the underlying substrate lattice. This process is called epitaxy. Its principles are already well established for inorganic systems,^{111,112}

and are being successfully exploited for the controlled growth of self-assembled nanostructures.^{113,114} However, the scenario is very different and far more complex for organic thin films, since the resulting structure depends on a much more delicate balance between the weak non-covalent intermolecular and molecule-substrate interactions.

In addition, there are other issues specific to organic films which can lead to quantitatively and qualitatively different growth behaviors not present in the conventional growth models for inorganic materials, such as the molecular size and shape.^{115,116} The highly anisotropic structures of most organic molecules introduce three additional orientational degrees of freedom relevant for the growth processes, their molecular packing, and for the physical film properties. Furthermore, the low molecular symmetry is generally translated into low symmetry crystalline structures (with monoclinic or triclinic cells), which in turn can lead to the formation of twin domains within the films. The large molecular sizes (in the nm range), as compared to the typical inorganic substrate lattice dimensions (in the Å range), induce the formation of translational domains. Besides, the lateral corrugation of the substrate potential is averaged over the molecular size, consequently smoothing and decreasing its corrugation as experienced by the molecule. Finally, the weak intermolecular forces (predominantly Van der Waals forces) lead in general to a rather smooth energetic landscape for the crystal packing with local minima of little energy differences, consequently favoring the formation of polymorphic phases and allowing larger strains to be accommodated in the given structures. All these multiple domains and polymorphic phases are additional sources of disorder to those already known from inorganic systems (vacancies, dislocations, impurities...) and thus hamper the achievement of organic devices with high performance. Additional efforts are needed to find routes to control the film growth and obtain the desired structures and morphologies.

Obviously, the substrate plays a major role. Strongly interacting substrates such as metals might induce an ordering of the organic films in terms of epitaxial or quasiepitaxial growth.^{117,118,119} However, a strong interaction reduces the molecular diffusion length, thus inducing a high grain density and small domains. In addition, the strain accumulated in these epitaxially grown pseudomorphic films, might lead to a change from layer-by-layer to island growth after a critical thickness for strain

release, or simply change to energetically more favorable structures at higher thicknesses, when the substrate influence gets weaker.^{117,118,120,121} On the other hand, on weakly interacting surfaces, the dominating intermolecular interactions as compared to the molecule-substrate interactions can lead to island growth, and the absence of any “ordering” effect by the substrate can lead to the formation of films consisting in crystalline powders. Thus, the tuning of the molecule-substrate interactions is a key aspect towards a controlled growth of organic films. Self-assembling monolayers (SAMs), whose basic principles will be introduced in the next section, have emerged as one of the most promising routes to modify and tailor the surface properties according to our needs and are being recently explored to modify the growth of organic semiconducting thin films.^{122,123,124,125,126}

2.2.3 Self-assembling monolayers (SAMs)

Self-assembling monolayers are ordered molecular assemblies formed spontaneously by the adsorption of a surfactant on a solid surface. They can be grown either under UHV conditions from the gas phase or simply from solution. The former has the advantages of the clean and well controllable environment together with the large number of in-situ characterization techniques available in UHV systems, while the ease of preparation is the most appealing aspect of the latter.

Figure 2.9 shows schematically the preparation process from solution, which is the method used in this thesis. In the molecular structure, three main parts can be distinguished (Figure 2.9):

- i. Headgroup: it is the molecular part that binds to the substrate. The major classification of the SAMs is made according to their headgroup, since its chemical specificity defines the substrates to which it shows affinity and can be bound. The most popular and best studied SAMs are thiols on Au, although they grow on other metals such as Ag, Cu, or Hg as well. Another well-studied group is formed by SAMs with their headgroup based on silanes, which bind to hydroxilated surfaces such as SiO₂ or Al₂O₃.

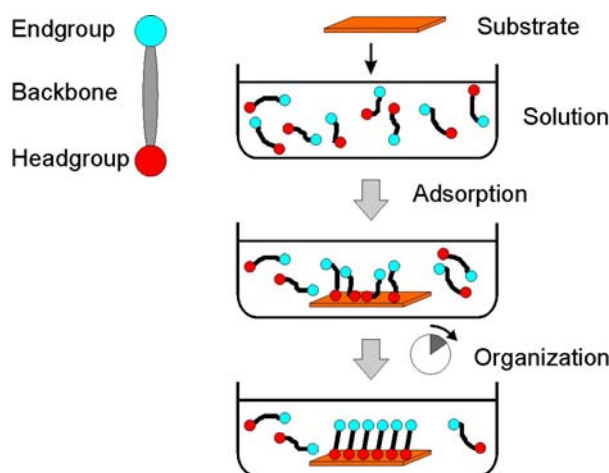


Figure 2.9. Schematic molecular structure and SAM growth process from solution.

ii. Endgroup: this is the final part of the molecule that defines the new surface. The surface properties basically depend on the endgroup and can thus be tuned by its appropriate choice.

iii. Chain or backbone: it is the intermediate part between headgroup and endgroup.

All the three parts can be changed or modified according to our needs, resulting in different substrates on which they can be prepared (depending on the headgroup), on different film structures (depending on the whole molecule as well as on the substrate), or different surface properties (determined mainly by the endgroup) such as hydrophobicity, adhesion, surface energy, etc. This possibility of designing surfaces with specific properties has motivated a vast number of studies in the field of self-assembling monolayers. Among the most interesting applications of SAMs, it can be cited their use in optoelectronic devices, as corrosion inhibitors, wear protection, in biorelated applications such as specific adsorption sites for biomolecules, or to serve themselves as substrates and, by changing the surface properties, tune the growth of films and crystals, or many others.¹²⁷ Furthermore, SAMs offer attractive opportunities for lateral structuring and patterning, since it can act as positive or negative resist in lithography,¹²⁸ or be grown itself with laterally defined structures by micro-contact printing,^{129,130} or “dip-pen” lithography.^{131,132} This further increases its interest for several of the applications mentioned above.

For a broader view on the general concepts of self-assembling monolayers, or to get a deeper insight into the growth or other processes related to the SAMs, we refer the reader to references 127,133,134.

In the work presented in this thesis, OTMS has been employed to functionalize SiO_2 and therewith influence the growth of the organic semiconducting thin films deposited on top. The OTMS molecule ($\text{CH}_3-(\text{CH}_2)_{17}-\text{Si}(\text{O}-\text{CH}_3)_3$) consists of a headgroup formed by a silane with three methoxyl groups, an alkane with a chain length of 17 carbon atoms as backbone, and a methyl endgroup (Figure 2.10a).

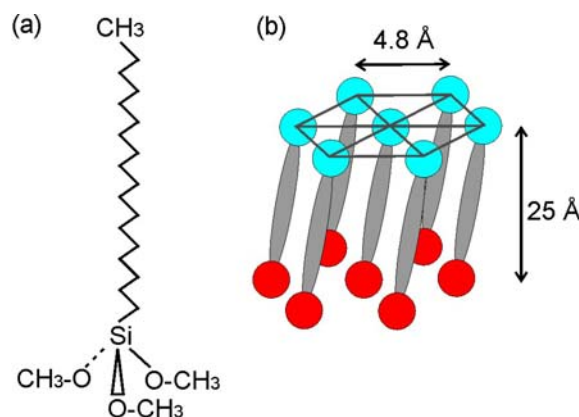


Figure 2.10. (a) Molecular structure of OTMS. (b) Hexagonal crystalline structure of the OTMS self-assembled monolayer.

Prior to the SAM formation the molecule is hydrolyzed, substituting the methoxyl by hydroxyl groups, which, during the self-assembly process, form bonds with other hydroxyl groups (generating water molecules as secondary reaction products) both from the substrate surface or other molecules (cross-links). The binding of the molecules not only to the substrate but also between each other leads to a high thermal stability of silane based SAMs.¹³⁴ However, since the bond length between neighboring silanes is lower than the equilibrium distance between alkane chains, cross-links introduce tensions, consequently reducing the order within the films.¹³⁴ The resulting structure for OTMS self-assembled monolayers is a layer with a height of about 25 Å, with the molecules arranged in a hexagonal packing with a lattice parameter of 4.8 Å and mean lateral domain sizes of about 80 Å (Figure 2.10b).^{135,136,137} The functionalization of SiO_2 by OTMS reduces the surface energy

from 78 to 20 mN/m^{138,139} and consequently influences the growth process of organic semiconducting thin films on top. This has an important impact on the physical film properties, as will be shown in section 4.3.

References

- ¹ P. Atkins, R. Waser, Organic molecules – electronic structures, properties and reactions, Wiley-VCH, Nanoelectronics and information technology 2nd Ed. (p. 127) 2005 Ed. R. Waser
- ² M. I. Alonso, M. Garriga, J. O. Ossó, F. Schreiber, E. Barrena, H. Dosch, Strong optical anisotropies of F₁₆CuPc thin films studied by spectroscopic ellipsometry, *J. Chem. Phys.* **119**, 6335 (2003)
- ³ F. Gamier, A. Yassar, R. Hajlaoui, G. Horowitz, F. Deloffre, B. Serve, S. Ries, P. Alnot, Molecular engineering of organic semiconductors: design of self-assembly properties in conjugated thiophene oligomers, *J. Am. Chem. Soc.* **115**, 8716 (1993)
- ⁴ V. C. Sundar, J. Zaumseil, V. Podzorov, E. Menard, R. L. Willet, T. Someya, M. E. Gershenson, J. A. Rogers, Elastomeric transistor stamps: reversible probing of charge transport in organic crystals, *Science* **303**, 1644 (2004)
- ⁵ Ed. C.C. Leznoff, A. B. P. Lever, Phthalocyanines, properties and applications, VCH Publishers, New York, Weinheim, Cambridge (1996)
- ⁶ Ed. H. S. Nalwa, Supramolecular photosensitive and electroactive materials, Academic Press (2001)
- ⁷ C. R. Newman, C. D. Frisbie, D. A. da Silva Filho, J.- L. Brédas, P. C. Ewbank, K. R. Mann, Introduction to organic thin film transistors and design of n-channel organic semiconductors, *Chem. Mater.* **16**, 4436 (2004)
- ⁸ Z. Bao, A. J. Lovinger, J. Brown, New air-stable n-channel organic thin-film transistors, *J. Am. Chem. Soc.* **120**, 207 (1998)
- ⁹ D. G. de Oteyza, E. Barrena, J. O. Ossó, H. Dosch, S. Meyer, J. Pflaum, Controlled enhancement of the electron field-effect mobility of F₁₆CuPc thin-film transistors by the use of functionalized SiO₂ substrates, *Appl. Phys. Lett.* **87**, 183504 (2005)
- ¹⁰ S. Hoshino, S. Nagamatsu, M. Chikamatsu, M. Misaki, Y. Yoshida, N. Tanigaki, K. Yase, LiF/Al bilayer source and drain electrodes for n-channel organic field-effect transistors, *Synth. Met.* **137**, 953 (2003)
- ¹¹ Y. Oh, S. Pyo, M. H. Yi, S.-K. Kwon, N-type organic field-effect transistor using polymeric blend gate insulator with controlled surface properties, *Org. Electron.* **5**, 135 (2005)
- ¹² Q. Tang, H. Li, Y. Liu, W. Hu, High performance air-stable n-type transistors with an asymmetrical device configuration based on organic single-crystalline submicrometer/nanometer ribbons, *J. Am. Chem. Soc.* DOI 10.1021/ja064476f (2006)
- ¹³ J. Wang, H. Wang, X. Yan, H. Huang, D. Jin, J. Shi, Y. Tang, D. Yan, Heterojunction ambipolar organic transistors fabricated by a two-step vacuum deposition process, *Adv. Func. Mat.* **16**, 824 (2006)
- ¹⁴ H. Wang, J. Wang, X. Yan, J. Shi, H. Tian, Y. Geng, D. Yan, Ambipolar organic field-effect transistors with air-stability, high mobility, and balanced transport, *Appl. Phys. Lett.* **88**, 133508 (2006)
- ¹⁵ J. Wang, H. Wang, X. Yan, H. Huang, D. Yan, Organic heterojunction and its application for double channel field-effect transistors, *Appl. Phys. Lett.* **87**, 093507, (2005)
- ¹⁶ J. Wang, H. Wang, X. Yan, H. Huang, D. Yan, Air-stable ambipolar organic field-effect transistors based on phthalocyanine composites heterojunction, *Chem. Phys. Lett.* **407**, 87 (2005)
- ¹⁷ R. Ye, M. Baba, Y. Oishi, K. Mori, K. Suzuki, Air-stable ambipolar organic field-effect transistors based on an organic homostructure, *Appl. Phys. Lett.* **86**, 253505 (2005)

-
- ¹⁸ Y.-Y. Lin, A. Dodabalapur, R. Sarpeshkar, Z. Bao, W. Li, K. Baldwin, V. R. Raju, H. E. Katz, Organic complementary ring oscillators, *Appl. Phys. Lett.* **74**, 2714 (1999)
- ¹⁹ B. Crone, A. Dodabalapur, Y.-Y. Lin, R. W. Filas, Z. Bao, A. LaDuca, R. Sarpeshkar, H. E. Katz, W. Li, Large scale complementary integrated circuits based in organic transistors, *Nature* **403**, 521 (2000)
- ²⁰ B. Crone, A. Dodabalapur, R. Sarpeshkar, R. W. Filas, Y.-Y. Lin, Z. Bao, J. H. O'Neill, W. Li, H. E. Katz, design and fabrication of organic complementary circuits, *J. Appl. Phys.* **89**, 5125 (2001)
- ²¹ J. Reynaert, V. I. Archipov, P. Heremans, J. Poortmans, Photomultiplication in disordered unipolar organic materials, *Adv. Func. Mater.* **16**, 784 (2006)
- ²² T. Basova, E. Kol'tsov, A. Hassan, A. Tsagorodskaya, A. Ray, I. Igumenov, Thin films of copper hexadecafluorophthalocyanine CuPcF₁₆, *Phys. Stat. Sol. (b)* **1** (2005)
- ²³ H. Tada, H. Touda, M. Takada, K. Matsushige, Field-effect mobility of F₁₆CuPc films in various gas atmospheres, *J. Porphyr. Phthal.* **3**, 667 (1999)
- ²⁴ B. Crone, A. Dodabalapur, A. Gelperin, L. torsi, H. E. Katz, A. J. Lovinger, Z. Bao, Electronic sensing of vapors with organic transistors, *Appl. Phys. Lett.* **778**, 2229 (2001)
- ²⁵ J. M. Robertson, An x-ray study of the structure of the phthalocyanines. Part I. The metal free, nickel, copper, and platinum compounds, *J. Chem. Soc.* 615 (1935)
- ²⁶ J. M. Robertson, An x-ray study of the phthalocyanines. Part II. Quantitative structure determination of the metal free compound, *J. Chem. Soc.* 1195 (1936)
- ²⁷ C. J. Brown, Crystal structure of β -copper phthalocyanine, *J. Chem. Soc. A* 2488 (1968)
- ²⁸ J. O. Ossó, PhD Thesis.
- ²⁹ R. D. Gould, Structure and electrical conduction properties of phthalocyanine thin-films, *Coord. Chem. Rev.* **156**, 237 (1996)
- ³⁰ S. M. Bayliss, S. Heutz, G. Rumbles, T. S. Jones, thin film properties and surface morphology of metal free phthalocyanine films, *Phys. Chem. Chem. Phys.* **1**, 3673 (1999)
- ³¹ O. Berger, W.-J. Fischer, B. Adolphi, S. Tierbach, V. Melev, J. Schreiber, Studies on phase transformations of Cu-phthalocyanine thin-films, *J. Mat. Sci.: Mat. Electron.* **11**, 331 (2000)
- ³² G. Maggioni, A. Quaranta, S. Carturan, A. Patelli, M. Tonezzer, R. Ceccato, G. Della Mea, Deposition of copper phthalocyanine by glow-discharge-induced sublimation, *Chem. Mater.* **17**, 1895 (2005)
- ³³ W. Y. Tong, A. B. Djuricic, M. H. Xie, A. C. M. Ng, K. Y. Cheung, W. K. Chan, Y. H. Leung, H. W. Lin, S. Gwo, Metal phthalocyanine nanoribbons and nanowires, *J. Phys. Chem B* **110**, 17406 (2006)
- ³⁴ J. Pflaum, S. Hirschmann, W. Frey, N. Karl, in preparation.
- ³⁵ A. Hoshino, S. Isoda, T. Kobayashi, Epitaxial growth of organic crystals on organic substrates polynuclear aromatic hydrocarbons, *J. Cryst. Growth* **115**, 826 (1991)
- ³⁶ A. C. Dürr, N. Koch, M. Kelsch, A. Rühm, J. Ghijsen, R. L. Johnson, J.-J. Pireaux, J. Schwartz, F. Schreiber, H. Dosch, A. Kahn, Interplay between morphology, structure and electronic properties at diindenoperylene-gold interfaces, *Phys. Rev. B* **68**, 115428 (2003)
- ³⁷ A. C. Dürr, F. Schreiber, M. Münch, N. Karl, B. Krause, V. Kruppa, H. Dosch, High structural order in thin films of the organic semiconductor diindenoperylene, *Appl. Phys. Lett.* **81**, 2276 (2002)
- ³⁸ A. C. Dürr, F. Schreiber, K. A. Ritley, V. Kruppa, J. Krug, H. Dosch, B. Struth, Rapid roughening in thin film growth of the organic semiconductor diindenoperylene (DIP), *Phys. Rev. Lett.* **90**, 016104 (2003)
- ³⁹ X. Zhang et al. In preparation.
- ⁴⁰ S. Kowarik, A. Gerlach, S. Sellner, F. Schreiber, L. Cavalcanti, O. Konovalov, Real-time observation of structural and orientational transitions during growth of organic thin films, *Phys. Rev. Lett.* **96**, 125504 (2006)
- ⁴¹ N. Karl, Charge carrier transport in organic semiconductors, *Synth. Met.* **133-134**, 649 (2003)

-
- ⁴² J. Pflaum et al. In preparation.
- ⁴³ R. Schmechel, M. Ahles, H. Von Seggern, A pentacene ambipolar transistor: Experiment and theory, *J. Appl. Phys.* **98**, 084511 (2005)
- ⁴⁴ T. Yasuda, T. Goto, K. Fujita, T. Tsutsui, Ambipolar pentacene field-effect transistors with calcium source-drain electrodes, *Appl. Phys. Lett.* **85**, 2098 (2004)
- ⁴⁵ Th. B. Singh, P. Senkarabacak, N. S. Sariciftci, A. Tanda, C. Lackner, R. Hagelauer, G. Horowitz, Organic inverter circuits employing ambipolar pentacene field-effect transistors, *Appl. Phys. Lett.* **89**, 033512 (2006)
- ⁴⁶ R. Ruiz, D. Choudhary, B. Nickel, T. Toccoli, K.-C. Chang, A. C. Mayer, P. Clancy, J. M. Blakely, R. L. Headrick, S. Iannotta, G. G. Malliaras, Pentacene thin film growth, *Chem. Mater.* **16**, 4497 (2004)
- ⁴⁷ S. E. Fritz, S. M. Martin, C. D. Frisbie, M. D. Ward, M. F. Toney, Structural characterization of a pentacene monolayer on an amorphous SiO₂ substrate with grazing incidence X-ray diffraction, *J. Am. Chem. Soc.* **126**, 4084 (2004)
- ⁴⁸ R. Ruiz, A. C. Mayer, G. G. Malliaras, B. Nickel, G. Scoles, A. Kazimirov, H. Kim, R. L. Headrick, Z. Islam, Structure of pentacene thin films, *Appl. Phys. Lett.* **85**, 4926 (2004)
- ⁴⁹ C. C. Mattheus, A. B. Dros, J. Baas, G. T. Oostergetel, A. Meetsma, J. L. de Boer, T. T.M. Palstra, Identification of polymorphs of pentacene, *Synth. Met.* **138**, 475 (2003)
- ⁵⁰ R. Ruiz, B. Nickel, N. Koch, L. C. Feldman, R. F. Haglund, A. Kahn, G. Scoles, Pentacene ultrathin film formation on reduced and oxidized Si surfaces, *Phys. Rev. B* **67**, 125406 (2003)
- ⁵¹ R. Ruiz, B. Nickel, N. Koch, L. C. Feldman, R. F. Haglund, A. Kahn, F. Family, G. Scoles, Dynamic scaling, island size distribution and morphology in the aggregation regime of sub-monolayer pentacene films, *Phys. Rev. Lett.* **91**, 136102 (2003)
- ⁵² A. C. Mayer, R. Ruiz, R. L. Headrick, A. Kazimirov, G. G. Malliaras, Early stages of pentacene film growth on silicon oxide, *Org. Electron.* **5**, 257 (2004)
- ⁵³ R. B. Campbell, J. M. Robertson, J. Trotter, The crystal structure of hexacene, and a revision of the crystallographic data for tetracene and pentacene. *Acta Crystallogr.* **15**, 289 (1962)
- ⁵⁴ A. Tsumura, K. Koezuka, T. Ando, Macromolecular electronic device: field effect transistor with a polythiophene thin film, *Appl. Phys. Lett.* **48**, 1210 (1986)
- ⁵⁵ G. Horowitz, D. Fichou, X. Z. Peng, Z. G. Xu, F. Garnier, A field effect transistor based on conjugated alpha-sexiphenyl, *Sol. State Commun.* **72**, 381 (1989)
- ⁵⁶ G. Horowitz, Organic thin-film transistors: from theory to real devices, *J. Mater. Res.* **19**, 1946 (2004)
- ⁵⁷ Ed. D. A. Neamen, Semiconductor physics and devices: basic principles, Irwin, Chicago (1996)
- ⁵⁸ S. M. Sze, Physics of semiconductor devices, Wiley and Son, New York (1981)
- ⁵⁹ M. E. Gershenson, V. Podzorov, A. F. Morpurgo, Electronic transport in single-crystal organic transistors, *Rev. Mod. Phys.* **78**, 973 (2006)
- ⁶⁰ C. D. Dimitrakopoulos, A. R. Brown, A. Pomp, Molecular beam deposited thin films of pentacene for organic field effect transistor applications, *J. Appl. Phys.* **80**, 2501 (1996)
- ⁶¹ T. Heim, K. Lmimouni, D. Vuillaume, Ambipolar charge injection and transport in a single pentacene monolayer island, *Nanolett.* **4**, 2145 (2004)
- ⁶² R. W. I. De Boer, M. E. Gershenson, A. F. Morpurgo, V. Podzorov, Organic single-crystal field-effect transistors, *Phys. Stat. Sol. (a)* **201**, 1302 (2004)
- ⁶³ H. E. Katz, C. Klov, V. sundar, J. Zaumseil, A. L. Briseno, Field-effect transistors made from macroscopic single crystals of tetracene and related semiconductors on polymer dielectrics, *J. Mater. Res.* **19**, 1995 (2004)
- ⁶⁴ J. Niemax, A. K. Tripathi, J. Pflaum, Comparison of the electronic properties of sublimation- and vapor-Bridgman-grown crystals of tetracene, *Appl. Phys. Lett.* **86**, 122105 (2005)

-
- ⁶⁵ T. W. Kelley, C. D. Frisbie, Gate voltage dependent resistance of a single organic semiconductor grain boundary, *J. Phys. Chem. B* **105**, 4538 (2001)
- ⁶⁶ A. B. Chwang, C. D. Frisbie, Temperature and gate voltage dependent transport across a single organic semiconductor grain boundary, *J. Appl. Phys.* **90**, 1342 (2001)
- ⁶⁷ T. Hassenkam, D. R. Greeve, T. Bjornholm, direct visualization of the nanoscale morphology of conducting polythiophene monolayers studied by electrostatic force microscopy, *Adv. Mater.* **13**, 631 (2001)
- ⁶⁸ T. W. Kelley, E. L. Granstrom, C. D. Frisbie, Conducting probe atomic force microscopy: a characterization tool for molecular electronics, *Adv. Mater.* **3**, 261 (1999)
- ⁶⁹ N. Karl, K.-H. Kraft, J. Marktanner, M. Münch, F. Schatz, R. Stehle, H.-M. Uhde, Fast electronic transport in organic molecular solids?, *J. Vac. Sci. Tech. A* **17**, 2318 (1999)
- ⁷⁰ N. Karl, The influence of doping on charge carrier transport in organic molecular crystals, *Chem. Scr.* **17**, 201 (1981)
- ⁷¹ J. Veres, S. Ogier, G. Lloyd, D. de Leeuw, Gate insulators in organic field-effect transistors, *Chem. Mater.* **16**, 4543 (2004)
- ⁷² I. Kyminsis, C. D. Dimitrakopoulos, S. Purushothaman, High performance bottom electrode organic thin film transistors, *IEEE Trans. Elec. Dev.* **48**, 1060 (2001)
- ⁷³ T. Muck, J. Fritz, V. Wagner, Better bottom contact properties in organic field effect transistors with ultrathin layers, *Appl. Phys. Lett.* **86**, 232101 (2005)
- ⁷⁴ G. B. Blanchet, C. R. Fincher, M. Lefenfeld, Contact resistance in organic thin film transistors, *Appl. Phys. Lett.* **84**, 296 (2004)
- ⁷⁵ K. P. Puntambekar, P. V. Pesavento, C. D. Frisbie, Surface potential profiling and contact resistance measurements on operating pentacene thin film transistors by Kelvin probe microscopy, *Appl. Phys. Lett.* **83**, 5539 (2003)
- ⁷⁶ K. Seshadri, C. D. Frisbie, Potentiometry of an operating organic semiconducting field effect transistor, *Appl. Phys. Lett.* **78**, 993 (2001)
- ⁷⁷ J. A. Nichols, D. J. Gundlach, T. N. Jackson, Potential imaging of pentacene organic thin film transistors, *Appl. Phys. Lett.* **83**, 2366 (2003)
- ⁷⁸ L. Bürgi, T. J. Richards, R. H. Friend, H. Sirringhaus, Close look at charge carrier injection in polymer field effect transistors, *J. Appl. Phys.* **94**, 6129 (2003)
- ⁷⁹ R. A. Street, A. Salleo, Contact effects in polymer transistors, *Appl. Phys. Lett.* **81**, 2887 (2002)
- ⁸⁰ K. Müller, A. Goryachko, Y. Burkov, C. Schwietz, M. Ratzke, J. Köble, J. Reif, D. Schmeisser, Scanning Kelvin probe and photoemission electron microscopy of organic source-drain structures, *Synth. Meth.* **146**, 377 (2004)
- ⁸¹ S. R. Forrest, The path to ubiquitous and low cost organic electronic appliances on plastic, *Nature* **428**, 911 (2004)
- ⁸² G. Horowitz, M. E. Hajlaoui, grain size dependent mobility in polycrystalline organic field-effect transistors, *Synth. Met.* **122**, 185 (2001)
- ⁸³ A. Dodalabatur, L. Torsi, H. E. Katz, Organic transistors: two-dimensional transport and improved electrical characteristics, *Science* **268**, 270 (1995)
- ⁸⁴ M. J. Loiacono, E. L. Granstrom, C. D. Frisbie, Investigation of charge transport in thin, doped sexithiophene crystals by conducting probe atomic force microscopy, *J. Phys. Chem. B* **102**, 1679 (1998)
- ⁸⁵ T. Muck, V. Wagner, U. Bass, M. Leufgen, J. Geurts, L.W. Molenkamp, In situ electrical characterization of DH4T field-effect transistors, *Synth. Met.* **146**, 317 (2004)
- ⁸⁶ F. Dinelli, M. Murgia, P. Levy, M. Cavallini, F. Biscarini, Spatially correlated charge transport in organic thin film transistors, *Phys. Rev. Lett.* **92**, 116802 (2004)

-
- ⁸⁷ R. Ruiz, A. Papadimitratos, A. C. Mayer, G. G. Malliaras, Thickness dependence of mobility in pentacene thin film transistors, *Adv. Mater.* **17**, 1795 (2005)
- ⁸⁸ Y.-Y. Lin, D. J. Gundlach, S. F. Nelson, T. N. Jackson, Stacked pentacene layer organic thin film transistors with improved characteristics, *IEEE Elec. Dev. Lett.* **18**, 606 (1997)
- ⁸⁹ J. Collet, O. Tharaud, C. Legrand, A. Chapoton, D. Vuillaume, Performances of sexithiophene based thin film transistors using self-assembled monolayers, *Mat. Res. Soc. Symp. Proc.* **488**, 407 (1998)
- ⁹⁰ J. Collet, O. Tharaud, A. Chapoton, D. Vuillaume, Low-voltage, 30 nm channel length, organic transistors with a self-assembled monolayer as gate insulating thin film, *Appl. Phys. Lett.* **76**, 1941 (2000)
- ⁹¹ J. Xue, S. R. Forrest, Organic thin-film transistors based on bis(1,2,5-thiadiazolo)-p-quinobis(1,3-dithiole), *Appl. Phys. Lett.* **79**, 3714 (2001)
- ⁹² D. J. Gundlach, J. A. Nichols, L. Zhou, T. N. Jackson, Thin-film transistors based on well-ordered thermally evaporated naphthacene films, *Appl. Phys. Lett.* **80**, 2925 (2002)
- ⁹³ M. Shtein, J. Mapel, J. B. Benzinger, S. R. Forrest, Effects of film morphology and gate dielectric surface preparation on the electrical characteristics of organic-vapor-phase-deposited pentacene thin-film transistors, *Appl. Phys. Lett.* **81**, 2668 (2002)
- ⁹⁴ D. Knipp, R. A. Street, A. Völkel, J. Ho, Pentacene thin film transistors on inorganic dielectrics: Morphology, structural properties, and electronic transport, *J. Appl. Phys.* **93**, 347 (2003)
- ⁹⁵ T. W. Kelley, L. D. Boardman, T. D. Dunbar, D. V. Muryes, M. P. Pellerite, T. P. Smith, High performance OTFTs using surface modified alumina dielectrics, *J. Phys. Chem. B* **107**, 5877 (2003)
- ⁹⁶ T. C. Gorjanc, I. Lévesque, M. D'Iorio, Organic field effect transistors based on modified oligo-p-phenylenes, *Appl. Phys. Lett.* **84**, 930 (2004)
- ⁹⁷ K. Shankar, T. N. Jackson, Morphology and electrical transport in pentacene films on silylated oxide surfaces, *J. Mater. Res.* **19**, 2003 (2004)
- ⁹⁸ S. Kobayashi, T. Nishikawa, T. Takenobu, S. Mori, T. Shimoda, T. Mitani, H. Shimotani, N. Yoshimoto, S. Ogawa, Y. Iwasa, Control of carrier density by self-assembled monolayers in organic field-effect transistors, *Nat. Mater.* **3**, 317 (2004)
- ⁹⁹ S. C. Lim, S. H. Kim, J. H. Lee, M. K. Kim, D. J. Kim, T. Zyung, Surface-treatment effects on organic thin-film transistors, *Synth. Met.* **148**, 75 (2005)
- ¹⁰⁰ S. Y. Yang, K. Shin, C. E. Park, The effect of gate-dielectric surface energy on pentacene morphology and organic field-effect transistor characteristics, *Adv. Func. Mater.* **15**, 1806 (2005)
- ¹⁰¹ S. J. Kang, Y. Yi, C. Y. Kim, C. N. Whang, T. A. Callcott, K. Krochak, A. Moewes, G. S. Chang, Analysis of octadecyltrichlorosilane treatment of organic thin-film transistors using soft x-ray fluorescence spectroscopy, *Appl. Phys. Lett.* **86**, 232103 (2005)
- ¹⁰² A. Facchetti, M.-H. Yoon, T. J. Marks, Gate dielectrics for organic field-effect transistors: new opportunities for organic electronics, *Adv. Mater.* **17**, 1705 (2005)
- ¹⁰³ K. S. Pyo, C. K. Song, The effects of simultaneous treatment of SiO₂ gate and Au electrode with octadecyltrichlorosilane and charge transfer molecules on characteristics of pentacene thin film transistors, *Thin Sol. Films* **485**, 230 (2005)
- ¹⁰⁴ M. Leufgen, U. Bass, T. Muck, T. Borzenko, G. Schmidt, J. Geurts, V. Wagner, L. W. Molenkamp, Optimized sub-micron organic thin film transistors: the influence of contacts and oxide thickness, *Synth. Met.* **146**, 341 (2004)
- ¹⁰⁵ D. J. Gundlach, L. Jia, T. N. Jackson, Pentacene TFT with improved linear region characteristics using chemically modified source and drain electrodes, *IEEE Elec. Dev. Lett.* **22**, 571 (2001)
- ¹⁰⁶ P. K. H. Ho, J.-S. Kim, J. H. Burroughes, H. Becker, S. F. Y. Li, T. M. Brown, F. Cacialli, R. H. Friend, Molecular-scale interface engineering for polymer light-emitting diodes, *Nature* **404**, 481 (2000)
- ¹⁰⁷ A. Pimpinelli, J. Villain, Physics of crystal growth, Cambridge University Press, Cambridge (1999)

-
- ¹⁰⁸ Z. Zhang, M. G. Lagally, Atomistic processes in the early stages of thin-film growth, *Science* **276**, 377 (1997)
- ¹⁰⁹ J. A. Venables, G. D. T. Spiller, M. Hanbücken, Nucleation and growth of thin films, *Rep. Prog. Phys.* **47**, 399 (1984)
- ¹¹⁰ E. Bauer, Phänomenologische Theorie der Kristallabscheidung an Oberflächen, *I. Z. Kristallogr.* **110**, 372 (1958)
- ¹¹¹ Ed. J. W. Matthews, Epitaxial growth, Academic, New York (1975)
- ¹¹² Ed. A.-L. Barabási, M. Krishnamurthy, Epitaxial growth-Principles and applications, Materials Research Society symposium proceedings, San Francisco (1999)
- ¹¹³ R. Nötzel, Self-organized growth of quantum dot structures, *Semicond. Sci. Tech.* **11**, 1365 (1996)
- ¹¹⁴ J. Stangl, V. Holý, G. Bauer, Structural properties of self-organized semiconductor nanostructures, *Rev. Mod. Phys.* **76**, 725 (2004)
- ¹¹⁵ Ed. W. Brütting, Physics of organic semiconductors, Wiley-VCH Verlag, Weinheim (2005)
- ¹¹⁶ F. Schreiber, Organic molecular beam deposition: growth studies beyond the first monolayer, *Phys. Stat. Sol. (a)* **201**, 1037 (2004)
- ¹¹⁷ S. R. Forrest, Ultrathin organic films grown by organic molecular deposition and related techniques, *Chem. Rev.* **97**, 1793 (1997)
- ¹¹⁸ G. Witte, C. Wöll, Growth of aromatic molecules on solid substrates for applications in organic electronics, *J. Mater. Res.* **19**, 1889 (2004)
- ¹¹⁹ D. E. Hooks, T. Fritz, M. D. Ward, Epitaxy and molecular organization on solid substrates, *Adv. Mater.* **13**, 227 (2001)
- ¹²⁰ P. Fenter, F. Schreiber, L. Zhou, P. Eisenberger, S. R. Forrest, In situ studies of morphology, strain and growth modes of a molecular organic thin film, *Phys. Rev. B* **56**, 3046 (1997)
- ¹²¹ H. Peisert, I. Biswas, L. Zhang, M. Knupfer, M. Hanack, D. Dini, M.J. Cook, I. Chambrier, T. Schmidt, D. Batchelor, T. Chassé, Orientation of substituted phthalocyanines on polycrystalline gold: distinguishing between the first layers and thin films, *Chem. Phys. Lett.* **403**, 1 (2005)
- ¹²² F. Schreiber, Self-assembled monolayers: from “simple” model systems to biofunctionalized interfaces, *J. Phys. – Condens. Mat.* **16**, R881 (2004)
- ¹²³ X. Liu, S. H. Mohamed, J. M. Ngaruiya, M. Wuttig, T. Michely, Modifying the growth of organic thin films by a self-assembled monolayer, *J. Appl. Phys.* **93**, 4852 (2003)
- ¹²⁴ M. C. Gerstenberg, F. Schreiber, T. Y. B. Leung, G. Bracco, S. R. Forrest, G. Scoles, Organic semiconducting thin film growth on an organic substrate: 3,4,9,10-perylenetetracarboxylic dianhydride on a monolayer of decanethiol self-assembled on Au(111), *Phys. Rev. B* **61**, 7678 (2000)
- ¹²⁵ R. Staub, M. Toerker, T. Fritz, T. Schmitz-Hübsch, F. Sellam, K. Leo, Scanning tunneling microscope investigation of organic heterostructures prepared by a combination of self-assembly and molecular beam epitaxy, *Surf. Sci.* **445**, 368 (2000)
- ¹²⁶ F. Schreiber, M. C. Gerstenberg, B. Edinger, B. Toperberg, S. R. Forrest, G. Scoles, H. Dosch, Phase sensitive surface x-ray scattering study of a crystalline organic-organic heterostructure, *Physica B* **283**, 75 (2000)
- ¹²⁷ F. Schreiber, Self-assembled monolayers: from “simple” model systems to biofunctionalized interfaces, *J. Phys. – Condens. Mat.* **16**, R881 (2004)
- ¹²⁸ T. Felgenhauer, C. Yan, W. Geyer, H.-T. Rong, A. Götzhäuser, M. Buck, Electrode modification by electron-induced patterning of aromatic self-assembled monolayers, *Appl Phys. Lett.* **79**, 3323 (2001)
- ¹²⁹ J. L. Wilbur, A. Kumar, E. Kim, G. M. Whitesides, Microfabrication by microcontact printing of self-assembled monolayers, *Adv. Mater.* **6**, 600 (1994)
- ¹³⁰ J. L. Wilbur, A. Kumar, H. A. Biebuyck, E. Kim, G. M. Whitesides, Microcontact printing of self-assembled monolayers: applications in microfabrication, *Nanotech.* **7**, 452 (1996)

-
- ¹³¹ R. D. Piner, J. Zhu, F. Xu, S. H. Hong, C. A. Mirkin, „Dip-pen“ nanolithography, *Science* **283**, 661 (1999)
- ¹³² S. Hong, C. A. Mirkin, A nanoplotter with both parallel and serial writing capabilities, *Science* **288**, 1808 (2000)
- ¹³³ A. Ulman, Formation and structure of self-assembled monolayers, *Chem. Rev.* **96**, 1533 (1996)
- ¹³⁴ F. Schreiber, Structure and growth of self-assembling monolayers, *Prog. Surf. Sci.* **65**, 151 (2000)
- ¹³⁵ I. M. Tidswell, B. M. Ocko, P. S. Pershan, S. R. Wasserman, G. M. Whitesides, J. D. Axe, X-ray specular reflection studies of silicon coated by organic monolayers (alkylsiloxanes), *Phys. Rev. B* **41**, 1111 (1990)
- ¹³⁶ A. Baptiste, A. Gibaud, J. F. Bardeau, K. Wen, R. Maoz, J. Sagiv, B. M. Ocko, X-ray, micro-Raman, and infrared spectroscopy structural characterization of self-assembled multilayer silane films with variable numbers of stacked layers, *Langmuir* **18**, 3916 (2002)
- ¹³⁷ Y. Wang, M. Lieberman, Growth of ultrasmooth octadecyltrichlorosilane self-assembled monolayers on SiO₂, *Langmuir* **19**, 1159 (2003)
- ¹³⁸ J. Collet, O. Tharaud, A. Chapoton, D. Viillaume, Low-voltage, 30 nm channel length, organic transistors with a self-assembled monolayer as gate insulating films, *Appl. Phys. Lett.* **76**, 1941 (2000)
- ¹³⁹ J. Collet, O. Tharaud, C. Legrand, A. Chapoton, D. Viillaume, Performances of sexithiophene thin film transistors using self-assembled monolayers, *Mat. Res. Symp. Proc.* **488**, 407 (1998)

3 Experimental

3.1 *Scanning probe microscopy*

The first instrument capable of obtaining three dimensional images of solid surfaces was developed by G. Binnig and H. Rohrer in 1981.^{1,2,3} It was the scanning tunneling microscope (STM), which consisted in a fine probe that was scanned at a close distance over the surface measuring a tunneling current between probe and sample. Its resolution reached the atomic level, a phenomenal success in the world of microscopy, which was rewarded with the Nobel Prize in 1986. The major drawback was (and still is) that only electrically conductive surfaces can be imaged. Few years later (1986) the atomic force microscope (AFM) was developed, allowing the measurement of virtually any arbitrary surface.⁴ Since their invention, and promoted by the growing understanding of the underlying theoretical principles, STM and AFM have been further developed or modified, giving rise to a large number of complementary techniques grouped under the name of scanning probe microscopies (SPM), with the common principle of a probe which scans the surface measuring different properties. SPMs have thus become a standard technique even outside basic research. Their use ranges from the study of surface topography, to the study of friction or adhesion,⁵ the mapping of surface potentials,⁶ the study of magnetic⁷ or optic⁸ properties, manipulation of molecules⁹ or surfaces,¹⁰ nanomachining,¹¹ nanofabrication,¹² etc. This wide range of applications together with the subnanometer resolution of the instruments, have converted the SPMs in one of the most important tools responsible for the impressive development of the nanotechnology within the last decades.

SPMs are all closely related, share some of the key components, as is the case of the scanner, and face common problems such as noise or scanning distortions. Most of the SPMs use piezo translators to scan either the probe or the sample. Among them, the (nowadays) more extended model are tube scanners, due to their simplicity and small size. These consist in a piezoelectric tube metallized both in the outer and inner surfaces, with the outside metal coating sectioned into four quadrants. The vertical movement (z axis) is controlled by applying voltages to the inner electrode, while the

outer side is responsible for the x-y scanning of the sample surface.^{5,13} Opposite quadrants of the outer side are driven by signals of the same amplitude and opposite sign, resulting in a bending of the tube that leads to a two dimensional movement on, approximately, a sphere. This makes the scanning process with tube scanners inherently non-linear, leading to image distortions when scanning large areas on very flat samples. Additional sources of distortions are the non-linearity of the piezo response versus applied voltage, the hysteresis of its response (retraction and extension curves versus voltage do not coincide), or creep (i.e. a “memory” effect in the piezo related to a slower relaxation of the piezo with logarithmic time dependence in addition to the initial immediate one).⁵ Nevertheless, these distortions can be overcome by software corrections either directly during the data acquisition or afterwards in the data analysis.

As previously mentioned, noise is another important factor common to SPMs. Mechanical vibrations are among the noise sources, and since the desired resolution in SPMs goes down to 0.1 Å in the vertical direction, the noise amplitudes should be lowered below 0.01 Å. Typical vibrations arise from the buildings (1-50 Hz), the table or chamber housing of the SPMs (30-100 Hz), acoustic noise from machines operating at 50-60 Hz, from components of the SPM itself (frequencies up to several kHz), or others. There are many factors to take into account for an efficient vibration isolation and different solutions,^{13,14,15} but as a general rule, the resonance frequency of the microscope itself should be as high as possible, while for the natural frequency of the isolation system “the-lower-the-better” applies.^{13,15}

3.1.1 Scanning Tunneling Microscopy (STM)

The working principle of an STM is relatively simple, based on the quantum tunneling effect, by which an electron has a non-negligible probability of crossing an energy barrier. In the case of the STM, a metallic tip is brought in proximity to a conductive surface. Upon application of a voltage, the electrons can tunnel between tip and surface through the vacuum (or air, if measuring in ambient conditions) with a transmission probability, and consequently a tunneling current, that depends on the tip-surface distance as

$$I \propto \exp(-2\kappa d) \quad (3.1)$$

where I is the current, d the tip-surface distance, and κ the decay constant for the wave function in the barrier, given by

$$\kappa = \hbar^{-1} \sqrt{2m\phi} \quad (3.2)$$

with ϕ being the effective barrier height (for low voltages it corresponds in good approximation to the average local work function of tip and surface) and m the mass of the electron.^{13,14,15} For a typical work function in the range of 4 eV, the current decreases by one order of magnitude when d is increased by only 1 Å. This is the reason for the high resolution one can obtain by STM, since a control over the current within 2% of its value leads to changes in d below 0.01 Å. In addition, it also implies that most of the current tunnels only from the very last atom of the STM tip apex, leading to a lateral resolution in the atomic range.

The description above helps to understand the general working principle of an STM, but a more refined formalism is needed to get a thorough understanding of the images obtained by scanning the surfaces. Tersoff and Hamann developed a theory which allowed a quantitative comparison between the calculated tunneling currents and the real measurements.^{16,17} Based on the Bardeen formalism,¹⁸ the tunneling current can be expressed as

$$I = \frac{2e\pi}{\hbar} \sum_{\mu,\nu} |M_{\mu,\nu}|^2 f(E_\mu) [1 - f(E_\nu + eV)] \delta(E_\mu - E_\nu) \quad (3.3)$$

where $f(E)$ is the Fermi function, V the applied voltage and $M_{\mu,\nu}$ the tunneling matrix element between the state φ_μ with energy E_μ of the probe and the state φ_ν with energy E_ν of the sample. The matrix elements are defined by

$$M_{\mu\nu} = \frac{\hbar^2}{2m} \int d\vec{S} (\varphi_\mu^* \vec{\nabla} \varphi_\nu - \varphi_\nu \vec{\nabla} \varphi_\mu^*) \quad (3.4)$$

where the quantity in brackets is the current operator. If we consider the current given by equation (3.3) in the limit of low temperature and low voltage for an ideal “point-tip”, that is, with an arbitrary localized wave function, we obtain

$$I \propto \sum_\nu |\varphi_\nu(\vec{r}_0)|^2 \delta(E_\nu - E_F) = \rho(\vec{r}_0, E_F). \quad (3.5)$$

In this simple limit, which can be interpreted as a measurement with ideal conditions, i.e., an unperturbed surface and an ideal tip with maximal resolution, the current is proportional to the surface local density of states (LDOS) at E_F and at the probe position. Thus, by scanning the surface adjusting the tip-sample distance with a feedback loop to keep the current constant, the tip maps the contour of constant LDOS at the Fermi level. However, in many measurements, such as in the characterization of semiconductors, the applied voltages are in the range of 1-2 V, which clearly do not correspond to this limit any more. In these cases, the tunneling current can be approximated by^{19,20}

$$I \propto \int_{E_F}^{E_F+eV} dE \cdot \rho_T(E-eV) \rho_S(\vec{r}_0, E) \cdot T(\vec{r}_0, E, eV) \quad (3.6)$$

where $\rho_T(E-eV)$ is the density of states associated with the tip atom, $\rho_S(\vec{r}_0, E)$ the density of states of the sample at the tip position \vec{r}_0 , and $T(\vec{r}_0, E, eV)$ the transmission probability of the electrons through the barrier between tip and sample. At this point, it is important to notice two important factors that affect the interpretation of STM images:

- i. That the measured current results from a convolution of the density of states of both tip and sample, and
- ii. the measured signal is only related to the LDOS, which does not necessarily have maxima corresponding to the atomic positions.

In materials with directed bonds, as is the case of semiconductors, the bonds might lead to an enhanced charge density along specific directions and consequently to LDOS maxima not coincident with the atomic positions. In these cases, it is useful for the image interpretation to compare the images with calculations of the LDOS for the given surface.

Figure 3.1 shows an explanatory scheme of the tunneling electrons upon application of a positive bias to the sample. As can be seen in the scheme, the electrons of the tip with energies between E_F and E_F-eV can tunnel to the available free states in the sample. However, given the energy dependence of the transmission probability, which has its maximum value for the highest energy and decays exponentially towards lower energies, the main contribution to the tunneling comes from electrons emitted within about 0.3 eV of the Fermi level.²¹

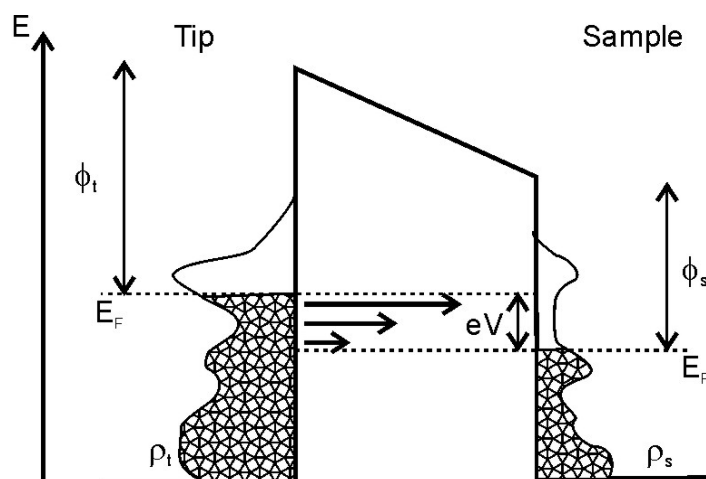


Figure 3.1 Scheme showing the relevant work functions and shifted Fermi energies upon application of a positive bias V to the sample, leading to the tunneling of electrons from the occupied states of the tip to the free states of the sample.

By varying the tip-sample bias, one shifts the Fermi levels of the tip and sample with respect to each other (measuring the tunneling current versus applied voltage at a fixed tip-sample distance, one obtains spectroscopic information about the LDOS on a very local scale). For positive sample bias the recorded current, arising from the electrons in the tip close to the E_F , is sensitive to the available states in the sample (in the case of organic molecules this corresponds to the LUMO and higher molecular orbitals) and thus to the energy-level dependent LDOS of the sample. On the contrary, with the inverse bias, a correlation of the obtained currents to the LDOS of the occupied states in the sample (HOMO and lower energy levels in the case of organic molecules) is difficult, since the main contribution to the current arises in this case from electrons close to the Fermi level in the sample, tunneling to free states in the tip. This local spectroscopic sensitivity also allows obtaining chemical sensitivity when measuring heterogeneous samples.²¹

There are two main data acquisition modes when imaging a sample surface by STM: the constant current mode and the constant height mode. For the constant current imaging, fixed tunneling current I and bias V are specified, and the surface is scanned with a feedback that regulates the z motion in order to maintain the current constant. The registered signal is the z displacement for each x - y position. In the absence of large changes in the local work functions, this can be considered to correspond in good approximation to the topography of the surface (this mode is thus

also tentatively called topography imaging), though keeping in mind that it is actually the LDOS what is being mapped. The constant height imaging is performed by scanning the surface with fixed bias V and height z . In this case the resulting image is the current value versus x - y position, and the signal modulation arises mainly from the variation of the energy barrier width while scanning. The main disadvantage of this measurement mode is that only very flat surfaces can be measured, to avoid the tip crashing with the sample at topographic features larger than the initial tip-sample distance. However, since it does not need any feedback regulation of the z axis, the measurements can be performed much faster, an advantage for the minimization of image distortion due to creep or thermal drift, or for the study of processes in real time. In addition to this two main imaging modes, I/V , I/Z and Z/V curves can be acquired to obtain spectroscopic information about the sample surface, or even combine them with the imaging modes, as in the “current imaging tunneling spectroscopy” (CITS), where an I/V curve is taken at each x - y point of a constant current or “topographic” image.²¹ However, these techniques have not been applied in the present studies and their detailed description is thus beyond the scope of this thesis.

3.1.2 Atomic Force Microscopy (AFM)

The atomic force microscopy was first implemented in 1986 with the goal of overcoming the STM limitation of imaging only sufficiently conductive samples. Its principle is thus not related to the measurement of a tunneling current, but of the probe-sample interactions. The idea is to use a tip attached to the end of a cantilever with elastic constant K , and measure the tip-sample forces by the cantilever deflection, which are related, according to Hooks law, by

$$F_z = K_z \Delta z. \quad (3.7)$$

The same relation applies for the x direction if the force on the tip has also a component along the surface plane. There are various detection systems for the cantilever deflection,²² but the most common one is the optical beam deflection method shown in Figure 3.2. In this system, a laser beam is focused on the cantilever and reflected towards a position-sensitive photodiode. Initially the reflection is centered with respect to the photodiode, but as soon as the cantilever is deflected by

the tip-sample forces, the reflection on the photodiode is displaced. Normal forces bend the cantilever in the z direction, while the main effect of lateral forces is the torsion of the cantilever, leading to displacements of the reflection in the vertical and horizontal directions, respectively. The photodiode is divided into four independent parts (sectors A, B, C and D as shown in Figure 3.2).

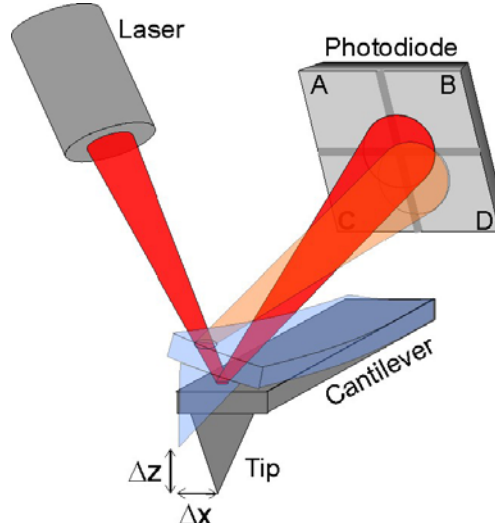


Figure 3.2 Schematic description of the detection system of the cantilever deflection.

Each of them generates a voltage proportional to the total intensity it receives, and the displacements of the reflected beam on the photodiode are quantified by measuring the changes in the relative voltages of the four sectors. Thus, normal forces are related to the signal

$$V_Z = (V_A + V_B) - (V_C + V_D) \quad (3.8)$$

and lateral forces to the signal

$$V_X = (V_A + V_C) - (V_B + V_D). \quad (3.9)$$

The calibration to correlate the measured signals to the tip displacements Δz and Δx , or to the tip-sample forces by applying Hooks law, depends on the cantilever and tip characteristics (dimensions, Young modulus) and thus has to be performed for every different tip.²²

The general behavior of the tip-sample forces versus distance is shown in Figure 3.3.

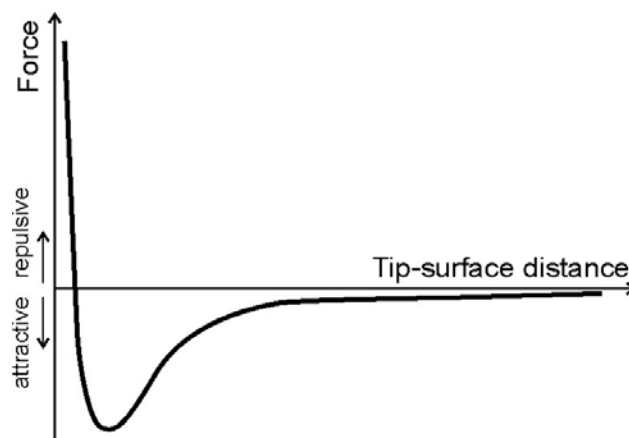


Figure 3.3 Schematic representation of the general behavior of tip-sample forces versus distance.

An important difference with respect to the STM becomes apparent in this plot: the non monotonic behavior of the forces versus distance (as opposed to the monotonic behavior of the tunneling current) with contributions of long range attractive interactions and short range repulsive interactions. This presents an additional complication inherent to AFM, since a stable feedback is only possible on a monotonic subbranch of the feedback signal.

The AFM measurements can be performed in different modes, which can be classified into the contact mode and the dynamic modes.

a. Contact mode

In the contact-mode, the tip is brought in contact with the surface and the tip-sample interaction forces are measured recording the cantilever deflection. At this point, many different interaction forces contribute to the deflection. Among them, there are long range Van der Waals or electrostatic forces, short range repulsive forces due to the overlap of tip and sample electronic orbitals, or adhesion forces. The adhesion forces depend on the contact area, which in turn depends on the tip radius and the stiffness of probe and sample. Furthermore, adhesion is greatly enhanced in presence of water adsorbed on the surface, which forms meniscus bridges between tip and sample. This contribution, however, can be canceled by performing the measurements in a liquid environment.

The adhesion can be easily characterized by force-distance curves, which consist in recording the cantilever deflection (which is in turn correlated to the tip-sample forces), while approaching and later retracting the cantilever from the sample (either sample or cantilever can be moved). An example of a force-distance curve as measured with the AFM is shown in the upper graph of Figure 3.4. The curve does not coincide with the shape of the tip-sample force versus distance shown in Figure 3.3 (plotted again in the lower graph of Figure 3.4). The correlation will be explained in the following by describing the situation at the specific points marked on the graphs. For each of the points, a schematic representation of the tip-sample positions is shown in the right part of the figure to further clarify the scenario taking place during the performance of the curves.

(a) At the beginning, the tip is far away from the surface and senses no force. The cantilever thus remains in its original position without deflection. (b) As the tip-surface distance becomes smaller, the tip feels attractive forces (lower graph) and the cantilever is slightly bend downward (upper graph). (c) At this point, the force gradient (slope) sensed by the tip exceeds the spring constant k of the cantilever (marked with a dashed line on the lower graph). This generates an instability that leads to a snapping of the tip into contact until position (d). In this movement only the cantilever deflection is involved while the cantilever base remains in its position. Thus, in the measurement (upper graph) it appears as a sudden force jump. (e) A further approach leads to the reduction of the cantilever deflection, until there is no bending and the net force equals zero. (f) Since the tip is in repulsive contact with the surface, by approaching even further the cantilever is deflected upwards and applies an external load on the sample. The displacement direction is reversed at a point chosen by the user, reducing the applied load until it becomes again negative. The tip remains in contact with the sample because the adhesion forces counterbalance the tensile strain of the cantilever. (g) Once again an instability is generated when the force gradient exceeds the cantilever spring constant, causing the tip to jump out of contact until position (h). Also in this case only the cantilever deflection is involved, leading to a sudden jump in the deflection or force signal versus cantilever displacement. The pull-off force measured at point (g) is considered to be the adhesion force.

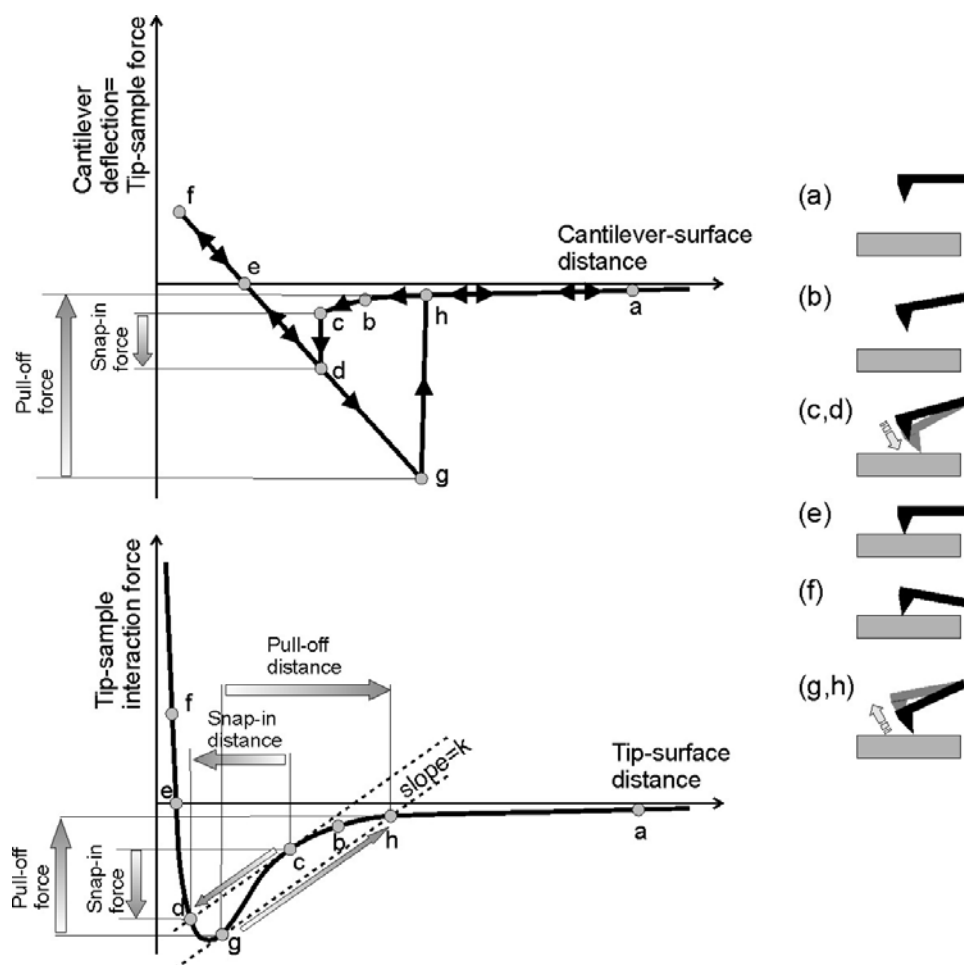


Figure 3.4 The upper graph shows a typical tip-sample force-distance curve as measured with the AFM upon approach and retraction, as shown by the arrows. The lower graph shows the tip-sample interaction forces vs the distance. Both graphs show different shapes, and the correlation is explained in the text. At the right side, schematic pictures of the relative tip-sample positions are shown for the specific points marked on both graphs.

In general, the topography measurements are performed by scanning the surface at constant force (i.e., constant cantilever deflection). When the tip is scanned over a bump or hollow, the tip will follow the surface by changing the cantilever deflection. The consequent change in the measured signal is used as a feedback to readjust the cantilever-surface distance and get back to the initial deflection. In this way, the recorded changes in the cantilever-surface displacements correspond to the topography of the sample. Obviously, the deflection of the cantilever should be significantly larger than the deformation of tip and sample upon contact. To satisfy this, the cantilever should be softer than the interatomic bonds in tip and sample. Typical interatomic spring constants range from 10 to 100 N/m, though in biological

samples they can be as low as 0.1 N/m. Thus, typical values for contact-mode cantilever spring constants are 0.01-5 N/m.

The images of the measured topographic features are broadened (for protrusions) or narrowed (for hollows) by the lateral size of the tip (with typical curvature radius for commercial tips from 5 to 15 nm). This effect consequently has to be considered in the interpretation of images with features in the nm range.^{22,23,24} Nevertheless, sub-nanometer resolution images can be obtained on crystalline surfaces, resolving the surface structure. This is explained taking into consideration the large contact area of tip and sample (in comparison with the crystal periodicity) and considering that the forces matching the surface periodicity are transmitted to the tip, resulting in an “averaged image” of the periodic lattice. In this way, small periodicities can be resolved if they extend over distances much larger than the contact area.

The optical beam deflection method used for the detection of the cantilever deflection allows the simultaneous measurement of both the normal deflection and the cantilever torsion generated by lateral forces. It is well known that, during the lateral displacement of a solid over a surface, there is a force opposing to the movement. This force is the friction and is also present when scanning the surface with the tip, consequently leading to a measurable torsion of the cantilever. On a microscopic scale, there are many different processes involved in the friction, but for a thorough description of the underlying theory the reader is referred to references 5, 25 and 26. In the frame of this thesis, the most important characteristic is that the friction is material sensitive, and thus allows a chemical distinction in laterally inhomogeneous samples.

b. Dynamic modes

In the dynamic modes the cantilever is deliberately vibrated by externally exciting it with an excitation amplitude A_{ex} and an excitation frequency ω . The cantilever oscillation is characterized by its amplitude, the frequency, and the phase difference between excitation and oscillation. In order to provide an understanding of the fundamental concepts involved in dynamic mode AFM, the cantilever can be described by harmonic approximations. In the absence of tip-surface interactions (i.e.

tip far away from the surface) the movement of the tip can be considered as a forced harmonic oscillator with damping, thus following

$$m\ddot{z}(t) = -\frac{m\omega_0}{Q}\dot{z}(t) - kz(t) - kA_{ex}\cos(\omega t) \quad (3.10)$$

where $\omega_0 = (k/m)^{1/2}$ is the resonance frequency of the free cantilever, and Q is the dimensionless quality factor related to the damping of the cantilever. The solution is a linear combination of a transient term related to the adaptation of the cantilever movement to the excitation frequency, and a steady-state term with constant frequency, amplitude and phase over time:

$$z(t) = A_t e^{-\omega_0 t / 2Q} \sin(\omega_0 t + \varphi_t) + A_0 \cos(\omega t + \varphi). \quad (3.11)$$

After a time $\tau = 2Q/\omega_0$ the transient term is reduced by a factor $1/e$ and the motion is dominated by the steady term. If we evaluate now the steady solution in the differential equation, the following expressions are found for the amplitude and phase as a function of ω :

$$A_0 = \frac{A_{ex} Q \omega_0^2}{\sqrt{\omega^2 \omega_0^2 + Q^2 (\omega_0^2 - \omega^2)^2}} \quad (3.12)$$

$$\varphi = \arctan\left(\frac{\omega \omega_0}{Q(\omega_0^2 - \omega^2)}\right). \quad (3.13)$$

The corresponding diagrams of amplitude and phase vs. ω are shown in Figure 3.5, calculated for A_{ex} , Q , and ω_0 values of 10 nm, 10 and 10 kHz respectively. From equation (3.12) it can be seen that the damping causes the maximal amplitude to be obtained at a frequency

$$\omega_0^* = \omega_0 \sqrt{1 - \frac{1}{2Q^2}}. \quad (3.14)$$

However, the shift is negligible for Q values in the usual range of 100 or more.

Up to now, no interaction forces have been considered. The simplest case would be a tip-sample force whose range of interaction is much larger than the oscillation amplitude and with a gradient with respect to the tip-sample distance which does not vary significantly over one oscillation cycle.

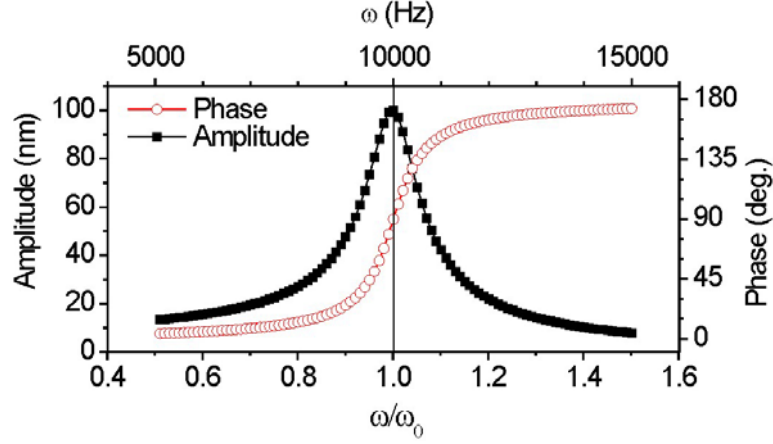


Figure 3.5 Amplitude and phase diagrams versus frequency for a free cantilever, calculated for A_{ex} , Q , and ω_0 values of 10 nm, 10 and 10 kHz respectively.

This gradient can thus be represented by a spring constant k_{ts} which varies with the average tip-sample distance but is nearly constant within an oscillation cycle. In this case, the tip-sample force can be included in the movement equation (3.10) by simply considering a new spring constant

$$k_{total} = k + k_{ts} = k + \frac{\partial F_{ts}}{\partial z} \quad (3.15)$$

which consequently leads to a new resonance frequency shifted by $\Delta\omega$ (neglecting the damping) at

$$\omega^2 = (\omega_0 + \Delta\omega)^2 = \frac{k_{total}}{m} = \frac{k + \frac{\partial F_{ts}}{\partial z}}{m} \quad (3.16)$$

A change in the resonance frequency leads to a shift of the curves in Figure 3.5, consequently changing also the oscillation amplitude and phase.

This analytic and simplified model shows qualitatively that in dynamic force microscopy the oscillation parameters depend on the force gradient, as opposed to the dependence on the force itself in the contact-mode, and that the tip-sample interaction influences all of the oscillation parameters, that is, the resonance frequency, amplitude and phase. However, the approximations made often do not hold for real

measurements, and much more complex models and numeric calculations have to be developed to get quantitative agreement with the experiments.

Dynamic force microscopy is performed in two different measurement modes: tapping mode or amplitude modulation, and non-contact mode or frequency modulation. Both of them have been used in the frame of this thesis and are briefly presented in the following.

i. Tapping mode

In this mode the cantilever is excited externally with a constant excitation amplitude at a constant frequency near its resonance. The measured signals are the oscillation amplitude and phase, and the former is used as feedback parameter while scanning the sample. The initial oscillation amplitude decreases upon reduction of the tip-sample distance, which is typically reduced until the amplitude is decreased to 40 to 90 % of its initial value. Then, while scanning the surface, a feedback loop controls the cantilever-sample distance in order to maintain the amplitude constant. Typical oscillation amplitudes are in the range of 10 to 100 nm, consequently encountering a wide range of tip-sample interactions within each cycle, including both attractive as well as repulsive forces. This is what makes an analytical description of the processes taking place very difficult. Some of the models and numerical simulations applied to get some understanding of the tip-sample interactions can be found in references 22,27,28.

The phase signal is recorded simultaneously to the amplitude. The phase shift is intimately related to the dissipative processes taking part in the tip-sample interactions, and various groups have tried to develop a general model to interpret the phase-shift signal in terms of adhesion energy hysteresis, stiffness, plastic deformation and viscoelasticity.^{27,29,30,31} Due to the complexity of the problem,^{27,32} a thorough and general understanding of the interactions present in the tapping mode imaging is still missing. For the studies performed in the frame of this thesis the basic interest in the phase signal is the sensitivity to material properties, consequently allowing the distinction of different materials in laterally inhomogeneous samples.

ii. Non-contact mode

The time constant τ for the transient term in the oscillation amplitude to adjust to a change in the tip-sample interaction scales with $2Q/\omega_0$ (equation 4.11). In vacuum, typical quality factors are in the range of 10000, making the data acquisition in the tapping mode (with the amplitude as feedback parameter) too slow for vacuum applications. Albrecht et al. developed in 1991 the non-contact measurement mode, where the change in frequency settles on a time-scale of $1/\omega_0$, thus overcoming this problem.³³ Its working principle is as follows: the cantilever is excited and the oscillation parameters recorded. These are in turn used in a feedback loop to control the excitation signal in such a way that the excitation is with the same frequency but phase-shifted by 90 degrees (therefore exciting in resonance) and with a variable excitation amplitude that keeps the oscillation amplitude constant. Consequently, the only degree of freedom left for the cantilever to adjust to a changing tip-sample interaction is a change of its resonance frequency. This signal is used in a second feedback loop to adjust the cantilever-surface distance while scanning the surface and keeping a constant oscillation frequency. Despite the fact that there is no tip-surface mechanical contact while measuring, upon the appropriate choice of the experimental parameters, the tip-sample interactions can include contributions of short-range forces when the tip is closest to the surface. This in turn allows obtaining images with atomic resolution and corrugations in the same order of magnitude as for STM imaging.^{22,34} The excitation amplitude necessary to keep the oscillation amplitude constant is simultaneously recorded and is directly related to the energy dissipation within one oscillation cycle. This, together with maps of the averaged tunneling current for the oscillating tips, or frequency shift vs. cantilever-surface distance curves, are additional data available with non-contact AFM, which are related to different material properties. However, these kinds of measurements have not been used in this thesis and their description can be found elsewhere.^{22,34}

3.2 X-ray diffraction

In this section we provide an overview of the basic X-ray scattering theory necessary to understand the experiments performed in the frame of this thesis. A more

detailed description of the underlying principles can be found in references 35,36,37,38,39.

3.2.1 Scattering

The elementary scattering unit of X-rays is the electron, and its “ability” to scatter is expressed in terms of a scattering length. For elastic scattering, it is called the Thomson scattering length and it corresponds to the classical electron radius r_0 . In a scattering process, we have an incident beam with momentum $\vec{k}_i = 2\pi/\lambda$ and a scattered beam with momentum $\vec{k}_s = 2\pi/\lambda$, giving rise to a momentum transfer $\vec{q} = \vec{k}_s - \vec{k}_i$. If we consider now an atom with Z electrons, the total scattering length of the atom is

$$r_0 f^0(\vec{q}) = r_0 \int \rho(\vec{r}) e^{i\vec{q}\cdot\vec{r}} d\vec{r} \quad (3.17)$$

where $f^0(\vec{q})$ is known as the atomic form factor, $\rho(\vec{r})$ corresponds to the electron density within the atom and $\vec{q} \cdot \vec{r}$ to the phase difference between the waves scattered in different volume elements. This stands for free electrons. Taking into account that their bonds to the atom lead to absorption processes, two additional energy dependent terms (called dispersion correction factors) have to be added to the atomic form factor, which is then finally given by

$$f(\vec{q}, \hbar\omega) = f^0(\vec{q}) + f'(\hbar\omega) + f''(\hbar\omega). \quad (3.18)$$

The form factors of the free atoms can be expressed by the analytical approximation

$$f^0(q) = \sum_{j=1}^4 a_j \exp[b_j (\frac{q}{4\pi})^2] + c \quad (3.19)$$

where a_j , b_j and c are fitted parameters for each atom type, which can be found in the International tables for X-ray crystallography⁴⁰, together with the energy-dependent dispersion correction factors.

This can now be used to calculate the structure factor of a molecule, which is simply given by the sum of the atomic form factors, taking into account the phase shifts related to their position within the molecule. It results in

$$F^{mol}(\vec{q}, \hbar\omega) = \sum_k f_k(\vec{q}, \hbar\omega) e^{i\vec{q} \cdot \vec{r}_k} \quad (3.20)$$

where f_k are the form factors for each atom and \vec{r}_k the respective atomic positions. The same applies for the unit cell structure factor of a crystalline sample, summing over the l molecules within the cell, and resulting in

$$F^{u.c.}(\vec{q}, \hbar\omega) = \sum_l F^{mol}_l(\vec{q}, \hbar\omega) e^{i\vec{q} \cdot \vec{r}_l} . \quad (3.21)$$

The last level of complexity is now the structure factor for the whole crystal, which results summing over all the n unit cells of the sample located at \vec{r}_n , and resulting in

$$F^{crystal}(\vec{q}, \hbar\omega) = F^{u.c.}(\vec{q}, \hbar\omega) \sum_n e^{i\vec{q} \cdot \vec{r}_n} . \quad (3.22)$$

Let us consider a one dimensional crystal with periodicity a , and N unit cells. The momentum transfer q can be given in terms of the reciprocal lattice vector $a^* = 2\pi/a$ as $q = ha^*$. Then, the sum can be evaluated by the sum formula for geometrical series, and combined with some mathematical transformations it leads to

$$\sum_{n=0}^{N-1} e^{iq \cdot r_n} = \sum_{n=0}^{N-1} e^{i \frac{2\pi}{a} h \cdot na} = \frac{1 - e^{i2\pi Nh}}{1 - e^{i2\pi h}} = e^{i\pi(N-1)h} \frac{\sin(\pi Nh)}{\sin(\pi h)} . \quad (3.23)$$

The measured intensity is proportional to the modulus squared of the structure factor, and thus proportional to

$$I \propto \frac{\sin^2(\pi Nh)}{\sin^2(\pi h)} . \quad (3.24)$$

Figure 3.6 shows the calculated scattered intensity from a crystal with N unit cells ($N=10$) and $F^{u.c.}=1$. The main maxima appear at integer h values, i.e., when the momentum transfer coincides with a reciprocal lattice vector (“Laue condition”). The maximum peak intensity is proportional to N^2 and its full-width-at-half-maximum (FWHM), in units of the reciprocal lattice vector, is approximately $\text{FWHM} \approx 1/N$. Thus, the peak width in momentum transfer units (Δq) is inversely proportional to the

crystal size ($d=Na$) as shown in equation 3.25, resulting in a delta function around the reciprocal lattice vectors for infinite crystals

$$\Delta q \approx \frac{1}{N} a^* = \frac{2\pi}{Na}. \quad (3.25)$$

Additional secondary maxima appear between the main peaks, separated by minima located at h values of $h=n/N$, whose width is thus similarly related to the crystal size.

This is calculated for one dimension, but applies similarly for the three dimensional formalism. In three dimensions, the peak width along a certain direction is then related to the crystal size along that specific crystallographic direction.

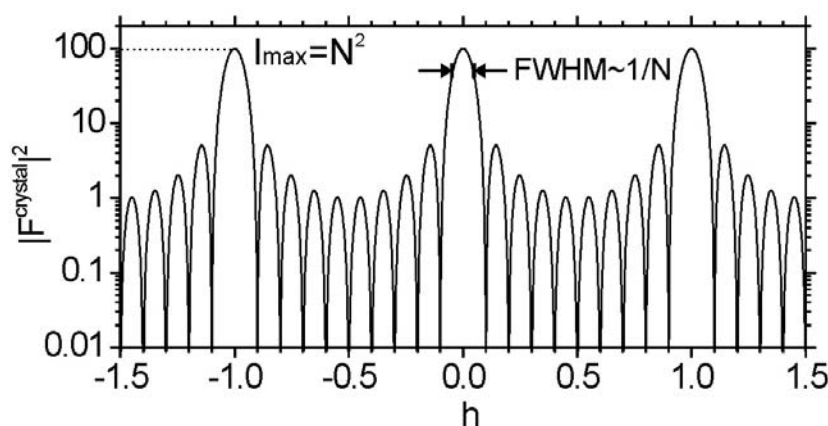


Figure 3.6 Squared structure factor calculated for a one dimensional crystal with 10 unit cells and $F^{u.c.}=1$.

3.2.2 X-ray reflectivity

The refraction index of a medium for incident X-rays with wave vector $k=2\pi/\lambda$ is

$$n = 1 - \delta + i\beta \quad (3.26)$$

with $\delta=2\pi\rho r_0/k^2$ and $\beta=\mu/2k$, where ρ corresponds to the electron density and μ to the absorption coefficient. Since $n<1$, total external reflection occurs for incidence

angles θ (angle between the beam and the surface plane) below the critical angle $\theta_c = (2\delta)^{1/2}$.

The reflection and transmission of X-rays at a perfectly smooth vacuum/medium interface can be treated as the classical problem of an electromagnetic wave at an interface, leading to the well known Fresnel formulas for the reflection and transmission coefficients. For media with a varying electron density along the z axis (surface normal), the X-rays are reflected at each z point with a gradient in the refractive index, thus related to a gradient in the electronic density. It can be thought of as a medium divided in arbitrarily thin slabs of different electron densities and thicknesses, where the reflected intensity results from the sum over all reflections and transmissions at each interface, including multiple reflection effects. Additionally, the reflected intensity depends on the interfacial roughnesses, and on the absorption. Thus, in a reflectivity measurement, i.e. intensity vs. q_z ($q_z = 4\pi \sin\theta/\lambda$), the resulting intensity holds information about the projection of the electron density along the surface normal, which is directly related to the crystalline structure in this direction, and to the film roughness, both of them laterally averaged over the in-plane coherence length of the X-ray beam. Figure 3.7 shows in a few examples how the reflectivity depends on these parameters.

The case (a) represents the Fresnel reflectivity of a perfectly smooth vacuum/medium interface. In case (b) the reflection of an additional perfectly smooth and homogeneous film is included, leading to the appearance of interference fringes (Kiessig fringes) arising from the interference of X-rays scattered at the vacuum/film and film/substrate interfaces. The width of the fringes is thus related to the film thickness d by $\Delta q_z = 2\pi/d$. Case (c) shows how the addition of an interfacial roughness leads to a damping of the Kiessig fringes. Finally, case (d) shows how the periodic modulation of the electron density within the film (with periodicity d_{crys}) leads to intensity peaks (Bragg peaks) when the Bragg condition $2d_{crys}\sin\theta = n\lambda$, with n being an integer, is satisfied. This is equivalent to q_z coinciding with a reciprocal lattice vector " $n(2\pi/d_{crys})$ ", which corresponds to the Laue condition introduced in the previous section. The peak position thus informs about the film periodicity along the surface normal. In addition the peak width, as well as the width of its surrounding fringes, also gives information about the crystalline thickness of the films.

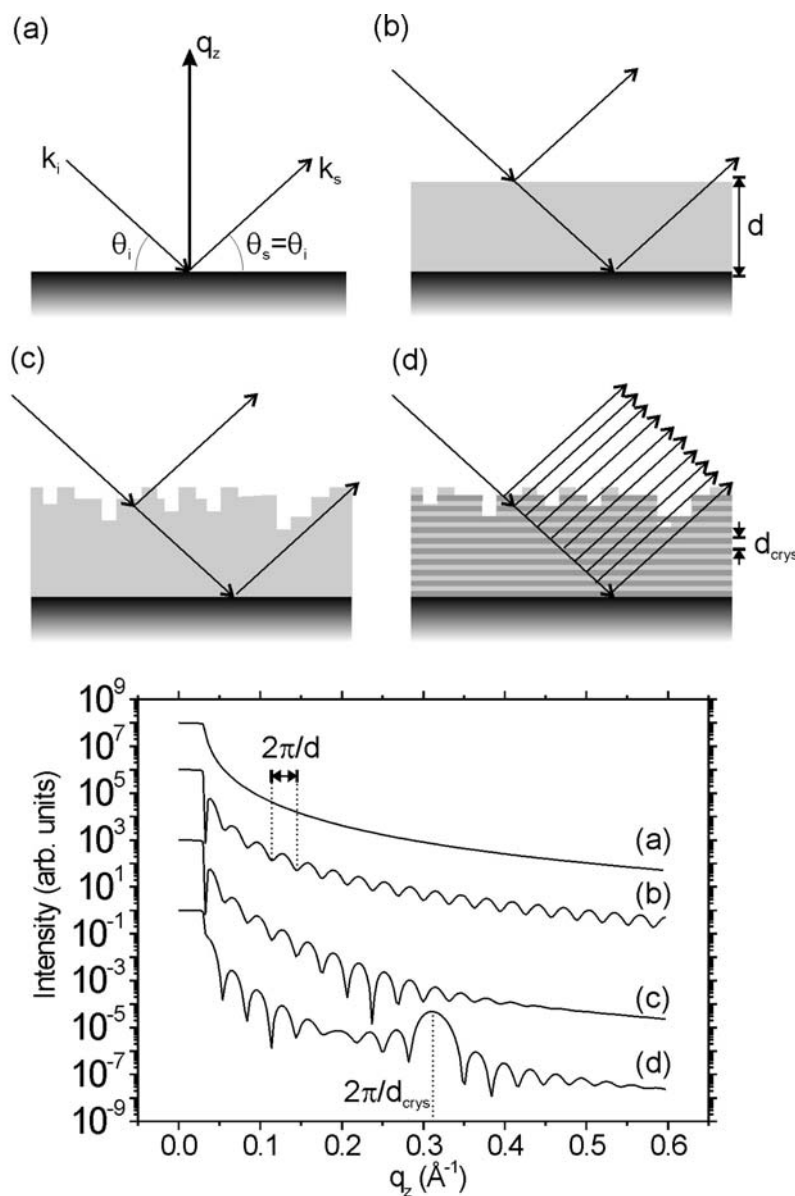


Figure 3.7 Calculated reflectivity curves (bottom) corresponding to samples schematically shown at the top. (a) Fresnel reflectivity of a perfectly smooth vacuum/medium interface. (b) Intensity from a perfectly smooth, homogeneous film of thickness “ d ” on the substrate. (c) Similar as (b) but including a film roughness. (d) Similar as (c) but including a modulation of the electron density with periodicity “ d_{crys} ”.

Refined information about the density profile of the sample can be obtained by fitting the reflectivity curves, i.e., modeling a density profile whose calculated reflectivity is in accordance with the measurement. This can be performed by different methods.

In the Parrat formalism,⁴¹ the sample is divided into a number of slabs. Each of them is characterized by the thickness, electron density, absorption coefficient and roughness. The exact reflectivity is calculated numerically with a recursive formalism based on the transmission and reflection at each interface together with multiple reflection effects, and the parameters of each of the layers are adjusted by a fitting routine to optimize the concordance between the calculated and the measured reflectivity.

Neglecting multiple scattering, which is justified for incidence angles larger than about twice the critical angle, the reflectivity curves can be fitted by analytical density profile models, making use of the kinematical approximation. In this case, the reflected intensity can be written as^{35,36,42}

$$I(q_z) = R_F(q_z) \left| \frac{1}{\rho_s} \int_{-\infty}^{\infty} \frac{d\rho(z)}{dz} e^{iq_z z} dz \right|^2 \quad (3.27)$$

where $R_F(q_z)$ represents the Fresnel reflectivity, and ρ_s the substrate electron density, and $\rho(z)$ the electron density profile to be fitted.

However, prior to the fitting procedure, the experimental data have to be corrected, since the measured intensity differs from the calculated one due to various different reasons. (i) The diffuse scattering contributing to the intensity in the specular direction has to be subtracted. This is easily done by subtracting the intensity obtained from $\theta-2\theta$ (i.e. radial) offset scans in which the sample orientation is slightly deviated from the specular condition. (ii) The intensity at low angles has to be additionally corrected for the illumination area. For low incidence angles, the footprint of the X-ray beam, determined by the beam size A_0 and the incidence angle θ as $A=A_0/\sin\theta$, is larger than the sample dimensions. Thus only the part impinging on the sample contributes to the measured intensity, which is related to the total intensity I_0 by

$$I_{\text{exp}} = I_0 \cdot \frac{A_{\text{sample}}}{A_0} \cdot \sin \theta . \quad (3.28)$$

(iii) Furthermore, depending on the scattering geometry and the polarization of the X-ray beam, a polarization correction factor has to be taken into account. Supposing we have a polarized beam (as is the case in synchrotron sources), if the scattering

plane (formed by the incident and diffracted beams) is perpendicular to the polarization direction, no correction has to be made, whereas a correction factor of $\cos^2 \theta$ has to be applied if the polarization direction lies within the scattering plane. For an unpolarized source (as the conventional X-ray tubes) the correction factor is $1/2(1+\cos^2 \theta)$.

For a more detailed treatment of the corrections we refer to 35,39,43.

3.2.3 Grazing incidence X-ray diffraction (GIXD)

Total external reflection occurs for incidence angles θ_i below the critical angle $\theta_c = (2\delta)^{1/2}$. Under these conditions, the incident beam generates a totally reflected beam and an additional wave, which is exponentially damped into the medium and travels parallel to the surface according to

$$E_T \propto e^{ik_{xy}r_{xy}} e^{-z/\Lambda} \quad (3.30)$$

where k_{xy} and r_{xy} are the components in the surface plane of the momentum transfer and position, respectively, and Λ the penetration depth of the wave into the medium.³⁷ When this evanescent wave encounters scattering centers upon propagation, newly scattered intensity is observable under a grazing exit angle θ_s and a scattering angle 2θ parallel to the surface. The momentum transfer has thus a component in the surface plane q_{xy} , which is sensitive to the crystallinity in the plane, as shown schematically in Figure 3.8.

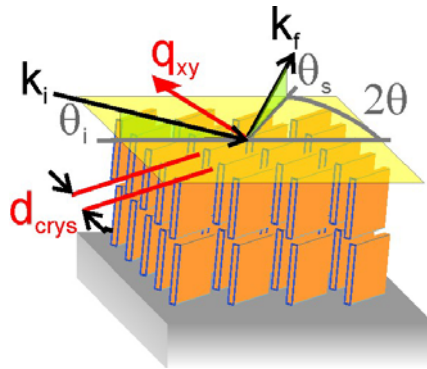


Figure 3.8 Scattering geometry in GIXD.

The depth into the medium from which the observed scattering originates, depends on both the incidence and scattering angles θ_i and θ_s , thus allowing by their appropriate choice the performance of depth-dependent structural studies.³⁷

3.2.4 Real-time measurements at the specular anti-Bragg point

At the anti-Bragg point $q_z = \pi/d_{layer}$, the specularly reflected intensity from subsequent layers is out-of-phase, consequently interfering destructively. Thus, assuming that the scattering amplitudes of the layers and the lattice spacings between them do not change during the film growth, the scattering amplitude (whose square is proportional to the intensity) can be written within the kinematical approximation as

$$S(t) = |R_{sub}| + |R_{layer}| e^{i\varphi} \sum_n \theta_n(t) (-1)^{n-1} \quad (3.31)$$

where all the growth independent scattering parameters of film and substrate are included in the amplitudes R_{sub} , R_{layer} and the phase φ , and the evolution of the scattering amplitude only depends on the time dependent coverage θ_n of each of the layers.⁴⁴

This has been modeled in Figure 3.9 for two examples with different growth behaviors. The upper graphs represent the evolution of the occupancy of the different layers, and the lower graphs the corresponding intensities at the anti-Bragg point. When perfect layer-by-layer growth takes place (left side), the intensity oscillates showing minima and maxima corresponding to the completion of subsequent layers, while a deviation of the perfect layer-by-layer growth (right side) leads to a damping of these oscillations.

This dependence of the scattered intensity on the evolution of the layer occupancy thus gives an insight into the growth process. Various groups have taken advantage of it to study the growth of different inorganic^{45,46,47,48} as well as organic thin films.

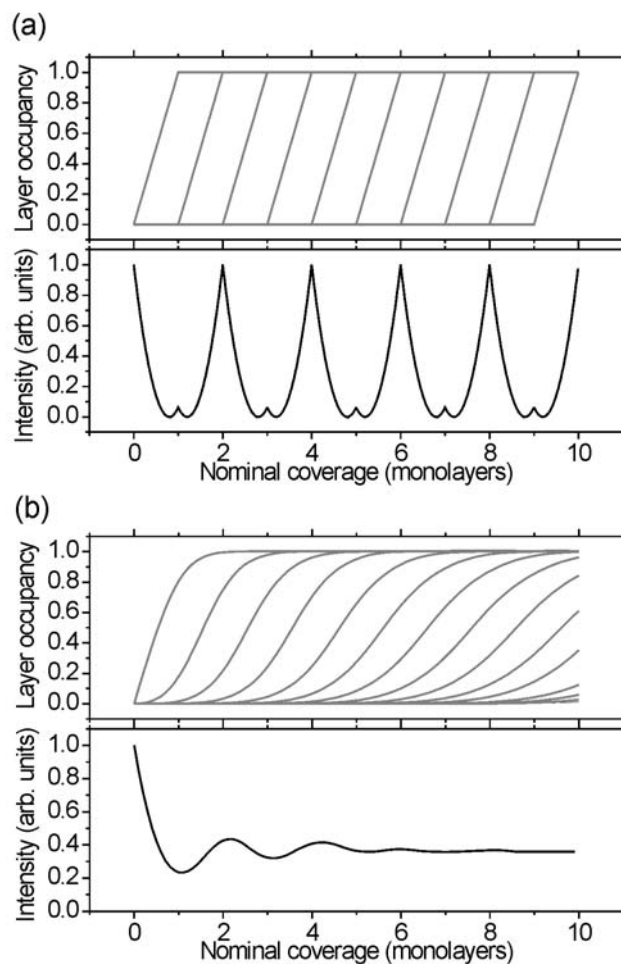


Figure 3.9 Evolution of the layer occupancy for subsequent layers (top graphs) and the corresponding scattered intensity at the anti-Bragg point (lower graphs) for a perfect layer-by-layer growth (a) and a growth approaching the 3D-growth mode for increasing coverage (b).

3.2.5 Synchrotron beamlines

The use of high-brilliance synchrotron radiation, as compared to the conventional X-ray tubes, has greatly enhanced the measurable range of scattering angles (which translates into the measurable reciprocal space) and thus allows a deeper insight into the structural properties of the materials. Synchrotrons consist in storage rings, where electrons are kept circulating at constant and relativistic speeds in a closed orbit (Figure 3.10). The radiation is produced either at the bending magnets needed to keep the electrons in the orbit, or in insertion devices (wigglers or undulators) situated in

the straight sections of the storage ring, in which an alternating magnetic field forces the electrons to follow an oscillating trajectory. For further details on synchrotrons or synchrotron radiation the reader is referred to reference 35. In the following we briefly describe the experimental details of the beamlines used in this thesis.



Figure 3.10. Photo of the storage ring of the ESRF in Grenoble, France.

a. Max-Planck Surface Diffraction Beamline at the Angströmquelle Karlsruhe (ANKA)^a

The MPI Surface Diffraction Beamline is a multi-purpose bending magnet beamline. The ANKA storage ring is operated at 2.5 GeV with 200 mA electron current. The beamline optics consist in a Rh coated Si toroidal mirror for vertical beam focusing, followed by a Si(111) double crystal monochromator (energy range 6-20 keV) with sagittal bender and a relative energy resolution of 10^{-4} . The main part of the experimental endstation is a multi-circle (2+3) diffractometer, that can handle various (up to 200 kg heavy) sample environments and detectors, and includes vertical and horizontal diffraction geometry for surface/interface diffraction.

^a More details on the storage ring and beamline setup and characteristics are available at: <http://ankaweb.fzk.de> and http://www.mf.mpg.de/en/abteilungen/dosch/anka/anka_en.shtml

Figure 3.11 shows a schematic view of the experimental setup for specular and grazing-incidence X-ray diffraction. σ_{iV} and σ_{iH} are the vertical and horizontal slits in front of the sample, whereas σ_{fV} and σ_{fH} are the detector slits governing the resolution of the experiment. α_i denotes the incident angle of the X-rays on the sample. 2θ is the detector angle in grazing-incidence X-ray diffraction scans. In specular scans, $2\theta(HK0)$ is set to 0° and the detector angle is set to $2\alpha_i$.⁵¹

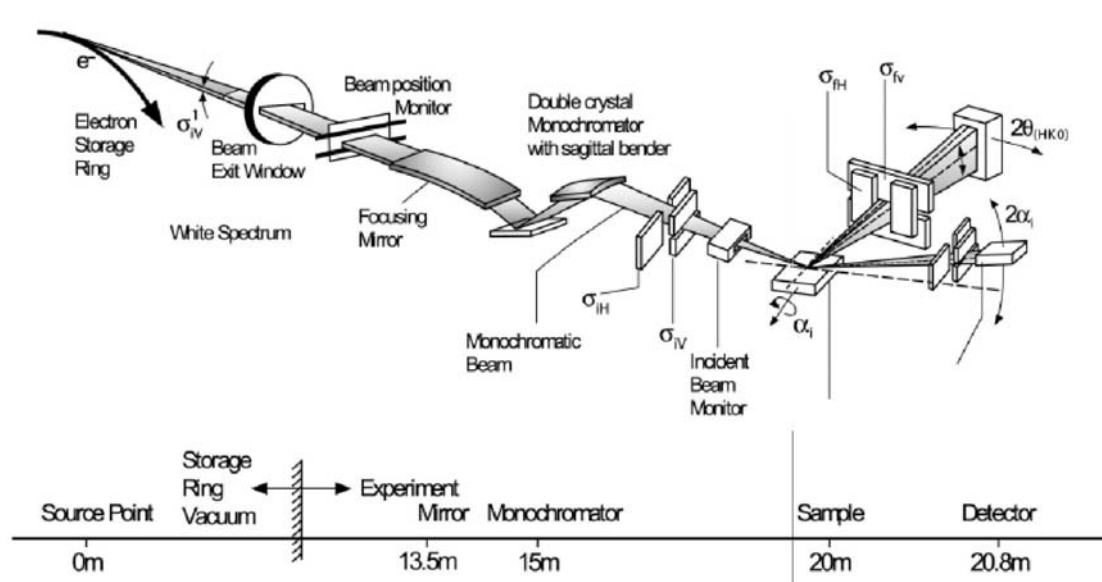


Figure 3.11. Schematic representation of the MPI Surface diffraction Beamline, including the distances between the different elements (From reference 51).

b. ID-10B at the European Synchrotron Radiation Facility (ESRF)^a

ID-10B is a multi-purpose, high-brilliance undulator beamline for high resolution X-ray scattering. The ESRF storage ring is operated at 6 GeV with 200 mA electron current. The beamline optics include a diamond (111) or (220) double crystal monochromator (intrinsic energy resolution $\Delta E/E$ of 5.9×10^{-5} and 2.3×10^{-5} , respectively) which allow an energy tunability of 8-13 keV and 13-22 keV, respectively. A further double-mirror setup leads to strong suppression of higher harmonics. The diffractometer in the endstation is a Huber z-axis diffractometer in the vertical scattering geometry, which allows the mounting of portable UHV chambers or other sample environments.

^a More details on the storage ring and beamline setup and characteristics are available at: <http://www.esrf.fr/UsersAndScience/Experiments/SCMatter/ID10B> and <http://www.esrf.fr>

c. ID-3 at the ESRF^a

ID-3 is a high-brilliance undulator beamline at the ESRF optimized for surface diffraction. The beamline optics consist in a Si(111) double crystal monochromator and two flat Rh-coated Si mirrors to reject harmonics. The relative energy resolution is of 10^{-4} . The experimental hutch is equipped with a z-axis diffractometer with its main sample axis vertical, specially suited for horizontal sample surfaces. On the diffractometer it is possible to mount "baby chambers".

3.3 Sample preparation

The samples have been prepared by organic molecular beam deposition (OMBD, see section 2.2.2). The growth of the organic films has taken place in three different systems: a stationary Omicron system, a stationary JEOL system, and a portable UHV chamber optimized for in-situ X-ray diffraction experiments. Each of them is briefly described in the following.

3.3.1 Omicron system

The Omicron system consists of three independent chambers: the load-lock to allow a fast introduction and extraction of the sample, the deposition chamber, and the analysis chamber, which are connected via a transfer system and arranged as displayed in Figure 3.12. The deposition chamber is equipped with various Knudsen cells, a quartz crystal microbalance (QCM) to monitor the deposition rate and nominal coverage, a sample manipulator allowing variable substrate temperature by heating or cooling with liquid nitrogen, and a quadrupole mass spectrometer.

^a More details on the storage ring and beamline setup and characteristics are available at: <http://www.esrf.fr/UsersAndScience/Experiments/SurfaceScience/ID03> and <http://www.esrf.fr>

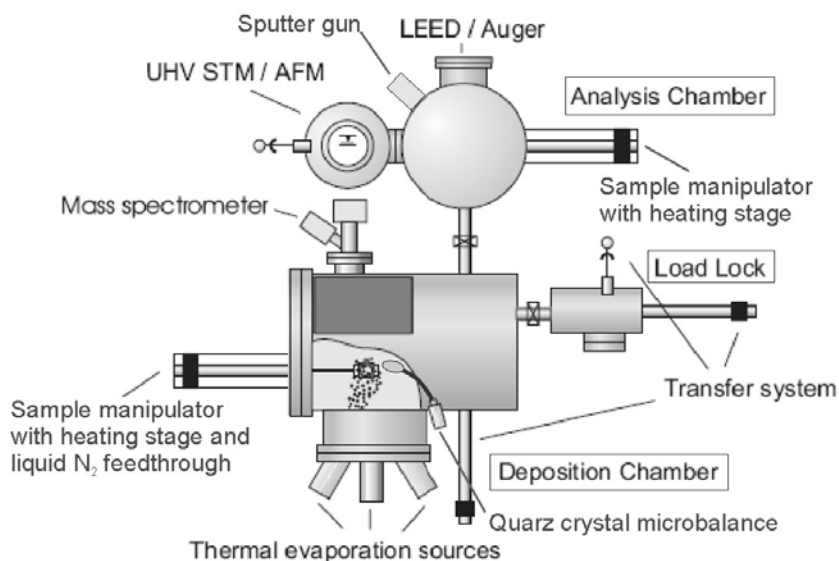


Figure 3.12. Schematic arrangement of the stationary Omicron system with its relevant mounted equipment. (From reference 52)

The analysis chamber is equipped with a sputter gun and a sample manipulator with heating stage to allow the preparation of substrates by sputter-anneal cycles, a combined LEED/Auger setup, and a combined AFM/STM allowing the characterization of the samples prior to and after growth without breaking the vacuum. The system is equipped with a turbo-molecular pump and both the deposition and analysis chamber each have additionally an ion-pump and a titanium sublimation pump, leading to base pressures in the range of 10^{-10} to 10^{-11} mbar.

3.3.2 JEOL system

The JEOL system is similarly divided into three independent but interconnected chambers: the load-lock, the preparation, and the analysis chamber. In this case, the preparation chamber is equipped with two Knudsen cells, a sputter gun and a manipulator with heating stage to allow the sputter-anneal cycles during substrate preparation, whereas the analysis chamber is equipped with a variable temperature STM. The base pressures in this system are in the range of 10^{-9} to 10^{-10} mbar.

3.3.3 Portable UHV chamber

This chamber (Figure 3.12) is specially designed to allow in-situ growth studies by X-ray diffraction. In this context, the chamber is portable and mountable on common diffractometer tables. It is equipped with a beryllium window of 1mm thickness. Given the low atomic number of Be, its consequently low x-ray absorption makes the window virtually transparent for the x-ray diffraction experiments. The sample holder has a heating stage and a “cold finger” connected to a feedthrough for liquid nitrogen, thus allowing variable substrate temperatures. In addition, two or three Knudsen cells and a sputter gun can be mounted. Electrical feedthroughs also allow the characterization of the electrical film properties during growth. The chamber is pumped with a turbo-molecular and an ion-pump, and shows base pressures around 10^{-9} mbar. The arrangement of the equipment parts can be seen in the photos in Figure 3.12.

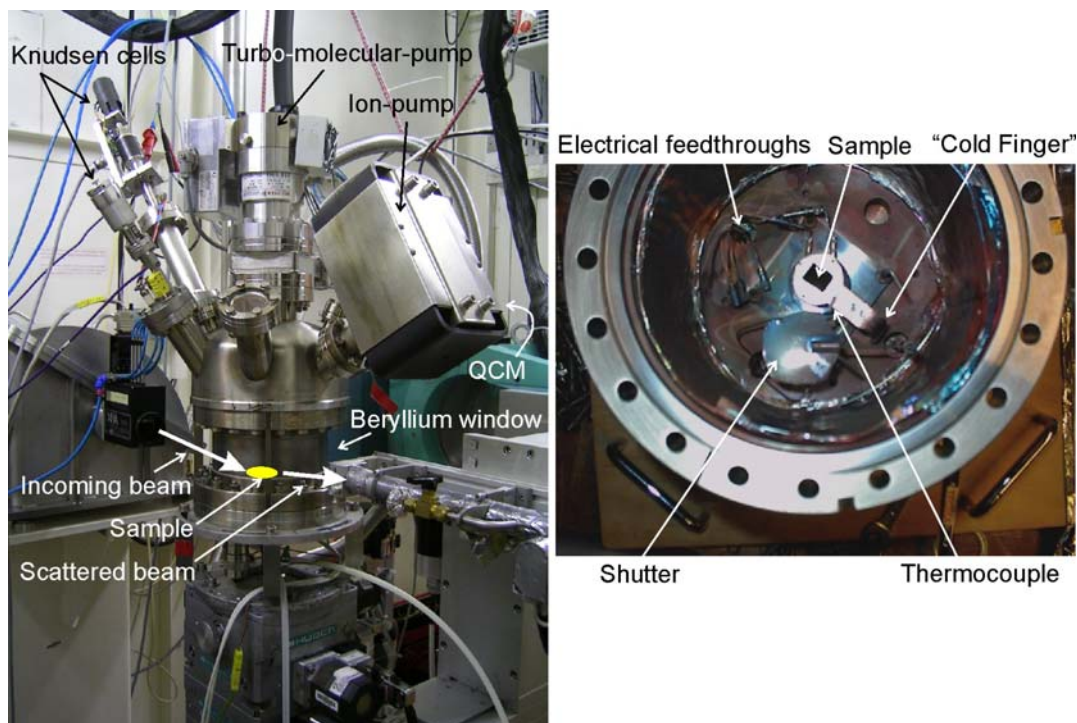


Figure 3.12 Photos of the portable chamber mounted on a diffractometer table (left) and of the inside of the chamber (right). The most relevant parts are labeled.

3.3.4 Substrate preparation

The cleanliness or any other general conditions of the substrates are of crucial importance for the subsequent growth of the films. Thus, the substrate preparation is an important step before the growth studies. The substrates used in this thesis have been Si (100) wafers covered by its native oxide, SiO₂ functionalized by a self-assembled monolayer (SAM) of OTMS (see section 2.2.3), and a Cu(111) single crystal surface. The preparation procedure for each of them is described in the following:

a. SiO₂/Si(100)

For the preparation of the Si wafers two cycles, each consisting in ultrasonic cleaning in acetone (15 min.) and ethanol (15 min.), were applied. Subsequently, they were dried with nitrogen gas and introduced in the UHV chamber. Then they were annealed to temperatures above 500 °C and cooled down to the growth temperature.

b. SiO₂/Si(100) functionalized by OTMS

In a first step, a pre-hydrolysis of the OTMS molecules was induced by diluting 0.2 g OTMS and 0.2 g HCl 1N in 25 ml Tetrahydrofuran (THF). After 2 days stirring at room temperature, the hydrolysate was diluted 1:20 (v:v) with n-hexane. The SiO₂ was cleaned by piranha solution (7/3 vol. of 98% H₂SO₄/30% H₂O₂) and then dipped into the OTMS solution for about 20 min. Afterwards, the substrates were first rinsed several times in n-hexane and, finally, cleaned in an n-hexane ultrasonic-bath for 5 minutes. The OTMS monolayers were controlled by contact-mode AFM in air and later transferred into the UHV chamber.

c. Cu(111)

The cleaning procedure of the Cu(111) single crystal consisted in repeated sputter-annealing cycles. The Ar sputtering energies and periods were reduced as the surface conditions improved. It was performed at Ar pressures of 2×10^{-4} mbar, with an energy

of 600 to 700 eV and for 20 to 60 minutes. This was alternated with annealing periods of the substrates, which was performed at temperatures from 500 to 670 °C for 20 to 60 minutes, also in this case reducing the temperatures and times as the surface conditions improved.

References

- ¹ G. Binnig, H. Rohrer, Scanning tunneling microscopy, *Helv. Phys. Acta* **55**, 726 (1982)
- ² G. Binnig, H. Rohrer, Ch. Gerber, E. Weibel, Tunneling through a controllable vacuum gap, *Appl. Phys. Lett.* **40**, 178 (1982)
- ³ G. Binnig, H. Rohrer, Ch. Gerber, E. Weibel, Surface studies by scanning tunneling microscopy, *Phys. Rev. Lett.* **49**, 57 (1982)
- ⁴ G. Binnig, C. F. Quate, Ch. Gerber, Atomic force microscope, *Phys. Rev. Lett.* **56**, 930 (1986)
- ⁵ B. Bushan, Handbook of nanotechnology, Springer (2004)
- ⁶ M. Nonnenmacher, M. P. O'Boyle, H. K. Wikramasinghe, Kelvin probe force microscopy, *Appl. Phys. Lett.* **58**, 2921 (1991)
- ⁷ U. Hartmann, Magnetic force microscopy, *Annu. Rev. Mat. Sci.* **29**, 53 (1999)
- ⁸ E. Betzig, J. K. Troutman, T. D. Harris, J. S. Weiner, R. L. Kostelak, Breaking the diffraction barrier-optical microscopy on a nanometer scale, *Science* **251**, 1468 (1991)
- ⁹ A. L. Weisenhorn, J. E. McDougall, J. A. C. Gould, S. D. Cox, W. S. Wise, J. Massie, P. Maivald, V. B. Elings, G. D. Stucky, P. K. Hansma, Imaging and manipulating of molecules on a zeolite surface with an atomic force microscope, *Science* **247**, 1330 (1990)
- ¹⁰ I. W. Lyo, Ph. Avouris, Field-induced nanometer-to-atomic-scale manipulation of silicon surfaces with the STM, *Science* **253**, 173 (1991)
- ¹¹ B. Parkinson, Layer-by-layer nanometer scale etching of two-dimensional substrates using a scanning tunneling microscope, *J. Am. Chem. Soc.* **112**, 7498 (1990)
- ¹² A. Majumdar, P. I. Oden, J. P. Carrejo, L. A. Nagahara, J. J. Graham, J. Alexander, Nanometer-scale lithography using the atomic force microscopy, *Appl. Phys. Lett.* **61**, 2293 (1992)
- ¹³ C. J. Chen, Introduction to scanning tunneling microscopy, Oxford University Press, Oxford (1993)
- ¹⁴ D. A. Bonnell, Scanning tunneling microscopy and spectroscopy. Theory, techniques and applications, VCH Publishers, New York (1993)
- ¹⁵ P. K. Hansma, J. Tersoff, Scanning tunneling microscopy, *J. Appl. Phys.* **61**, R1 (1987)
- ¹⁶ J. Tersoff, D. R. Hamann, Theory and application of the scanning tunneling microscopy, *Phys. Rev. Lett.* **50**, 1998 (1983)
- ¹⁷ J. Tersoff, D. R. Hamann, Theory of the scanning tunneling microscope, *Phys. Rev. B.* **31**, 805 (1985)
- ¹⁸ J. Bardeen, Tunneling from a many particle point of view, *Phys. Rev. Lett.* **6**, 57 (1961)
- ¹⁹ N. D. Lang, Spectroscopy of single atoms in the scanning tunneling microscope, *Phys. Rev. B* **34**, 5947 (1986)
- ²⁰ R. M. Feenstra, J. A. Stroscio, A. P. Fein, Tunneling spectroscopy of the Si(111)2x1 surface, *Surf. Sci.* **181**, 295 (1987)
- ²¹ R. Wiesendanger, Scanning probe microscopy, Springer Verlag, Berlin (1998)

-
- ²² B. Bushan, Handbook of nanotechnology, Springer (2004)
- ²³ D. J. Keller, F. S. Franke, Envelope reconstruction of probe microscope images, *Surf. Sci.* **294**, 409 (1993)
- ²⁴ F. Biscarini, P. Levy, Nanoscale caliper for direct measurement of scanning force microscopy probes, *Appl. Phys. Lett.* **71**, 888 (1997)
- ²⁵ B. Persson, Sliding friction, physical principles and applications, Springer Verlag, Berlin, Heidelberg, New York (1998)
- ²⁶ F. P. Bowden, D. Tabor, The friction and lubrication of solids, Clarendon, Oxford (1964)
- ²⁷ R. Garcia, R. Perez, Dynamic atomic force microscopy methods, *Surf. Sci. Rep.* **47**, 197 (2002)
- ²⁸ R. Garcia, C. J. Gomez, N. F. Martinez, S. Patil, C. Dietz, R. Magerle, Identification of nanoscale dissipation processes by dynamic atomic force microscopy, *Phys. Rev. Lett.* **97**, 016103 (2006)
- ²⁹ X. Chen, M. C. Davies, C. J. Roberts, S. J. B. Tendler, P. M. Williams, J. Davies, A. C. Dawkes, J. C. Edwards, Interpretation of tapping mode atomic force microscopy data using amplitude-phase-distance measurements, *Ultramicroscopy* **75**, 171 (1998)
- ³⁰ J. Tamayo, R. Garcia, Effects of elastic and inelastic interactions on phase contrast images in tapping-mode scanning force microscopy, *Appl. Phys. Lett.* **71**, 2394 (1997)
- ³¹ J. P. Cleveland, B. Anczykowski, A. E. Schmid, V. B. Elings, Energy dissipation in tapping-mode atomic force microscopy, *Appl. Phys. Lett.* **72**, 2613 (1998)
- ³² O. P. Behrend, L. Odoni, J. L. Loubet, N. A. Burnham, Phase imaging: Deep or superficial?, *Appl. Phys. Lett.* **75**, 2551 (1999)
- ³³ T. R. Albrecht, P. Grütter, D. Horne, D. Rugar, Frequency modulation detection using high-Q cantilevers for enhanced force microscopy sensitivity, *J. Appl. Phys.* **69**, 668 (1991)
- ³⁴ F. J. Giessibl, Advances in atomic force microscopy, *Rev. Mod. Phys.* **75**, 949 (2003)
- ³⁵ J. A. Nielsen, D. McMorrow, Elements of modern X-ray physics, John Wiley & Sons Ltd., Chichester (2001)
- ³⁶ M. Tolan, X-ray scattering from soft matter thin films-Materials science and basic research-, Springer, Berlin, Heidelberg (1998)
- ³⁷ H. Dosch, Critical phenomena at surfaces and interfaces, evanescent x-ray and neutron diffraction, Springer, Berlin, Heidelberg (1992)
- ³⁸ V. Holý, U. Pietsch, T. Baumbach, High-resolution x-ray scattering from thin films and multilayers, Springer, Berlin, Heidelberg (1999)
- ³⁹ B. E. Warren, X-ray diffraction, Dover Publications, inc (1990)
- ⁴⁰ Eds. A. J. C. Wilson, E. Prince, International tables for X-ray crystallography, Kluwer Academic Publisher (1999)
- ⁴¹ L. G. Parrat, Surface studies of solids by total reflection of x-rays, *Phys. Rev.* **95**, 359 (1954)
- ⁴² I. M. Tidswell, B. M. Ocko, P. S. Pershan, S. R. Wasserman, G. M. Whitesides, J. D. Axe, X-ray specular reflection studies of silicon coated by organic monolayers (alkylsiloxanes), *Phys. Rev. B* **41**, 1111 (1990)
- ⁴³ E. Vlieg, Integrated intensities using a six-circle surface X-ray diffractometer, *J. Appl. Cryst.* **30**, 532 (1997)
- ⁴⁴ A. C. Mayer, R. Ruiz, R. L. Headrick, A. Kazimirov, G. G. Malliaras, Early stages of pentacene film growth on silicon oxide, *Org. Electron.* **5**, 257 (2004)
- ⁴⁵ H. A. Van der Vegt, H. M. van Pinxteren, M. Lohmeier, E. Vlieg, Surfactant induced layer-by-layer growth of Ag on Ag(111), *Phys. Rev. Lett.* **68**, 3335 (1992)
- ⁴⁶ E. Vlieg, A. W. D. Van der Gon, J. F. van der Veen, J. E. Macdonald, C. Norris, Surface x-ray scattering during crystal growth: Ge on Ge(111), *Phys. Rev. Lett.* **61**, 2241 (1988)

-
- ⁴⁷ E. Weshke, C. Schüssler-Langeheine, R. Meier, G. Kaindl, C. Sutter, D. Abernathym G. Grübel, q dependence of the growth oscillation period of x-ray reflectivity in heteroepitaxy: Ho/W(110), *Phys. Rev. Lett.* **79**, 3954 (1997)
- ⁴⁸ H. A. Van der Vegt, J. Alvarez, X. torrelles, S. Ferrer, E. Vlieg, Indium-induced layer-by-layer growth and suppression of twin formation in the homoepitaxial growth of Cu(111), *Phys. Rev. B* **52**, 17443 (1995)
- ⁴⁹ B. Krause, A. C. Dürr, F. Schreiber, H. Dosch, O. H. Seek, Late growth stages and post-growth diffusion in organic epitaxy: PTCDA on Ag(111), *Surf. Sci.* **572**, 385 (2004)
- ⁵⁰ B. Krause, F. Schreiber, H. Dosch, A. Pimpinelli, O. H. Seek, Temperature dependence of the 2D-3D transition in the growth of PTCDA on Ag(111): A real time x-ray and kinetic Monte-Carlo study, *Europhys. Lett.* **65**, 372 (2004)
- ⁵¹ A. C. Dürr, N. Koch, M. Kelsch, A. Rühm, J. Ghijsen, R. L. Johnson, J.-J. Pireaux, J. Schwartz, F. Schreiber, H. Dosch, A. Kahn, Interplay between morphology, structure, and electronic properties at diindenoperylene-gold interfaces, *Phys. Rev. B* **68**, 115428 (2003)
- ⁵² B. Krause, PhD Thesis (2002)

4 Tuning the growth of F₁₆CuPc on SiO₂ by use of a self-assembled monolayer (OTMS)

This section is devoted to studies of F₁₆CuPc thin films deposited on SiO₂. Among the numerous different dielectrics, SiO₂ is the most widely used substrate for organic film growth because of the convenient use of silicon wafers for fabrication of thin film transistors, in which the doped Si acts as the gate contact and the SiO₂ as the dielectric. In addition, the highly sophisticated silicon technology allows the production of Si wafers with atomically flat surfaces, making them excellent model surfaces for growth studies and especially suitable for X-ray reflectivity studies.

The results are relevant by themselves, since the characterization of the structure and morphology are prerequisites to get a deeper understanding of the “structure-properties” relationships, one of the missing milestones in the development towards a directed organic device optimization. From previous studies it was known that the F₁₆CuPc molecules on SiO₂ organize in a layered structure of upright-standing molecules.¹ However, the detailed crystal structure of F₁₆CuPc films was still undetermined and instead, the film structure of the “sister” molecule CuPc is often taken as reference.^{2,3,4,5,6} In addition, the knowledge of the structure and morphology is also relevant for the studies on organic heterostructures presented in section 5, in which F₁₆CuPc on SiO₂ is used as substrate for the deposition of further molecular films.

We present a thorough characterization of the growth and structure of F₁₆CuPc on SiO₂, with a special elaborateness for the first layers in contact with the dielectric. Then, the results are compared with the growth of the F₁₆CuPc on functionalized SiO₂ with a methyl terminated self-assembled monolayer (OTMS). The morphological differences are correlated with the different electronic performance of devices based on both kinds of surfaces.

4.1 *Experimental details*

For this study, Si wafers covered by their native oxide have been used as substrate. The cleaning procedure is described in section 3.3.4. The F₁₆CuPc films involved in the in-situ X-ray diffraction characterization have been grown in a portable UHV chamber, while the films used for the AFM measurements have been grown in a commercial Omicron system. Both setups are described in section 3.3. The growth conditions have been similar for all samples: a substrate temperature of 195 °C and a growth rate of 3 Å/min. Some samples have been grown under different conditions, which are then indicated in the text.

The X-ray studies have been performed at the Max Planck Surface Diffraction Beamline of ANKA (Karlsruhe), and at the beamline ID-3 of the European Synchrotron Radiation Facility (ESRF, Grenoble). The AFM measurements have been performed in an Omicron scanning probe microscope (SPM) under UHV (in contact and non-contact modes), or under ambient conditions (in contact and tapping modes) in a Digital Nanoscope III SPM, or/and a Nanotec SPM. For the image processing the freeware WSxM program has been used.

4.2 *Study on the bare SiO₂*

4.2.1 *Structure and morphology*

In what follows, we present our study on the F₁₆CuPc growth and structure on top of the bare SiO₂. We describe the nominal film thickness in terms of the equivalent thickness D of a close packed film with the same mass as the deposited film. Alternatively, we normalize the thickness by the height of a layer of upright-standing molecules. The resulting fractions of a monolayer Θ and the equivalent thickness D are then related, in the case of F₁₆CuPc, through $\Theta = D/14.3$.

Figures 4.1a and b show topographic AFM images of films deposited on SiO₂ with nominal thickness of 0.4 and 7 ML, respectively. As observed from the height profiles

(taken as marked in the topography images), the height of the first layer in Figure 4.1a (14.1 ± 2.6 Å), as well as the heights of subsequent layers (visible as discrete steps in the profile of Figure 4.1b) are in the range of the lateral molecular dimensions (~ 14.5 Å). This indicates an upright-standing molecular configuration within the layers.

The structure along the surface normal has been further probed by X-ray reflectivity for nominal coverages ranging from the monolayer regime to tens of layers, as shown in Figure 4.1c. The development of Bragg reflections upon increasing coverage is observed as a result of the diffraction from the layered structure in the film.

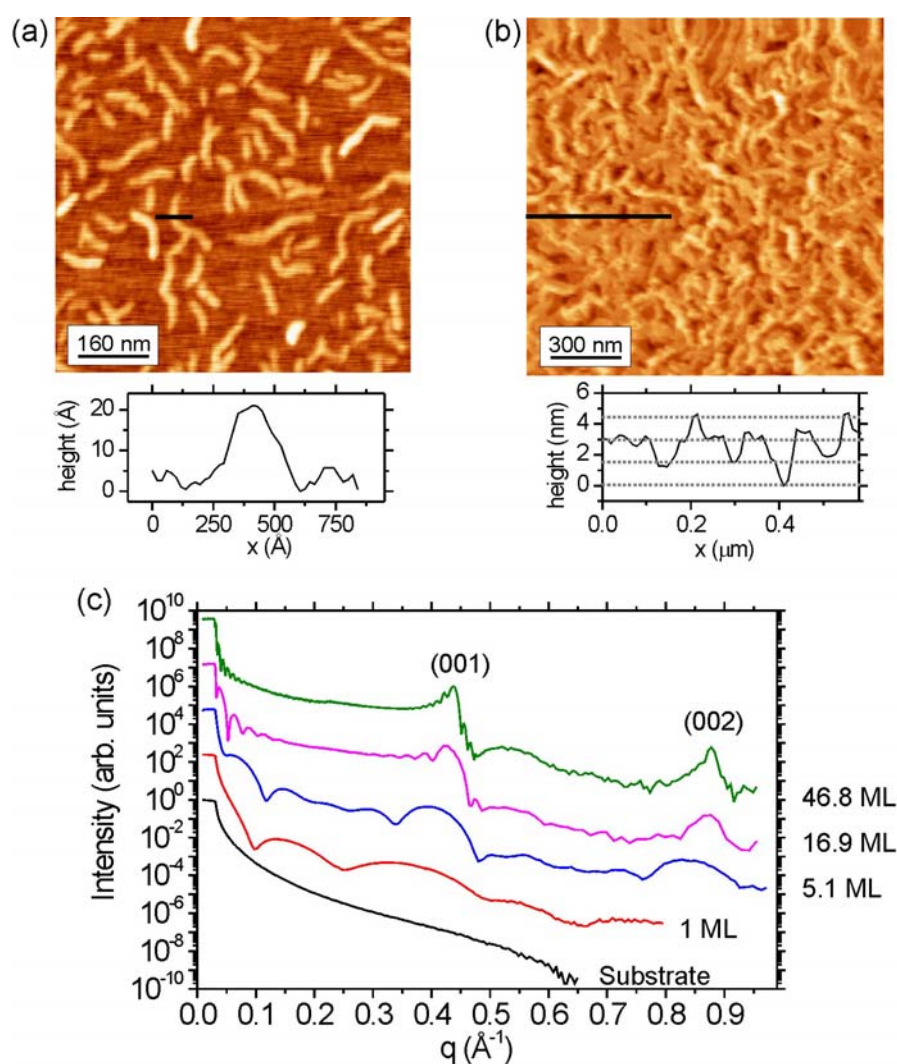


Figure 4.1. AFM topography images of films with nominal thicknesses of (a) 0.4 and (b) 7 ML. The profiles below are taken as marked on the respective images. (c) X-ray reflectivity data of F₁₆CuPc films with increasing thickness.

The position of the Bragg peak corresponds to a lattice spacing (layer height) of 14.30 ± 0.05 Å, confirming an upright-standing molecular configuration. The similar widths of the Kiessig fringes at low q_z values, related to the total film thickness, and the Laue fringes around the Bragg maxima, related to the coherently ordered film thickness, imply that the films are coherently ordered throughout the whole thickness. For the low coverage samples, in which the reduced number of layers does not give rise to Bragg reflections, an additional and more extended study based on fits to the reflectivity data is presented in the next section.

The observed molecular orientation of upright-standing molecules, consequently with the overlapping direction of their π -orbitals parallel to the surface, is the most favorable for those applications in which transport within the surface plane is required, as is the case in OFETs.^{7, 8, 9} This configuration is usually formed on weakly interacting substrates and has already been observed on Al_2O_3 ^{10, 11} or MgO .¹⁰ In contrast, on metals, where the molecule-substrate interaction predominates over the intermolecular interactions, the molecules grow with their molecular plane parallel to the surface (i.e., lying down),¹² as we will see in section 6.3 for the case of a copper substrate.

In grazing incidence X-ray diffraction (GIXD) measurements, the component of the momentum transfer directed within the surface plane allows us to probe the in-plane structure of the samples (see section 3.2.4). By performing in-situ GIXD measurements during the F_{16}CuPc growth, we have monitored the evolution of the in-plane order for increasing film thickness (Figure 4.2a). For the first monolayer (ML), two in-plane reflections corresponding to lattice spacings of 14.61 Å ($q=0.43$ Å⁻¹) and 3.31 Å ($q=1.90$ Å⁻¹) indicate the formation of an ordered structure. Since the former is in the range of the lateral molecular dimensions (Figure 4.2b) and the latter in the range of the intermolecular spacing between cofacially packed molecules, these peaks have been correlated to the (10) and (01) reflections of a rectangular unit cell,^a respectively, as shown in Figure 4.3a.

^a This is assumed for simplicity, since no exact angle determination is possible from two reflections.

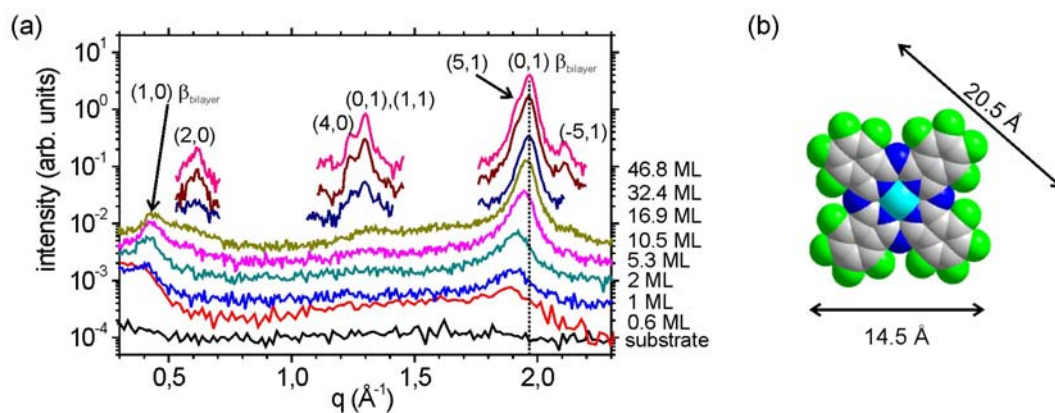


Figure 4.2. Evolution of the GIXD data upon increasing film thickness. The dotted line indicates the final position of the $(01)_{\beta\text{-layer}}$ reflection.

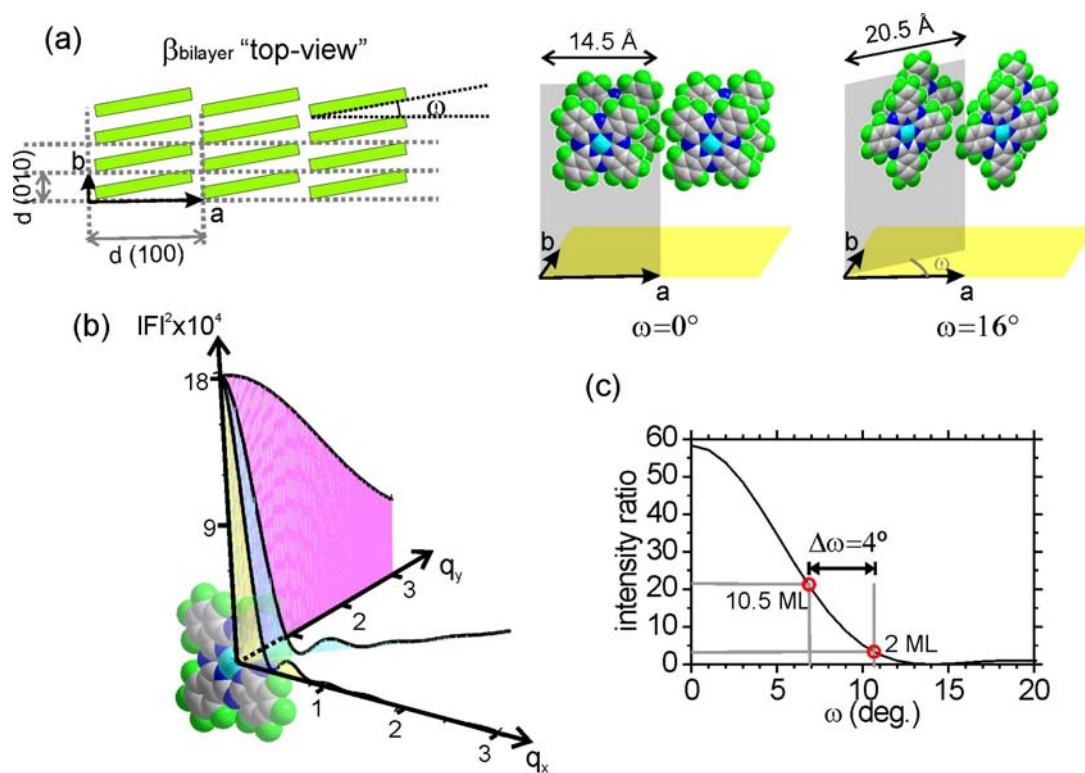


Figure 4.3. (a) Schematic top-view of the β -layer-structure, and explanatory pictures for the dependence of the angle ω on the molecular orientation (b) Squared molecular structure factor along various directions. (d) Ratios between the intensities of the (01) and (10) reflections as observed experimentally for various film thicknesses (symbols) and calculated for the β -layer-structure vs. the molecular tilt angle ω (line).

This implies that the upright-standing molecules are stacked in columns along the [01] direction with the molecular planes nearly parallel to the [10] direction. A small tilt angle $\omega=0^\circ \dots 16^\circ$ may exist between the molecular plane and the [10] direction depending on the exact molecular orientation, i.e. rotation of the molecule around the axis perpendicular to its plane (Figure 4.3a).

The formation of this phase is restricted to the first two $F_{16}CuPc$ layers, as evidenced by the saturation in the integrated intensity of the (10) reflection after a nominal thickness of about 2 ML (29 Å). This structure is referred to as β_{bilayer} -structure. With additional coverage, the (01) reflection continues to grow and experiences a shift which implies a contraction of the in-plane lattice parameter b towards a final value of 3.19 Å. The behavior of the integrated Bragg intensity ratio $I(01)/I(10)$ with the film thickness has been analyzed to provide a qualitative explanation of this puzzling structural change of the β_{bilayer} -structure. The very anisotropic molecular structure factor of $F_{16}CuPc$ (Figure 4.3b), calculated as exposed in section 3.2.1, has been exploited to estimate from the ratio $I(10)/I(01)$ the molecular tilt angle ω (Figure 4.3c). A comparison of the experimentally observed and the calculated $I(01)/I(10)$ ratio for the first 2 ML and for thicker films evidence a reduction in the tilt angle of about 4° upon film growth.^a Thus, the observed lattice contraction in b is intimately associated with a change in the molecular tilt angle ω . This calculation has been performed assuming upright-standing molecules with their molecular side parallel to the surface. A rotation of the molecule around the normal to the molecular plane leads only to minor changes in the resulting intensity.^b

Upon further deposition (above 14 ML), additional in-plane Bragg reflections can be distinguished (Figure 4.2) which are related to the growth of a new structure referred to as β -structure. The in-plane reflections of this β -structure correspond to an oblique unit cell containing two molecules with the parameters shown in Table 4.1 (summarizing also the β_{bilayer} -structure). The thin film structure consists in columns of

^a The X-ray intensities have been corrected for the polarization factor. Debye Waller factor (DWF) corrections are estimated to be rather small for these low-order reflections: the thermal DWF (associated with a Debye temperature of 199 K as reported by Bell et al. in *J. Chem. Soc., Faraday Trans. 94*, 3155 (1999) for $FePc$) results by way of example into $\exp(-2M)=0.99$ for the (01) reflection.

^b Notice that deviations from the assumed rectangular unit-cell, or a molecular tilt with respect to the surface normal, could slightly change the absolute values of ω , but would still lead to a similar reduction of the tilt angle.

cofacially oriented upright-standing molecules with a distance between them of $a/2=10.13$ Å. Comparing again the observed lattice spacing of 10.13 Å to the molecular dimensions, an average tilt angle between the molecular planes and the [10] direction of $\sim 45^\circ$ is obtained. By analogy to the β -H₁₆CuPc structure, based on the similar anisotropic morphology that both F₁₆CuPc and β -H₁₆CuPc exhibit, and further supported by the presence of two molecules within the unit cell (implying non-equivalent molecular orientations or positions between them) we suggest a configuration of molecules with alternating tilt in adjacent columns (Figure 4.4). The columnar stacking has been clearly observed by Atomic Force Microscopy (AFM) on F₁₆CuPc films grown on functionalized SiO₂, as will be shown in section 4.3.1. The parameters a , b and γ determined from the AFM images correspond to values of 18.7 Å, 4.5 Å and 85 degrees, respectively, in good agreement with the GIXD structural data (within the AFM error bar of ~ 10 %).

Table 4.1 further shows that the densities of the β and β_{bilayer} structures are rather similar and comparable to that of the bulk structure (Table 2.1).

	β_{bilayer} -structure	β -structure
a (Å)	14.61	20.26 ± 0.06
b (Å)	3.31	4.87 ± 0.04
γ (deg.)	~ 90	84.1 ± 0.2
Layer height (Å)	14.1 ± 2.6	14.3 ± 0.05
V/molecule	682 ± 126	701.1 ± 6.5

Table 4.1. Unit cell parameters and volume per molecule for the β_{bilayer} - and β -structures.

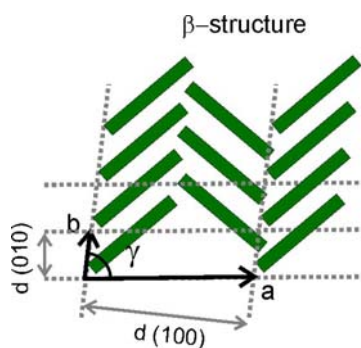


Figure 4.4. Schematic top view of the β -structure.

Interestingly, $F_{16}CuPc$ films grown at room temperature exhibit the same structure (Figure 4.5). This is in strong contrast with the $H_{16}CuPc$, often considered to be an analogous molecule, which exhibits a metastable α -phase for room temperature deposition.¹³

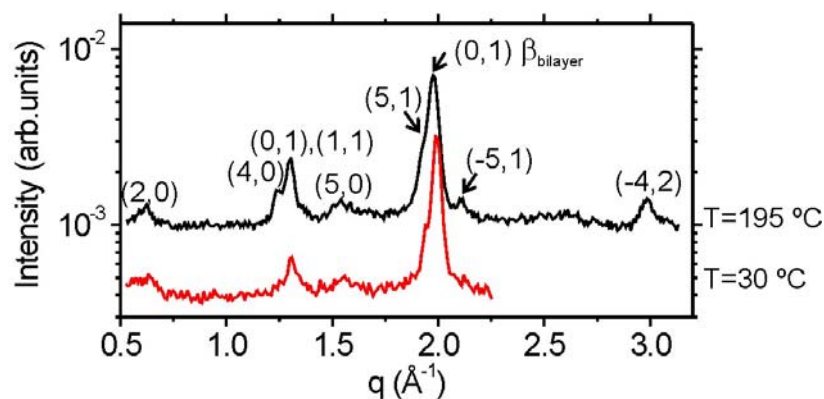


Figure 4.5. GIXD data for two films grown at 195 °C and at room temperature.

The observed structural changes are an unexpected result, because the formation of strained structures occurs in general on substrates for which the molecule-substrate interaction dominates the intermolecular interaction, as it is generally for organic film growth on metals.^{14,15,16,17,18,19} Although it is clear that, in comparison with metals, the molecule-substrate interaction for SiO_2 is rather weak, the present study shows that SiO_2 is apparently not so inert for $F_{16}CuPc$. A detailed structural analysis performed by X-ray reflectivity in the next section will further confirm this suspect.

4.2.2 Detailed focus on the first layers

a. Growth mode

The growth and evolution of the first $F_{16}CuPc$ layers have been monitored by AFM and in-situ X-ray reflectivity. Topographical AFM images are shown in Figure 4.6 for nominal film thicknesses ranging from 0.2 to 1.6 ML. At a coverage of $\Theta=0.2$ ML, the molecules nucleate in elongated islands forming an incomplete first layer.

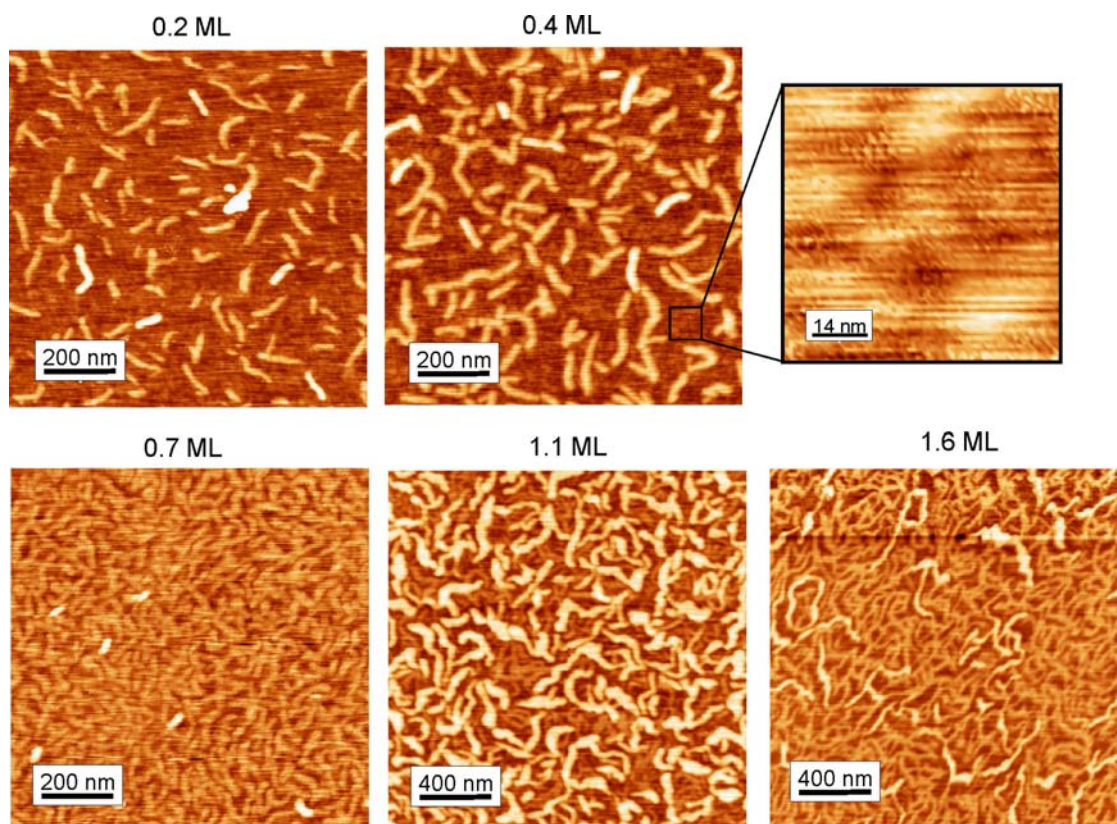


Figure 4.6. Topographic AFM images of $F_{16}CuPc$ films on SiO_2 with nominal thicknesses from 0.2 to 1.6 ML. The zoom shows the observed clusters between the crystallites of the upright-standing $F_{16}CuPc$.

Since the lateral surface diffusion on amorphous SiO_2 is isotropic, the elongated shape of the islands (Figure 4.6) must be related to an anisotropic sticking. It is the strong coupling of the electronic π -system which gives rise to this preferred anisotropic growth. Thus, also here the observed elongation direction is expected to be related to the stacking direction of $F_{16}CuPc$. As the coverage increases to $\Theta=0.4$ ML, the islands of the first layer grow predominantly in length (anisotropic two-dimensional growth). Upon further increase of the molecular deposition up to 0.7 ML, the film growth remains confined mainly to the first monolayer, although a few nucleation sites of the second layer are already present for the lowest coverages (0.2 to 0.7 ML). The anisotropic growth and the elongated shape of the crystallites prevent the complete coverage by coalescence, giving rise to the nucleation of new islands to fill the space between the existing islands. These new crystallites display smaller islands sizes as a consequence of the lower amount of free space, as can be clearly

distinguished in the image corresponding to 0.7 ML. Upon further deposition, the second layer grows (1.1 ML image) and also the nucleation of the third layer starts before the second monolayer is completed (1.6 ML image).

High resolution images taken with NC AFM in UHV (Figure 4.7) clearly show that the nucleation of the second layer takes place mainly at grain boundaries between adjacent islands of the first layer. This suggests that, without experiencing a significant Schwoebel type barrier, most of the molecules arriving on top of an island can diffuse to the lower layer at the initial growth stage (below the coalescence regime). In turn, at higher coverage, a fast growth of the subsequent layer occurs due to the higher abundance of grain boundaries that serve as nucleation centers.

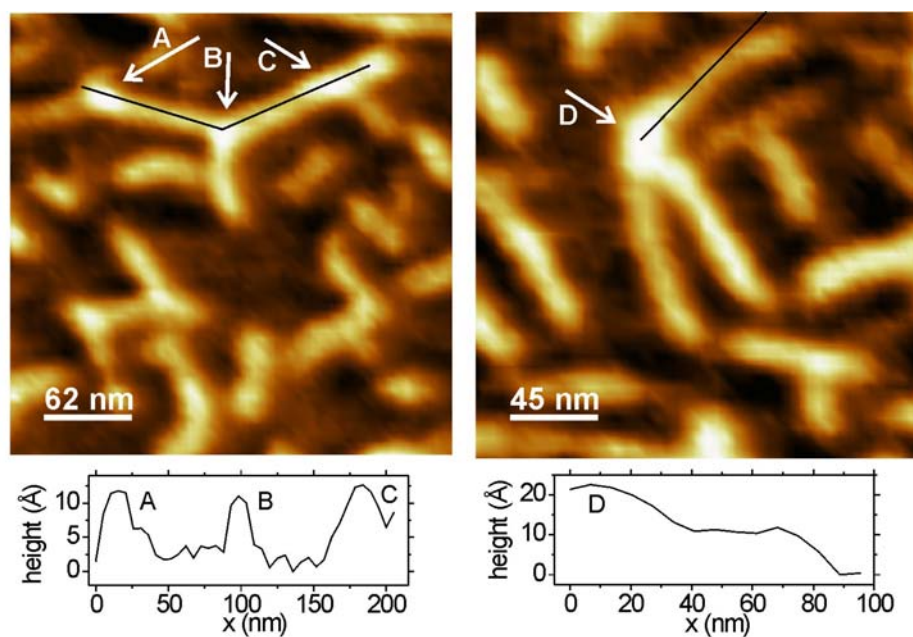


Figure 4.7. AFM topographic images showing the preferred nucleation sites for the second layer (brighter spots marked with labelled arrows) at the grain boundaries of the underlying first layer in two different areas, together with profiles taken along the crystallites as shown on the images. The nominal coverage corresponds to 0.34 ML.

The experimental X-ray reflectivity data (symbols) are shown in Figure 4.8a (the inset shows a rocking scan performed at a q_z value of 0.177 \AA^{-1} , evidencing the excellent data quality and the narrow peak width of 0.01 degrees) for film thicknesses ranging between 0.6 and 24 \AA (Θ between 0.04 and 1.68 ML). Their corresponding

fits performed with the Parrat algorithm (see section 3.2.2) are given by the solid lines. The fit parameters are given in Appendix A for each of the samples.

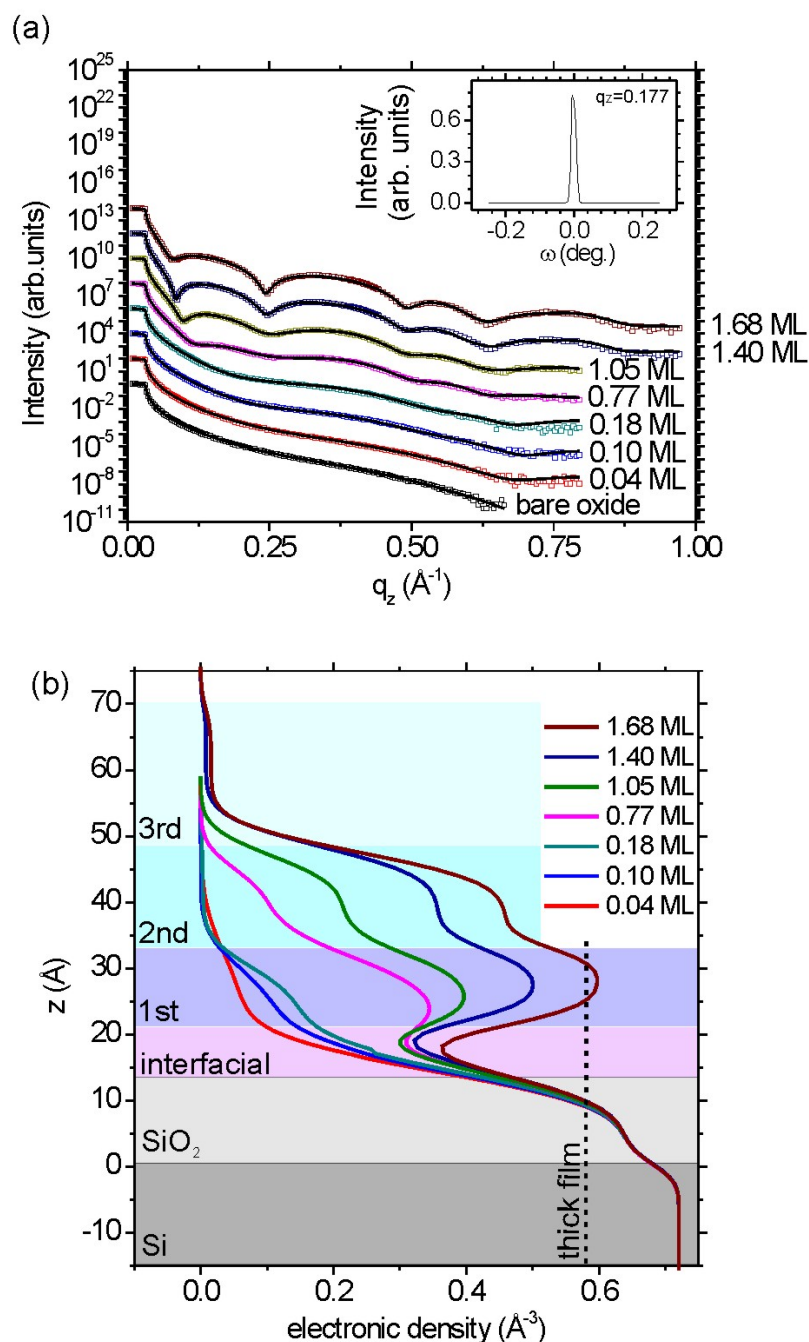


Figure 4.8. (a) X-ray reflectivity measurements of the clean substrate and F_{16}CuPc films of 0.04, 0.1, 0.18, 0.77, 1.05, 1.40 and 1.68 ML thickness (symbols). The solid lines are fits to the data. The data sets are shifted for clarity. The inset shows a rocking scan performed at a q_z value of 0.177 \AA^{-1} (b) Evolution of the electronic density profiles along the surface normal obtained from the fits for increasing coverage. The dashed line is the average electronic density of a thick F_{16}CuPc film and thus the expected saturation value of the layers. The colored fringes represent a guide to the eye to distinguish the different layers of the film.

The data associated with the bare substrate are fitted with a layer for Si and another for SiO₂. Electron densities of 0.720 Å⁻³ for the Si and 0.642 Å⁻³ for the SiO₂ are obtained, in good agreement with literature values. The oxide thickness and roughness derived from the fitted model are 14 Å and 4.3 Å, respectively. The value of the SiO₂ roughness as determined by AFM was 3.2 Å for maximal scanned areas of 3 x 3 μm². This is in rather good agreement with the reflectivity data. The slight discrepancy is most likely due to the fact that AFM averages over a much smaller area (microns in AFM versus millimetres in X-ray reflectivity) and to the size effect of the tip. The substrate parameters have been kept unchanged during the fitting of the F₁₆CuPc film. Additional layers were added whenever necessary to obtain satisfactory fits. The fit parameters for a certain thickness were used as the starting parameters for the subsequent fits. The fraction of area covered by each layer has been determined dividing the electronic density of the layer by the mean electronic density of a complete layer ($\delta = \rho/0.58$).

The development of the electron density of the molecular layers as a function of coverage can be followed in Figure 4.8b. As a guide for the eyes, the color boxes denote the different layers. The vertical dashed line marks the mean electronic density of $\rho = 0.58$ Å⁻³ obtained for thick films and, thus, the value expected for a complete compact layer of the organic material. It agrees perfectly with the electronic density estimated from the bulk unit cell.

The evolution of the partial coverage of each layer versus the total deposited film thickness, as obtained from X-ray reflectivity and AFM (by binary maps which show the percentage of area above a certain height), is displayed in Figure 4.9a. Both techniques show an excellent agreement and evidence that the film growth deviates from an ideal layer-by-layer growth. Figure 4.9b illustrates, as a control of internal consistency, the X-ray and AFM total coverage plotted versus the QCM coverage.

The similar morphology of the islands in the first and second layers (Figure 4.6) suggests that the growth of the subsequent layer proceeds with the same alignment as that of the islands underneath. The average length of the F₁₆CuPc islands is 150 Å, 350 Å and 400 Å for the first, second and third layers, respectively.

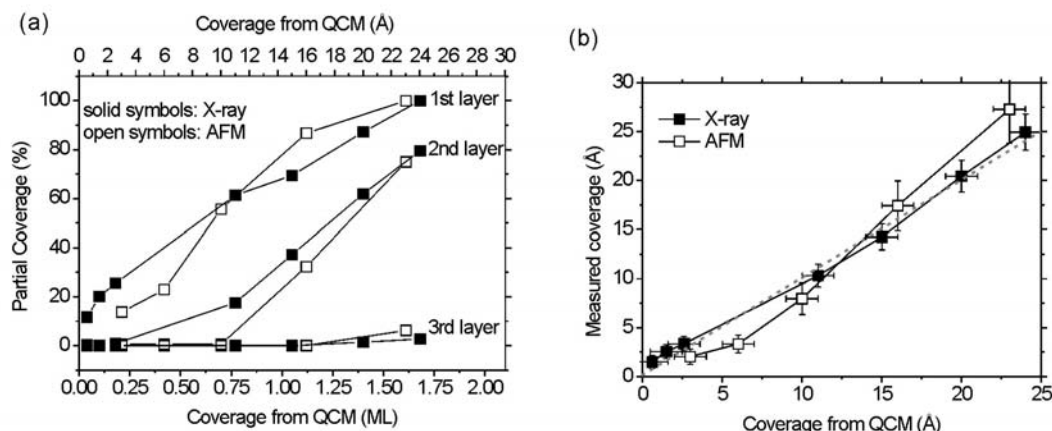


Figure 4.9. (a) Partial coverage of the first three layers of standing molecules as a function of the total coverage from X-ray (solid symbols) and AFM (open symbols) measurements (b) Estimated coverage as obtained from AFM (solid symbols) and X-ray (open symbols) data versus the nominal coverage obtained from the QCM during growth. The dashed line would indicate perfect agreement.

The mean lateral domain size $\xi_{||}$, estimated from the width of the $\beta_{\text{bilayer}}(01)$ Bragg reflection, is found to increase with the film thickness, from $\xi_{||} = 41 \pm 5$ Å for a coverage of 0.063 ML, to $\xi_{||} = 118 \pm 2$ Å for a coverage of 10.49 ML. The difference between the values obtained from AFM and GIXD is attributed to the existence of multiple domains inside an island. Nevertheless, both the increase in the domain and island size for subsequent layers, imply higher lateral mobility of F_{16}CuPc on the standing F_{16}CuPc molecules than on the SiO_2 (strictly seen the first layer does not grow directly on the SiO_2 , but on an interfacial layer described below). The factors responsible for the reduced surface mobility of the first layer of F_{16}CuPc might be the higher roughness and inhomogeneity of the interfacial layer or/and an increased interaction of the molecules with the interfacial layer compared to the interaction with subsequent layers.

b. Interfacial layer

The X-ray reflectivity data give an unambiguous evidence for the formation of an interfacial layer between the SiO_2 and the first layer of standing molecules (Figure 4.8b). The height of the interfacial layer, according to the reflectivity data, is about 3 Å for the first stages of the growth (0.2 ML) and increases to 6.5 ± 0.6 Å for higher

coverage. When the total coverage exceeds 0.77 ML (11 Å), the electronic density of this layer reaches a saturation regime and increases only very slightly with further deposition. Surprisingly, the saturation value of $\rho=0.35 \text{ Å}^{-3}$ is only 60% of the value expected for a closed F₁₆CuPc layer ($\rho=0.58 \text{ Å}^{-3}$). The effect of the X-ray exposure on the films has been carefully tested and gave no evidence for radiation damage during the X-ray reflectivity experiments. A closer inspection of Figure 4.6 shows that the region between the first layer islands is covered by some molecular aggregates, further displayed in a zoom into the area between islands in the sample with 0.4 ML coverage. This molecular film is inhomogeneous, with clusters of heights between 5 and 10 Å, resulting in an increased roughness (rms = 4.2 Å) compared to that measured on the bare SiO₂ (rms = 1.6 Å) in an area of 70 nm x 70 nm. We correlate this molecular film to the interfacial layer observed by X-ray reflectivity. Since the distance between layers of flat lying F₁₆CuPc molecules is of ~3.14 Å, (see section 5.1) the observed average height of ~6.5 Å suggests the formation of a bilayer of molecules lying flat on the SiO₂.

Regarding the initial growth of F₁₆CuPc on SiO₂, two scenarios can be considered:

- i. The growth of molecular clusters of lying-down molecules competing with the growth of ordered islands of standing molecules on the SiO₂.
- ii. The growth of standing molecules taking place on top of the interfacial layer of lying molecules.

The height of the first layer of standing molecules measured by AFM relative to the upper part of the surrounding clusters ($14.1 \pm 2.6 \text{ Å}$) supports the scenario where the islands nucleate on top. Furthermore, the fact that the first layer does not replicate the topography of the clusters as observed at low coverage by AFM (with heights varying between 5 and 10 Å) suggests that the clusters eventually merge (leading to a more uniform interfacial layer) prior to the completion of the first layer of standing molecules.

The existence of an underlying interfacial layer, could provide an explanation of the large dispersion of heights obtained by AFM (with mean square deviation of 2.6 Å) and of the high interfacial roughness obtained from X-ray reflectivity. The fact that the saturation value of the electronic density for this interfacial film is 60% of the value expected for a close packed F₁₆CuPc film seems to indicate a poor packing in

the interfacial layer due to numerous vacancies and defects. In fact, no evidence of ordering has been found by GIXD.

The formation of a film of lying-down molecules is unexpected on a low-interacting surface as is the case of SiO₂. Previous structural studies on the first stages of the growth on SiO₂ of pentacene^{20,21} and diindenoperylene (DIP)²² have not found any indication of a lying-down phase. Only for sexithiophen on SiO₂, the formation of a layer of lying-down molecules on the substrate in the submonolayer regime is observed, but these are not longer present when the first monolayer of upright-standing molecules is formed.²³ A possible reason for the formation of such interfacial layer in the case of F₁₆CuPc is the interaction of the fluorine atoms with the SiO₂ surface. A previous study of the electronic structure of F₁₆CuPc/SiO₂ by means of XPS has suggested that the strong interaction of F₁₆CuPc with SiO₂ leads to the breaking of the first F₁₆CuPc molecules, giving rise to the formation of a carbon-rich thin layer.²⁴

4.2.3 Thermal expansion

The relative values of the thermal expansion coefficients of different materials play an important role in the growth (e.g. in epitaxial film growth), as well as in the mechanic stability of heterostructures. Thus, the thermal expansion coefficients of organic semiconducting thin films are an additional issue to take into account for the fabrication and stability of organic-based electronic devices.

We have measured the shift of the Bragg reflection positions of a 46.8 ML thick F₁₆CuPc film grown at 150 °C and cooled stepwise down to -5 °C. The evolution of the relative change of the F₁₆CuPc cell parameters (a , b and layer height of the β -structure, and the parameter b of the β_{bilayer} -structure) relative to the value at room temperature are displayed in Figure 4.10. Notice that the thermal expansion coefficient, corresponding to the slope in the graphs, has a non linear behavior with the temperature. For the β_{bilayer} -structure, the parameter b increases with T until it reaches a saturation at high temperatures (above 120 °C). The expansion coefficient thus shows a decrease with T until it reaches 0 at high temperatures. If we now bring our attention to the β structure, we can clearly observe a highly anisotropic thermal

expansion. The parameter a experiences a positive thermal expansion at low temperatures and changes to negative values above 75 °C, whereas the parameter b experiences a change to a slightly larger thermal expansion at about the same temperature.^a In contrast, the out-of-plane expansion is linear throughout the whole temperature range measured. These findings point to the occurrence of changes in the molecular orientation within the unit cell at temperatures above 75 °C. An increase of the tilt angle between the molecular plane and the (10) direction (Figure 4.4) can account for the decrease in the parameter a and increase of b .

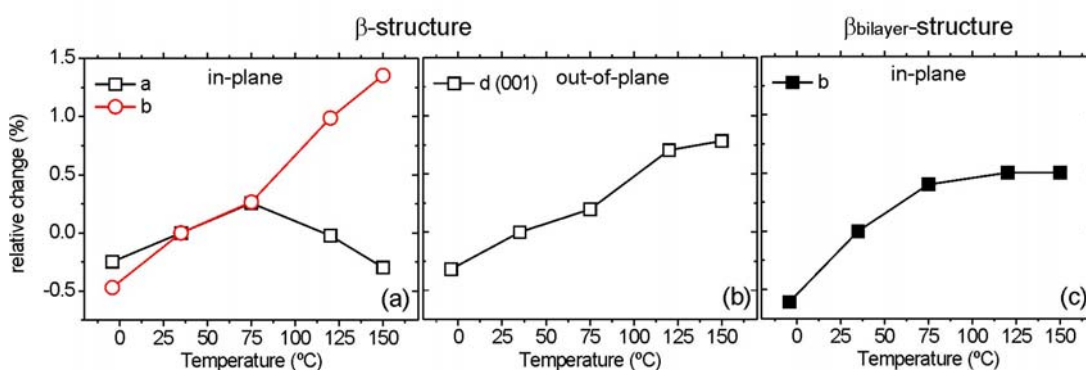


Figure 4.10. Relative change in the lattice spacing of the $F_{16}CuPc$ cell parameters vs. temperature for (a) the in-plane lattice parameters of the β -structure, (b) the out-of-plane spacing of the β -structure, and (c) the in-plane parameter “ b ” of the $\beta_{bilayer}$ -structure.

Considering the thermal expansion coefficients observed for the parameter b and for the layer height of the β -structure, values of 1.18×10^{-4} and $7.44 \times 10^{-5} \text{ K}^{-1}$ are obtained, respectively (ratio of 1.6 : 1). The anisotropy in the expansion coefficient of crystals or films of planar aromatic molecules is a rather general behaviour observed already some decades ago.²⁵ In general, the thermal expansion is largest along the crystallographic directions which are nearly normal to the molecular plane. A simple model by Smaalen et al.²⁶ explains this observation in terms of the number of the degrees of freedom of the molecules which contributes to the expansion along each direction. The molecules have three rotational and three translational degrees of freedom as marked in Figure 4.11. If we assume the crystal structure to be formed by stacks of cofacially oriented molecules along the z direction, the following degrees of

^a However, this change in the thermal expansion of b is within the error range and thus not conclusive.

freedom contribute to the thermal expansion along the z direction: translation along z , libration around the x axis, libration around the y axis. In contrast, only the translational degree of freedom contributes to the thermal expansion along x (and the same holds for the equivalent direction y) (Figure 4.11). This simple model thus yields a ratio of the thermal expansion coefficient along z , as compared to x or y , of 3 : 1. A more refined model based on energetic considerations²⁶ leads to a ratio of 2.1 : 1.

Thus, for F₁₆CuPc the higher expansion coefficient for the in-plane parameter b (“normal” to the molecular plane) as compared to the layer height (directed along the molecular plane) with a ratio of 1.6 : 1, is in rather good agreement with the predicted models. Because the thermal expansion coefficients of Si and SiO₂ ($2.6 \times 10^{-6} \text{ K}^{-1}$ and $0.4 \times 10^{-6} \text{ K}^{-1}$, respectively) are orders of magnitude smaller, the SiO₂ substrate evidently does not limit or “anchor” the in-plane expansion of the film on top.

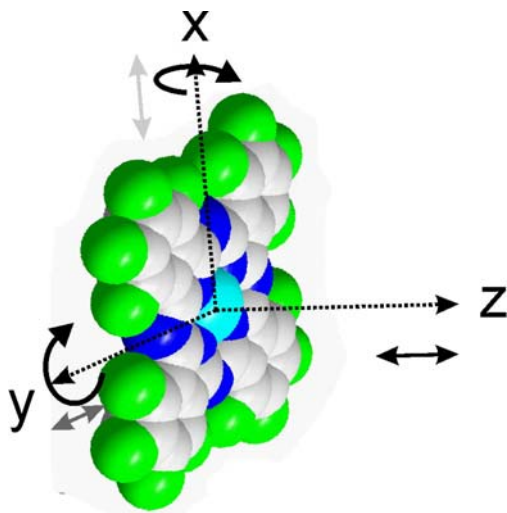


Figure 4.11. Schematic representation of the degrees of freedom contributing to the thermal expansion along the z direction (marked in black), and along the x and y directions (marked in light and dark grey, respectively). In a first approximation, the rotation around the z -axis does not contribute to any expansion.

4.2.4 Conclusions

For the first time, the detailed structure of F₁₆CuPc films grown on SiO₂ has been determined by means of in-situ x-ray diffraction from the first monolayer to thicker films. The results reveal a scenario that is more complex than what is expected on a

low-interacting surface like SiO_2 . It has been shown that a low density interfacial layer of around 6.5 Å is formed on the SiO_2 , on top of which the nucleation and two-dimensional growth of long and narrow islands of upright standing molecules take place. Upon further deposition, subsequent layers form with a similar morphology and layer height but with an increased elongation. We have disclosed a thickness-dependent polymorphism manifested in the in-plane crystal structure, which implies large differences in the molecular tilt within the cofacial stacking of the molecules.

In contrast to the homologous H_{16}CuPc molecule, the F_{16}CuPc films exhibit the same structure independently from the deposition temperature.

The general growth scenario is summarized in Figure 4.12.

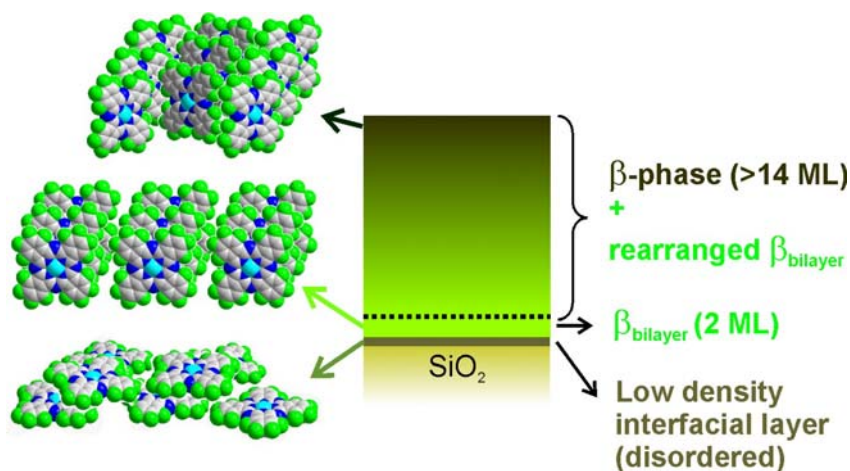


Figure 4.12. Scheme of the structure of F_{16}CuPc films grown on SiO_2 .

4.3 Comparative study on SiO_2 functionalized by OTMS

The functionalization of dielectrics in organic devices by self-assembling-monolayers, as a tool to optimize the device performance, has been proven to be effective and consequently of high interest. In particular, methyl-terminated SAMs seem to facilitate the ordering of the organic molecules and to avoid the generation of additional charge carrier traps due to the low reactivity of their endgroups.^{27,28} To our knowledge, the substrate functionalization by methyl-terminated silanes has only been employed to p-channel semiconductors with exception of C_{60} (n-type).²⁹ For C_{60} on

methyl-terminated silanized SiO_2 a decreased mobility has been reported, but because no structural characterization is provided, the effect of the surface treatment remains unclear. However, several studies on p-type semiconductors have shown a trend of improved field-effect mobility when SiO_2 is functionalized with methyl-terminated silanes.^{29,30,31,32,33,34} Although it is apparent that the reduction of surface energy on these silanized substrates may lead to a higher molecular surface diffusion, its correlation with improved structural properties is not established yet.^{30,31,32,33,34} Studies trying to correlate the electronic transport properties with the domain size or the grain density are often affected by the occurrence of changes in the molecular orientation and/or in the structure as well.^{30,32,34} In turn, the interpretation of surface treatment effects varies considerably and is sometimes even contradictory.³²

In the following we show that the field-effect mobility of F_{16}CuPc films grown on SiO_2 can be significantly improved by functionalizing the SiO_2 with OTMS. OTMS is a methyl-terminated SAM (see section 2.2.3), which lowers the surface energy of the silicon oxide from 78 to 20 N/m. We further show, based on a comparative study of the growth of F_{16}CuPc on both surfaces, that this enhanced mobility is related to an improved lateral order of the organic films and to the decrease of grain boundaries when deposited on functionalized SiO_2 .

4.3.1 Morphology

Figure 4.13a shows a schematic plot of the simultaneous growth of F_{16}CuPc films on top of SiO_2 and SiO_2 functionalized by OTMS, together with topographic AFM images of the films on the respective substrates. The samples are thermally deposited at a substrate temperature of 195 °C with a growth rate of 6 Å/min. The F_{16}CuPc films grown on SiO_2 form smooth and closed layers, whereas the functionalization of SiO_2 by OTMS enhances the surface diffusion of the molecules leading to the formation of highly ordered F_{16}CuPc crystallites. These crystallites have lengths of up to microns with aspect ratios of 5-10 and heights up to 700 Å. Similar film morphologies have been obtained over the investigated thickness range (100-450 Å, i.e. 7-31.5 ML), as shown in Figure 4.13b.

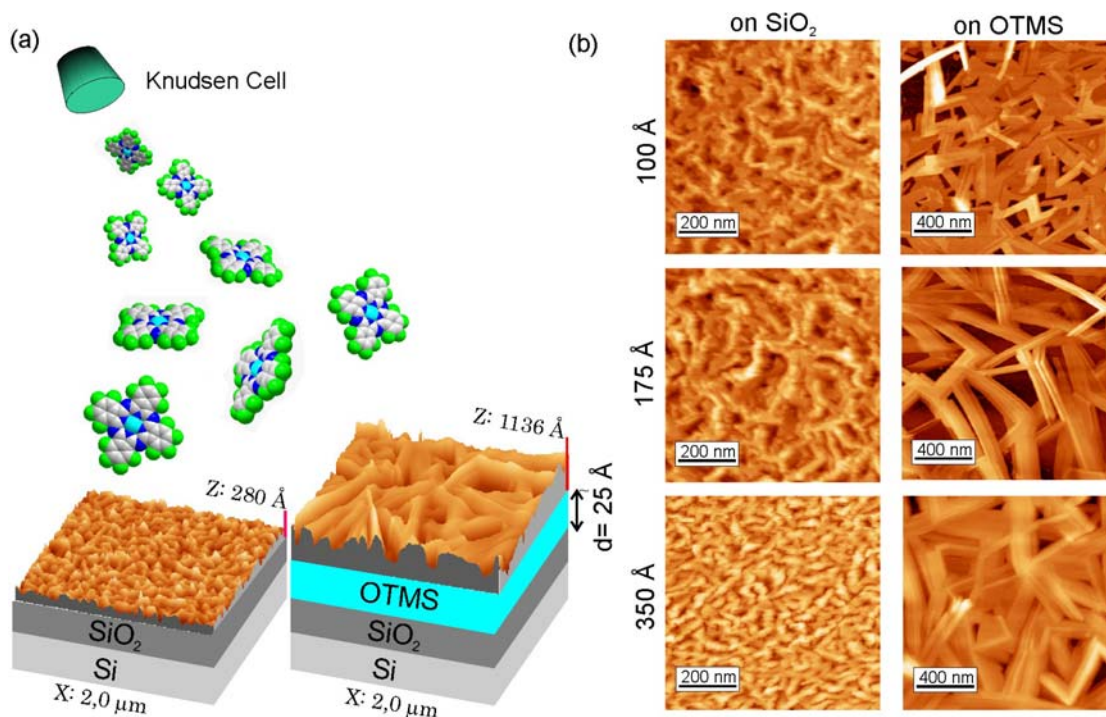


Figure 4.13. (a) Schematic plot of the simultaneous growth of the different F₁₆CuPc films and AFM topographic images of the films on bare SiO₂ (left) and SiO₂ functionalized by a self-assembled monolayer of OTMS (right). The nominal thickness is 450 Å (31.5 ML), deposited at a growth rate of 6 Å/min. (b) Additional topographic images of films with nominal coverages of 100, 175 and 350 Å, grown under similar conditions.

Along the edges of some crystallites on OTMS-covered SiO₂ a stepped profile of molecular terraces is observed as shown in Figure 4.14d. The height of the smallest terraces is around 15 Å, as in the case of F₁₆CuPc on the bare SiO₂ (Figure 4.1). This evidences a layered structure of upright-standing molecules, as expected for this weakly interacting substrate. By scanning on top of the crystallites, the molecular order has been resolved as depicted in Figure 4.14c. Rows parallel to the long axis of the crystallites are observed with a spacing of 9.3 ± 0.5 Å. Along the rows a smaller periodicity of 4.5 ± 0.3 Å can be distinguished. The rows observed by AFM correspond to the cofacial columnar stacking of F₁₆CuPc molecules and are in fair agreement with the film structure concluded from X-ray diffraction measurements of F₁₆CuPc films on bare SiO₂ presented in section 4.2.1. In all the cases the largest edge of the crystallites is parallel to the stacking direction (as previously observed for films on Al₂O₃(11-20)),¹¹ and it is the strong coupling of the intermolecular electronic π -systems which gives rise to this preferred anisotropic growth.

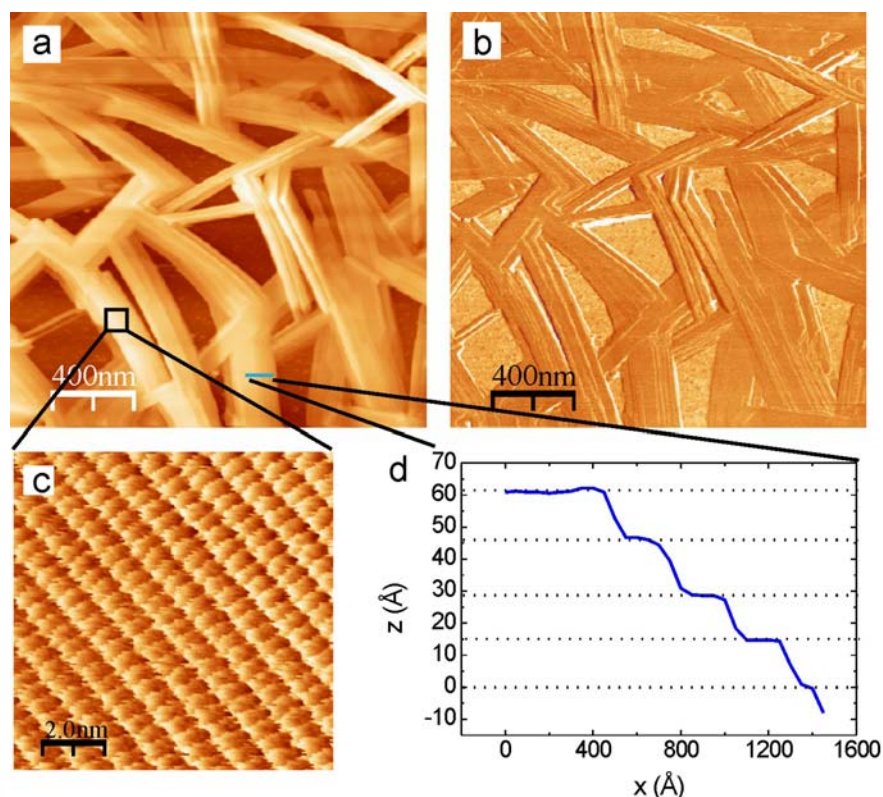


Figure 4.14. (a) AFM topographic image of a 175 Å thick $F_{16}CuPc$ film on OTMS. (b) Lateral force image showing the lower friction of the $F_{16}CuPc$ crystallites. (c) Molecular order in form of columns is observed parallel to the long edge of the crystallites. (d) Profile along a $F_{16}CuPc$ crystallite showing the stepped terraces formed by molecular layers. The step height of the terraces is in good accordance with an upright molecular configuration.

No molecular resolution could be obtained in the areas between the crystallites suggesting either the absence, or disorder of $F_{16}CuPc$ molecules in this region. This conclusion is supported by friction images showing a higher friction for the area surrounding the crystallites (see Figure 4.14b), which consequently implies different material properties.

The crystallites on the bare SiO_2 are smaller, up to 2000 Å along the long axis, and exhibit a morphologically less defined shape. No molecular order has been resolved on the films on the bare SiO_2 indicating a poorer structural coherence in the surface plane than for the samples on OTMS. This result is confirmed by X-ray diffraction. In spite of the morphological differences, the films on OTMS exhibit the same crystallographic structure as films on SiO_2 , as we will see below.

4.3.2 Structure

The order of the films perpendicular to the substrate surface has been measured by X-ray diffraction in a specular geometry. Figure 4.15a shows the specular X-ray data for two F₁₆CuPc films of the same thickness (12.2 ML) on the two different surfaces. The well ordered layered structure of the films gives rise to Bragg peaks which correspond to a similar distance between molecular planes of $d_{\perp}=14.30\pm0.05$ Å on both surfaces. The obtained layer spacing implies an upright-standing molecular configuration, in agreement with the AFM data. The Kiessig and Laue fringes (at low q_z values and around the Bragg maxima, respectively) visible for the films on SiO₂, are no longer present in the samples grown on OTMS, since the high roughness originating from the islanding of F₁₆CuPc destroys both kinds of interference fringes.

The degree of alignment of the molecular planes with respect to the surface normal (“mosaicity”) has been shown to have an important impact on charge carrier mobility.³⁵ It has been obtained for both films from the width of the rocking scans in the first and second order reflections, disclosing a very small mosaicity: $0.012\pm0.004^{\circ}$ for the samples on SiO₂ and $0.015\pm0.004^{\circ}$ on the OTMS functionalized SiO₂ (Figure 4.15b).^a

From the similar layer spacing and in-plane X-ray diffraction data shown in Figure 4.15c, one can directly conclude that similar structures form on both substrates. However, the reflections for the films grown on SiO₂ are broader, evidencing a poorer ordering. The mean domain size estimated from the FWHM of the peaks shows larger ordered domains in the samples on OTMS as compared to those on the bare SiO₂ (in agreement with the AFM results). For comparison, from the width of the (01) β_{bilayer} reflection a mean domain size of 140 Å is estimated on SiO₂ and of >275 Å on OTMS (resolution limited by the slits aperture), for the 12.2 ML thick F₁₆CuPc films. The films deposited on OTMS show an additional peak which corresponds to the OTMS structure, with a spacing of 4.15 Å. The resulting lattice parameter amounts to 4.8 Å for a hexagonal lattice, in agreement with reported data.^{36,37} This confirms that the OTMS layer is stable at the substrate temperature used during growth.

^a The third order reflection presents a very broad rocking scan ($\geq 0.5^{\circ}$), but the reason behind this effect remains unclear.

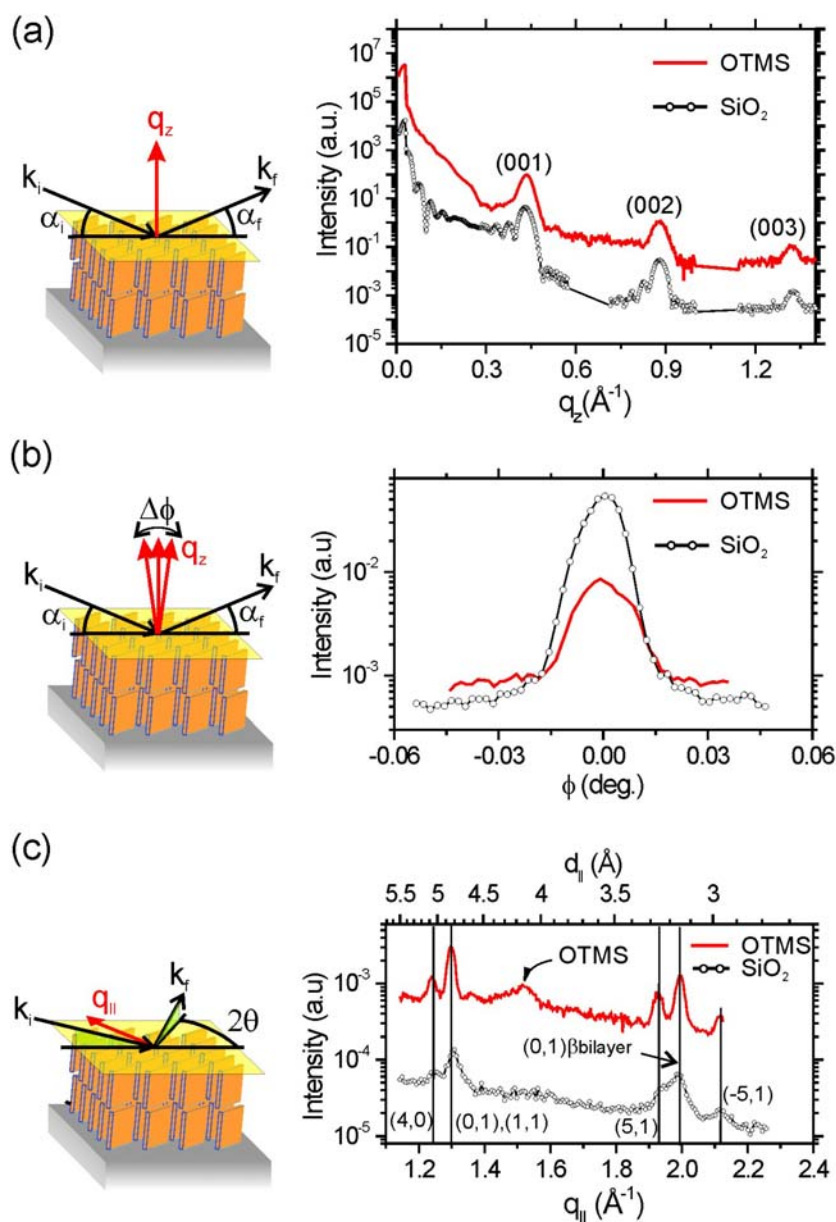


Figure 4.15. (a) Specular x-ray diffraction data for the 12.2 ML thick films on OTMS (line) and SiO₂ (symbol-line). Bragg reflexions (up to the 3rd order) are seen on both films indicating the same well ordered layered structure of upright-standing molecules. (b) Rocking scans for the first order Bragg peak on OTMS (line) and SiO₂ (symbol-line). (c) X-ray diffraction data of the structure in the surface plane for the 21 ML thick film on OTMS (line) and the 31.5 ML \AA thick film on SiO₂ (symbol-line). The schemes of the respective diffraction geometries are shown on the left.

The average OTMS domain size is estimated to be 75 \AA , thus smaller than the domain size of the F₁₆CuPc crystallites. This shows that the lateral order of the film is

not limited by OTMS domain boundaries. In contrast, pentacene and perylene grown on similar SAMs show an increased nucleation density and reduced grain size.^{30,34}

The X-ray data clearly demonstrate that molecular ordering in the surface plane is strongly enhanced in the organic films grown on OTMS, whereas the crystalline structure and low mosaicity remain the same.

4.3.3 Thermal desorption spectroscopy ^a

To analyze the adsorbant-substrate interaction comparative studies of the desorption profiles of F₁₆CuPc films on SiO₂ and on OTMS-covered SiO₂ substrates have been performed by means of thermal desorption spectroscopy (TDS). These studies have been carried out in UHV (10⁻¹⁰ mbar) by use of a top-mounted heater/sample-holder setup in combination with a thermocouple located directly on the sample surface. The thickness of the organic films was in the range between 14 and 28 ML. To detect possible fragmentation of the molecules during desorption which might affect the measured spectra, the signals of the single-ionised (F₁₆CuPc⁺¹) and of the double-ionised (F₁₆CuPc⁺²) were recorded simultaneously at a heating rate of 5 K/min. From the obtained peak intensities it follows, that the twofold-ionised molecular state is the preferred one, resulting in a signal about two orders of magnitude stronger than for the single-ionised state.

For both substrates a similar desorption temperature of 212±5° C for F₁₆CuPc is observed (Figure 4.16), indicating that the desorption energy is comparable for the two heterostructures. Therefore, the functionalization by OTMS leads to a change of the surface properties of SiO₂, e.g. higher hydrophobicity, accompanied by a change of the average diffusion length of the deposited molecules, but does not lead to a significant change of the interfacial bonding strength between molecular film and substrate. This conclusion is supported by similar desorption kinetics for both films deduced from the similar shape of both TDS peaks. The desorption is mainly governed by inter-molecular interactions and not by contributions from the F₁₆CuPc/SiO₂ or the F₁₆CuPc/OTMS-SiO₂ interfaces.

^a Measurements performed by S. Meyer and J. Pflaum, from the University of Stuttgart (Germany), in the frame of a collaboration.

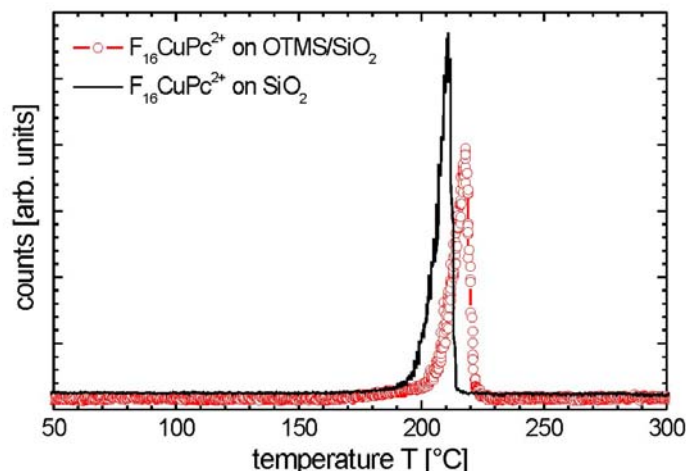


Figure 4.16. Thermal desorption spectra for $F_{16}CuPc$ films grown both on OTMS and on bare SiO_2 .

4.3.4 Electrical characterization ^a

Electrical measurements have been performed to study the influence of the OTMS-functionalized surface on the transport properties of the semiconducting layer via its morphology. $F_{16}CuPc$ was grown onto bottom-contact thin-film-transistor (TFT) structures with and without previous OTMS treatment. The TFT structures consist of a Si(100) wafer with a 2300 Å thick thermal oxide on top and Au/Cr source-drain-contacts. The gap dimensions are 2 mm in width and 15 μm in length. The organic films of about 400 Å (28 ML) thickness were evaporated on the functionalised structures and on bare SiO_2 at a substrate temperature of 100° C and a pressure of 1×10^{-7} mbar during preparation. AFM measurements reveal that the films grown at 100° C show the same morphological aspects and differences between both surfaces as observed for the films grown at 195° C. To avoid effects by moisture or oxygen, the electrical measurements have been performed in-situ in the dark just after evaporation. The reproducibility was controlled by characterization of several transistors of the same batch.

Figure 4.17a shows the transfer characteristics of the $F_{16}CuPc$ -TFT on OTMS- SiO_2 and SiO_2 , respectively. Electron transport (n-conduction) is favoured in

^a Measurements performed by S. Meyer and J. Pflaum, from the University of Stuttgart (Germany), in the frame of a collaboration.

perfluorinated CuPc, as already reported in former studies,² due to the small energy difference between the LUMO of the molecules and the workfunction of gold. Therefore, the output characteristics show a distinct field-effect behaviour for positive gate voltages as can be seen in Figure 4.17b for an OTMS-functionalised TFT. The associated input FET-curves in Figure 4.17a have been recorded at a positive source-drain voltage of $V_{SD} = 30$ V at room temperature.

According to the analysis of inorganic semiconducting devices,³⁸ the slope of the gate sweep is a direct measure for the charge carrier mobility in such transistors. The estimated electron mobility of the OTMS-functionalised SiO_2 -TFT amounts to $0.01 \text{ cm}^2/\text{Vs}$ and is about one order of magnitude higher than for the SiO_2 -TFT ($\sim 10^{-3} \text{ cm}^2/\text{Vs}$).

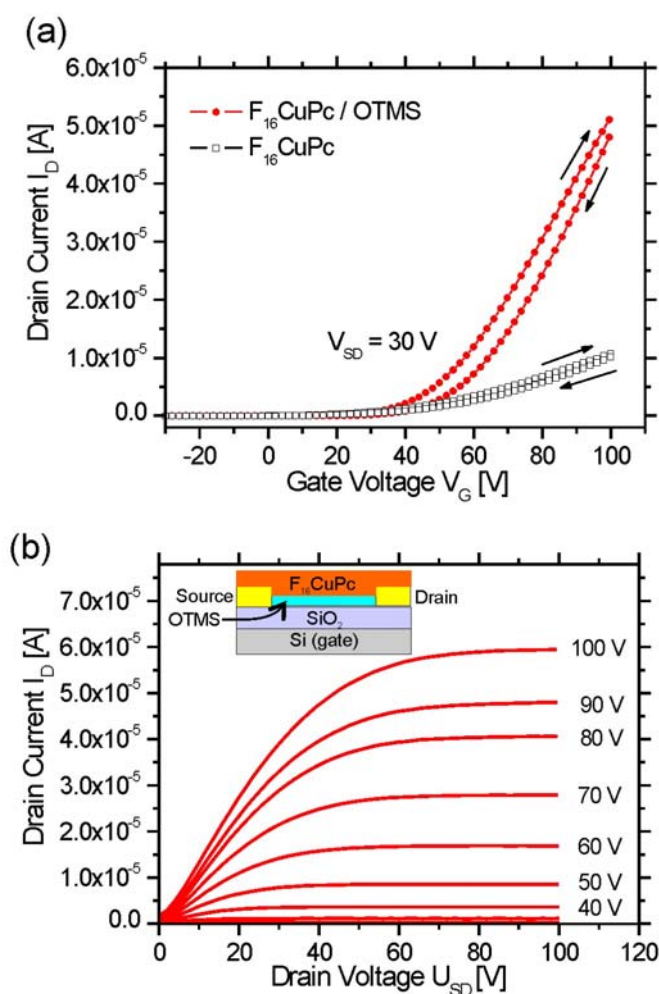


Figure 4.17. (a) Transistor characteristics of $F_{16}\text{CuPc}$ -based transistor on SiO_2 (open symbols) and OTMS-covered SiO_2 (solid symbols). (b) Output characteristic for an n-conducting $F_{16}\text{CuPc}$ transistor with OTMS-covered SiO_2 .

This improvement is directly correlated with the extended crystallite size for the OTMS-functionalised TFTs, as observed by the AFM and X-ray diffraction studies. The crystalline long range order in these films results in a reduction of domains and grain boundaries (which cause electrically active charge carrier traps) and in turn to an increase of the effective mobility.³⁹ The crystalline structure and film mosaicity remain the same and thus are not involved in the improved device performance. Despite the surface discontinuities associated with the island growth on the OTMS, the extended F₁₆CuPc crystals are well connected to each other. This is the first experimental observation in n-channel organic semiconductors of improved electron mobility by the use of methyl-terminated surfaces.

Extrapolating the drain-current in the linear range, from the intersection with the abscissa of V_G the threshold voltage can be estimated above which excess charges are injected into the semiconducting channel. The fact that for the bare SiO₂ and the OTMS-covered SiO₂ a similar value of 50 ± 5 V is observed is an indication of the formation of intergap states located at the metal-organic contact interfaces. Since for both substrate systems the contacts are not covered by the SAM, a preferred orientation of the F₁₆CuPc molecules with their planar ring system parallel to the metal contacts occurs. The standing-up orientation of the molecules on the weakly interacting oxide or OTMS-covered oxide results in a high density of domains and boundaries compensating the structural constraints near the injecting contacts. The OTMS-layer improves the long range structural order of the molecular layer but supports no relief from the structural constraints at the metal-organic contact interfaces.

4.3.5 Conclusions

We show that the electron mobility can be enhanced by about one order of magnitude by functionalizing the SiO₂ surface by self-assembled monolayers of OTMS. We disclose the microscopic origin of this effect by complementary X-ray diffraction and AFM studies. These studies reveal that OTMS induces the enlargement of the lateral domain size in F₁₆CuPc films while their crystalline

structure and excellent alignment with respect to the surface normal remain unchanged. We further conclude that the higher lateral order leads to a reduction of domains and grain boundaries within the F₁₆CuPc films and thus to a decreased density of traps. This is the first experimental observation in n-channel organic semiconductors of improved electron mobility by the use of methyl-terminated surfaces. These results underline the importance of surface functionalization as a method to improve the molecular order and thereby the electronic transport properties.

References

- ¹ J. O. Ossó, F. Schreiber, M. I. Alonso, M. Garriga, E. Barrena, H. Dosch, Structure, morphology and optical properties of thin films of F₁₆CuPc grown on silicon oxide, *Org. Electron.* **5**, 135 (2004)
- ² Z. Bao, A. J. Lovinger, J. Brown, New air-stable n-channel organic thin film transistors, *J. Am. Chem. Soc.* **120**, 207 (1998)
- ³ Y. Oh, S. Pyo, H. M. Yi, S.-K. Kwon, N-type organic field-effect transistor using polymeric blend gate insulator with controlled surface properties, *Org. Electron.* **7**, 72 (2006)
- ⁴ R. Ye, M. Baba, Y. Oishi, K. Mori, K. Suzuki, Air-stable ambipolar organic thin-film transistors based on an organic homostructure, *Appl. Phys. Lett.* **86**, 253505 (2005)
- ⁵ J. Wang, H. Wang, X. Yan, H. Huang, D. Jin, J. Shi, Y. Tang, D. Yan, Heterojunction ambipolar organic transistors fabricated by a two-step vacuum-deposition process, *Adv. Func. Mater.* **16**, 824 (2006)
- ⁶ W. Y. Tong, A. B. Djurisic, M. H. Xie, A. C. M. Ng, K. Y. Cheung, W. K. Chan, Y. H. Leung, H. W. Lin, S. Gwo, Metal phthalocyanine nanoribbons and nanowires, *J. Phys. Chem B* **110**, 17406 (2006)
- ⁷ F. Gamier, A. Yassar, R. Hajlaoui, G. Horowitz, F. Deloffre, B. Serve, S. Ries, P. Alnot, Molecular engineering of organic semiconductors: design of self-assembly properties in conjugated thiophene oligomers, *J. Am. Chem. Soc.* **115**, 8716 (1993)
- ⁸ C. R. Newman, C. D. Frisbie, D. A. da Silva Filho, J.-L. Brédas, P. C. Ewbank, K. R. Mann, Introduction to organic thin film transistors and design of n-channel organic semiconductors, *Chem. Mater.* **16**, 4436 (2004)
- ⁹ G. Horowitz, Organic thin-film transistors: from theory to real devices, *J. Mater. Res.* **19**, 1946 (2004)
- ¹⁰ J. O. Ossó, F. Schreiber, V. Kruppa, H. Dosch, M. Garriga, M. I. Alonso, F. Cerdeira, Controlled molecular alignment in phthalocyanine thin films on stepped sapphire surfaces, *Adv. Func. Mater.* **12**, 455 (2002)
- ¹¹ E. Barrena, J. O. Ossó, F. Schreiber, M. Garriga, M. I. Alonso, H. Dosch, Self organization of phthalocyanines on Al₂O₃ (11-20) in aligned and ordered films, *J. Mater. Res.* **19**, 2061 (2004)
- ¹² A. Gerlach, F. Schreiber, S. Sellner, H. Dosch, I. A. Vartanyants, B. C. C. Cowie, T.-L. Lee, J. Zegenhagen, Adsorption induced distortion of F₁₆CuPc on Cu(111) and Ag(111): An x-ray standing wave study, *Phys. Rev. B* **71**, 205425 (2005)
- ¹³ O. Berger, W.-J. Fisher, B. Adolphi, S. Tierbach, V. Melev, J. Schreiber, Studies on phase transformations of Cu-phthalocyanine thin films, *J. Mater. Sci.-Mater. E.* **11**, 331, (2000)
- ¹⁴ G. Witte, C. Wöll, Growth of aromatic molecules on solid substrates for applications in organic electronics, *J. Mater. Res.* **19**, 1889 (2004)
- ¹⁵ P. Fenter, F. Schreiber, L. Zhou, P. Eisenberger, S.R. Forrest, In situ studies of morphology, strain, and growth modes of a molecular organic thin film, *Phys. Rev. B* **56**, 3046 (1997)

-
- ¹⁶ L. Casalis, M. F. Danisman, B. Nickel, G. Bracco, T. Toccoli, S. Iannotta, G. Scoles, Hyperthermal molecular beam deposition of highly ordered organic thin films, *Phys. Rev. Lett.* **90**, 206101 (2003)
- ¹⁷ H. Peisert, I. Biswas, L. Zhang, M. Knupfer, M. Hanack, D. Dini, M.J. Cook, I. Chambrier, T. Schmidt, D. Batchelor, T. Chassé, Orientation of substituted phthalocyanines on polycrystalline gold: distinguishing between the first layers and thin films, *Chem. Phys. Lett.* **403**, 1 (2005)
- ¹⁸ B. Krause, A.C. Dürr, F. Schreiber, H. Dosch, O.H. Seeck, Thermal stability and partial dewetting of crystalline organic thin films: 3,4,9,10-perylenetetracarboxylic dianhydride on Ag (111), *J. Chem. Phys.* **119**, 3429 (2003)
- ¹⁹ S. Lukas, S. Söhnchen, G. Witte, C. Wöll, Epitaxial growth of pentacene films on metal surfaces, *Chem. Phys. Chem.* **5**, 266 (2004)
- ²⁰ S. E. Fritz, S. M. Martin, C. D. Frisbie, M. D. Ward, M. F. Toney, Structural characterization of a pentacene monolayer on an amorphous SiO₂ substrate with grazing incidence X-ray diffraction, *J. Am. Chem. Soc.* **126**, 4084 (2004)
- ²¹ R. Ruiz, B. Nickel, N. Koch, L. C. Feldman, R. F. Haglund, A. Kahn, G. Scoles, Pentacene ultrathin film formation on reduced and oxidized Si surfaces, *Phys. Rev. B* **67**, 125406 (2003)
- ²² S. Kowarik, A. Gerlach, S. Sellner, F. Schreiber, L. Cavalcanti, O. Konovalov, Real-time observation of structural and orientational transitions during growth of organic thin films, *Phys. Rev. Lett.* **96**, 125504 (2006)
- ²³ M. A. Loi, E. Da Como, F. Dinelli, M. Murgia, R. Zamboni, F. Biscarini, M. Muccini, Supramolecular organization in ultra-thin films of α -sexithiophene on silicon dioxide, *Nat. Mater.* **4**, 81 (2005)
- ²⁴ L. Lozzi, S. Santucci, XPS study of the FCuPc/SiO₂ interface, *Surf. Sci.* **976**, 532 (2003)
- ²⁵ K. Lonsdale, Experimental studies of atomic vibrations in crystals and their relationship to thermal expansion, *Z. Kristallogr.* **112**, 188 (1959)
- ²⁶ S. van Smaalen, J. L. De Boer, C. Haas, J. Kommandeur, Anisotropic thermal expansion in crystals with stacks of planar molecules, such as tetracyanoquinodimethanide (TCNQ) salts, *Phys. Rev. B* **31**, 3496 (1985)
- ²⁷ X. Liu, S. H. Mohamed, J. M. Ngaruiya, M. Wuttig, T. Michely, Modifying the growth of organic thin films by a self-assembled monolayer, *J. Appl. Phys.* **93**, 4852 (2003)
- ²⁸ M. C. Gerstenberg, F. Schreiber, T. Y. B. Leung, G. Bracco, S. R. Forrest, G. Scoles, Organic semiconducting thin film growth on an organic substrate: 3,4,9,10-perylenetetracarboxylic dianhydride on a monolayer of decanethiol self-assembled on Au(111), *Phys. Rev. B* **61**, 7678 (2000)
- ²⁹ S. Kobayashi, T. Nishikawa, T. Takenobu, S. Mori, T. Shimoda, T. Mitani, H. Shimotani, N. Yoshimoto, S. Ogawa, Y. Iwasa, Control of carrier density by self-assembled monolayers in organic field-effect transistors, *Nat. Mater.* **3**, 317 (2004)
- ³⁰ M. Shtein, J. Mapel, J. B. Benzinger, S. R. Forrest, Effects of film morphology and gate dielectric surface preparation on the electrical characteristics of organic-vapor-phase-deposited pentacene thin-film transistors, *Appl. Phys. Lett.* **81**, 2668 (2002)
- ³¹ D. J. Gundlach, J. A. Nichols, L. Zhou, T. N. Jackson, Thin-film transistors based on well-ordered thermally evaporated naphthalene films, *Appl. Phys. Lett.* **80**, 2925 (2002)
- ³² J. Veres, S. Ogier, G. Lloyd, D. de Leeuw, Gate insulators in organic field-effect transistors, *Chem. Mater.* **16**, 4543 (2004)
- ³³ S. C. Lim, S. H. Kim, J. H. Lee, M. K. Kim, D. J. Kim, T. Zyung, Surface-treatment effects on organic thin-film transistors, *Synth. Met.* **148**, 75 (2005)
- ³⁴ D. Knipp, R. A. Street, A. Völkel, J. Ho, Pentacene thin film transistors on inorganic dielectrics: Morphology, structural properties, and electronic transport, *J. Appl. Phys.* **93**, 347 (2003)
- ³⁵ N. Karl, Charge carrier transport in organic semiconductors, *Synth. Met.* **133-134**, 649 (2003)

-
- ³⁶ I. M. Tidswell, B. M. Ocko, P. S. Pershan, S. R. Wasserman, G. M. Whitesides, J. D. Axe, X-ray specular reflection studies of silicon coated by organic monolayers (alkylsiloxanes), *Phys. Rev. B* **41**, 1111 (1990)
- ³⁷ A. Baptiste, A. Gibaud, J. F. Bardeau, K. Wen, R. Maoz, J. Sagiv, B. M. Ocko, X-ray, micro-Raman, and infrared spectroscopy structural characterization of self-assembled multilayer silane films with variable numbers of stacked layers, *Langmuir* **18**, 3916 (2002)
- ³⁸ S. M. Sze, *Physics of semiconductor devices*, Wiley and Son, New York (1981)
- ³⁹ E. A. Silinsh, *Organic Molecular Single Crystals, Their Electronic States*, Springer, Heidelberg, 1980

5 p-n organic heterostructures

The microscopic structure of organic p-n heterojunctions plays a key role in current and future electronic devices built from semiconducting organic molecules. Very little is known about how such organic interfaces evolve during growth and how the emerging morphology and microscopic structure affects the function, performance and lifetime of organic devices, such as organic light emitting diodes (OLEDs), organic ambipolar transistors or organic solar cells. Although numerous studies have been devoted to the fabrication and performance of devices based on p-n organic heterojunctions,^{1,2,3,4,5,6,7,8,9} leading to a rapid progress in this field, there are rather few structural studies addressing this important issue.^{8,9,10,11,12,13,14,15,16,17,18,19,20} In turn, our present-day knowledge on the physical principles of the growth of organic heterostructures is still very poor, and the tailored growth of highly ordered organic heterojunctions is still in an early stage.

Because of the different properties inherent to organic materials, i.e., large size, anisotropy, and relatively weak intermolecular interaction (Van der Waals), issues like “strain” or “epitaxy” are expected to lessen in significance with respect to their role in heteroepitaxy of inorganic semiconductors. Yet their role on the evolving morphology, as well as other issues like molecular interdiffusion and structure at the organic-organic interface, remain largely unexplored, mainly due to the difficulty in accessing the structure at the organic-organic interface. We have used the capabilities of X-ray diffraction to determine the structure of both films at the organic interface in-situ during the growth of the heterostructures. These measurements, in combination with ex-situ AFM studies, provide detailed insight into the microscopic processes which take place during the growth of organic on organic heterostructures.

This section presents the results obtained in the growth of organic heterostructures based on F₁₆CuPc (n-type) in combination with pentacene (p-type) and DIP (p-type).

5.1 *Experimental details*

The growth of the different organic heterostructures as been performed on (001) Si wafers covered by their native oxide and cleaned as reported in section 3.3.4. The growth parameters have been varied for the different samples and are thus given in the text for each different case.

The X-ray diffraction measurements on the F_{16} CuPc-pentacene heterostructures have been performed in-situ at the beamline ID-3 in the ESRF with a wavelength of $\lambda=0.72316$ Å. The in-situ measurements performed on the F_{16} CuPc-DIP heterostructures have been carried out within different beamtimes at the beamline ID-10B in the ESRF (with $\lambda=0.95452$ Å) and at the MPG Surface Diffraction Beamline in ANKA (with $\lambda=1.53067$ Å and $\lambda=1.23984$ Å). The AFM measurements have been performed in an Omicron scanning probe microscope (SPM) under UHV (in contact and non-contact mode), or under ambient conditions (in contact or tapping mode) in a Digital Nanoscope III SPM, or/and a Nanotec SPM. For the image processing the freeware WSxM program has been used.

5.2 *F_{16} CuPc and pentacene*

In order to study the growth of organic heterostructures with a high interest for potential applications, we have combined the so far most successful p-type oligomer (pentacene) with one of the few air stable n-type oligomers (F_{16} CuPc). The films have been grown in form of bilayers (one molecular type on top of the other) and the results are shown in the following for both deposition sequences.

Two of the factors influencing the growth morphology of heterostructures are the surface and the interface energies. These energies can be accessed by contact angle measurements. In our study, we have determined the water contact angle (which is inversely proportional to the surface energy) of freshly prepared F_{16} CuPc and pentacene films of 300 Å thickness (Figure 5.1), leading to values of $95.2\pm1.2^\circ$ and $83.5\pm2.5^\circ$, respectively.

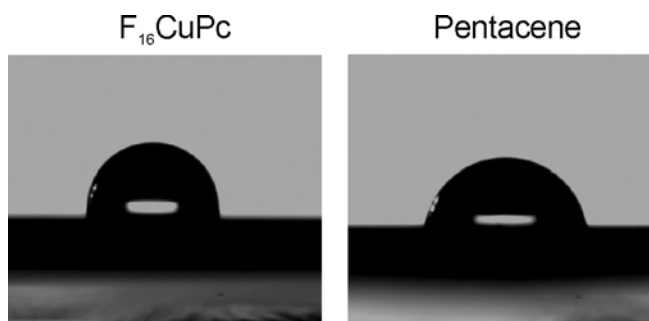


Figure 5.1. Water contact angle measurements on 150 Å thick films of F₁₆CuPc and pentacene.

5.2.1 F₁₆CuPc on pentacene

a. Growth mode, structure and morphology.

When F₁₆CuPc is deposited on top of pentacene at room temperature, the X-ray diffraction data reveal the formation of different phthalocyanine crystalline structures: the expected β - and β_{bilayer} -structures of standing molecules (described in section 4.2.1 and referenced in the following as *s*-configuration), and an additional structure formed by lying down molecules (called in the following *l*-structure). Figure 5.2 shows the evolution of both the out-of-plane and the in-plane data after subsequent F₁₆CuPc deposition steps on a 130 Å thick pentacene film.

Since the F₁₆CuPc *s*-configuration presents a layer height of 14.3 Å, which is similar to the layer height of the pentacene thin-film structure (15.6 Å), the associated (001) and (002) Bragg peaks (which are broadened in q_z -direction by the thin film geometry) almost coincide for both materials. Consequently, the growth of the F₁₆CuPc *s*-configuration gives rise to a characteristic increase of the (001) and (002) reflections, accompanied by a slight shift to higher q_z values, as shown in the inset of the out-of-plane graph. Most interestingly, we also observe the development of a new F₁₆CuPc-related Bragg reflection at $q_z=2.0011 \text{ Å}^{-1}$, corresponding to a molecular distance of 3.14 Å. Since this spacing is similar to the intermolecular distance of cofacially oriented molecules, this observation gives a clear evidence for the growth of a new structure of F₁₆CuPc molecules which lie flat on the pentacene surface (called *l*-structure in the following). The associated mosaicity is very small (0.017°) and close to that of the underlying pentacene structure (0.015°), implying an

extremely good alignment of these crystallites of lying F_{16} CuPc with respect to the pentacene surface.

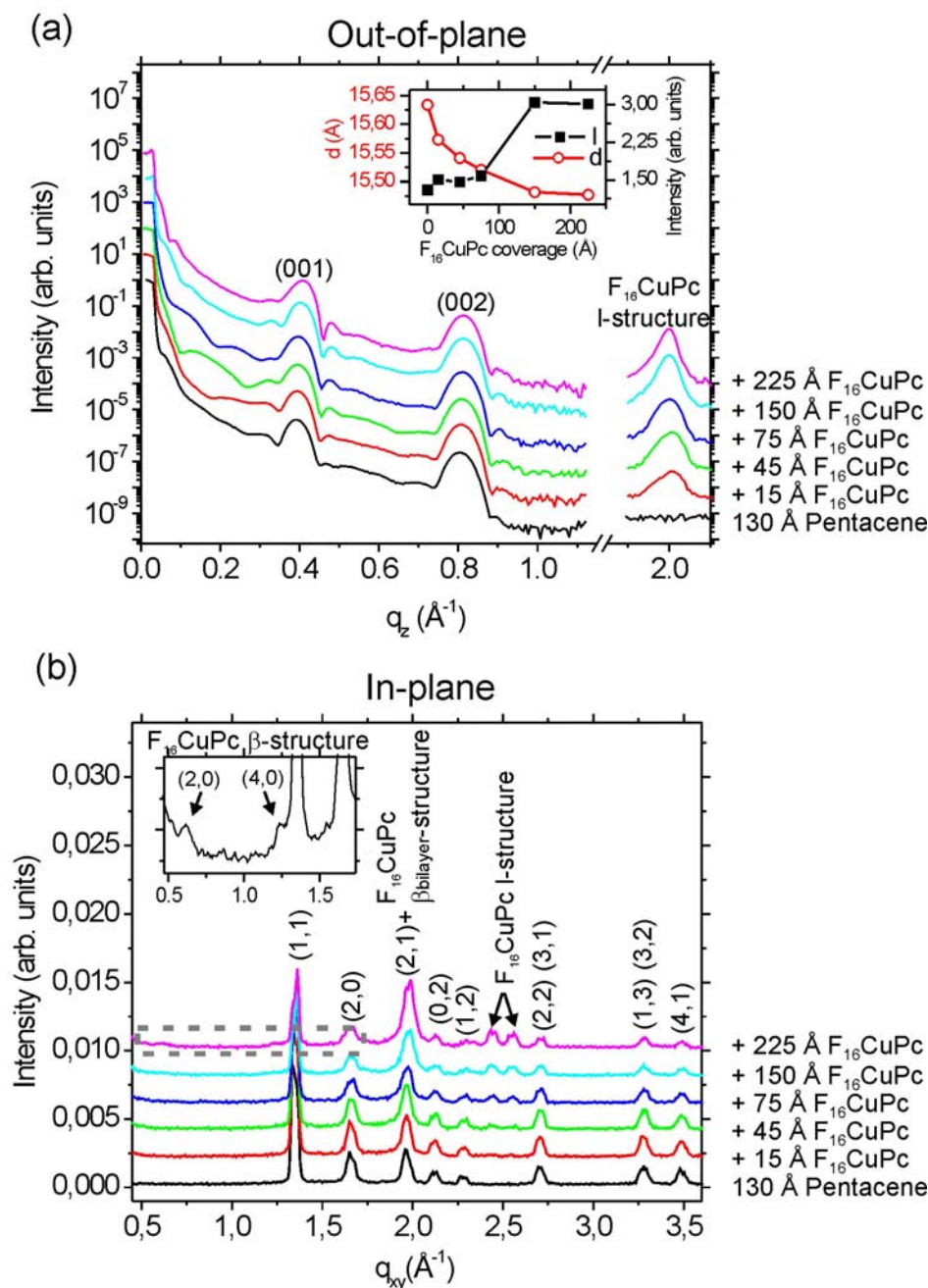


Figure 5.2 Evolution of the (a) out-of-plane and (b) in-plane X-ray diffraction data of a 130 \AA thick pentacene film upon subsequent deposition of F_{16} CuPc. The inset in the out-of-plane data represents the evolution of the position and integrated intensity obtained from fits to the (002) Bragg reflection. The in-plane peaks are labeled according to the pentacene in-plane structure,²¹ and to the F_{16} CuPc in-plane β_{bilayer} - and β -structures (s -configuration) reported in section 4.2, as well as to the new I -structure. The inset shows a zoom as marked by the dashed lines, revealing the weak reflections arising from the F_{16} CuPc β -structure.

The corresponding in-plane data confirm the previous findings. The growth of F₁₆CuPc in the β_{bilayer} -structure is evidenced by the development of its characteristic (0,1) reflection, which overlaps with the pentacene (2,1) Bragg peak. A closer look to the data also reveals the appearance, for higher coverages, of the weaker in-plane reflections related to the F₁₆CuPc β -structure. This is shown in the inset of the in-plane graph, which corresponds to a zoom taken as indicated by the dashed line. Thus, the growth of F₁₆CuPc on pentacene in an upright standing configuration apparently follows the same thickness dependent growth behavior observed on SiO₂, leading to the formation of the β_{bilayer} -structure for the first layers, which gradually changes to be dominated by the development of the β -structure for increasing coverage.

In addition, two new Bragg reflections appear at q values of 2.4387 and 2.5519 Å⁻¹, corresponding to lattice spacings of 2.576±0.003 and 2.462±0.001 Å, respectively. These reflections must be related to the new F₁₆CuPc l -structure, but the present data are not sufficient to determine its exact in-plane unit cell. The estimation of the domain sizes from the peak widths leads to values around 125 Å.

A similar experiment has been performed at a substrate growth temperature of 65 °C. For pentacene, this is virtually the highest practicable temperature not affected by simultaneous partial desorption, since already at 85 °C no pentacene deposition is observed. Also at this higher temperature the coexistent growth of F₁₆CuPc in the l - as well as in the s -configurations is observed, evidenced by the development of their corresponding Bragg reflections in Figure 5.3. Thus, the emergence of the new l -structure is most likely not a kinetic phenomenon,²² but rather induced by specific morphological details of the underlying pentacene substrate. For this higher substrate temperature, and due to the higher pentacene thickness, the growth of pentacene in the thin-film as well as in the bulk phase takes place, as evidenced by the emergence of additional Bragg reflections in the out-of-plane measurements, which correspond to a layer spacing of 14.5 Å.^{23,24}

To further explore which pentacene surface morphologies are responsible for these competing F₁₆CuPc growth modes, we have performed extensive AFM experiments. Figure 5.4 (left) shows a topographic image of a 40 Å thick pentacene film on SiO₂,

measured in contact-mode under UHV conditions without breaking the vacuum upon transfer to and from the growth chamber. The image reveals the layered pentacene structure with monomolecular steps of ~ 15 Å. The same film upon deposition of 60 Å of $F_{16}CuPc$ is shown in the right part. This image was taken in tapping mode under ambient conditions. The $F_{16}CuPc$ growth results in an interesting morphology consisting in islands of small lateral dimensions (50-100 nm) which decorate the pentacene steps. Their heights vary between 90 and 170 Å and, as we will discuss below, are associated with the $F_{16}CuPc$ *l*-structure. Due to the similar heights of $F_{16}CuPc$ and pentacene monomolecular layers ($h_{F_{16}CuPc}=14.3$ Å vs. $h_{pentacene}=15.6$ Å), the identification of the $F_{16}CuPc$ *s*-configuration in the topography images is rather difficult.

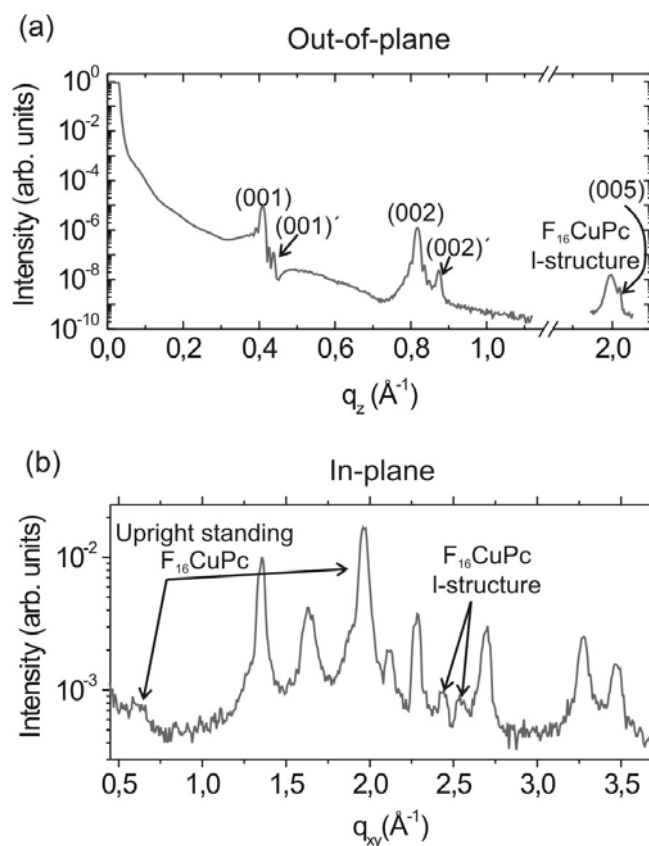


Figure 5.3 (a) Out-of-plane and (b) in-plane x-ray diffraction data of a bilayer of 100 Å $F_{16}CuPc$ deposited on 752 Å pentacene at a substrate growth temperature of 65 °C. The presence of the pentacene bulk phase is evidenced by the new out-of-plane Bragg peaks (labeled with a prime symbol). The coexistent growth of $F_{16}CuPc$ in the *l*-structure as well as the β - and $\beta_{bilayer}$ -structures can be seen from the corresponding reflections.

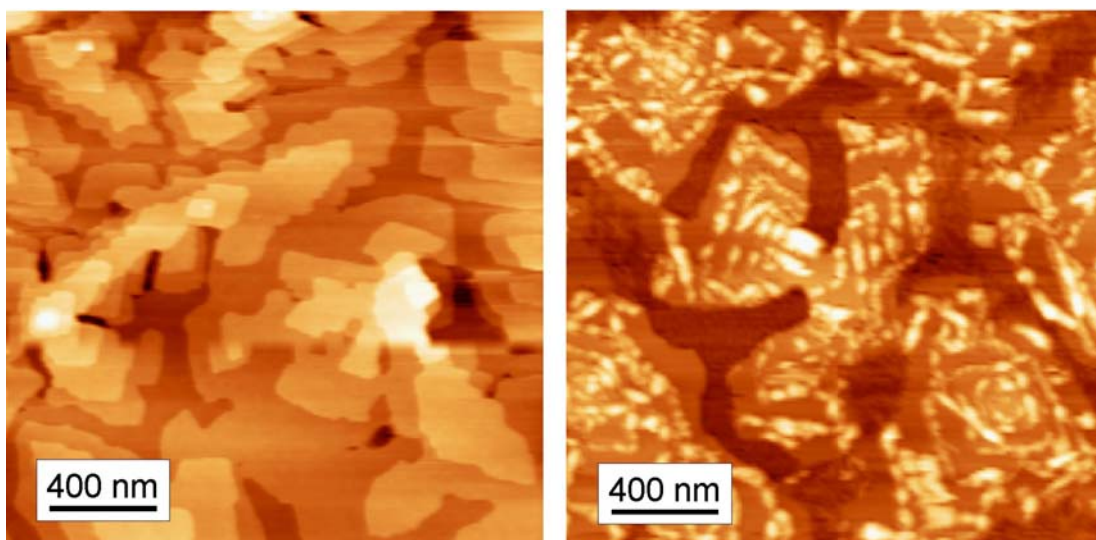


Figure 5.4. Topographic AFM images of a 40 Å thick pentacene film on SiO₂ (left), and of the same sample after deposition of 60 Å F₁₆CuPc on top (right).

Therefore, when measuring in tapping-mode we have employed the phase-shift signal, which is sensitive to the material-dependent dissipative processes related to the tip-sample interactions.²⁵ When measuring in contact mode we have used the friction signal, which also shows a similar material-sensitivity (see section 3.1.2). This provides us with a tool to distinguish between *s*-configuration F₁₆CuPc and uncovered pentacene in samples with submonolayer F₁₆CuPc coverage. An example is presented in Figure 5.5 for contact-mode measurements, where the simultaneously recorded topography (left) and friction (right) signals are shown for a sample with 10 Å (0.7 ML) F₁₆CuPc deposited on top of 20 Å pentacene. The sample consists in a pentacene film with a virtually completed first layer, on top of which the second layer forms dendritic islands with even partial nucleation of the third layer. The F₁₆CuPc on top arranges into high *l*-structure islands (bright spots on the topography image) but also into the *s*-configuration, giving rise to a network of elongated crystallites similar to the growth on SiO₂, or to more homogeneous layers on top of the pentacene second layer islands. Its lower friction as compared to the underlying uncovered pentacene, makes the phthalocyanines appear darker in the friction image, thus allowing an unambiguous differentiation of both materials. However, the measurements of these bilayers in contact mode results very cumbersome, because the low cohesion of the F₁₆CuPc *l*-structure usually leads to a sweeping of the molecules by the tip even at minimized applied loads, therewith hindering a proper imaging.

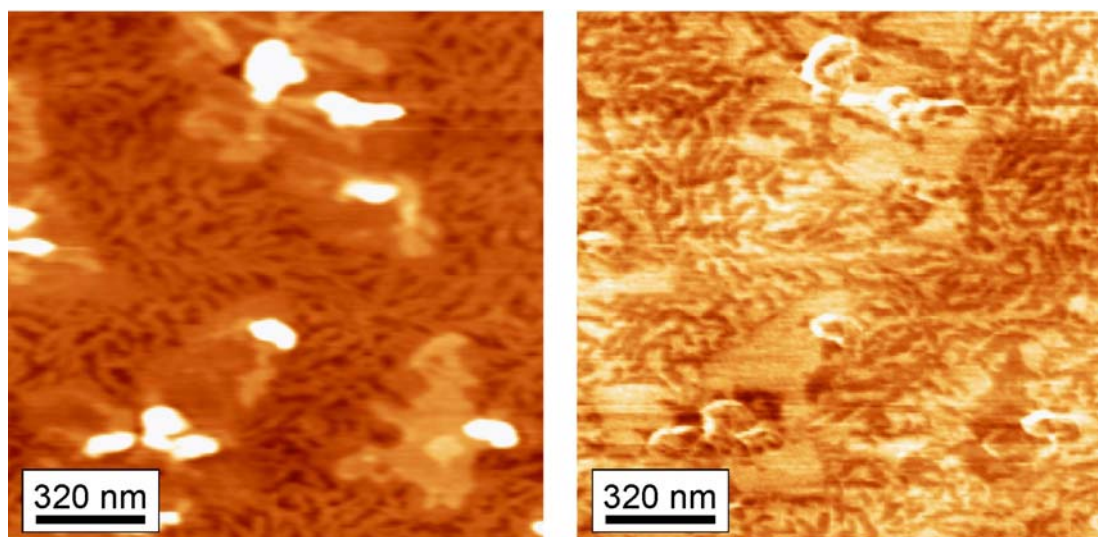


Figure 5.5. Contact-mode AFM images corresponding to the topography (left) and friction (right) signals recorded simultaneously on a sample with 10 Å $F_{16}CuPc$ on 20 Å pentacene.

By using tapping mode this problem is overcome, thus facilitating the measurements and improving the resolution. Figure 5.6, depicts the topography (Figure 5.6a) and phase-shift signal (Figure 5.6b) of a sample with 8 Å (0.56 ML) $F_{16}CuPc$ deposited onto 35 Å of pentacene. The phase-shift of the tapping-mode discloses the growth of the $F_{16}CuPc$ *s*-configuration (darker) on top of the pentacene terraces (uncovered pentacene appears lighter). The crystallites of $F_{16}CuPc$ *l*-structure are better distinguished in the topography than in the phase images, since the phase-shift contrast is dominated by large changes at the island edges caused by the limited response-speed of the feedback to abrupt topographic changes. The correlation between topography and phase-shift signal is further clarified in Figure 5.6c, which shows a cross-section for both signals on the same area (marked on the respective images) together with the deduced distribution of the different materials and structures which give rise to the observed topographic features. Interestingly, the heights of the $F_{16}CuPc$ *l*-structure crystallites show no apparent correlation with the pentacene terrace size or with the coverage of $F_{16}CuPc$ *s*-structure, suggesting that surface diffusion does not play a dominant role on their growth.

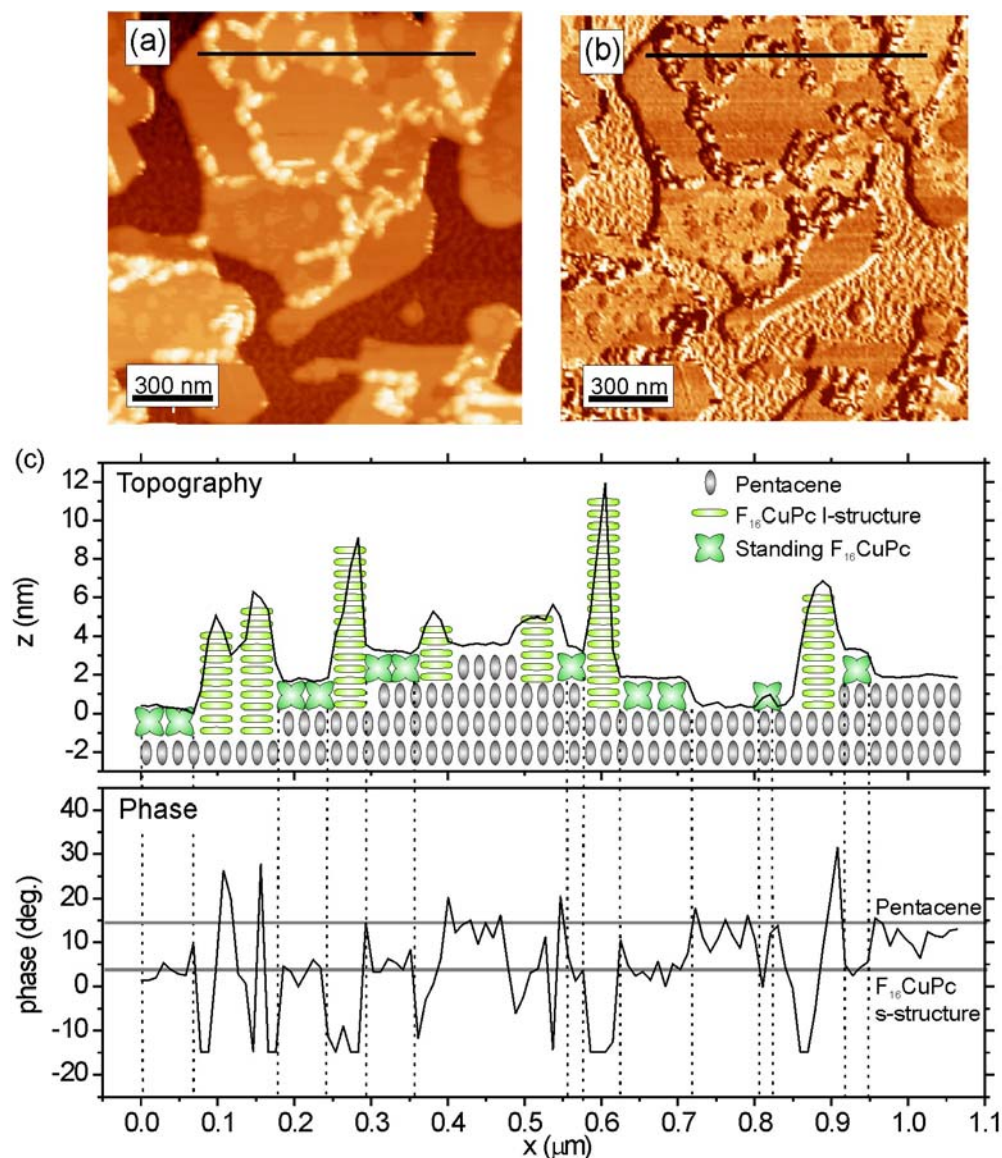


Figure 5.6. Tapping-mode AFM images of 8 \AA $F_{16}\text{CuPc}$ grown on 40 \AA pentacene corresponding to the simultaneously recorded (a) topography and (b) phase-shift signals. (c) Topography (top) and phase (bottom) signal profiles of the same region as marked on images (a) and (b), together with a schematic representation of the different molecules and structures forming the observed topographic features. The horizontal lines in the phase profile mark the mean values for the pentacene and upright-standing $F_{16}\text{CuPc}$. The vertical lines help with the correlation of both signals.

The following scenario has been so far discerned for the growth of $F_{16}\text{CuPc}$ on pentacene: the s -configuration forms on top of the pentacene terraces, while the l -structure develops along the pentacene step edges. Note that the pentacene terraces expose the (001)-facets, which correspond to the lowest energy pentacene planes.²⁶ On top of this weakly interacting surface, $F_{16}\text{CuPc}$ is able to adopt its energetically

preferred standing configuration, similarly to that observed for the $F_{16}\text{CuPc}$ on other weakly interacting surfaces like SiO_2 ,^{27, 28} Al_2O_3 ,^{29, 30} OTMS,²⁷ or polymers.³¹ However, for $F_{16}\text{CuPc}$ molecules at the pentacene steps, the different energetic and electric environment at the step edges favors the orientation of the phthalocyanines with their molecular planes parallel to the surface. The fact that similar results are obtained at higher substrate temperature ($T=65^\circ\text{C}$) implies a rather strong interaction ($\gg KT$) of $F_{16}\text{CuPc}$ with pentacene at the steps. In some occasions, the growth of the *l*-structure is also observed apart from the step edges, what might be related to other kinds of different environments such as grain boundaries, dislocations or other defects. Once an initial nucleus of molecules in the *l*-structure is formed, a rapid vertical growth of this crystallographic phase occurs simply as result of the strong interaction between π -orbitals, favoring the cofacial vertical stacking and promoting the observed morphology of narrow and high crystallites.

Since the steps of the underlying pentacene induce the growth of the phthalocyanine *l*-configuration, a larger step density is expected to increase the amount of $F_{16}\text{CuPc}$ molecules arranging in the *l*-configuration and consequently reduce the formation of *s*-configuration. This behavior becomes evident from experiments performed varying the nominal coverage of the pentacene film. Because the amount of $F_{16}\text{CuPc}$ in the *s*-configuration is difficult to discern from AFM measurements, especially for coverages above a monolayer, we make use of X-ray diffraction. Figure 5.7 depicts the evolution of the integrated intensity of the $F_{16}\text{CuPc}$ β_{bilayer} -structure (010) peak (*s*-configuration)^a and also of the reflection at $q_{\parallel}=2.4387 \text{ \AA}^{-1}$ (*l*-structure)^b vs. phthalocyanine coverage, deposited on pentacene films of 40 and 130 Å thickness.

The larger slope in the intensity evolution of the $F_{16}\text{CuPc}$ β_{bilayer} (010) reflection for the heterostructure with 40 Å pentacene (Figure 5.7c) implies a higher growth rate of the $F_{16}\text{CuPc}$ *s*-structure when deposited on pentacene films with lower thickness. In reasonable agreement with this, there is no appreciable X-ray intensity of the $F_{16}\text{CuPc}$ *l*-structure reflection on the 40 Å pentacene film (Figure 5.7d), and the *l*-structure grows onto the pentacene film with higher thickness (Figure 5.7d).

^a Notice that because the $F_{16}\text{CuPc}$ β_{bilayer} -structure (010) and the pentacene (210) Bragg peaks overlap, the initial intensity (for 0 $F_{16}\text{CuPc}$ coverage) corresponds uniquely to the amount of pentacene.

^b The intensity of the *l*-structure reflection at $q_{\parallel}=2.5519 \text{ \AA}^{-1}$ shows a similar behavior.

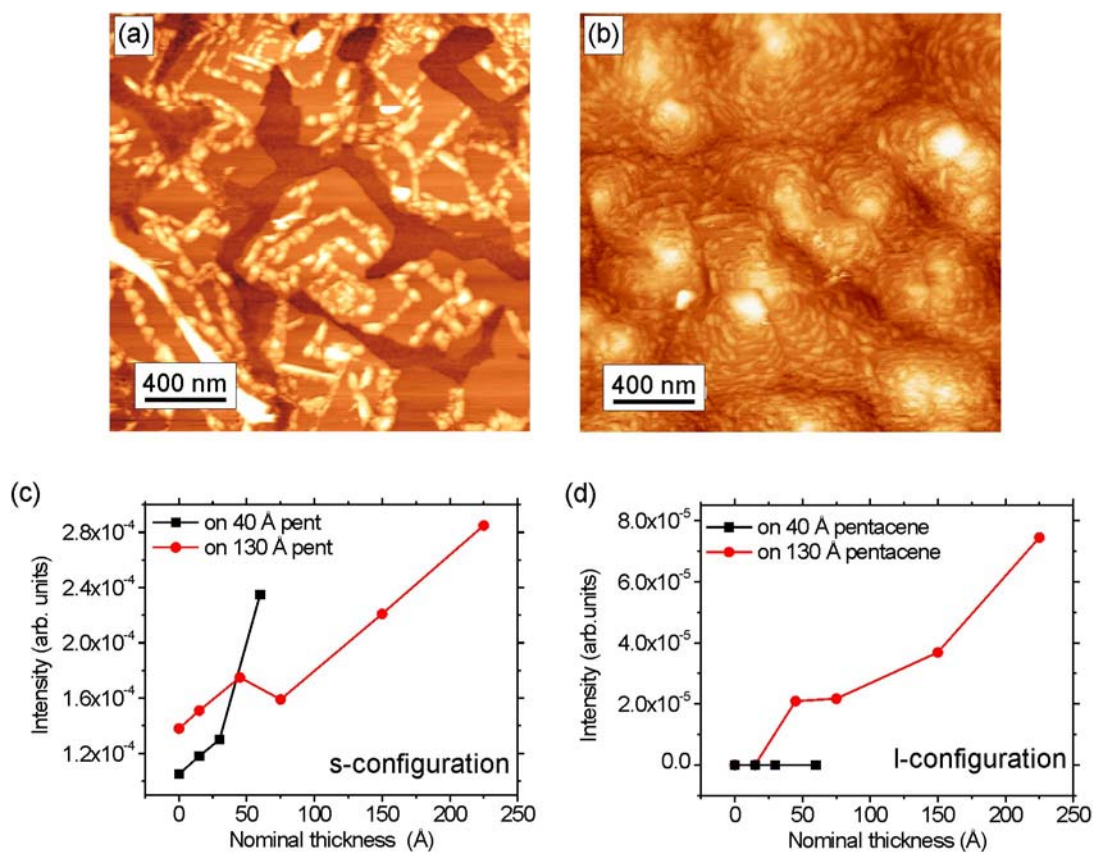


Figure 5.7. AFM topographic images of samples with 60 Å $F_{16}CuPc$ deposited on top of (a) 40 and (b) 280 Å thick pentacene films. Integrated intensity of the (c) $F_{16}CuPc$ β_{bilayer} -structure (010) and (d) out-of-plane l-structure reflection vs. phthalocyanine coverage when deposited on top of pentacene films with 40 and 130 Å thickness.

These results unambiguously show that large pentacene film thicknesses favor the growth of the $F_{16}CuPc$ l-structure at the expense of the $F_{16}CuPc$ s-structure.^a

This tendency is further evidenced by AFM measurements. Figure 5.7a and b show topographic AFM images of two heterostructures with 60 Å $F_{16}CuPc$ deposited on a 40 Å and a 280 Å thick pentacene film, respectively. The images reveal an unambiguous increase in the amount of $F_{16}CuPc$ l-structure crystallites for higher pentacene coverage, giving a coherent picture of the general organization conduct of the $F_{16}CuPc$ molecules on pentacene.

^a No absorption is taken into account, but given the comparative nature of the study it does not influence the conclusions. For a view of the influence of the absorption within the organic films, refer to appendix B.

Under the typical growth conditions used here (RT, low flux), pentacene initially grows in a quasi layer-by-layer mode and then changes to a rapid growth of several layers (3D growth) as the coverage increases due to kinetic processes.²³ Because this roughening is accompanied by an increase of the step density, the ratio between F₁₆CuPc in *l*-configuration/s-configurations increases for larger thicknesses of the underlying pentacene film, as confirmed by the AFM and GIXD studies.

Deviations from this growth scenario are observed, when the F₁₆CuPc is deposited on ultra-thin pentacene films. Figure 5.8 shows topographic images of heterostructures consisting in a submonolayer coverage of F₁₆CuPc (7 Å) deposited onto pentacene films with nominal thicknesses of 7, 20 and 35 Å. The pentacene film in Figure 5.8a (7 Å) exhibits islands of the first layer, whereas the pentacene films in Figure 5.8b (20 Å) and 5.8c (35 Å) show terraces associated with up to the 4th and 7th layer, respectively.

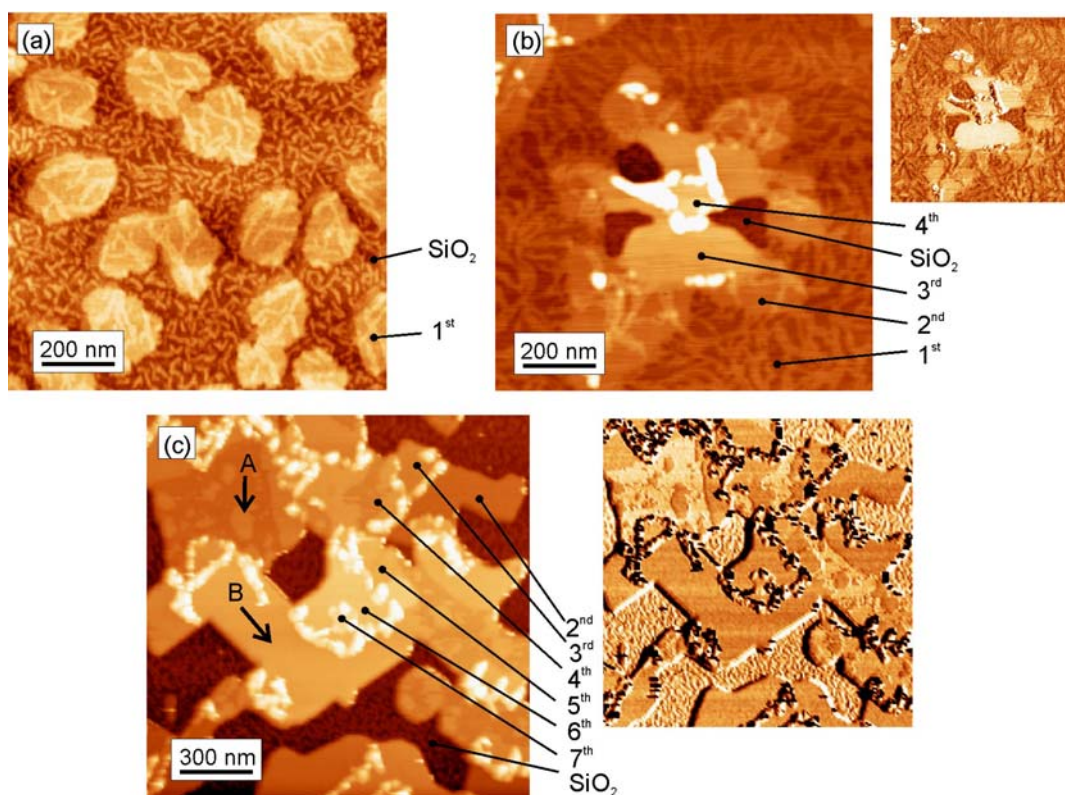


Figure 5.8. Topographic AFM images of heterostructures formed by 7 Å F₁₆CuPc deposited onto (a) 7, (b) 20, and (c) 35 Å thick pentacene films. The smaller images at the right are the simultaneously recorded phase-shift signals. The numbers indicate the pentacene layer corresponding to each of the observed terraces, disregarding the F₁₆CuPc. The arrows A and B in image c show examples of the rounded islands or homogeneous layers of F₁₆CuPc in the *s*-configuration, respectively.

The number of the pentacene layer forming the observed terraces (disregarding the deposited $F_{16}CuPc$) is marked in the AFM figures. The submonolayer pentacene islands can be distinguished in Figure 5.8a by their rounded shapes. All deposited $F_{16}CuPc$ has nucleated forming elongated islands in *s*-configuration on top of the pentacene islands as well as on the SiO_2 . This anisotropic growth is characteristic of $F_{16}CuPc$, as observed in the growth studies on SiO_2 (section 4). The length of the $F_{16}CuPc$ islands is larger on top of the pentacene, indicating a higher surface diffusion of $F_{16}CuPc$ on pentacene than on the SiO_2 surface. Notice that $F_{16}CuPc$ molecules do not assemble in the *l*-configuration at the edges of the pentacene islands (i.e first layer of pentacene). Figure 5.8b reveals a similar growth of $F_{16}CuPc$ on top of the first pentacene layer: no $F_{16}CuPc$ *l*-structure forms at the edges of the second layer (only a very small fraction). The simultaneously recorded phase-shift images are shown at the right side to allow the distinction between the $F_{16}CuPc$ *s*-structure (which appears darker) and uncovered pentacene (appears lighter). Like on SiO_2 , $F_{16}CuPc$ forms elongated islands in the *s*-configuration on top of the first and second pentacene layers. It is only on top of the third pentacene layer (at the edge of the fourth layer) where the growth of the $F_{16}CuPc$ *l*-structure takes place (Figures 5.8b and 5.8c). In addition, we observe that the $F_{16}CuPc$ islands in *s*-configuration show a rounded shape (e.g. highlighted with the arrow A in Fig. 5.8c) on top of n^{th} pentacene layers ($n \geq 3$) and give rise, upon coalescence, to very smooth and homogeneous layers (e.g. highlighted with the arrow B in Fig. 5.8c), as opposed to the defect-rich layer arising from the coalescence of the elongated islands (section 4). The round morphology vs. elongated morphologies suggests a different in-plane packing. However, since GIXD has disclosed a structural evolution of the *s*-configuration similar to that observed on SiO_2 , the understanding of this morphological difference remains a challenge.

This different growth of $F_{16}CuPc$ on the first and second pentacene layers as compared to higher ones can be traced back to different intermolecular interactions. Given that pentacene has the same structure for the first and subsequent layers (up to tens of layers),²¹ there is no basis to assume a different $F_{16}CuPc$ interaction with the first two pentacene layers. A further possibility is the influence of Van der Waals long range interactions with the substrate.³² Whereas this complies with the observation that the different $F_{16}CuPc$ growth occurs within distances less than ~ 3 nm from

substrate (i.e. on top of the first two pentacene layers), it is not clear how the long-range interactions with the substrate alter the kinetic growth processes and hinder the nucleation of the *l*-configuration. To date, direct experimental manifestations of long-range interactions with the substrate in kinetic growth processes have not yet been reported.

b. Thermal stability.

The thermal stability of F₁₆CuPc/pentacene heterostructures has also been studied. Figure 5.9 shows, for the sample with 225 Å F₁₆CuPc on top of 130 Å pentacene, the evolution of the out-of-plane (Figures 5.9a and 5.9b), as well as the in-plane (Figure 5.9c) Bragg reflections upon increasing temperature. The temperature was increased stepwise from room temperature (RT) to 140 °C as marked in the figure and maintained at each value for about two hours. The integrated intensity of the Bragg peaks, which is a measure of the amount of ordered molecules contributing to the reflection, is plotted below versus temperature for some of the representative reflections of both F₁₆CuPc and pentacene. The intensities are normalized to their initial value at room temperature.

i. Pentacene:

Figure 5.9d shows the evolution of the integrated intensity of the pentacene in-plane Bragg reflection (130) (other in-plane peaks present a similar behavior). Notice that an increase of the intensity occurs for T between RT and 100 °C, disclosing an improvement of the crystallinity by a post-annealing treatment of the film. At 100 °C partial desorption takes place and at 140 °C the complete desorption of the pentacene film is obtained. Taking into account that at a substrate temperature of 85 °C no pentacene growth occurred due to molecular desorption, it is evident that the enhanced thermal stability is promoted by the capping effect of the F₁₆CuPc adlayer (which has a higher desorption temperature). Enhancement of the thermal stability by “capping layers” has already been demonstrated for other systems such as organic DIP films capped with Al₂O₃.^{33,34}

ii. *l*-structure F₁₆CuPc:

As representative of the *l*-structure we have plotted its characteristic out-of-plane peak (Figure 5.9b) and the in-plane reflection with $q_{||}=2.44 \text{ Å}^{-1}$ (Figure 5.9c).

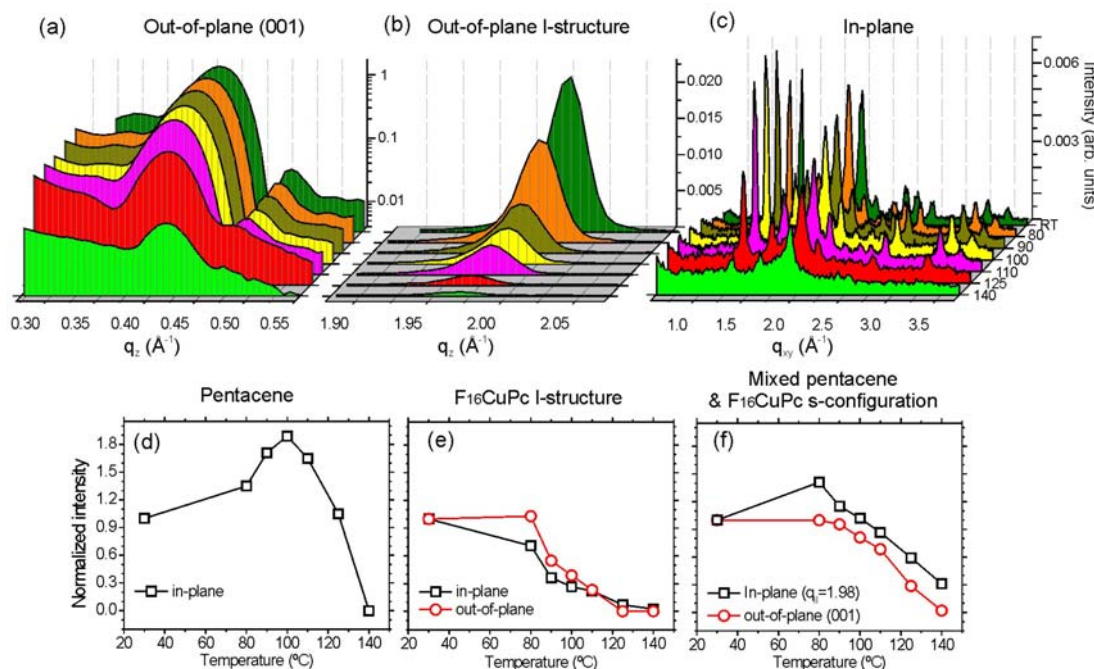


Figure 5.9. Measured intensities for (a) the out-of-plane (001) reflection (with contributions from both the standing $F_{16}CuPc$ and the pentacene), (b) the out-of-plane *l*-structure reflection and (c) the in-plane peaks for increasing temperatures from RT up to 140 °C. Below, the evolution of the integrated intensities vs. temperature are shown for specific representative reflections: (d) the (130) pentacene in-plane reflection, (e) the $F_{16}CuPc$ *l*-structure out-of-plane and in-plane ($q_{||}=2.44 \text{ \AA}^{-1}$) reflections and (f) the out-of-plane (001) and in-plane reflection with $q_{||}=1.98 \text{ \AA}^{-1}$, both of them with contributions of pentacene as well as *s*-configuration $F_{16}CuPc$.

Both follow, as expected, a similar evolution (Figure 5.9e). Already at $T=80 \text{ °C}$ the intensity slightly decreases, indicating partial desorption, but it is mainly above this temperature when a faster decrease of the intensity takes place. The low desorption temperature of this *l*-structure implies a low cohesion energy, which might in turn be related with the low cohesion observed when imaging this structure with the AFM in contact mode. The evolution of the in-plane and out-of-plane peak widths during desorption are different. While the width of the in-plane reflections remains virtually unchanged (implying a constant lateral domain size), the intensity decrease of the out-of-plane reflection is accompanied by a continuous increase in its width (implying a reduction in the crystallite heights). This implies a vertical desorption process, i.e. the molecules desorb from the upper part of the crystallites rather than from the sides.

iii. *s*-configuration F₁₆CuPc:

The two main reflections of the upright-standing phthalocyanines (the in-plane (010) β_{bilayer} and the out-of-plane (001) reflections) are mixed with contributions from the pentacene, thus making it difficult to discriminate the behaviour of each structure. However, both reflections start to decrease in intensity for temperatures above 80 °C (Figure 5.9f), an indication of partial desorption or disordering of the upright-standing F₁₆CuPc, since the intensity reduction can not arise from pentacene desorption (which starts at higher T). This is especially surprising given the high thermal stability of the phthalocyanine films when deposited on SiO₂ (with a desorption temperature of 205 °C, see section 4).

c. Thermal expansion

The thermal expansion coefficients have been characterized for the different crystalline structures in the same sample previously studied. Figure 5.10 shows the relative change in the in-plane and out-of-plane lattice spacings observed for the pentacene as well as for the F₁₆CuPc *l*-structure. Assuming a constant thermal expansion coefficient in the measured temperature range, i.e. approaching the evolution of the relative lattice changes vs. temperature (Figure 5.10) by linear functions, we obtain the thermal expansion coefficients.

The out-of-plane parameter of the F₁₆CuPc *l*-structure (which points along the normal to the molecular plane) exhibits a thermal expansion coefficient of $1.78 \times 10^{-4} \text{ K}^{-1}$, while the in-plane reflections corresponding to lattice spacings of 2.58 and 2.46 Å (which are directed along the molecular plane) show a similar expansion coefficient of $6.6 \times 10^{-5} \text{ K}^{-1}$. We remind that the thermal expansion coefficients obtained for the F₁₆CuPc β -structure on SiO₂ (see section 4.2.3) were $1.18 \times 10^{-4} \text{ K}^{-1}$ for the in-plane parameter “b” (directed to a large extent along the normal to the molecular plane) and $7.44 \times 10^{-5} \text{ K}^{-1}$ for the layer height (directed virtually along the molecular plane). Thus, the values corresponding to the thermal expansion along the normal to the molecular plane, or along directions within the molecular plane, are in the same order of magnitude for both F₁₆CuPc structures. This evidences that the thermal expansion is determined to a large extent by the anisotropic structure, without appreciable influence of the substrate.

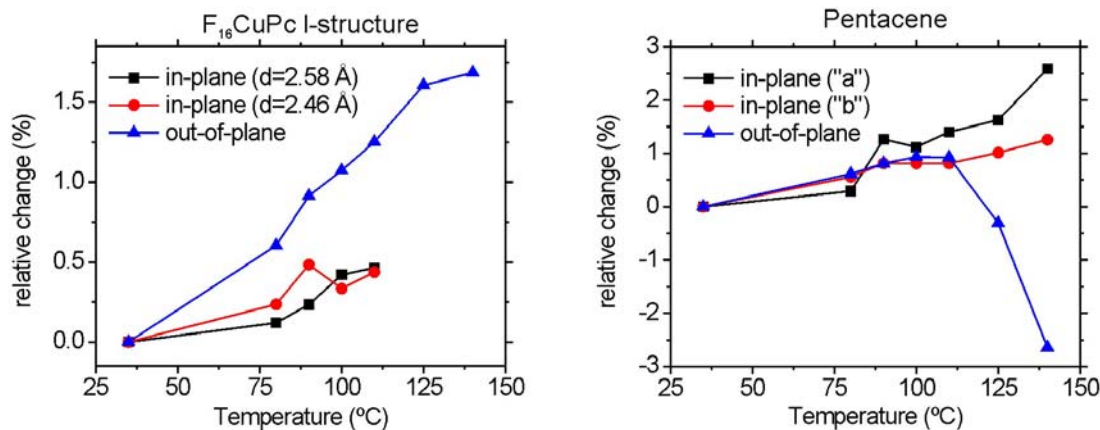


Figure 5.10. Relative change of the in-plane and out-of-plane lattice parameters for the F₁₆CuPc *l*-structure and pentacene.

In the case of pentacene, the in-plane unit-cell parameters “a” and “b” present coefficients of 2.05×10^{-4} and $1.19 \times 10^{-4} \text{ K}^{-1}$, respectively. The out-of-plane pentacene Bragg reflections are mixed with contributions from the F₁₆CuPc *s*-configuration and thus do not allow a conclusive characterization of the thermal expansion coefficient. Figure 5.10 shows the evolution of the obtained out-of-plane lattice spacing vs. temperature, in which an initial increase can be seen due to the thermal expansion, and a strong decrease for temperatures above 110 °C. This last regime is related to the partial desorption of the pentacene, by which the contribution of the F₁₆CuPc to the out-of-plane Bragg reflection becomes more important and consequently shifts the reflection towards higher *q* values (see also Figure 5.9a). From the linear part before desorption starts taking place, a thermal expansion coefficient of $1.25 \times 10^{-4} \text{ K}^{-1}$ is estimated.

In section 4.2.3, a model was presented explaining the anisotropic thermal expansion observed in most crystals or films of planar aromatic molecules, with larger expansion coefficients for the crystallographic directions along the molecular normal than for those along the molecular planes. Different models predict ratios of the coefficients of 3 : 1 and 2.1 : 1. For the *l*-structure, a ratio of 2.6 : 1 is obtained, thus within the range expected from the theoretical models.

5.2.2 Pentacene on F₁₆CuPc

In this section we study heterostructures grown in the inverse order, i.e. pentacene deposited onto F₁₆CuPc. The F₁₆CuPc films have been previously grown on SiO₂. In addition, we have just seen that an ordered phase of lying-down F₁₆CuPc molecules (*l*-configuration) can be obtained in coexistence with the upright-standing configuration (*s*-configuration) when depositing the F₁₆CuPc on pentacene. This provides us with a system where the impact of the F₁₆CuPc orientation on the pentacene growth can be tested. The study has thus been performed with two different types of heterostructures (Figure 5.11), i. e., pentacene grown on:

- i. F₁₆CuPc deposited directly on SiO₂ (consequently in an *s*-configuration) (Figure 5.11a) and
- ii. F₁₆CuPc deposited in turn on a previously grown pentacene film (therefore presenting coexistence of the F₁₆CuPc *s*- and *l*-configurations, in a ratio tunable by the pentacene substrate thickness) (Figure 5.11b).

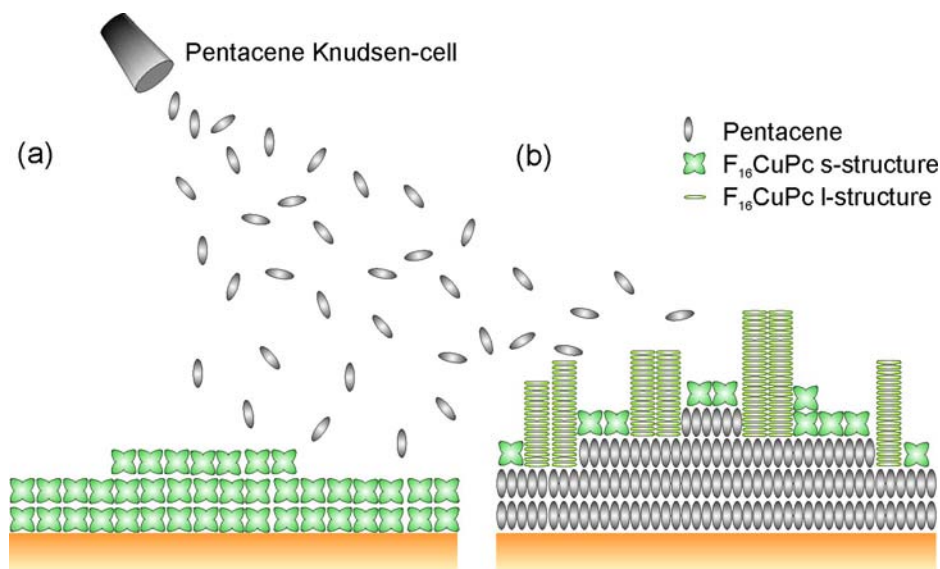


Figure 5.11. Scheme of the different heterostructures grown with pentacene on top of F₁₆CuPc

a. Pentacene on *s*-configuration F₁₆CuPc

We have started with the growth of pentacene on top of a 60 Å (~4 ML) thick F₁₆CuPc film on SiO₂. The pentacene has been deposited stepwise and measured by X-ray diffraction after each step. Figure 5.12 shows the out-of-plane and in-plane data as a function of the pentacene film thickness. Prior to the pentacene deposition, the first (001) and second (002) order Bragg reflections of the F₁₆CuPc film can already be distinguished (Figure 5.12a).

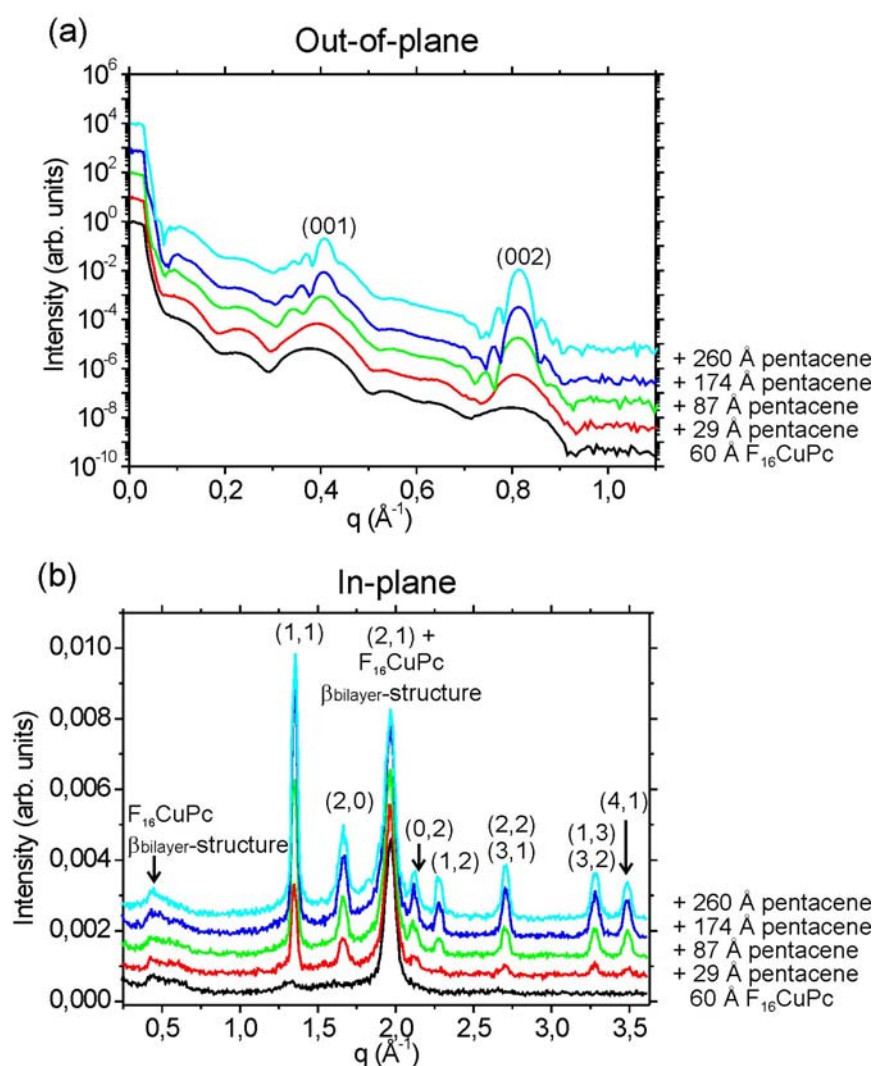


Figure 5.12. Evolution of the out-of-plane (a) and in-plane (b) X-ray diffraction data of a 60 Å thick F₁₆CuPc film upon pentacene deposition.

For increasing pentacene thickness, the $F_{16}\text{CuPc}$ reflections suffer a modulation, slowly giving rise to higher and sharper maxima corresponding to the pentacene Bragg reflections of the thin film phase ($d=15.5 \text{ \AA}$).^a The mosaicity of the pentacene film is as small as 0.015° . The appearance of Laue oscillations around the pentacene Bragg reflections evidences a laterally homogeneous coherent film thickness. However, the film thickness estimated from the width of the pentacene reflections is larger than the nominal thickness of deposited material, which is an indication of island growth. The area covered by the islands (in % of the total surface), estimated as the ratio between the nominal thickness and the estimated film thickness, increases upon pentacene deposition, passing from 30 % for 29 \AA pentacene (~ 2 monolayers) to 90 % for 260 \AA pentacene (~ 17 monolayers). Thus, despite an initial island growth, the islands finally cover virtually the whole surface with a laterally homogeneous coherently ordered film thickness. This is in clear contrast with pentacene growth on SiO_2 , where the surface roughens as result of 3D growth, therewith canceling the formation of Laue or Kiessig oscillations (see Figure 5.2 and references 21,23, and 24).

From the GIXD data probing the in-plane structure (Figure 5.12b) it can be seen that the $F_{16}\text{CuPc}$ film structure remains unchanged upon pentacene deposition. In addition, the development of the pentacene in-plane Bragg reflections can be observed. The reflections are labeled according to the pentacene thin film structure. The width of the peaks, related to the mean lateral domain size, indicate that the pentacene domain sizes for the films on top of the phthalocyanines are 30% smaller than those grown directly on SiO_2 under similar conditions.

This is further supported by the inspection of the morphology of the films by AFM. Figure 5.13a corresponds to a $F_{16}\text{CuPc}$ film grown at RT with a nominal thickness of 50 \AA . On top of this same sample, 40 \AA pentacene have been deposited, leading to the film morphology shown in Figure 5.13c, which consists in layered islands of rather homogeneous height and a correlation length of $\sim 270 \text{ nm}$ (Figure 5.13b).

^a Similarly as in the previous section, the comparable layer heights of pentacene and *s*-configuration $F_{16}\text{CuPc}$, together with the reflection broadening in q_z direction by the thin film geometry, leads to an overlap of the corresponding Bragg peaks.

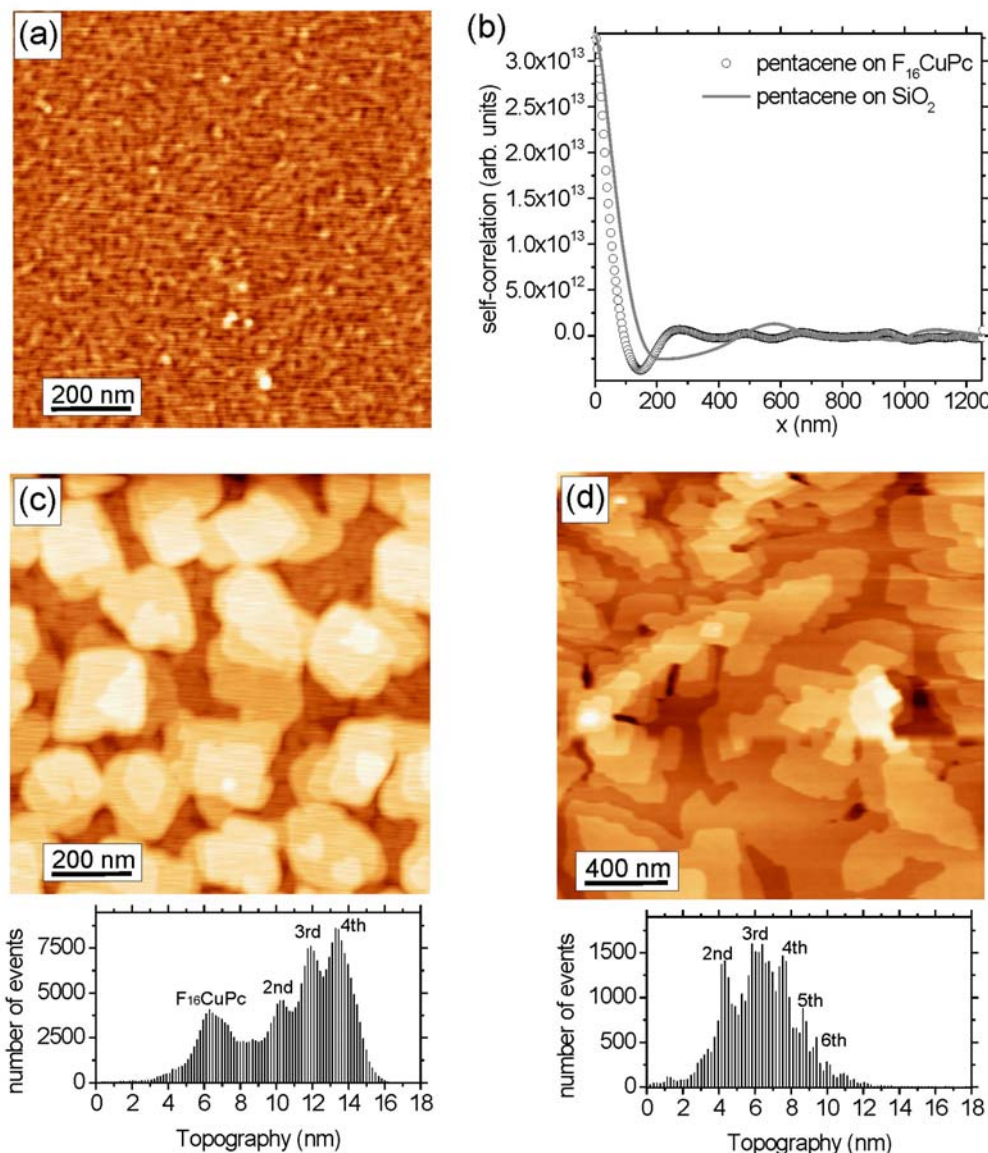


Figure 5.13. (a) Topographic AFM image of a 50 Å thick $F_{16}CuPc$ film. (b) Self-correlation functions of 40 Å thick pentacene films grown on $F_{16}CuPc$ and on SiO_2 , respectively. (c) Same sample as in (a) but after deposition of 40 Å pentacene on top. (d) Topographic AFM image of a 40 Å thick pentacene film directly on the SiO_2 under similar conditions as that in (c). Below, the height histograms corresponding to images (c) and (d) are shown.

The islands cover $\sim 80\%$ of the phthalocyanine surface. For comparison, Figure 5.13d shows a topographic image of a pentacene film with the same nominal thickness, grown on SiO_2 under similar conditions. The decreased domain sizes and improved uniformity in the island heights for pentacene films on $F_{16}CuPc$, as deduced

from the X-ray data, are corroborated. The self-correlation functions (Figure 5.13b) evidence a much larger correlation length for pentacene grown on SiO_2 .

b. Pentacene on *l*-structure F_{16}CuPc

In this case, we have deposited 75 Å of F_{16}CuPc on top of 127 Å of pentacene. On top of this bilayer, which is expected to expose a large amount of F_{16}CuPc *l*-structure (lying-down), further pentacene has been deposited in two steps (85 and 212 Å pentacene). Figure 5.14 shows the first and second order Bragg reflections of the out-of-plane X-ray data measured on this sample after each of its different growth steps. The lower graph corresponds to the bilayer used as substrate for further pentacene deposition. Upon pentacene deposition, we observe the growth of an additional, sharper contribution superimposed on the previous Bragg reflections. This evidences that the pentacene deposited on top forms high islands, ordered in the thin film structure. For 212 Å pentacene the island height estimated from the peak width is 450 Å, implying a surface coverage of the islands of less than 50%.

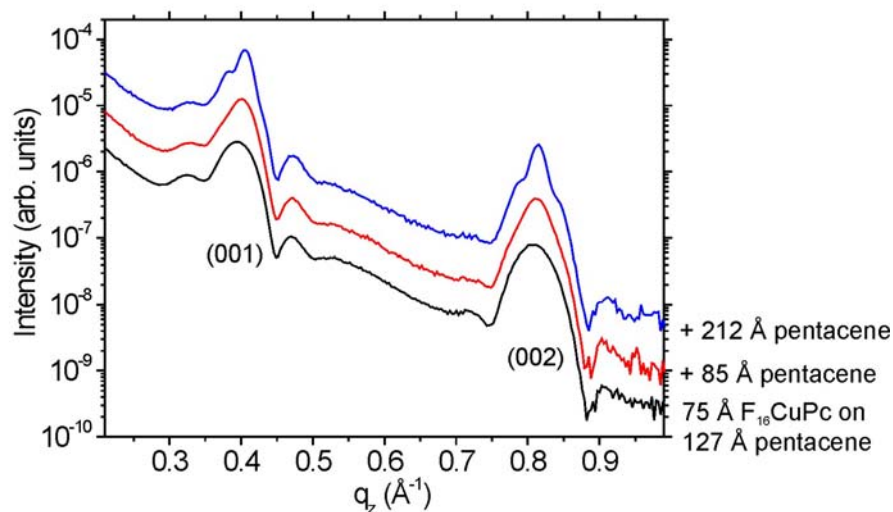


Figure 5.14. Evolution of the specular X-ray data of the first and second order reflections during the growth of pentacene on top of a F_{16}CuPc -pentacene bilayer exposing mainly lying down F_{16}CuPc molecules.

Interestingly, as opposed to the templating behavior observed on other organic heterostructures, in which a lying-down configuration of the underlying molecular film induces the growth of the subsequently deposited film with a lying-down configuration,^{16,18,19,20} no templating effect takes place here: The deposited pentacene arranges in an upright-standing configuration in spite of the lying-down configuration of the underlying F₁₆CuPc.

We recall that pentacene films have been shown to present polymorphism, with the formation of the “bulk” phase for film thicknesses above a critical value (~30 ML at RT).²⁴ In spite of the large island height obtained in this case, no bulk phase formation is observed. Furthermore, these pentacene islands show an excellent alignment along the surface normal, disclosing a mosaicity of only $0.015 \pm 0.001^\circ$, similar to the mosaicities observed for the pentacene and *l*-structure F₁₆CuPc of the underlying bilayer ($0.015 \pm 0.001^\circ$ and $0.013 \pm 0.001^\circ$ respectively).

The pentacene island growth has also been observed by AFM. The left part of Figure 5.15 is a topography image of the organic bilayer used as substrate, consisting in 60 Å F₁₆CuPc deposited on a 280 Å thick pentacene film. The observed morphology corresponds to the 3D pentacene islands, exposing concentric monolayer steps which are decorated by the F₁₆CuPc *l*-structure crystallites with lateral sizes of 50-100 nm (see previous section 5.2.1). The right part of the figure shows the resulting morphology after deposition of 80 Å pentacene on top of the bilayer. The pentacene molecules show a pronounced island growth with heights from 60 to 100 nm (see profile below), and cover only 20% of the total surface. The majority of the pentacene islands show an elongated shape which resembles the rows of F₁₆CuPc *l*-structure crystallites and whose short axis is in the range of 80-100 nm. In addition, few areas appear covered by laterally more extended (up to 300nm), and lower pentacene islands, as can be seen in the upper or left parts of the image. However, the general scenario of pentacene forming high islands is in perfect accordance with the findings of the previous X-ray study.

In summary, the pentacene film morphology presents a strong dependence with the molecular orientation of the underlying F₁₆CuPc (but preserves the same pentacene thin film structure with its upright-standing molecular orientation). If the deposition takes place on top of upright-standing F₁₆CuPc, the pentacene forms excellently ordered films with a laterally homogeneous coherently ordered film

thickness. In contrast, when deposited on lying-down phthalocyanines (*l*-structure), the pentacene presents pronounced island growth.

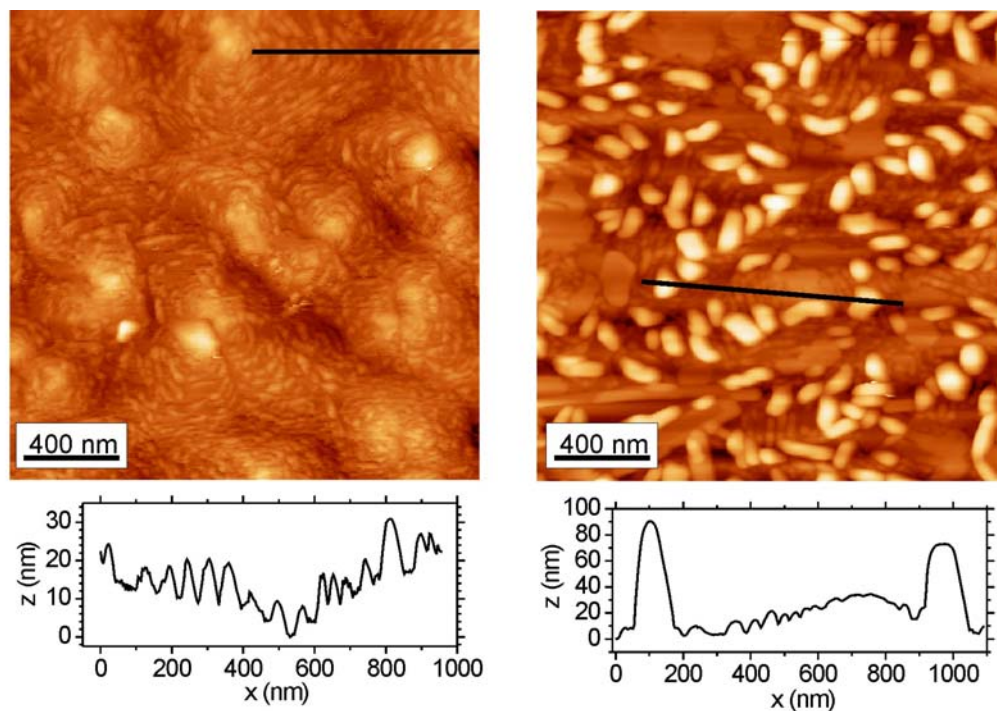


Figure 5.15. Topographic AFM images of a sample consisting in 60 Å F₁₆CuPc on a 280 Å thick pentacene film (left). The right image corresponds to the same sample after deposition of 80 Å pentacene on top. Below, two profiles (marked on the images) show the different length-scales of the F₁₆CuPc *l*-structure and pentacene islands.

5.2.3 Conclusions

We have shown the different growth behaviours of pentacene and F₁₆CuPc when deposited on top of each other. The results evidence a highly anisotropic F₁₆CuPc-pentacene interaction, since the growth presents a strong dependence with the relative orientation between both types of molecules. When depositing F₁₆CuPc on top of a pentacene film, the molecules arrange into different configurations. On the pentacene terraces exposing the low energy (001) planes, the F₁₆CuPc molecules organize in their preferred upright-standing configurations, similarly as on SiO₂ (see section 4.2). However, at the step edges, where the pentacene molecules expose the molecular planes, the F₁₆CuPc molecules arrange with their molecular planes parallel to the

substrate surface, and consequently perpendicular to the molecular planes of the pentacene molecules at the steps. This configuration of lying-down phthalocyanines (*l*-structure) gives rise to high and narrow islands. This general growth scenario of F₁₆CuPc on pentacene shows additionally a dependence on the pentacene layer on top of which it grows. The phthalocyanines do not arrange into the *l*-configuration neither at the step edges of the first nor of the second layer (i.e. on top of the SiO₂ or the first pentacene layer, respectively). This is accompanied by an alteration of the *s*-structure crystallite morphology from elongated to an isotropic shape. We have suggested that the long-range interactions with the substrate are responsible for the distinct F₁₆CuPc growth on the two first pentacene layers.

When deposited in reversed order, i.e. pentacene on F₁₆CuPc, the pentacene growth differs noticeably depending on the molecular orientation of the underlying phthalocyanines. This affects the film morphology, but the pentacene film structure is the same and, interestingly, is not subject to any templating effect when grown on lying-down F₁₆CuPc.

5.3 *F₁₆CuPc and DIP*

In order to elucidate the specificity of the intermolecular interactions and to obtain a general picture of the growth of organic heterostructures, it is mandatory to further investigate these issues with other molecules.

We have performed a similar study, combining now F₁₆CuPc with DIP (see section 2.1.2), another organic aromatic molecule. The DIP molecule, as well as the DIP films deposited on SiO₂, present some similarities with the pentacene molecule or films, as is the chemical composition (C₃₂H₁₆ vs. C₂₂H₁₄, respectively), the film morphology, the step height between subsequent layers (16.6 vs. 15.5 Å, respectively), the water contact angle of the films (87.5±3.6° vs. 83.5±2.5°, respectively), or the preferential p-type semiconducting behavior in combination with Au contacts. However, different and new processes are observed in the growth of these heterostructures, as we present below for both deposition sequences.

Beyond its interest from the fundamental point of view, the absorption spectra of $F_{16}\text{CuPc}$ (n-type material) and DIP (p-type material) cover the whole visible light range, thus making heterostructures formed by these two materials highly interesting as potential building blocks of organic solar cells.³⁵

5.3.1 DIP on $F_{16}\text{CuPc}$

The deposition of DIP onto $F_{16}\text{CuPc}$ results in a strongly temperature dependent behavior. Figure 5.16, shows topographic AFM images of heterostructures consisting in 120 Å DIP (7.2 ML), deposited at a growth rate of ~ 3 Å/min, on top of 30 Å $F_{16}\text{CuPc}$ (2 ML) at different substrate temperatures.^a

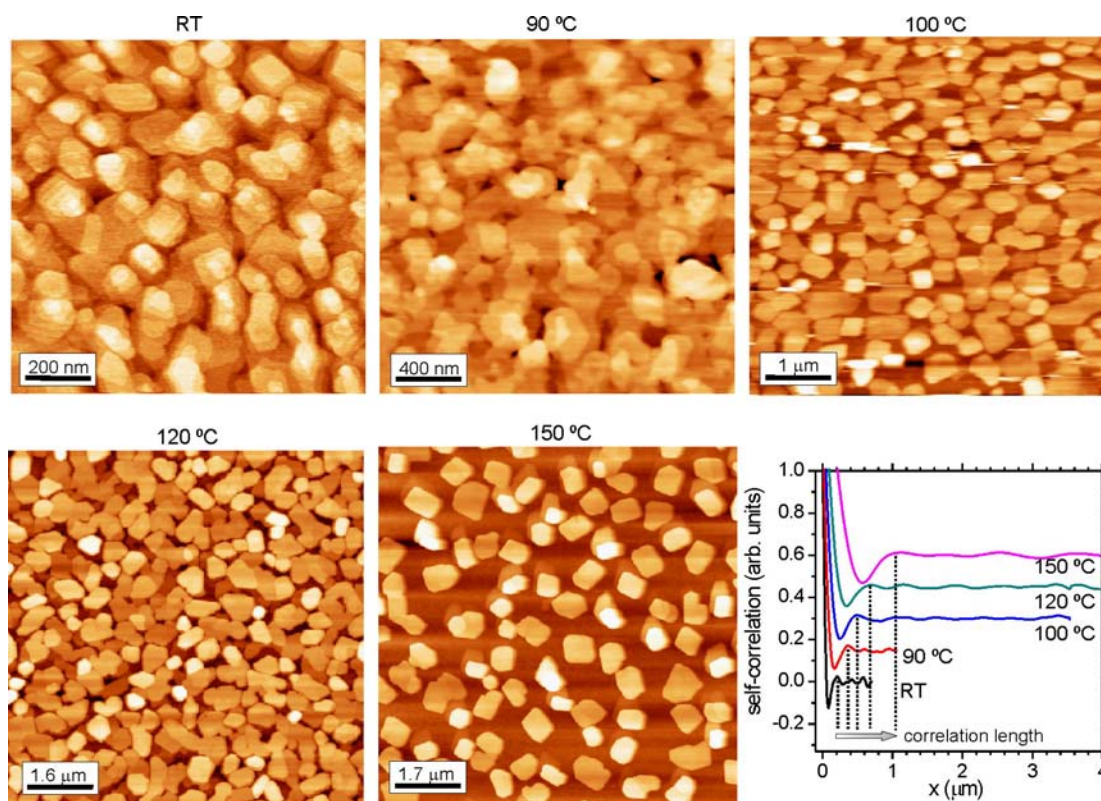


Figure 5.16. Bilayer samples consisting in 120 Å DIP deposited on 30 Å $F_{16}\text{CuPc}$ at substrate temperatures of RT, 90, 100, 120 and 150 °C respectively (the DIP coverage is 166 Å for the sample grown at RT). At the lower right side the self-correlation function is displayed for the different samples (shifted for clarity), evidencing the increase in the correlation length for increasing temperature.

^a The DIP thickness of the sample grown at RT is slightly higher: 166 Å

At low temperatures, DIP forms a rather homogeneous closed film, while for increasing temperature the resulting surface morphology gets rougher, until a clear island growth is evident for temperatures above 90 °C. In addition, the self-correlation functions of the resulting surfaces, which show for all samples a damped oscillatory behavior as displayed in Figure 5.16, evidence a strong increase in the correlation length with higher temperatures. This can in turn be traced back to the higher surface mobility of the molecules at higher temperatures, and offers the possibility to tailor the mean lateral distance between the DIP islands.

In the following, we study in more detail the growth under high (120 to 150 °C) and low (RT down to -10 °C) substrate temperatures.

a. High temperature (120 to 150 °C)

The spontaneous emergence of well-defined DIP dots during DIP deposition on F₁₆CuPc at high temperature can directly be observed by AFM measurements. Figure 5.17 shows the evolution of the topography of a 2.2 ML thick F₁₆CuPc film upon subsequent deposition of 0.35, 0.8 and 2.4 ML DIP on top at 120 °C. The measurements have been performed in contact mode under UHV conditions, without breaking the vacuum upon transfer to and from the growth chamber. The F₁₆CuPc sample prior to the DIP deposition shows a virtually closed second layer and some third layer islands with their typical elongated shape. Upon deposition of 0.35 ML DIP, the DIP starts completing the third layer, showing a preferred nucleation along the edges of the F₁₆CuPc islands. Further DIP deposition (0.8 ML) leads to an almost complete third layer. Upon completion of this third layer, most of the DIP arranges into a rather well ordered nanostructure composed out of DIP nanodots (2.4 ML image). They exhibit very flat and smooth surfaces and quite homogeneous sizes with narrow dispersion, being the average size of 100 nm (lateral) x 7 nm (vertical). The dot-dot auto-correlation function discloses a decaying oscillatory behaviour with a mean distance of 270 nm between the organic dots.

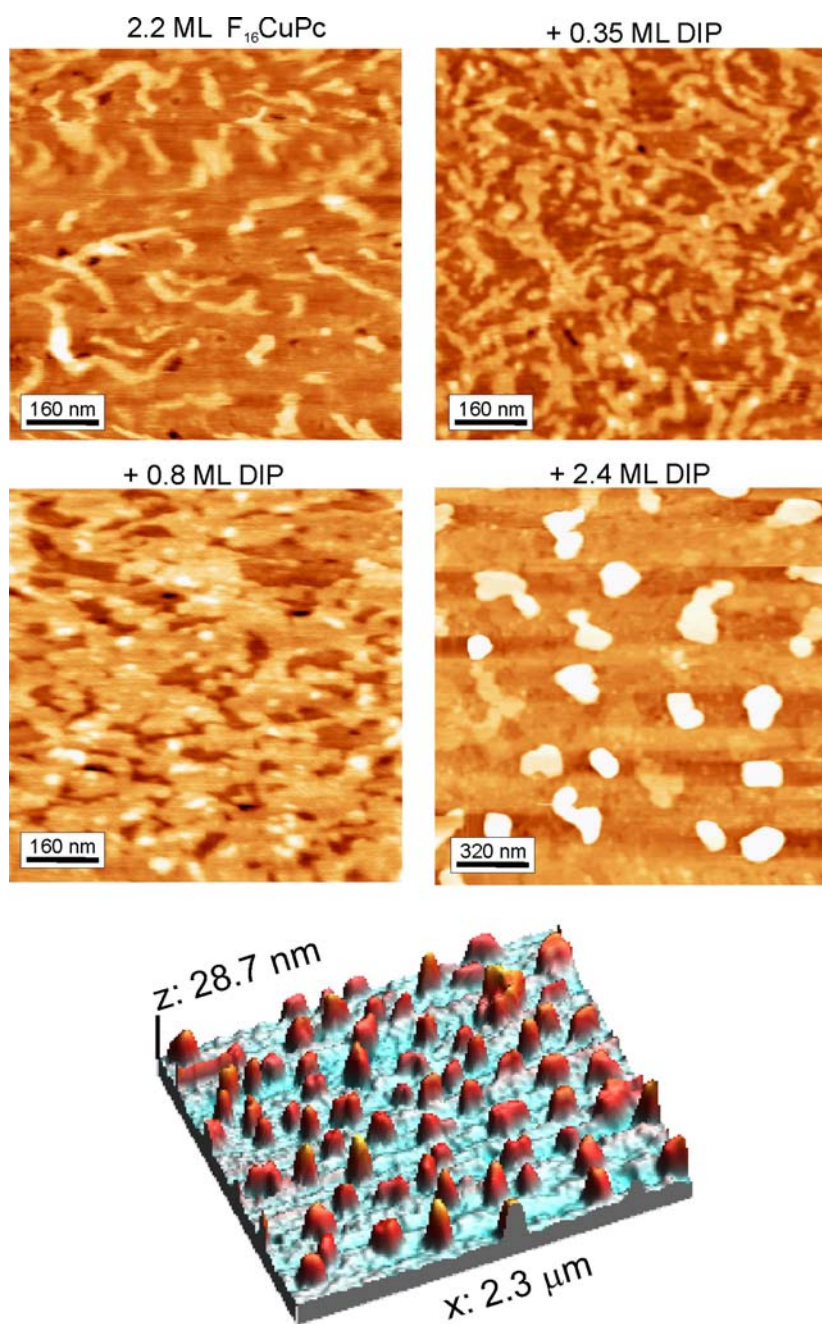


Figure 5.17. Topographic AFM images of a 2.2 ML thick $F_{16}CuPc$ film upon deposition of 0.35, 0.8 and 2.4 ML DIP on top. The lowest image shows a 3D picture of the sample in its final state.

Larger and higher DIP dots are found for higher coverage, thereby maintaining their narrow size distribution (Figure 5.16 and 5.18). A high degree of crystallinity can already be expected from the AFM images in Figure 5.18a, revealing the presence

of well defined crystalline facets and regular shapes of the organic dots. Among the most frequent shapes we find hexagonal and rectangular dots. However, a closer look at the rectangular crystallites reveals in most of the cases the formation of additional small facets avoiding the presence of subsequent facets perpendicular to each other. This is especially surprising given the rectangular unit cell of the DIP and the fact that the low energy and thus the preferred facets in crystals are in general low index planes. A statistical analysis of the observed angles between the facets is shown in Figure 5.18b. It can be clearly seen that there are favored angles, related to the presence of preferred facets to minimize the crystal surface energy. Nevertheless, the low accuracy and high dispersion of the angles as measured by AFM does not allow the correlation to specific crystallographic planes of the organic dots.

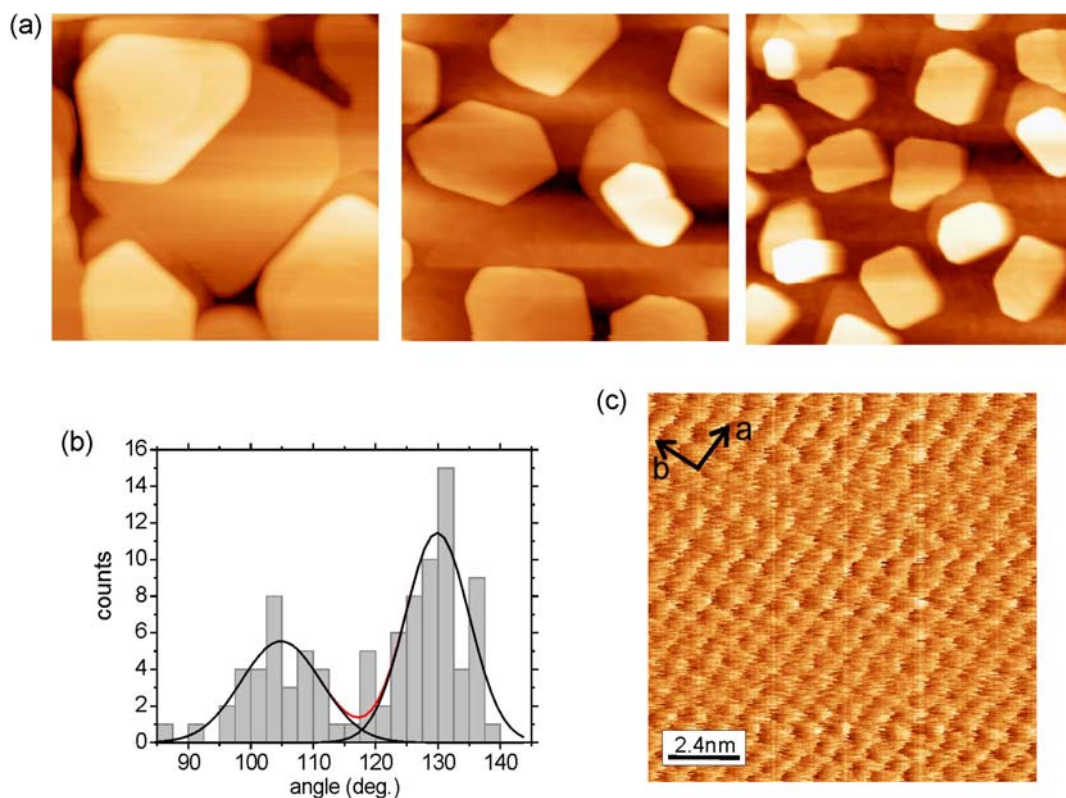


Figure 5.18. (a) Topography images of self-assembled DIP nanodots on $F_{16}CuPc$. (b) Statistical analysis of the angles observed between facets of the nanodots. (c) Molecular resolution obtained on the dots by lateral force imaging, evidencing the crystalline structure marked with the basis vectors $a=8.12\pm0.9$ Å, $b=7.31\pm0.8$ Å, $\gamma=91\pm3$ degrees.

A further indication of the high crystallinity of the DIP nanodots is the molecular resolution obtained by AFM lateral force imaging on top of the crystallites. This is shown in Figure 5.18c, together with the basis vectors concluded from the images. The obtained values for the in-plane unit cell parameters are $a=8.12\pm0.9$ Å, $b=7.31\pm0.8$ Å and $\gamma=91\pm3^\circ$, thus in very good agreement with the values concluded from previous X-ray diffraction studies (see Table 2.2).

In order to shed light onto the growth processes, which finally lead to such self-organized organic structures, we have carried out an in-situ X-ray study of the microscopic structure which evolves at the DIP-F₁₆CuPc interface during DIP deposition. The experimental findings from an extended X-ray reflectivity study during the initial deposition of DIP (1 to 8 MLs) onto F₁₆CuPc are summarized in Figures 5.19a and 5.19b. By using the Parratt fitting algorithm (see section 3.2.2) the X-ray reflectivity intensity profile can be converted into an absolute electron density profile $\rho(z)$ along the surface normal (right part of Figure 5.19a). After deposition of 1 ML F₁₆CuPc (14 Å), an almost complete F₁₆CuPc monolayer of standing molecules forms with a partial nucleation of the second layer. This can directly be deduced from the in-situ X-ray reflectivity and the fitted electron density profile (Figure 5.19a, top-right). The subsequent evaporation of 1 ML of DIP (17 Å) leads to the formation of a DIP wetting layer with a very well defined organic-organic interface (Figure 5.19a, bottom-right). We find that the DIP molecules complete the second layer and start the growth of the third layer. The electronic density of the underlying F₁₆CuPc remains unchanged upon DIP deposition, implying that molecular interdiffusion does not occur. X-ray signals from the internal crystal structure of the DIP nanodots emerge, as soon as the nominal DIP coverage exceeds 3 MLs: The two Bragg reflections in Figure 5.19b are identified as the DIP(001) and DIP(002) reflections associated with a spacing of $d=16.6$ Å between adjacent molecular layers. This coincides with the ordered structure of upright standing molecules observed on SiO₂.³⁶ From the narrow width of the (001) rocking curves of only 0.0076° , we deduce an excellent microscopic alignment of the DIP dots with respect to the surface normal. In addition, the DIP growth behavior was followed in real time by monitoring the intensity at the $3/2$ (001) Bragg point (Figure 5.19c) while depositing it onto 5.5 ML F₁₆CuPc (80 Å) at 120 °C.

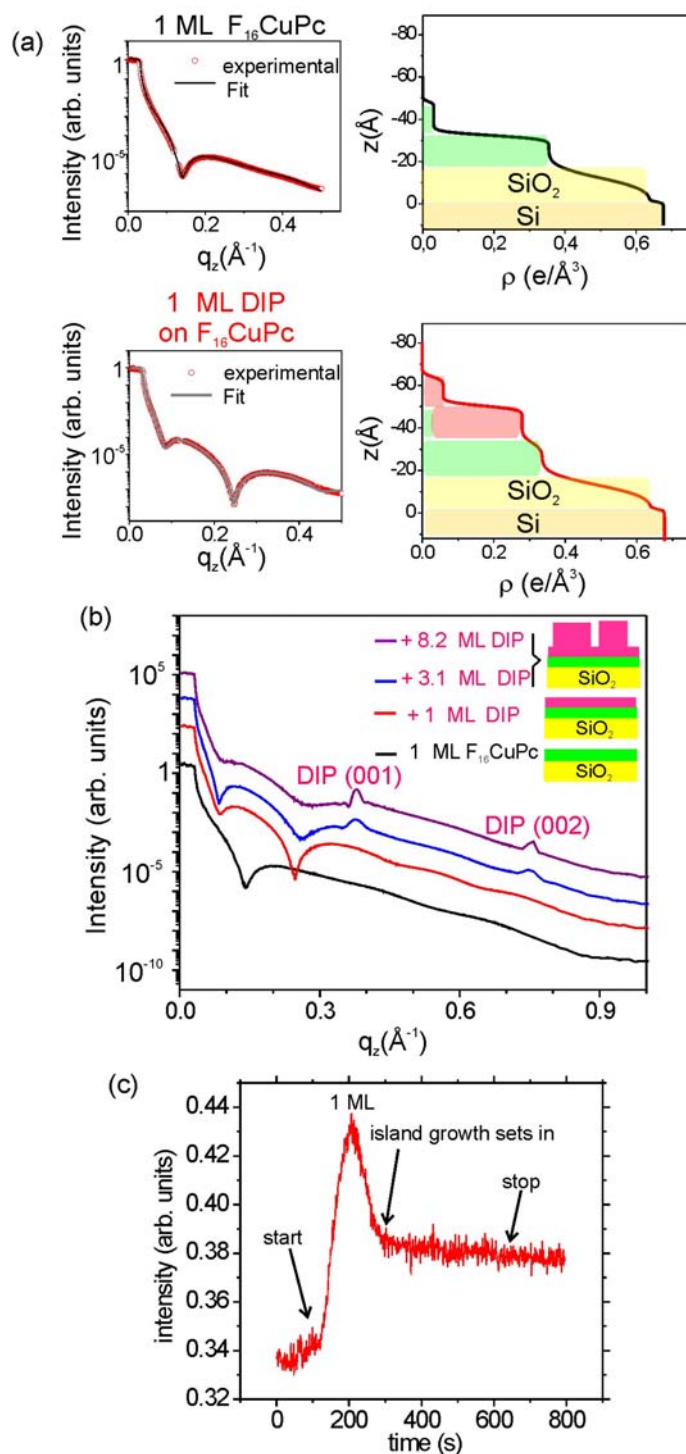


Figure 5.19. (a) On the left: measured and fitted X-ray reflectivity data for 1 ML (14 Å) of $F_{16}CuPc$ on SiO_2 (top) and after deposition of 1 ML of DIP (17 Å) onto the $F_{16}CuPc$ (bottom). On the right: deduced electron density profiles. As a guide for the eyes, boxes in different colour mark the layers of different materials. (b) X-ray reflectivity for further DIP coverage. The inset depicts the deposition situation. (c) Real time monitoring of the DIP growth onto 5.5 ML at the 3/2 (001) Bragg point, with a substrate temperature of 120 °C and a growth rate of 9 Å/min. The final nominal DIP film thickness was 6 ML.

The scattered intensity depends on the evolution of the layer occupancy, leading to nice oscillations upon layer-by-layer growth or to a constant intensity upon island growth, thus giving an insight into the growth process (see section 3.2.5). The obtained intensity evolution reveals the initial formation of a DIP layer followed by island growth, thus confirming the observed growth behavior observed by AFM.

The results obtained by complementary measurements thus present a fully unanimous scenario, revealing the formation of a wetting layer of 1 ML of DIP, followed by the formation of crystalline 3D islands upon further DIP coverage. This growth scenario, referred to as Stranski-Krastanov (SK) growth, is well known in inorganic semiconductor heteroepitaxy and is held responsible for the self-organization of quantum dots.³⁷

The remarkable observation in our case is that the SK growth of DIP on F₁₆CuPc involves a reconstruction of the underlying F₁₆CuPc film adjacent to the organic p-n interface. This phenomenon has been disclosed by grazing incidence X-ray diffraction (GIXD), which allows us to access the in-plane crystal structure of F₁₆CuPc and DIP during the growth (Figure 5.20a). As illustrated schematically in Figure 5.21, F₁₆CuPc stands upright arranged in the β_{bilayer} -structure, adopting a columnar stacking of cofacially oriented molecules with a distance between molecular columns of $d(100)=14.59 \text{ \AA}$ and an intermolecular distance of $d(010)=3.20 \text{ \AA}$ (lower curve in Figure 5.20a). Most interestingly, we observe a clear shift of the F₁₆CuPc in-plane reflections upon the evaporation of 1 ML of DIP, which is highlighted by the arrows in Figure 5.20a. This shift reveals the reconstruction of the underlying F₁₆CuPc film, which adopts new lateral lattice spacings, being $d(100)=11.83 \text{ \AA}$ and $d(010)=3.32 \text{ \AA}$. This change in $d(100)$ (by 14%) points to the formation of a columnar stacking with an average tilt of the F₁₆CuPc molecular plane relative to the [100] direction of about 35 ° (see Figure 5.21). Such a F₁₆CuPc structure has never been observed before and is, according to our experimental observations, induced by the deposition of a DIP monolayer which assumes its characteristic herringbone structure with two molecules per unit cell (the lattice parameters are $a=8.55 \text{ \AA}$, $b=7.09 \text{ \AA}$, $\gamma=90^\circ$).^{38,a}

^a The emergence of two additional DIP reflections close to the (110) and (210) reflections have been tentatively related to the formation of another DIP structure in a previous work,³⁸ but this structure is not yet sufficiently known.

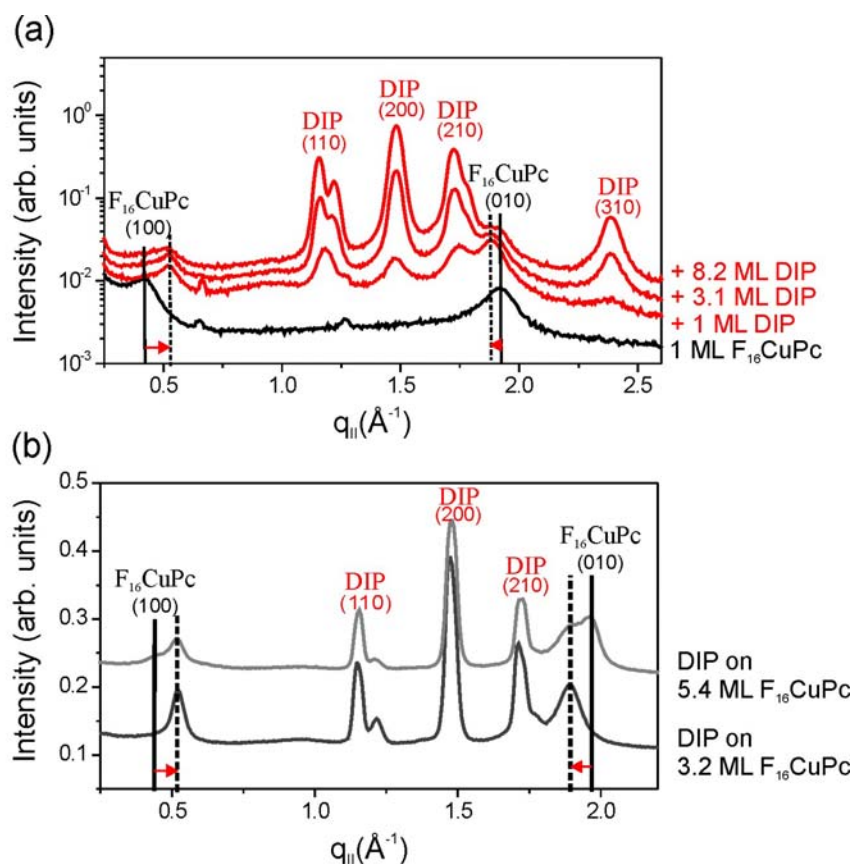


Figure 5.20. (a) GIXD data for DIP (from 1 ML to 8.2 ML) grown on top of 1 ML of $F_{16}CuPc$ obtained for the same sample as in Figure 5.19 (substrate temperature = 120 °C). The deposition of 1 ML of DIP onto the $F_{16}CuPc$ film results in a shift of the $F_{16}CuPc$ in-plane reflections (dashed bars) evidencing a reconstruction of the $F_{16}CuPc$ film. (b) GIXD data for the deposition of ~5 ML DIP onto a 3.2 ML $F_{16}CuPc$ film and onto a 5.4 $F_{16}CuPc$ films (substrate temperature = 120 °C). The thin $F_{16}CuPc$ film undergoes a total reconstruction. In the thicker $F_{16}CuPc$ film, we estimate from the integrated intensities that 3 ML of $F_{16}CuPc$ close to the organic-organic interface reconstruct.

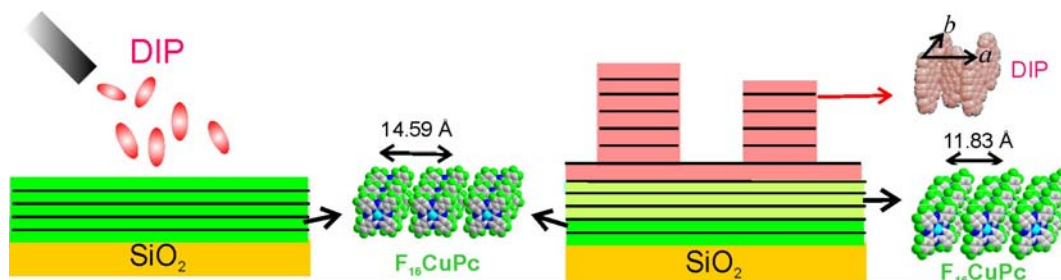


Figure 5.21. Schematic summary of the growth behavior observed upon deposition of DIP onto $F_{16}CuPc$ at high temperature.

In contrast to the rather large reconstruction of the underlying $F_{16}\text{CuPc}$, the DIP wetting layer shows no apparent structural changes i.e. same structure as that exhibited on SiO_2 .^a This reconstruction of the underlying $F_{16}\text{CuPc}$ film and the subsequent formation of DIP nanodots on top of the DIP wetting layer also occur for thicker $F_{16}\text{CuPc}$ films, as confirmed experimentally up to a $F_{16}\text{CuPc}$ film thickness of 17 ML. We find from a detailed analysis of the diffraction data (summarized in Figure 6.18b) that the reconstruction of $F_{16}\text{CuPc}$ is limited to three layers adjacent to the organic-organic interface. The general growth scenario of DIP deposited on $F_{16}\text{CuPc}$ at high temperature is summarized in Figure 5.21.

b. Low temperature (RT down to -10 °C)

A key question now is whether or not the observed DIP-induced interface reconstruction of the underlying $F_{16}\text{CuPc}$ film is prerequisite for the formation of the DIP nanodot array. The clue to answer this question is found in growth experiments performed for substrate temperatures of -10 °C and 35 °C.

Figure 5.22a shows the reflectivity data of a 5.1 ML thick $F_{16}\text{CuPc}$ film before and after deposition of 7 ML DIP on top at RT. Upon DIP deposition, the emergence of the DIP (001) and (002) Bragg reflections evidences the standing-upright arrangement of the DIP in its thin film phase. The development of well defined Kiessig fringes at low q_z values and Laue fringes around the DIP Bragg reflections (Figure 5.22a), are related to the formation of laterally homogeneous and smooth DIP films on the $F_{16}\text{CuPc}$. The real time monitoring of the scattered intensity at the 1/2 (001) Bragg reflection during DIP deposition at room temperature (Figure 5.22b) displays clear oscillations indicative of a nearly layer by layer DIP growth within the studied coverage range (up to a nominal thickness of 7 ML).

Most interestingly, the GIXD data of the $F_{16}\text{CuPc}$ film before and after DIP deposition (Figure 5.22c) reveal that, at these (low) temperatures, the DIP growth does not lead to the rearrangement of the underlying $F_{16}\text{CuPc}$ film (most likely because of kinetic barriers).

^a Taking into account that both on SiO_2 and $F_{16}\text{CuPc}$ the DIP is affected by similar structural changes which take place within the first layers.

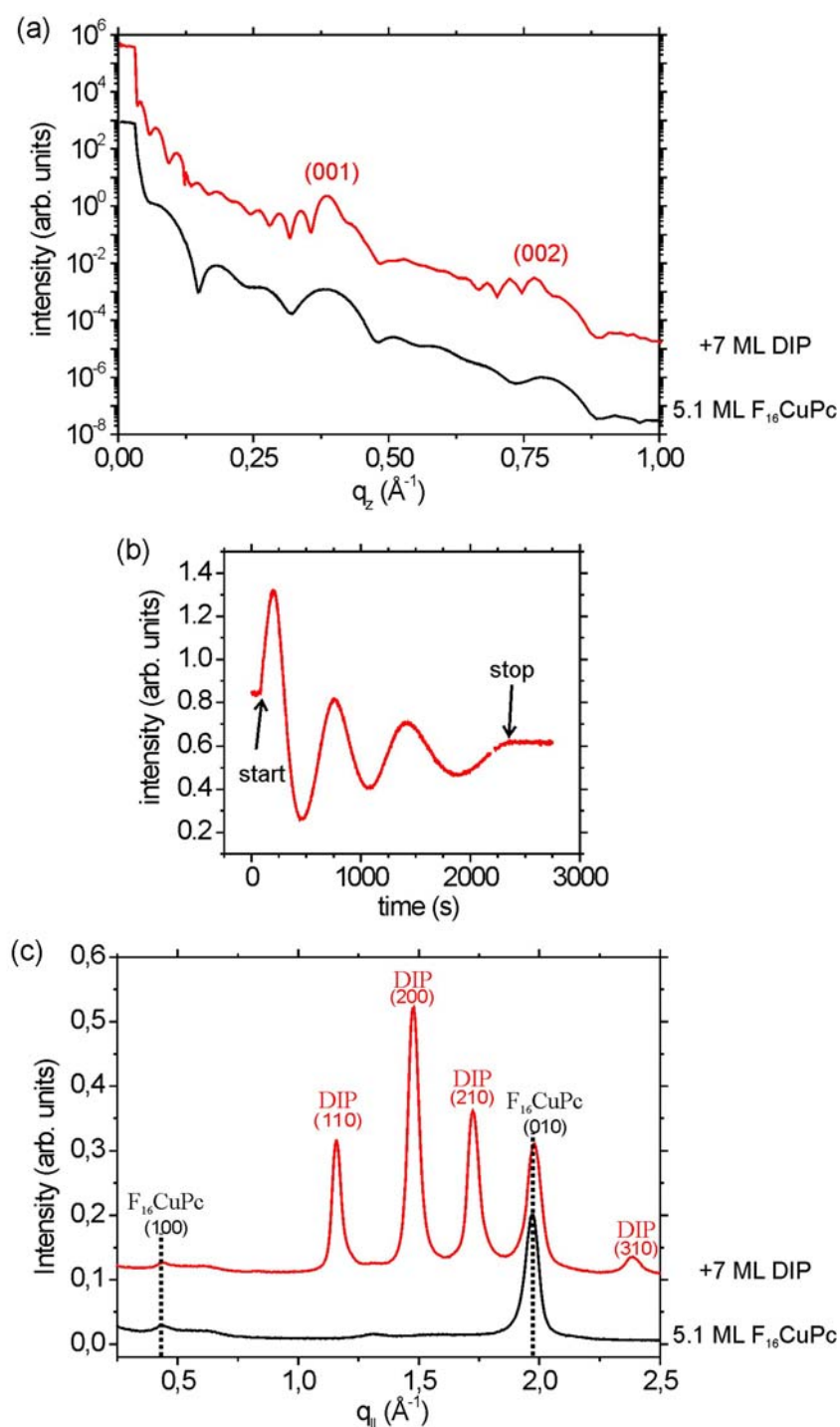


Figure 5.22. (a) Reflectivity data before and after DIP deposition on a 5.1 ML thick $F_{16}CuPc$ film at RT. (b) Real time monitoring of the scattered intensity at the $\frac{1}{2}$ (001) DIP Bragg reflection during the DIP deposition (with a growth rate of $\sim 4 \text{ \AA}/\text{min}$). (c) GIXD data before and after DIP deposition on a 5.1 ML thick $F_{16}CuPc$ film at RT.

This clearly shows that it is the interface reconstruction of the $F_{16}CuPc$ film which apparently modifies the energy landscape of the organic heterojunction such that SK growth of the DIP sets in, and that other factors which could be associated with the SK growth, such as intermixing or strain in the DIP wetting layer (in the form of in-plane lattice distortion) play no role.

The microscopic aspects of the growth of DIP on $F_{16}CuPc$ at RT has been further probed by AFM as shown in Figure 5.23, which displays topographic non-contact AFM images of a 2.5 ML thick $F_{16}CuPc$ film before and after subsequent DIP deposition of 0.3, 1, 1.9, 3.4 and 8.5 ML. The experiment has been performed under UHV without breaking the vacuum upon transfer to and from the growth chamber in each of the deposition steps. The bare $F_{16}CuPc$ shows a virtually closed second molecular layer and the partial coverage of the third layer formed by the typical elongated crystallites. Upon DIP deposition (0.3 ML), the DIP nucleates at the step edges of the $F_{16}CuPc$ crystallites and grows completing the third layer.

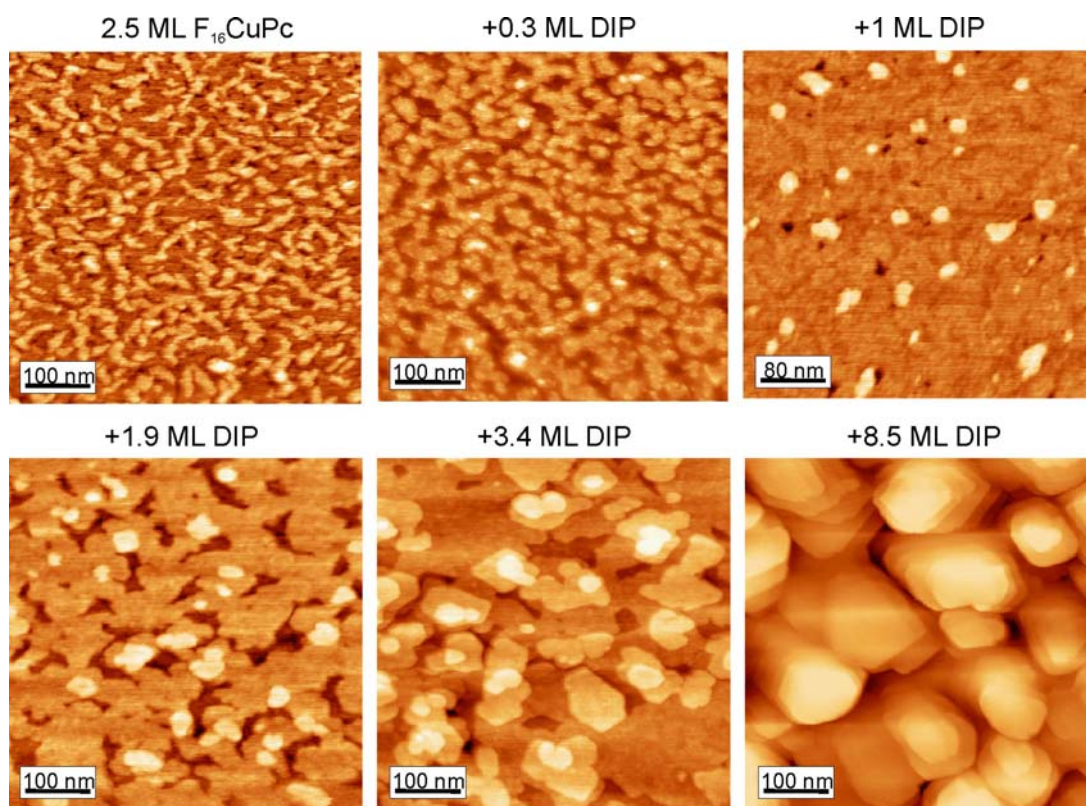


Figure 5.23. Non-contact AFM topographic images of a 2.5 ML thick $F_{16}CuPc$ film before and after deposition of 0.3, 1, 1.9, 3.4, and 8.5 ML DIP at RT.

Interestingly, upon completion of the third (mixed layer), the elongated $F_{16}\text{CuPc}$ crystallites can be distinguished from the surrounding DIP by their lower height (darker, elongated regions in the image with 1 ML DIP) as compared to the DIP layer. A close to layer-by-layer growth is observed for the first DIP layers, though a deviation from the layer-by-layer growth sets in for higher thicknesses, as can be seen in the image corresponding to the deposition of 8.5 ML DIP.

The question on the stability of this smooth layered heterostructures grown at low temperature has been addressed by a post-annealing treatment experiment, in which a heterostructure consisting in 6.3 ML DIP deposited onto 3.9 ML $F_{16}\text{CuPc}$ at RT was annealed to 120 °C. The sample was checked by X-ray diffraction before and after the treatment, by which, as shown in Figure 5.24, no evidence was found neither for the formation of DIP islands nor for the associated $F_{16}\text{CuPc}$ reconstruction.^a

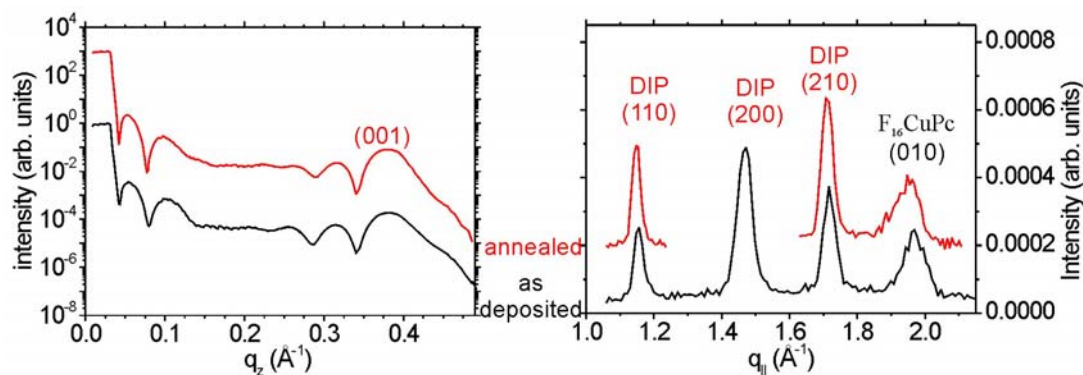


Figure 5.24. Out of plane (left) and in-plane (right) XRD data of a sample consisting in 6.3 ML DIP deposited on 3.9 ML $F_{16}\text{CuPc}$ at RT and subsequently annealed at 120 °C.

5.3.2 $F_{16}\text{CuPc}$ on DIP

The opposite deposition sequence ($F_{16}\text{CuPc}$ onto DIP) also shows a strongly temperature dependent growth behavior. Two sets of experiments have been performed at high (120 °C to 150 °C) and low (RT) temperatures, and are sequentially presented below.

^a A slight shift of the $F_{16}\text{CuPc}$ (010) reflection is visible from $q=1.969 \text{ \AA}^{-1}$ ($d=3.19 \text{ \AA}$) to $q=1.950 \text{ \AA}^{-1}$ ($d=3.22 \text{ \AA}$) related to the thermal expansion rather than to the reconstruction.

a. High temperature (120 °C, 150 °C)

The out-of-plane structure has been determined in-situ by X-ray reflectivity measurements during deposition of F₁₆CuPc on 1.8 ML DIP at 120 °C. The emergent (001) reflection (up to the third order) corresponds to a layer spacing of 14.9 Å, thus slightly (though clearly beyond the error margin) larger than the spacing of the β - or β_{bilayer} -structures observed on SiO₂. In addition, the growth of F₁₆CuPc on top of a 4.2 ML thick DIP film at 150 °C has been monitored in real time at the 1/2 (001) Bragg position (Figure 5.25b). Clear oscillations are observed, indicative of a close to layer-by-layer growth, at least during the deposition of the first 10 layers, after which the oscillations are almost completely damped due to film roughening (3D growth).

The in-plane structure has also been measured by in-situ GIXD after subsequent deposition of F₁₆CuPc onto a 2 ML thick DIP film at 120 °C (Figure 5.25c). First of all, note that no changes occur in the underlying DIP film structure. Interestingly, the development of peaks at q values of 0.5312 and 1.9062 Å⁻¹ (corresponding to 11.83 and 3.3 Å, respectively) evidence the formation of the same F₁₆CuPc “reconstructed” structure observed when DIP is deposited on F₁₆CuPc at high temperature. While this “reconstructed” structure is associated with the formation of the DIP nanodots on the F₁₆CuPc, in this case, with F₁₆CuPc on top of DIP, a rather smooth, layered heterostructure is formed. As opposed to the growth of DIP on F₁₆CuPc, which leads to the reconstruction of the three upper F₁₆CuPc layers in proximity to the DIP, in this case (F₁₆CuPc on DIP) all the deposited F₁₆CuPc organizes into the “reconstructed” structure. Notice that three new reflections emerge, corresponding to lattice spacings of 6.05, 7.01 and 14.14 Å. The first may correspond to the second order reflection of the reconstructed structure (now visible due to the larger amount of scattering molecules). The last two may correspond to the second and first order reflections of an in-plane structure similar to the β_{bilayer} structure which develops with increasing film thickness. However, further work, out of the scope of this thesis, is necessary to confirm the proposed scenario.

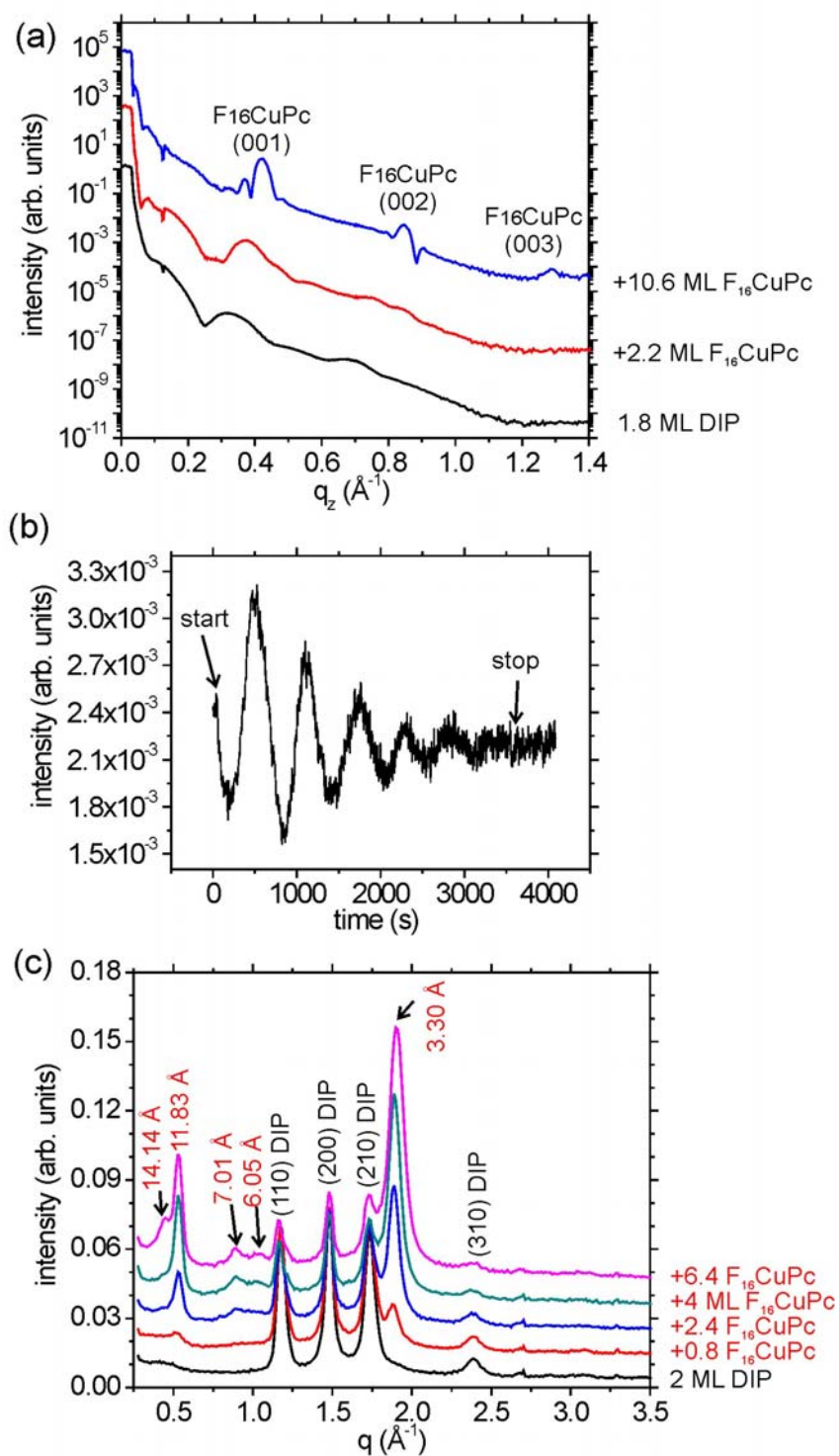


Figure 5.25. (a) Reflectivity data of 1.8 ML DIP before and after deposition of 2.2 and 10.6 ML $F_{16}CuPc$ at 120 °C. (b) Real time monitoring of the intensity at the 1/2 (001) Bragg position during deposition of 13.3 ML $F_{16}CuPc$ on 4.2 ML DIP at 150 °C and with a growth rate of 3.5 $\text{\AA}/\text{min}$. (c) GIXD data of 2 ML DIP before and after deposition of 0.8, 2.4, 4 and 6.4 ML $F_{16}CuPc$ at 120 °C.

Figure 5.26a shows a topographic contact-mode AFM image of the sample consisting in 13.3 ML $F_{16}CuPc$ deposited onto 4.2 ML DIP at 150 °C. The resulting morphology displays rather isotropic islands with heights around 20 nm (see the topographic profile in Figure 5.26b), covered by a network of elongated structures with heights around 3 to 8 nm. These elongated structures form preferentially along the step edges on top of the isotropic islands, but also along other arbitrary directions. By analogy of the resulting morphologies to previously observed morphologies formed by $F_{16}CuPc$ and DIP, we correlate the isotropic islands to DIP and the network of elongated structures to $F_{16}CuPc$. However, it has been shown that DIP grown at high temperature forms rather flat and smooth films.^{39,39,40,41} Consequently we must conclude that a dewetting process of the underlying DIP takes place upon the $F_{16}CuPc$ deposition at high temperature, leading to the spontaneous formation of islands. This is a surprising behavior, which is furthermore not reflected in the reflectivity data in Figure 5.25a. This discrepancy can be due to the difference in the growth temperature, being 150 °C for the sample measured by AFM showing the islands and 120 °C for the sample measured by reflectivity. Because 150 °C is very close to the DIP desorption temperature,^{33,34} this morphology could be the result of a complex interplay between desorption and readsorption phenomena related to the impinging of hot $F_{16}CuPc$ molecules on the DIP. In order to either obtain conclusive evidence or discard the dewetting of the underlying DIP film, further measurements are mandatory.

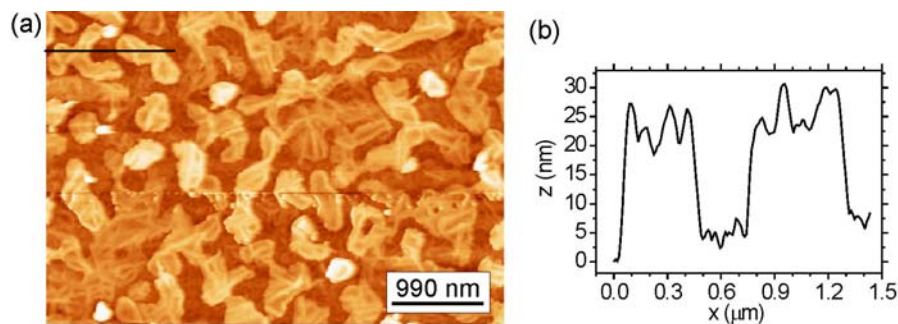


Figure 5.26. (a) AFM topographic image of a heterostructure consisting in 190 Å $F_{16}CuPc$ deposited on 70 Å DIP at 150 °C and with a growth rate of 3.5 Å/min. (b) Topographic profile taken as shown in image (a). (c) AFM topographic image of a 85 Å thick DIP film grown at 120 °C with a growth rate of 3 Å/min.

b. Low temperature (RT)

The X-ray reflectivity data for the stepwise deposition of $F_{16}CuPc$ on 3 ML DIP are shown in Figure 5.27a. For high $F_{16}CuPc$ coverages, the (001) and (002) Bragg reflections corresponding to a layer height of 14.36 Å emerge, in accordance with the formation of the β -structure. In addition, the continuous decrease in the width of the Kiessig fringes with $F_{16}CuPc$ coverage indicates its smooth growth on top of the DIP film.

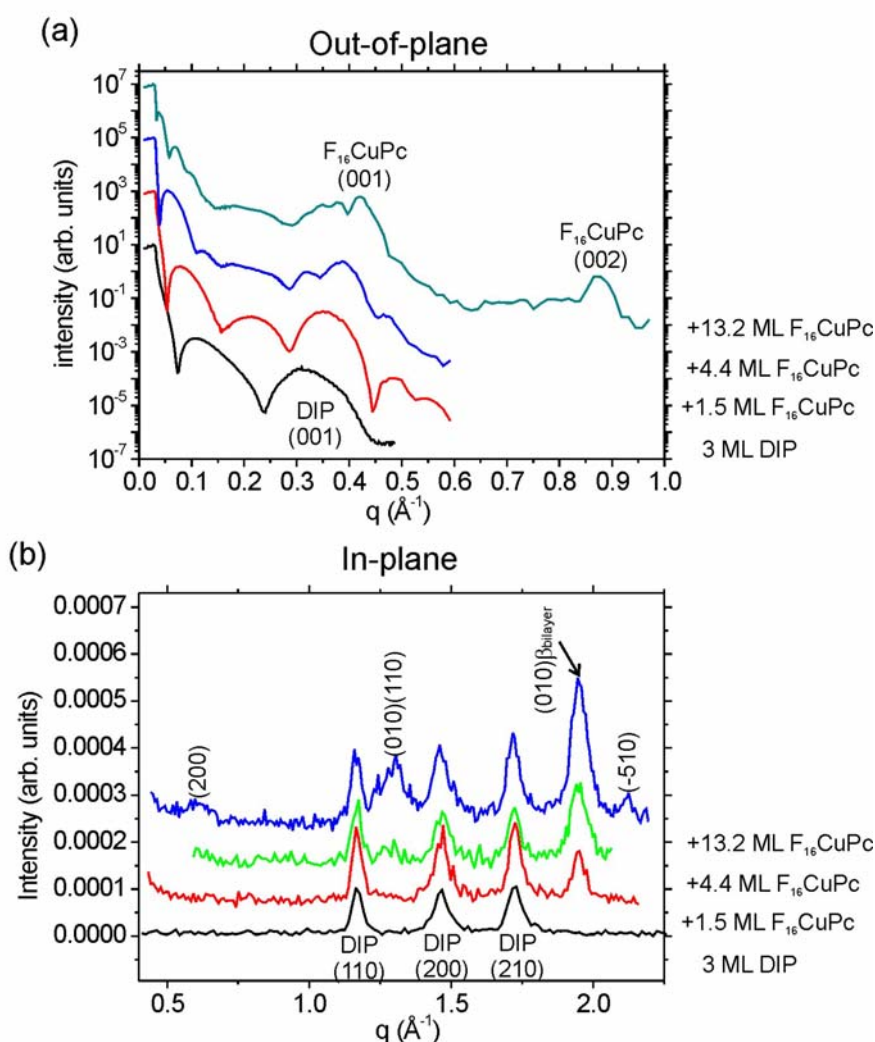


Figure 5.27. Reflectivity (a) and GIXD (b) measurements of a 51 Å thick DIP film before and after deposition of 21, 63 and 189 Å $F_{16}CuPc$ on top at room temperature. The emerging $F_{16}CuPc$ reflections are indexed according to the β_{bilayer} - (labeled accordingly) and β -structure (indexed but unlabeled).

The GIXD data corresponding to the same sample are shown in Figure 5.27b. Here, we can confirm the initial arrangement of the $F_{16}\text{CuPc}$ into the β_{bilayer} -structure, followed by the appearance of the β -structure at higher thicknesses as already observed on SiO_2 and pentacene. Thus, the reconstructed structure formed by the $F_{16}\text{CuPc}$ on DIP at high temperature is not observed at RT.

5.3.3 Conclusions

In conclusion, we demonstrate the self-organization of well-ordered DIP nanodots with high crystallinity by Stranski-Krastanov growth in organic heterostructures consisting in DIP deposited onto $F_{16}\text{CuPc}$ at high temperatures. We provide strong evidence that their growth is intimately related to a novel type of interface reconstruction of the underlying $F_{16}\text{CuPc}$ film which affects three monolayers adjacent to the organic-organic interface (with changes in the lateral lattice parameter by 14%). In contrast, the DIP wetting layer shows no apparent structural changes.

When the DIP deposition is performed at low substrate temperature, the phthalocyanine reconstruction does not take place and a smooth layered heterostructure is formed instead (Figure 5.28). The opposite deposition sequence ($F_{16}\text{CuPc}$ onto DIP) evidences similarities in the sense that the $F_{16}\text{CuPc}$ grows with the same “reconstructed” structure as when deposited at high temperature, while at low temperature the β_{bilayer} - and β -structures form, as on SiO_2 . The deposition at low as well as at high temperature leads to smooth layered heterostructures. These results evidence that the organization of the $F_{16}\text{CuPc}$ molecules into the “reconstructed” structure, either above or below the DIP, requires the overcoming of an energetic barrier. This is achieved by performing the heterostructure growth at high temperature ($\sim 120^\circ\text{C}$). However, post-deposition annealing treatments do not lead to the reconstruction of $F_{16}\text{CuPc}$. In this case the energetic barrier is higher because it involves the collective rearrangement of the whole molecular film.

The formation of the “reconstructed” $F_{16}\text{CuPc}$ structure suggests a rather strong intermolecular interaction between DIP and $F_{16}\text{CuPc}$ at the organic interface.

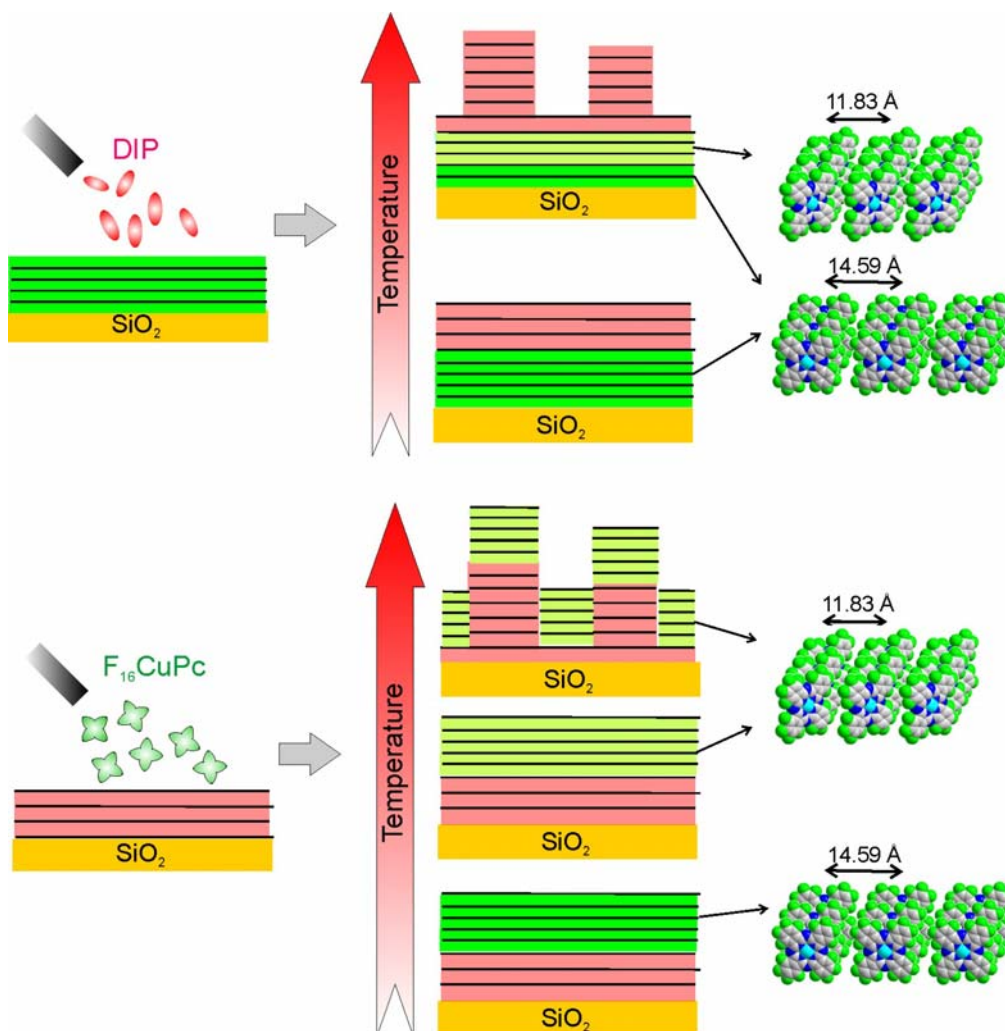


Figure 5.28. Schematic summary of the growth behavior observed in $F_{16}\text{CuPc}$ –DIP heterostructures grown in both deposition sequences.

Notice that the growth scenario differs from the growth modes in inorganic heteroepitaxy: Here, the deposition of the overlayer with a “reconstructed” structure ($F_{16}\text{CuPc}$ on DIP) does not lead to the Stranski-Krastanov growth of islands. Even more surprising, the growth of an apparently relaxed wetting layer (DIP on $F_{16}\text{CuPc}$) induces the reconstruction of the underlying film, followed by the growth of islands. These differences show that concepts like strain or epitaxy, as defined for the inorganic materials, play a completely different (and still largely unknown) role in the growth of organic materials.

Furthermore, the different growth scenarios observed for heterostructures consisting in $F_{16}\text{CuPc}$ combined either with DIP or pentacene, evidence the specificity

of the intermolecular interactions and involved processes, and thus the difficulties in the task of establishing a paradigm for the growth of organic heterostructures, which could allow at some point their tailored and controlled growth.

References

- ¹ C. D. Dimitrakopoulos, S. Purushothaman, J. Kyminis, A. Callegari, J. M. Shaw, Low-voltage organic transistors on plastic comprising high-dielectric constant gate-insulators, *Science* **283**, 822 (1999)
- ² H. E. A. Huitema, G. H. Gelinck, J. B. P. H. van der Putten, K. E. Kuijk, C. M. Hart, E. Cantatore, P. T. Herwig, A. J. J. M. van Breemen, D. M. de Leeuw, Plastic transistors in active-matrix displays, *Nature* **414**, 599 (2001)
- ³ C. D. Dimitrakopoulos, P.R.L. Malefant, Organic thin film transistors for large area electronics, *Adv. Mater.* **14**, 99 (2002)
- ⁴ P. Peumans, S. Uchida, S. R. Forrest, Efficient bulk heterojunction photovoltaic cells using small molecular-weight organic thin films, *Nature* **425**, 158 (2003)
- ⁵ C. R. Newman, C. D. Frisbie, D. A. da Silva Filho, J.-L. Brédas, P. C. Ewbank, K. R. Mann, Introduction to Organic Thin Film Transistors and design of n-channel organic semiconductors, *Chem. Mater.* **16**, 4436 (2004)
- ⁶ S. R. Forrest, The path to ubiquitous and low-cost organic electronic appliances on plastic, *Nature* **428**, 911 (2004)
- ⁷ H. Yamamoto, J. Wilkinson, J. P. Long, K. Bussman, J. A. Christodoulides, Z. H. Kafafi, Nanoscale organic light-emitting diodes, *Nano Lett.* **5**, 2485 (2005)
- ⁸ F. Yang, M. Shtein, S. R. Forrest, Controlled growth of a molecular bulk heterojunction photovoltaic cell, *Nat. Mater.* **4**, 37 (2005)
- ⁹ Y. Kim, S. Cook, S. M. Tuladhar, S. A. Choulis, J. Nelson, J. R. Durrant, D. D. C. Bradley, M. Giles, I. McCulloch, C.-S. Ha, M. Ree, A strong regioregularity effect in self-organizing conjugated polymer films and high-efficiency polythiophene: fullerene solar cells, *Nat. Mater.* **5**, 197 (2006)
- ¹⁰ F. F. So, S. R. Forrest, Y. Q. Shi, W. H. Steier, Quasi-epitaxial growth of organic multiple quantum well structures by organic molecular beam deposition, *Appl. Phys. Lett.* **56**, 674 (1990)
- ¹¹ A. Hoshino, S. Isoda, T. Kobayashi, Epitaxial growth of organic crystals on organic substrates-polynuclear aromatic hydrocarbons, *J. Cryst. Growth* **115**, 826 (1991)
- ¹² H. Akimichi, T. Inoshita, S. Hotta, H. Noge, H. Sakaki, Structure of pentacene/tetracene superlattices deposited on glass substrate, *Appl. Phys. Lett.* **63**, 3158 (1993)
- ¹³ M. L. Anderson, V.S. Williams, T.J. Schuerlein, G.E. Collins, C.D. England, L.-K. Chau, P.A. Lee, K.W. Nebesny, N.R. Armstrong, RHEED and optical characterization of ordered multilayers of phthalocyanine / perylene-tetracarboxylicdianhydride (PTCDA), *Surf. Sci.* **307–309**, 551 (1994)
- ¹⁴ T. J. Schuerlein, N. R. Armstrong, Formation and characterization of epitaxial phthalocyanine and perylene monolayers and bilayers on Cu(100): Low energy electron diffraction and thermal desorption mass spectroscopy studies, *J. Vac. Sci. Technol. A* **12**, 1992 (1994)
- ¹⁵ S. R. Forrest, P. E. Burrows, E. I. Haskal, F. F. So, Ultrahigh-vacuum quasiepitaxial growth of model Van der Waals thin films II, Experiment, *Phys. Rev. B* **49**, 11309 (1994)
- ¹⁶ S. Heutz, R. Cloots, T. S. Jones, Structural templating effects in molecular heterostructures grown by organic molecular beam deposition, *Appl. Phys. Lett.* **77**, 3938 (2000)

- ¹⁷ F. Sellam, T. Schmitz-Hübsch, M. Toerker, S. Mannsfeld, H. Proehl, T. Fritz, K. Leo, C. Simpson, K. Müllen, LEED and STM investigations of organic-organic heterostructures grown by molecular beam epitaxy, *Surf. Sci.* **478**, 113 (2001)
- ¹⁸ S. Heutz, T. S. Jones, Structural and morphological modifications in double layer heterostructures containing H₂Pc, perylene-3, 4, 9, 10-tetracarboxylic dianhydride and Alq₃, *J. Appl. Phys.* **92**, 3039 (2002)
- ¹⁹ S. Yim, S. Heutz, T. S. Jones, Influence of intermolecular interaction on the structure of phthalocyanine layers in molecular thin film heterostructures, *Phys. Rev. B* **67**, 165308 (2003)
- ²⁰ G. Koller, S. Berkebile, J. R. Krenn, F. P. Netzer, M. Oehzelt, T. Haber, R. Resel, M. G. Ramsey, Heteroepitaxy of organic-organic nanostructures, *Nano Lett.* **6**, 1207 (2006)
- ²¹ R. Ruiz, A. C. Mayer, G. G. Malliaras, B. Nickel, G. Scoles, A. Kazimirov, H. Kim, R. L. Headrick, Z. Islam, Structure of pentacene thin films, *Appl. Phys. Lett.* **85**, 4926 (2004)
- ²² A. C. Dürr, B. Nickel, V. Sharma, U. Täffner, H. Dosch, Observation of competing modes in the growth of diindenoperylene on SiO₂, *Thin Solid Films* **503**, 127 (2006)
- ²³ R. Ruiz, D. Choudhary, B. Nickel, T. Toccoli, K.-C. Chang, A. C. Mayer, P. Clancy, J. M. Blakely, R. L. Headrick, S. Iannotta, G. G. Malliaras, Pentacene thin film growth, *Chem. Mater.* **16**, 4497 (2004)
- ²⁴ C. C. Mattheus, A. B. Dros, J. Baas, G. T. Oostergetel, A. Meetsma, J. L. de Boer, T. T.M. Palstra, Identification of polymorphs of pentacene, *Synth. Met.* **138**, 475 (2003)
- ²⁵ R. Garcia, R. Perez, Dynamic atomic force microscopy methods, *Surf. Sci. Rep.* **47**, 197 (2002)
- ²⁶ J. E. Northrup, M. L. Tiago, S. G. Louie, Surface energetics and growth of pentacene, *Phys. Rev. B* **66**, 121404 (2002)
- ²⁷ D. G. de Oteyza, E. Barrena, J. O. Ossó, H. Dosch, S. Meyer, J. Pflaum, Controlled enhancement of the charge carrier mobility in F₁₆CuPc thin film transistors by the use of functionalized SiO₂ surfaces, *Appl. Phys. Lett.* **87**, 183504 (2005)
- ²⁸ J. O. Ossó, F. Schreiber, M. I. Alonso, M. Garriga, E. Barrena, H. Dosch, Structure, morphology and optical properties of thin films of F₁₆CuPc grown on silicon oxide, *Org. Electron.* **5**, 135 (2004)
- ²⁹ E. Barrena, J. O. Ossó, F. Schreiber, M. Garriga, M. I. Alonso, H. Dosch, Self organization of phthalocyanines on Al₂O₃ (11-20) in aligned and ordered films, *J. Mater. Res.* **19**, 2061 (2004)
- ³⁰ J. O. Ossó, F. Schreiber, V. Kruppa, H. Dosch, M. Garriga, M. I. Alonso, F. Cerdeira, Controlled molecular alignment in phthalocyanine thin films on stepped sapphire surfaces, *Adv. Func. Mater.* **12**, 455 (2004)
- ³¹ Y. Oh, S. Pyo, M. H. Yi, S.-K. Kwon, N-type organic field-effect transistor using polymeric blend gate insulator with controlled surface properties, *Org. Electron.* **7**, 72 (2006)
- ³² R. Seemann, S. Herminghaus, K. Jacobs, Dewetting patterns and molecular forces: a reconciliation, *Phys. Rev. Lett.* **86**, 5534 (2001)
- ³³ S. Sellner, A. Gerlach, F. Schreiber, M. Kelsch, N. Kasper, H. Dosch, S. Meyer, J. Pflaum, M. Fischer, B. Gompf, Strongly Enhanced Thermal Stability of Crystalline Organic Semiconductor Thin Films Induced by Aluminum Oxide Capping Layers, *Adv. Mater.* **16**, 1750 (2004)
- ³⁴ S. Sellner, A. Gerlach, F. Schreiber, M. Kelsch, N. Kasper, H. Dosch, S. Meyer, J. Pflaum, M. Fischer, B. Gompf, G. Ulbricht, Mechanisms for the Enhancement of the Thermal Stability of Organic Thin Films by Aluminum Oxide Capping Layers, *J. Mater. Res.* **21**, 455 (2006)
- ³⁵ J. Pflaum et al., to be published.
- ³⁶ A. C. Dürr, F. Schreiber, M. Münch, N. Karl, B. Krause, V. Kruppa, H. Dosch, High structural order in thin films of the organic semiconductor diindenoperylene, *Appl. Phys. Lett.* **81**, 2276 (2002)
- ³⁷ R. Nötzel, Self-organized growth of quantum dot structures, *Semicond. Sci. Tech.* **11**, 1365 (2003)
- ³⁸ A. C. Dürr, N. Koch, M. Kelsch, A. Rühm, J. Ghijsen, R. L. Johnson, J.-J. Pireaux, J. Schwartz, F. Schreiber, H. Dosch, A. Kahn, Interplay between morphology, structure and electronic properties at diindenoperylene-gold interfaces, *Phys. Rev. B* **68**, 115428 (2003)

³⁹ S. Kowarik, A. Gerlach, S. Sellner, F. Schreiber, L. Cavalcanti, O. Konovalov, Real-time observation of structural and orientational transitions during growth of organic thin films, *Phys. Rev. Lett.* **96**, 125504 (2006)

⁴⁰ X. Zhang et al., to be published.

⁴¹ A. C. Dürr, F. Schreiber, K. A. Ritley, V. Kruppa, J. Krug, H. Dosch, B. Struth, Rapid roughening in thin film growth of an organic semiconductor (Diindenoperylene), *Phys. Rev. Lett.* **90**, 016104 (2003)

6 Self-assembly of mixed two-dimensional supramolecular structures

The striking behavior observed for the $F_{16}\text{CuPc}/\text{DIP}$ heterostructures grown at high temperature point to strong intermolecular interactions between these two molecules. Their study in a combined system of reduced dimensionality is expected to facilitate the understanding of the nature of the interactions. Therefore, their growth has been studied by STM in a two dimensional system varying the relative molecular ratios. The substrate chosen for this study has been a single crystalline metal surface. $\text{Cu}(111)$ is suitable for this aim, and it is additionally interesting, because Cu is among the most widely used metals in the contacts of electronic devices. Therefore, it represents the third kind of interfaces present in organic devices, the organic-metal (contact) interface.

Furthermore, the desired break-through in the miniaturization processes of the microelectronics industry, envisioned as a revolution of the nanotechnology, requires the development of new “bottom-up” approaches based on self-assembly of hierarchical structures.^{1,2,3} Organic molecules are amongst the most promising materials as building blocks for new functional nanomaterials. Self-assembly of multiple kinds of nanostructures has been shown, ranging from clusters,^{4,5} to molecular chains,^{5,6} highly ordered layers^{7,8,9,10,11,12} or two dimensional networks.^{13,14,15,16} However, a thorough control over the self-assembly of supramolecular structures is still missing, thus motivating further studies on self-assembling systems.

6.1 *Experimental details*

All STM measurements have been performed in constant current mode with a commercial JEOL system (described in the experimental section). The samples have been grown at room temperature with a very low molecular flux (growth rate of ~ 0.1 ML/min.). The resulting structures are thus expected to be in thermodynamic equilibrium rather than being kinetically induced metastable structures. For the

samples with mixed molecular species, the growth was performed alternating the substrate exposure to the DIP and $F_{16}\text{CuPc}$ molecular beams, adjusting the exposure time according to the desired molecular ratio. Typical periods varied between 10 and 30 seconds.

The Cu substrate was cleaned as reported in section 3.3.4. Cu presents a face centered cubic (fcc) crystal structure. Consequently, the (111) facet, which corresponds to the lowest energy plane, shows a hexagonal symmetry. This is displayed in Figure 6.1. The nearest-neighbor directions (called in the following NN) correspond to the $[\bar{1}10]$ and related crystallographic directions, while the next-nearest-neighbor directions (called in the following NNN) correspond to the $[\bar{1}12]$ and related directions. Cu has a lattice parameter of 361.49 pm, which implies a NN distance of 2.5561 Å. This is much smaller than the molecular dimensions of DIP or $F_{16}\text{CuPc}$. Thus, the substrate potential, as “felt” by the molecules, is sort of a laterally averaged potential over the molecular size.

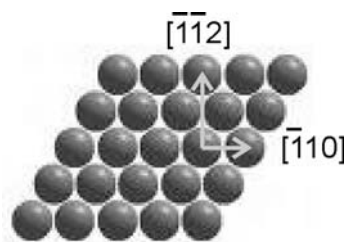


Figure 6.1. Schematic picture of the atom arrangement in the (111) plane.

6.2 Deposition of pure DIP

As expected, DIP molecules adsorb lying down on the Cu(111) surface and appear with an ellipsoid shape. The nucleation begins at the Cu step edges. The formation of stable DIP clusters start on the terraces only when the step edges are completely covered. This pinning effect of the steps is common and has been previously reported for other organic systems.^{17,18,19,20,21} No single molecules are observed apart from steps or defects, implying a high molecular surface mobility on the terraces at RT.

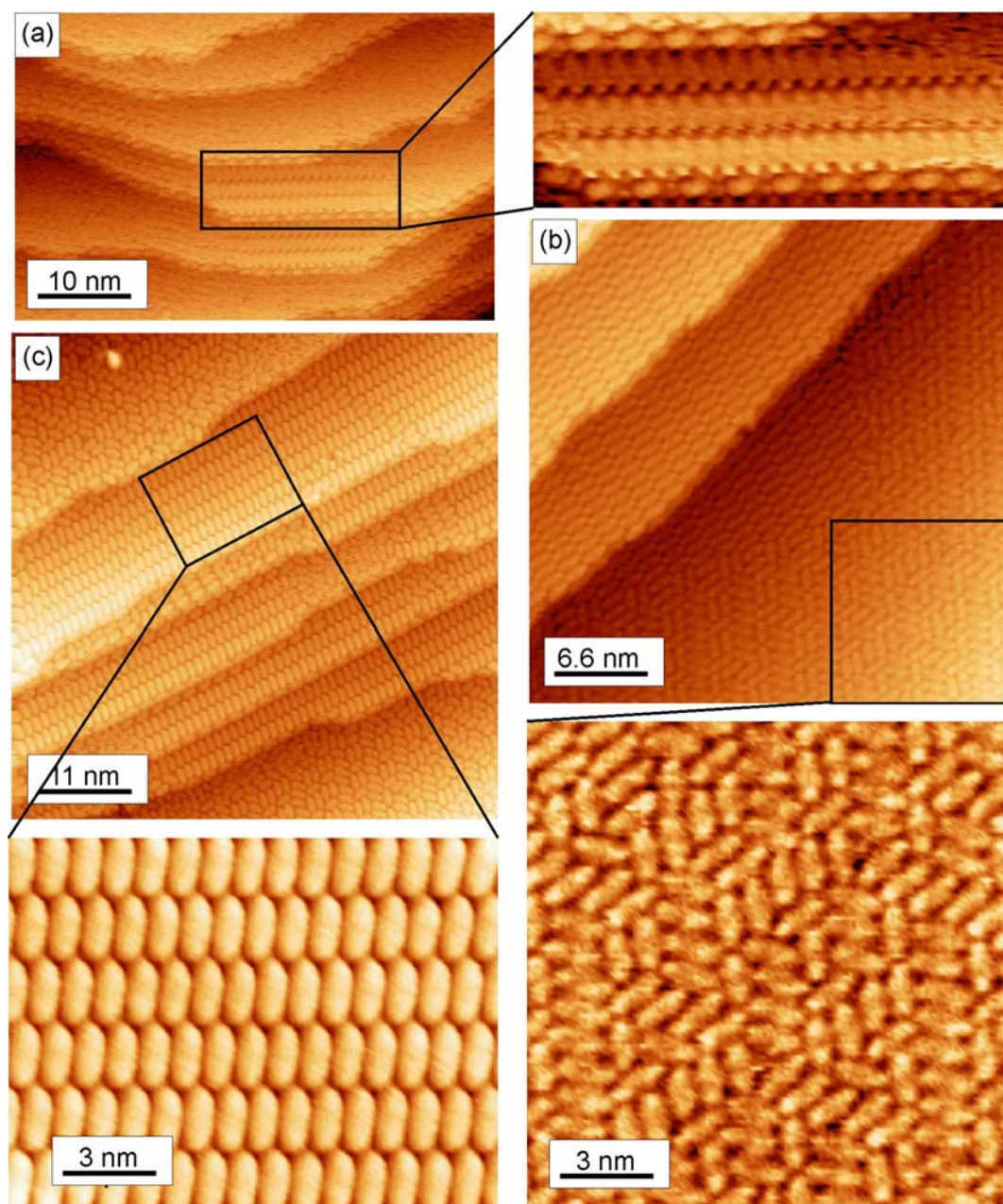


Figure 6.2. STM images corresponding to DIP coverages of about (a) 0.05 ML (0.244 nA, 0.448 V), and (b) 0.95 ML (0.225 nA, 0.339 V) and (c) 0.95 ML (0.254 nA, 0.326 V). The lower images correspond to zooms (marked areas), representing the short-range (b) and long-range (a and c) ordered structures.

Figure 6.2a shows an STM image of a sample in the first growth stages, displaying the described scenario. In addition to the DIP molecules at the steps, which align their long molecular axis parallel to the step direction, the nucleation of ordered molecular arrays (consisting in columns of molecules stacked side by side) is already visible on the terraces in the central part of the image (zoom). Upon further deposition up to 0.95

ML (Figure 6.2b and c), the majority of the terraces are covered by the DIP, with the molecules showing different assembling behaviors depending on the terrace size. On larger terraces (lower part in Figure 6.2b) the molecules arrange into an apparently short-range ordered structure. The long axis of the DIP molecules is directed only along discrete directions, which evidently must be related with the hexagonal symmetry of the Cu(111) surface. Six different molecular orientations are observed (two sets of three directions related by 60 degrees). On smaller terraces (central part in Figure 6.2b), DIP forms long-range ordered structures as described above, with the molecules stacked side by side in columns.^a The molecular orientations in these ordered arrays coincide with the directions observed in the short-range ordered structure on the larger terraces. In some areas, irregular streaks related to random tip excursions of single molecular height are visible, characteristic of mobile molecules in a two-dimensional gas phase which diffuse faster than the imaging process.¹⁷

6.2.1 Short-range ordered structure

a. General observations

We now take a closer look at the structure observed on large terraces. Figure 6.3a shows the molecular arrangement in an area of $26 \times 26 \text{ nm}^2$. At a first glance, the structure appears short-range ordered, with DIP molecules aligned along three directions related by 60 degrees. The DIP shows a preferential side by side stacking which gives rise to columnar stacks of parallel oriented molecules, as marked e.g. by the parallelogram in Figure 6.3a. Along these columns, the molecules are packed in groups of two or three (as marked e.g. by the dotted lines), which are slightly shifted with respect to each other along the direction of the long molecular axis. The columnar stacks are always delimited by molecules following any of the other two directions, thus avoiding adjoining columns.

^a An approximate upper limit for the lateral width of the terraces inducing this structure is 15 nm. However, also the short-range ordered structure forms sometimes on smaller terraces. Similarly, the long-range ordered structure forms sometimes on large terraces, though not extending further than $\sim 15 \text{ nm}$ perpendicular to the step edge.

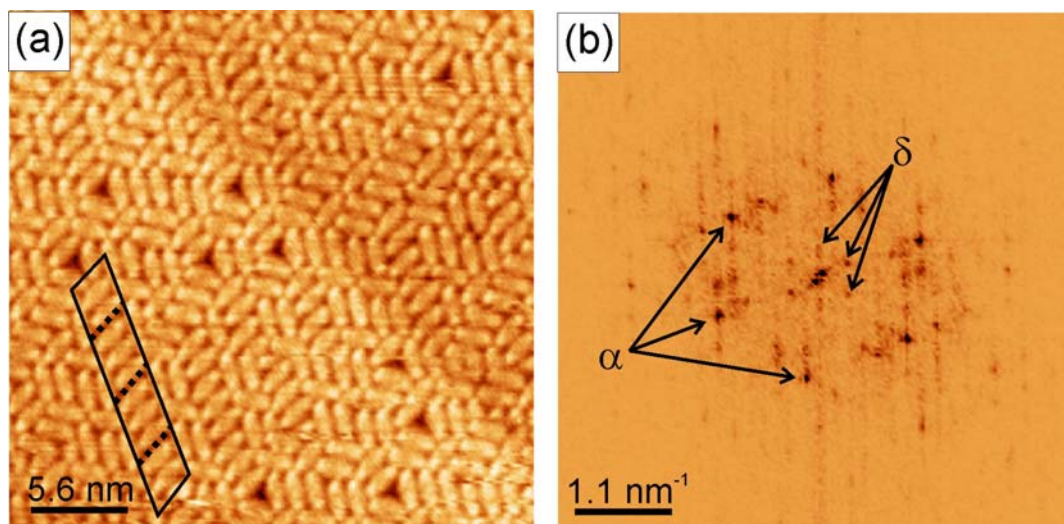


Figure 6.3. (a) STM image (0.124 nA, 0.674 V) displaying the short-range ordered structure observed on the large terraces. The parallelogram shows, by way of example, one of the molecular columns formed by the preferential side-by-side stacking of the molecules. The dotted lines separate different molecular groups within the column which are shifted with respect to each other. (b) FFT image revealing the peaks corresponding to the molecular side-by-side stacking (labeled with α) and to the lateral correlation between the molecular columns (labeled with δ).

The molecular stacking order is reflected as a hexagonal pattern in the Fast Fourier Transform image (FFT, Figure 6.3b). The main peaks (labeled with α) correspond to the spacing between molecules in the side-by-side stacking, namely of $7.8 \pm 0.6 \text{ \AA}$, along the three different directions. In addition, there is a characteristic correlation length of $24.6 \pm 2 \text{ \AA}$ giving rise to the peaks labeled with δ . This spacing is related to the lateral distance between molecular columns. Further evidence of the lateral correlations in this short-range ordered structure can be observed when looking at the distribution of the point-defect vacancies. These vacancies are limited by three DIP molecules separated by 60° angles defining a triangle. Notice that all vacancy triangles on top of the same terrace point in the same direction. The discrete molecular orientations can not account for this effect, since the molecules forming a triangle which points in the opposite direction would have the same orientations. It thus seems to be related to an optimized molecular packing which would be hindered by triangles in both directions. Figure 6.4 shows two different terraces. On the upper and lower terrace, the triangles are pointing in virtually opposite directions (representative triangles are included in the zooms of each of the terraces). A FFT performed on this image reveals the presence of two similar domains (called α_1 and α_2) rotated by $15 \pm 2^\circ$. From filtered inverse Fourier transformations we unambiguously observe that each of

the domains is limited to one terrace. Taking a closer look at the molecular orientations in each of the domains, we actually observe that these are different, being rotated by $\sim 15^\circ$ and thus in accordance with the FFT image.

In summary, DIP molecules deposited on large Cu(111) terraces lie-down and form a short-range ordered structure. The molecules arrange preferentially in a side-by-side packing which gives rise to characteristic correlation lengths. Six different molecular orientations are observed on the Cu(111) surface, though only three of them, related by 60° , coexist on each terrace. Both sets of orientations are rotated with respect to each other by 15° .

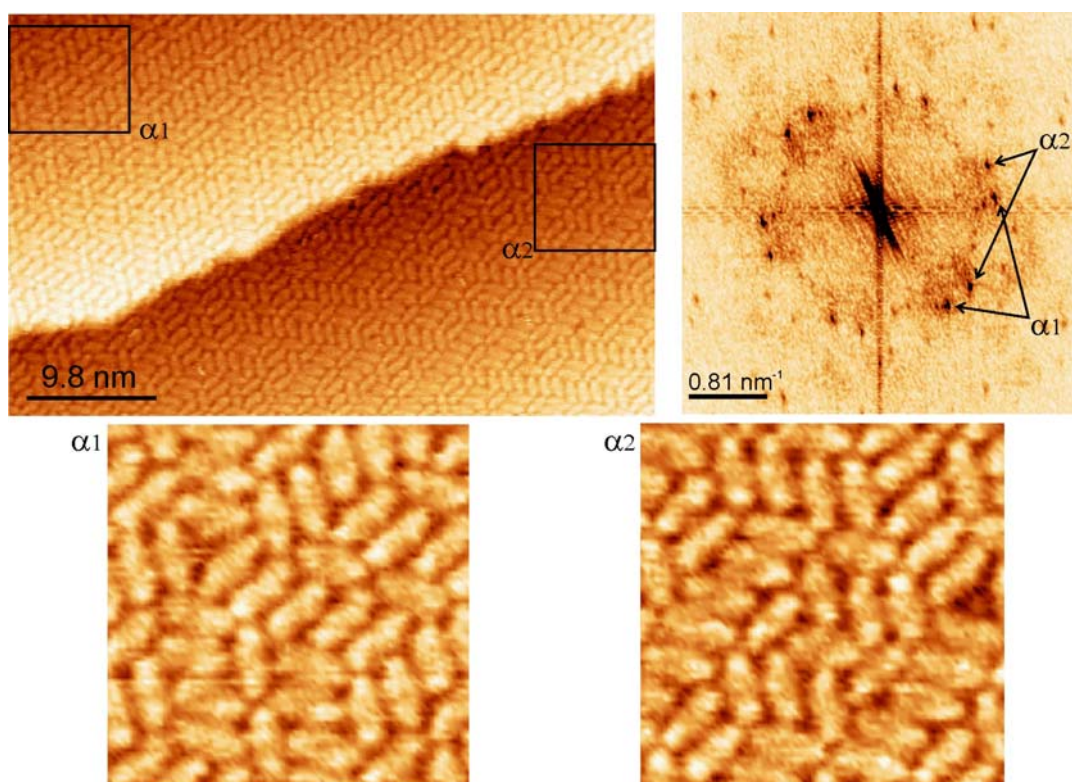


Figure 6.4. STM image (0.225 nA, 0.339 V) of two terraces covered by a complete DIP monolayer (left) and the corresponding FFT image revealing the presence of two different domains labeled as α_1 and α_2 . Below, zooms into each of the domains show the virtually opposite orientation of the “vacancy triangles”.

b. Attempt to determine the epitaxial relation with the Cu(111) surface structure

The discrete orientations followed by the DIP molecules imply an epitaxial relation with the substrate. Given that we did not obtain atomic resolution images on the Cu(111) surface, two different approaches have been tried to determine the substrate orientation. (i) The orientation of the Cu crystal has been determined ex-situ by X-ray diffraction. The crystal has then been introduced in the UHV equipment. The error in the orientation arises from possible deviations mounting the sample on the sample holder (estimated to be about ± 5 degrees). (ii) The step edges separating different Cu(111) terraces align preferentially along the compact NN directions for energetic reasons. This can be used to determine the substrate orientation from images in well-ordered faceted regions. However, comparing various images, we observe six different directions related by 30° rotations which must correspond to the NN and NNN directions (see Figure 6.5). Because a higher amount of steps is observed aligned along the direction shown in Figure 6.5a (and those related by 60° rotations), we ascribe it to the NN direction. The orientation obtained from the X-ray data supports this conclusion. Three of the observed molecular directions appear deviated ~ 7 degrees from the NN directions, while the other three are deviated ~ 22 degrees (i.e., 8 degrees with respect to the NNN directions), as shown schematically in Figure 6.6a.

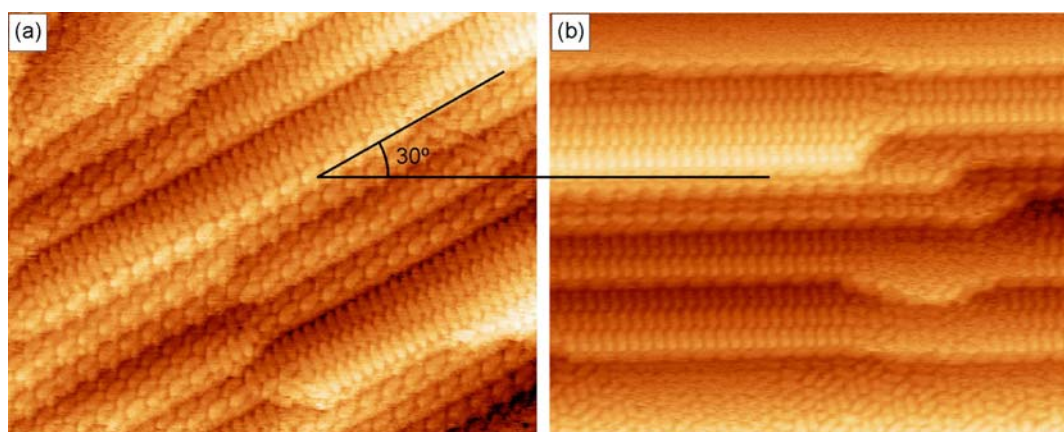


Figure 6.5. Images evidencing two of the preferred directions along which the steps align, related by 30° .

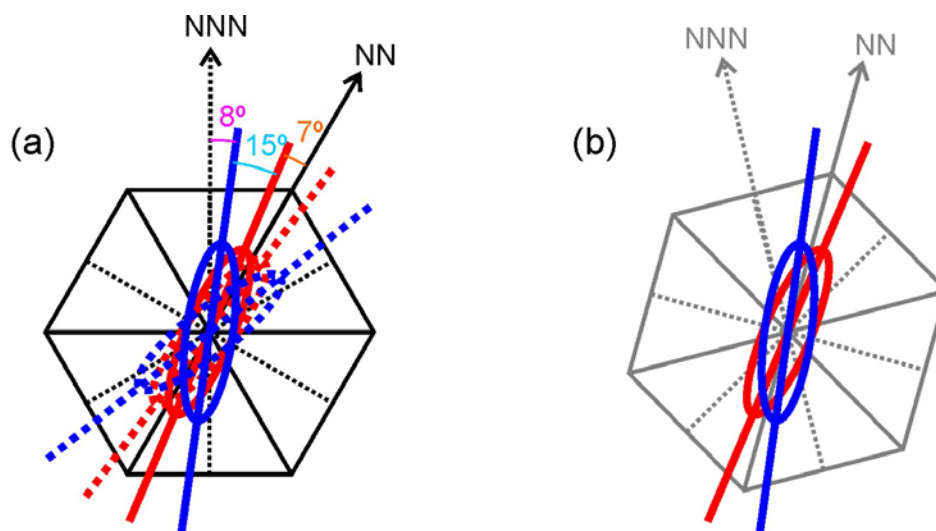


Figure 6.6. (a) Schematic representation of the substrate surface structure, showing the NN (full lines) and NNN (dotted lines) directions. The observed molecular orientations, in relation with the substrate structure, are shown with the full lines. The molecular orientations expected for symmetry reasons are shown with the dotted lines. The missing directions corresponding to 60° rotations are omitted for clarity. (b) Orientation scenario supposing the substrate surface structure to be deviated by 15° from our estimation.

Given the mirror symmetry along the NN directions, the presence of six additional molecular orientations is expected for symmetry reasons (dashed molecules in Figure 6.6a). However, these are not observed in neither of all measured images. There are two possible explanations for these puzzling observations. (i) Because of the local nature of the STM measurements, the missing molecular orientations might be present on the sample but not have been probed. This possibility, however, would be very surprising, given the large number of measurements on different spots of the sample. (ii) The substrate orientation is deviated by ~ 15 degrees from our estimation. Under these circumstances, three of the molecular orientations would be related by a mirror plane with the other three (as shown schematically in Figure 6.6b), giving a coherent picture. Nevertheless, this possibility would be similarly surprising, since 15 degrees is far above the possible error estimated for our orientation methods. The actual explanation thus remains unclear, and further measurements with more sensitive techniques such as e.g. LEED are necessary to determine accurately the DIP orientations and their epitaxial relation with the substrate.

6.2.2 Long-range ordered structure

The ordered molecular arrays on the smaller terraces are formed by molecules (which follow the same crystallographic directions as those on the larger terraces) stacked side-by-side. In contrast to the molecular columns observed in the short-range ordered structure on the large terraces, there is no formation of shifted molecular groups within the stacks in this structure. The structure is given by an oblique unit cell (as shown in Figure 6.7) with parameters $a=8.6\pm0.5$ Å, $b=16.9\pm1.4$ Å and $\gamma=71\pm3^\circ$. Its low symmetry also leads to the formation of twin domains. Because this structure forms on smaller terraces it is highly influenced by the step edges. It is observed that the formation of different domains depends on the delimiting steps. An example is given in Figure 6.7, which shows two domains growing in regions influenced by steps with different directions. A change in the step direction of only $\sim 10^\circ$ leads to the formation of two twin domains (labeled A and B) additionally rotated 60° .

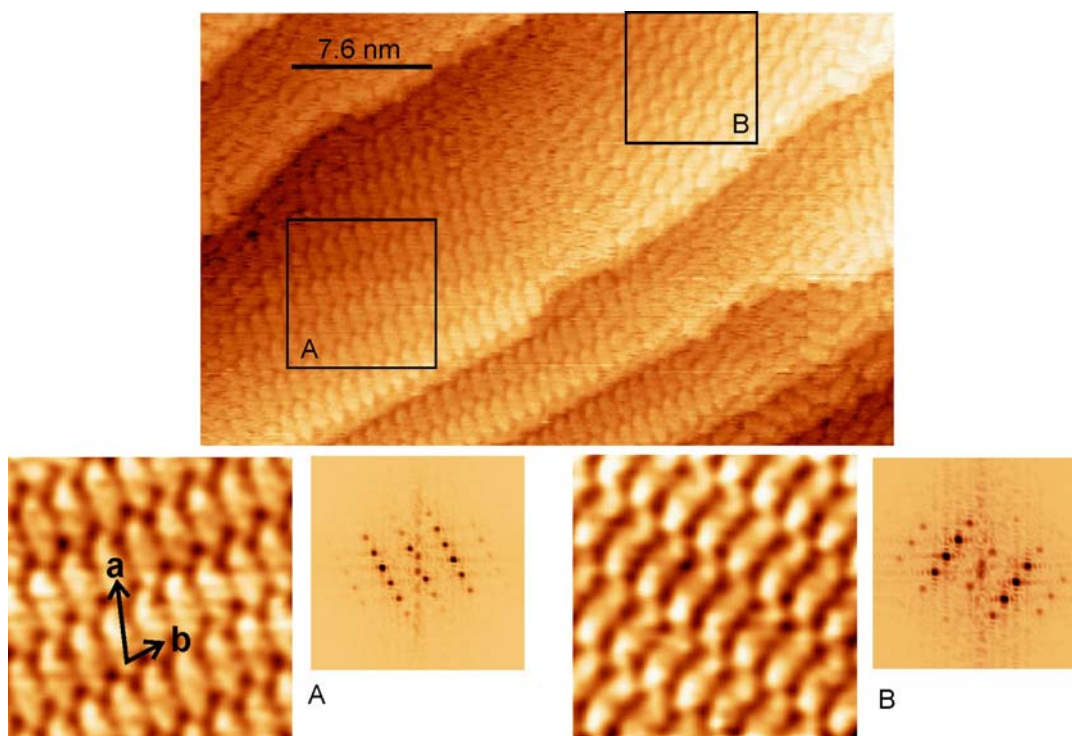


Figure 6.7. STM image (0.254 nA, 0.292 V) and the corresponding FFT images, displaying different domains of the ordered DIP on small terraces. The zooms show two different twin-domains additionally rotated by 60° (and the corresponding FFT images). The unit cell is shown in the zoom A.

6.3 Deposition of pure $F_{16}\text{CuPc}$ ^a

Similarly to the DIP, the $F_{16}\text{CuPc}$ also starts its nucleation at the Cu step edges before growing on the terraces, as can be discerned from Figure 6.8a. High resolution images of the molecules at the steps reveal a preferred alignment of the molecular diagonal along the step direction, with the molecule lying mainly on the lower terrace, though having at least one of the four aromatic rings on the upper terrace (Figure 6.8b). The absence of single molecules on the terraces implies a high $F_{16}\text{CuPc}$ surface mobility at RT, as previously observed in the case of DIP. However, upon further deposition, the molecules on the terraces nucleate and form an ordered structure different from that observed at the steps, namely with an oblique unit-cell with parameters $a=14.5$ Å, $b=14.5$ Å and $\gamma=75^\circ$.²² Once again, the low symmetry of the structure leads to the formation of twin domains (Figure 6.9a).

The molecules are lying flat on the surface, though previous studies have shown the $F_{16}\text{CuPc}$ on Cu(111) to be distorted, with the C-F bonds forming an angle of 11.5° with respect to the surface plane.²³ The molecular arrangement is shown in Figure 6.9a, in which the unit cell of both twin structures is also displayed.

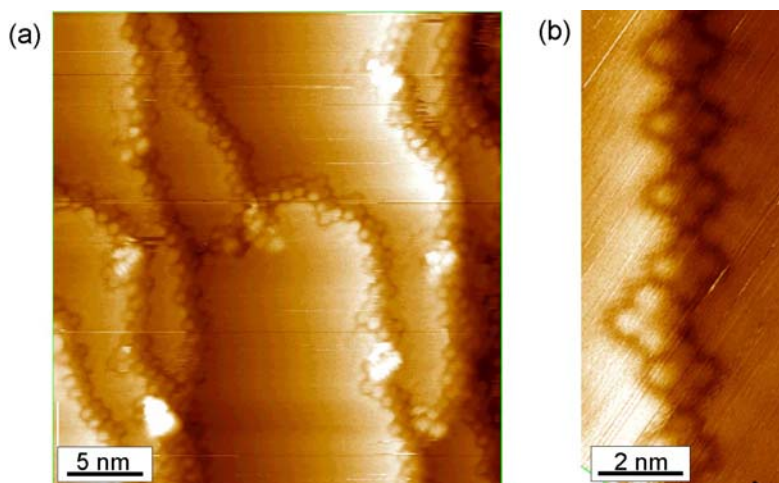


Figure 6.8 STM images displaying the initial nucleation behavior of $F_{16}\text{CuPc}$ at the steps of the Cu(111) surface.

^a Measurements performed by Y. Wakayama, from the National Institute for Materials Science in Tsukuba, Japan, in the frame of a collaboration.

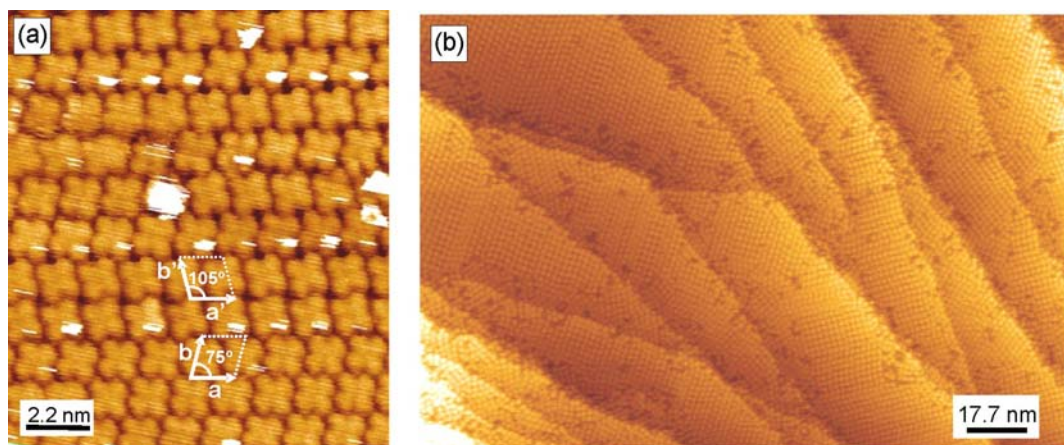


Figure 6.9. (a) STM image displaying the $F_{16}\text{CuPc}$ film structure and the presence of twin domains with their corresponding unit cells. (b) Large scale image revealing the highly defective monolayer with multiple rotational domains, twin domains and vacancies.

It is only along one direction that long range order takes place, because along the perpendicular direction the frequent switching between different twin domains limits the range of order to few repetitions. Figure 6.9b shows a larger scale image of a monolayer, revealing the highly defective structure due to the presence of the numerous rotational domains, twin domains and vacancies. It is interesting to note that the long range order direction (along the unit cell vector “a”, as shown in Figure 6.9) follows mainly three orientations related by 60° rotations, though also few domains oriented along the bisecting lines (i.e. related by 30° rotations) are observed. The alignment of the order direction apparently coincides with the main crystallographic directions, NN and NNN.

6.4 *Binary molecular layers of DIP and $F_{16}\text{CuPc}$*

The high surface mobility observed for both kinds of molecules at RT is expected to favor the intermixing of the molecules upon alternated substrate exposure to each of the molecular beams with periods of 10-30 seconds, thus resulting comparable to a codeposition experiment. The codeposition of different molecular species on substrates has been shown to lead, for certain molecular combinations and under the proper conditions of the molecular ratios, to well ordered binary structures.^{7,8,9,10,13,15}

However, demixing and formation of disordered mixed layers has also been reported.^{7,24}

6.4.1 DIP to F₁₆CuPc ratio 1 : 1

Upon codeposition of DIP and F₁₆CuPc in a 1 : 1 ratio, a highly ordered, hexagonal structure with a lattice parameter of 21.5 ± 1.5 Å and one F₁₆CuPc and one DIP molecule per unit cell forms. The different molecules can be unambiguously distinguished. The DIP-F₁₆CuPc interactions make the structure very stable, thus allowing its STM imaging with excellent submolecular resolution even at RT. F₁₆CuPc shows its characteristic shape with a four fold symmetry, and the elongated DIP shape is also clearly observed. The structure is shown in Figure 6.10, in which also the unit cell vectors are plotted. It is worth to mention that F₁₆CuPc appears brighter than DIP under any of the used measurement conditions, which range from 0.03 to 0.25 nA and from 0.25 to 1.5 V under both potential polarizations. The corresponding FFT image evidences a long-range ordered hexagonal structure. In spite of the six fold symmetry of the unit cell, the base (formed by one F₁₆CuPc and one DIP molecule) lowers the whole structure symmetry to be only two fold.

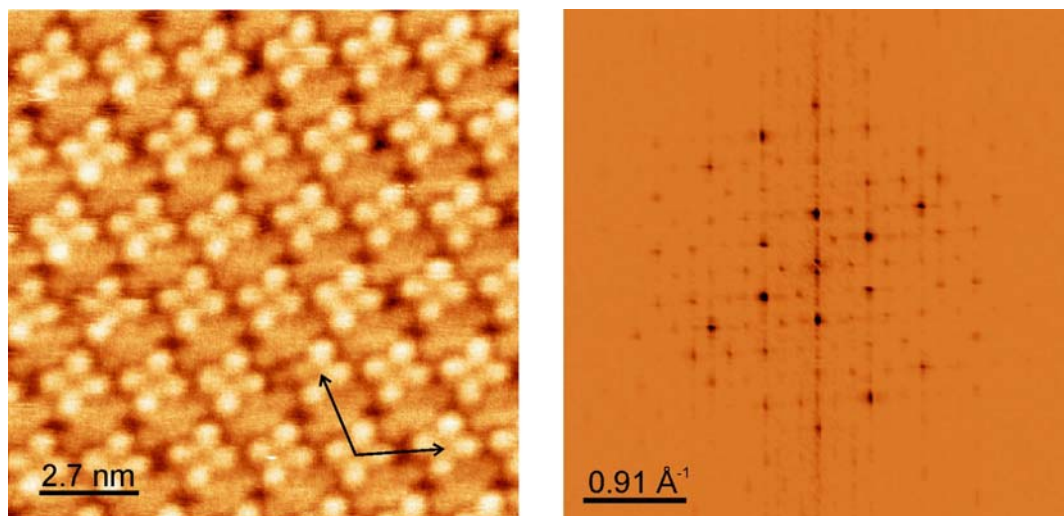


Figure 6.10. STM image (0.245 nA, -1.417 V) displaying the ordered structure (and the corresponding FFT image) formed by the mixed layers in a 1:1 ratio. The unit cell vectors are plotted on the real space image. The F₁₆CuPc (brighter) and the DIP (darker) can be unambiguously distinguished.

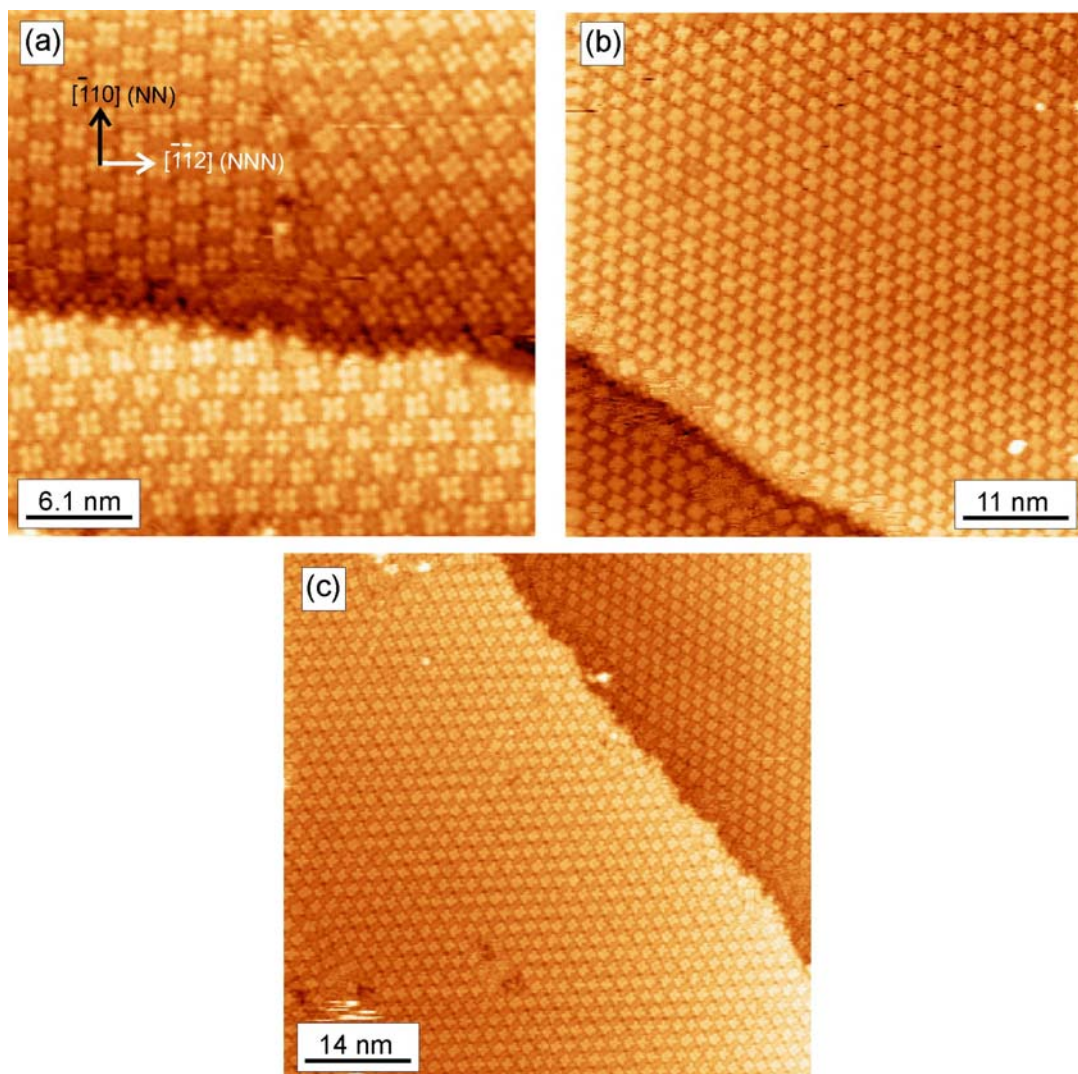


Figure 6.11. STM images (a and c: 0.245 nA, -0.265 V; b: 0.21 nA, 0.965 V) displaying different rotational domains, related by 30° or multiples thereof.

Figure 6.11 shows larger images displaying different rotational domains. Six different rotational domains related by 30 degrees are observed in the sample. The lattice vectors are aligned with the main crystallographic directions NN and NNN (within an error margin of roughly $\pm 3^\circ$, see Figure 6.11a). The $F_{16}CuPc$ molecules at the steps maintain their tendency of aligning their molecular diagonal with the step, and thus lead to locally disordered regions in the step vicinity (Figure 6.11). At defect sites such as domain boundaries, vacancies or the step vicinity, random tip excursions of molecular height are again observed related to diffusing molecules (Figure 6.11), evidencing their high surface mobility. Hence, the DIP- $F_{16}CuPc$ intermolecular

interactions lead to the formation of large mixed domains which extend to sizes above 100 nm, without segregation of pure F₁₆CuPc or DIP.

6.4.2 DIP to F₁₆CuPc ratio 2 : 1

The codeposition of DIP and F₁₆CuPc in a 2 : 1 ratio leads to the formation of a different, also highly ordered structure (Figure 6.12). F₁₆CuPc molecules are positioned in a quasi-hexagonal structure with two non-equivalent F₁₆CuPc orientations (the two directions differ by $\sim 20^\circ$). The different F₁₆CuPc orientations are evidently accompanied by changes in the surrounding DIP arrangement (also two different DIP directions related by $\sim 50^\circ$ rotations are observed), consequently leading to a larger and more complex unit cell formed by two F₁₆CuPc and four DIP molecules. The unit cell parameters are $a=20.5\pm 1.5$ Å, $b=42.2\pm 1.5$ Å, $\gamma=90\pm 3^\circ$, and the vectors are displayed in Figure 6.12. Similarly as for the 1 : 1 ratio, the structure is very stable and allows the imaging with excellent submolecular resolution even at RT. The FFT image is shown in the right part of Figure 6.12. The strongest reflections arise from the quasi-hexagonal F₁₆CuPc positioning. Along the direction of b^* (in reciprocal space), peaks with half of the previous periodicity are observed, related to the larger (double) spacing of the real unit cell in this direction.

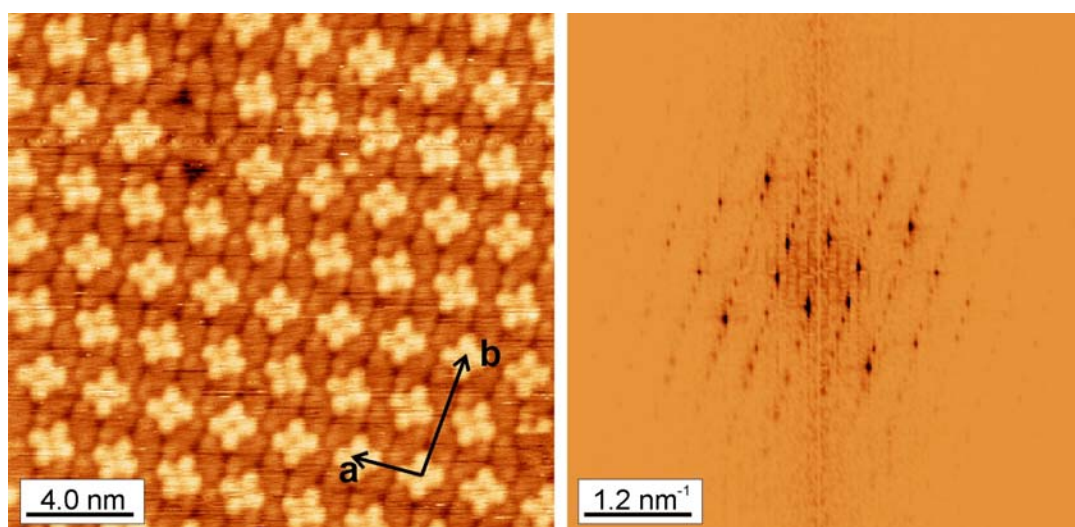


Figure 6.12. STM image (0.21 nA, 0.965 V) and the corresponding FFT image, displaying the ordered structure of a 2:1 DIP-F₁₆CuPc mixed layer.

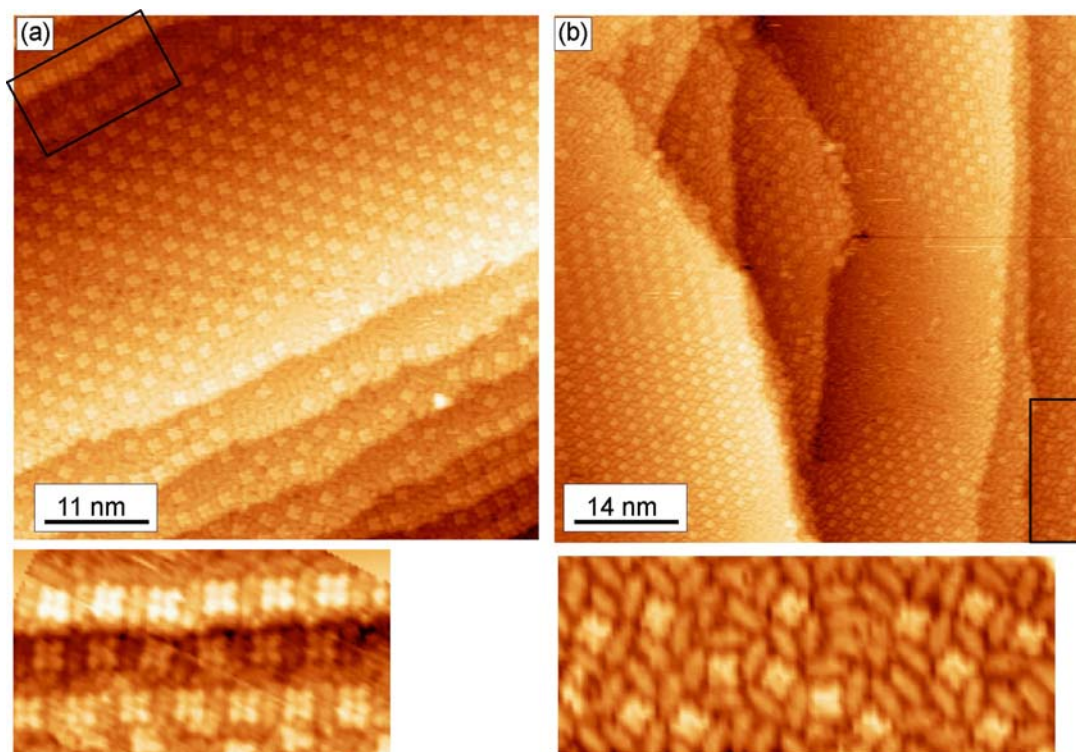


Figure 6.13. STM images (a: 0.14 nA, 0.59 V; b: 0.19 nA, 0.41 V) revealing the presence of rotational domains and the influence of the steps on the resulting structure. The zoom in image b shows the disorder in the regions with excess of DIP.

Three rotational domains related by 60° have been observed for this structure. Two of them are present in Figure 6.13b, in which the ordered structures in the upper and lower part of the images correspond to two different domains. Figure 6.13 shows larger scale images of a sample with a coverage of about 0.7 ML, in which the actual amount of DIP exceeds the planned molecular ratio of 2 : 1. The resulting scenario is the growth of the 2 : 1 structure with some $F_{16}\text{CuPc}$ vacancies (as observed also in Figure 6.12), and the growth of a disordered mixed structure in those areas with a larger amount of DIP (e.g. zoom in Figure 6.13b). The absence of order in these regions suggests that no stable ordered mixed phase exists with a 3 : 1 molecular ratio.

Furthermore, an additional, different, ordered structure is formed in the vicinity of the steps. It consists in $F_{16}\text{CuPc}$ molecules with their lateral side parallel to the steps and surrounded by four DIP molecules positioned parallel to each of the $F_{16}\text{CuPc}$ sides (e.g. see the zoom in Figure 6.13a). However, it barely extends into the terraces and changes fast into the previously seen 2 : 1 structure.

6.4.3 DIP to F₁₆CuPc ratio 1 : 2

The result of a mixed layer with the molecules deposited in a ratio of 1 : 2 is almost similar to the case with a 1 : 1 ratio, i.e. the same highly ordered structure forms, and virtually no excess of F₁₆CuPc is observed. This evidences an increased sticking coefficient of DIP as compared to F₁₆CuPc under this deposition conditions. The reason behind it might be a favored adsorption and inclusion of DIP into the growing layer to form the highly stable 1 : 1 structure, while the adsorption of F₁₆CuPc, whose excess leads to a (probably less stable) disordered structure (Figure 6.14), is not favored. Thus, in order to obtain films with an excess of F₁₆CuPc as compared to DIP, the substrate must be exposed to a DIP-F₁₆CuPc molecular ratio above 1 : 3. The result is then a layer with areas ordered with the known 1 : 1 structure, but also a noticeable amount of area with a higher amount of F₁₆CuPc in which only a disordered structure is observed, as displayed in Figure 6.12. However, no segregation of ordered monomolecular phthalocyanine domains has been observed, in contrast to the case of CuPc and C60 on Au(111),²⁴ or F₁₆CoPc and NiTPP on Au(111).⁷

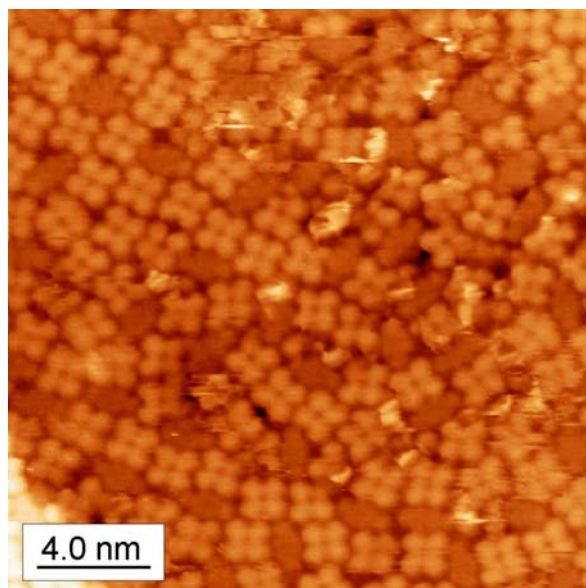


Figure 6.14. STM image (0.179 nA, -0.43 V) revealing the disorder of a 1:2 DIP-F₁₆CuPc mixed layer.

6.5 *Conclusions and comparison to the results on Au(111)*^a

The obtained structures for each of the studied molecular ratios are summarized in Figure 6.15. For the pure DIP, the steps have a crucial influence, leading to absolutely different growth scenarios on large and small terraces. This difference could be exploited by the use of vicinal surfaces to control the resulting film structure. Phthalocyanine layers are characterized by a highly defective structure, with the presence of numerous domain boundaries, twin domains and vacancies.

However, upon codeposition of both molecules, the DIP-F₁₆CuPc intermolecular interactions drive the assembly of the two molecules to form highly ordered structures with domain sizes extending over up to 100 nm. Among the most important intermolecular interactions are the Van der Waals forces, arising from the mutually induced polarization fluctuations within the molecules. In addition, dipole moments pointing along the surface normal are often generated when the organic molecules are deposited on metals. In the case of monomolecular layers, this leads to a long-range repulsive dipole-dipole interaction, whereas for binary structures the interaction can also be attractive if dipoles of opposite sign are induced in each molecule. This is expected to apply for our system, given the opposite donor and acceptor character of the DIP and F₁₆CuPc, respectively. Furthermore, the approach of the outer H atoms of the DIP to the F atoms of the F₁₆CuPc might also play an important role, since H-F interactions have already been reported to be of major importance in previously studied systems.²⁵ All together, the resulting structures are more stable than the monolayers grown from either parent compound. This scenario takes place for codeposition in a DIP:F₁₆CuPc ratio of 1 : 1 and 2 : 1. However, for ratios of 3 : 1 and 1 : 2, disordered structures form.

^a Measurements on Au(111) performed by E. Barrena, at the National Institute of Material Science in Tsukuba, Japan, in the frame of a collaboration.

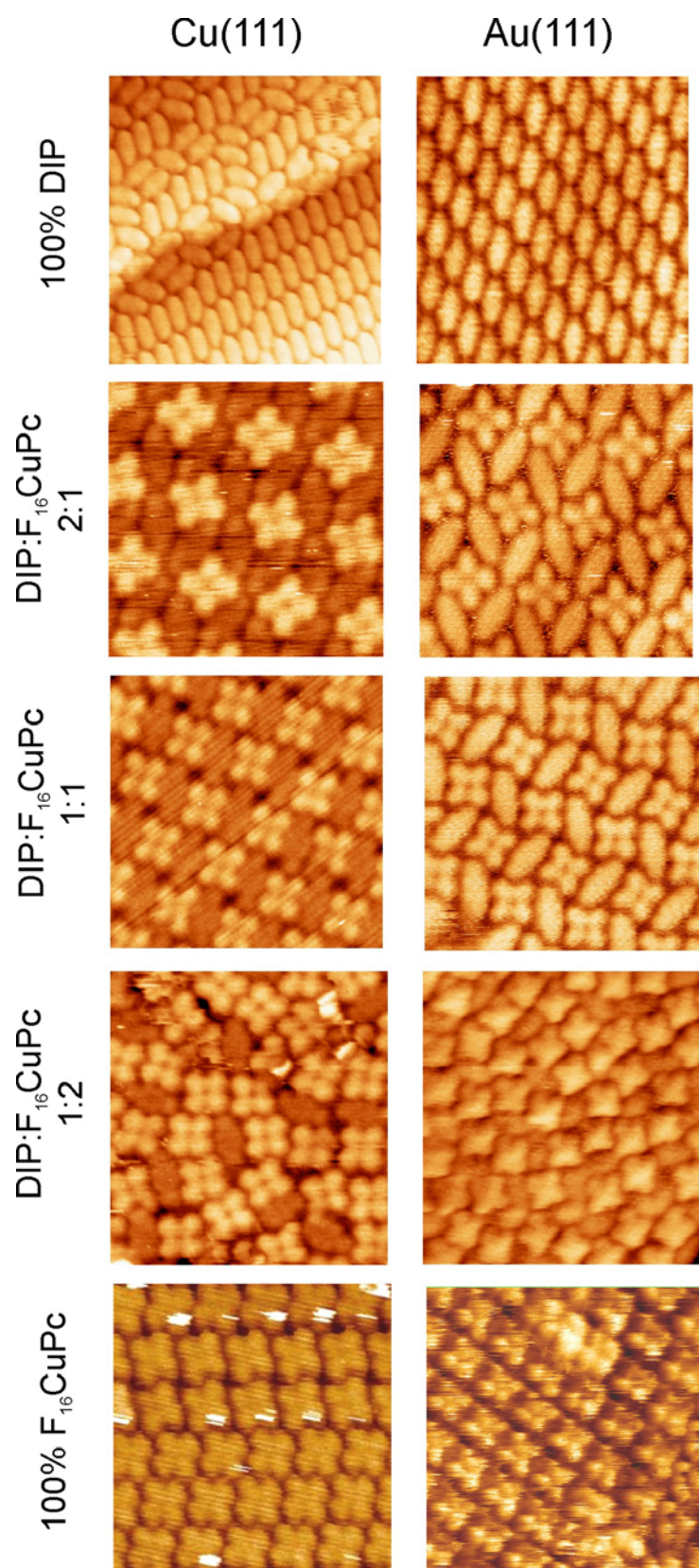


Figure 6.15. Summary of the obtained structures and comparison with those obtained on Au(111).

A similar study has been performed on Au(111), leading to the results summarized in Figure 6.15. Au has the same crystal structure as Cu, namely fcc. Consequently, the Au(111) plane presents the same hexagonal symmetry as Cu(111). Au has a lattice parameter of 407.82 pm and Cu of only 361.49 pm. The lattice difference is thus as high as -11.36 %, but this is not expected to introduce strong differences in the growth of the organic overlayer, since the molecular dimensions (in the nm range) are much larger than the substrate lattice parameters (NN distances of 2.8837 Å on Au and 2.5561 Å on Cu) and thus the molecules only “feel” some sort of “averaged” surface potential. A stronger difference is expected to arise from the higher reactivity of the Cu as compared to the Au, which consequently enhances the substrate-molecule interactions, highly relevant for the final structure. An additional difference is that the Au(111) surface is subject to the so-called herringbone reconstruction,^{26,27} which consequently reduces the symmetry of the surface.

Comparing the results on both surfaces, we observe important similarities. The F₁₆CuPc exhibits a similarly poor ordering on both surfaces. The DIP presents higher ordering on Au(111), where the influence of the steps is not so relevant as on Cu. However, the most important common aspect is the formation of highly ordered mixed phases extending over large domain sizes for the same DIP-F₁₆CuPc molecular ratios. For a 1 : 1 ratio, the structures slightly differ from each other, while for a 2 : 1 ratio very similar structures form on either substrate. This implies that the given structure is mainly determined by the intermolecular interactions which predominate over the molecule-substrate interactions even for the growth on Cu. The scenario for the 1 : 2 ratio is also similar on both substrates, leading to disordered mixed layers.

The stability of the mixed layers (larger than that of monomolecular layers of either molecule) and the low relevance of the substrate-molecule interactions, give strong evidence of the strength of the DIP-F₁₆CuPc interactions.

References

¹ J. Barth, G. Costantini, K. Kern, Engineering atomic and molecular nanostructures at surfaces, *Nature* **437**, 671 (2005)

² S. Hecht, Welding, organizing, and planting organic molecules on substrate surfaces-Promising approaches towards nanoarchitectonics from the bottom-up, *Angew. Chem. Int. Ed.* **42**, 24 (2003)

- ³ S. De Feyter, F. C. De Schryver, Two-dimensional supramolecular self-assembly probed by scanning tunneling microscopy, *Chem Soc. Rev.* **32**, 139 (2003)
- ⁴ M. Bohringer, K. Morgenstern, W. D. Schneider, R. Berndt, Separation of a racemic mixture of two-dimensional molecular clusters by scanning tunneling microscopy, *Angew. Chem. Int. Ed.* **38**, 821 (1999)
- ⁵ J. Méndez, R. Caillard, G. Otero, N. Nicoara, J. A. Martín-Gago, Nanostructured organic material: From molecular chains to organic nanodots, *Adv. Mater.* **18**, 2048 (2006)
- ⁶ J. V. Barth, J. Weckesser, C. Cai, P. Günter, L. Bürgi, O. Jeandupeaux, K. Kern, Building supramolecular nanostructures at surfaces by hydrogen bonding, *Angew. Chem. Int. Ed.* **39**, 1230 (2000)
- ⁷ K. W. Hipps, L. Scudiero, D. E. Barlow, M. P. Cooke, A self-organized 2-dimensional bifunctional structure formed by supramolecular design, *J. Am. Chem. Soc.* **124**, 2126 (2002)
- ⁸ M. de Wild, S. Berner, H. Suzuki, H. Yanagi, D. Schleckwein, S. Ivan, A. Baratoft, H.-J. Guentherodt, T. A. Jung, A novel route to molecular self-assembly: self-intermixed monolayer phases, *ChemPhysChem* **10**, 881 (2002)
- ⁹ C. Bobish, Th. Wagner, A. Bannani, R. Möller, Ordered binary monolayer composed of two organic molecules: copper-phthalocyanine and 3,4,9,10-perylene-tetra-carboxylic-dianhydride on Cu(111), *J. Chem. Phys.* **119**, 9804 (2003)
- ¹⁰ S. Xu, M. dong, E. Rauls, R. Otero, T. R. Linderoth, F. Besenbacher, Coadsorption of guanine and cytosine on graphite: Ordered structure based on GC pairing, *Nano Lett.* **6**, 1434 (2006)
- ¹¹ S. B. Lei, C. Wang, S. X. Yin, H. N. Wang, F. Xi, H. W. Liu, B. Xu, L. J. Wan, C. L. Bai, Surface stabilized porphyrin and phthalocyanine two dimensional network connected by hydrogen bonds, *J. Phys. Chem. B* **105**, 10838 (2001)
- ¹² P. Samorì, N. Severin, C. D. Simpson, K. Müllen, J. P. Rabe, Epitaxial composite layers of electron donors and acceptors from very large polycyclic aromatic molecules, *J. Am. Chem. Soc.* **124**, 9454 (2002)
- ¹³ J. A. Theobald, N. S. Oxtoby, M. A. Phillips, N. R. Champness, P. H. Beton, Controlling molecular deposition and layer structure with supramolecular surface assemblies, *Nature* **424**, 1029 (2003)
- ¹⁴ M. Stöhr, M. Wahl, C. H. galka, T. Riehm, T. A. Jung, L. H. Gade, Controlling molecular assembly in two dimensions: The concentration dependence of thermally induced 2D aggregation of molecules on a metal surface, *Angew. Chem. Int. Ed.* **44**, 7394 (2005)
- ¹⁵ L. M. A. Perdigao, E. W. Perkins, J. Ma, P. A. Staniec, B. L. Rogers, N. R. Champness, P. H. Beton, Bimolecular networks and supramolecular traps on Au(111), *J. Phys. Chem B* DOI 10.1021/jp060062x
- ¹⁶ S. Stepanov, M. Lingenfelder, A. Dmitriev, H. Spillmann, E. Delvigne, N. Lin, X. Deng, C. Cai, J. V. Barth, K. Kern, Steering molecular organization and host-guest interactions using two-dimensional nanoporous coordination systems, *Nat. Mater.* **3**, 229 (2004)
- ¹⁷ M.M. Kamna, T.M. Graham, J.C. Love, P.S. Weiss, Strong electronic perturbation of the Cu{111} surface by 7,7',8,8'-tetracyanoquinonodimethane, *Surf. Sci.* **419**, 12 (1998)
- ¹⁸ S. Berner, M. Brunner, L. Ramoino, H. Suzuki, H.-J. Güntherodt, T. A. Jung, Time evolution analysis of a 2D solid-gas equilibrium: a model system for molecular adsorption and diffusion, *Chem. Phys. Lett.* **348**, 175 (2001)
- ¹⁹ F. Rosei, M. Schunack, P. Jiang, A. Gourdon, E. Lægsgaard, I. Stensgaard, C. Joachim, F. Besenbacher, Organic molecules acting as templates on metal surfaces, *Science* **296**, 328 (2002)
- ²⁰ L. Gross, F. Moresco, P. Ruffieux, A. Gourdon, C. Joachim, K.-H. Rieder, Tailoring molecular self-organization by chemical synthesis: Hexaphenylbenzene, hexa-peri-hexabenzocoronene, and derivatives on Cu (111), *Phys. Rev. B* **71**, 165428 (2005)
- ²¹ S. Lukas, S. Vollmer, G. Witte, Ch. Wöll, Adsorption of acenes on flat and vicinal Cu(111) surfaces: Step induced formation of lateral order, *J. Chem. Phys.* **114**, 10123 (2001)
- ²² Y. Wakayama, (submitted)

-
- ²³ A. Gerlach, F. Schreiber, S. Sellner, H. Dosch, I. A. Vartanyants, B. C. C. Cowie, T.-L. Lee, J. Zegenhagen, Adsorption induced distortion of F₁₆CuPc on Cu(111) and Ag(111): An x-ray standing wave study, *Phys. Rev. B* **71**, 205425 (2005)
- ²⁴ M. Stöhr, T. Wagner, M. Gabriel, B. Weyers, R. Möller, Binary molecular layers of C60 and copper phthalocyanine on Au(111): self-organized nanostructuring, *Adv. Func. Mater.* **11**, 175 (2001)
- ²⁵ A. DerHovanesian, J. B. Doyon, A. Jain, P. R. Rablen, A.-M. Sapse, Models of F-H contacts relevant to the binding of fluoroaromatic inhibitors to carbonic anhydrase II, *Org. Lett.* **1**, 1359 (1999)
- ²⁶ K. G. Huang, D. Gibbs, D. M. Zehner, A. R. Sandy, S. G. J. Mochrie, Phase behavior of the Au(111) surface: Discommensurations and kinks, *Phys. Rev. Lett.* **65**, 3313 (1990)
- ²⁷ S. Narasinhham, D. Vanderbilt, Elastic stress domains and the herringbone reconstruction on Au(111), *Phys. Rev. Lett.* **69**, 1564 (1992)

7 Summary

This thesis has pursued the understanding of the growth processes of organic semiconductors in different architectures relevant for electronic devices. For that purpose, F₁₆CuPc has been chosen, because in spite of its relevance among the diverse studied materials, there are only few studies in the literature regarding its ordering structure and growth. By the use of complementary techniques such as atomic force microscopy (AFM), scanning tunneling microscopy (STM), as well as ex-situ and in-situ X-ray diffraction (XRD), different systems have been addressed. These systems comprise the growth of F₁₆CuPc on SiO₂, the growth of p-n organic heterostructures based on F₁₆CuPc (n-type) combined with pentacene (p-type) as well as DIP (p-type), and finally the self-assembly of two-dimensional supramolecular structures formed by mixed layers of F₁₆CuPc and DIP.

The studies devoted to the growth of F₁₆CuPc on SiO₂ have been performed with a special emphasis on the very first layers in proximity with the dielectric (those most relevant in the charge transport). We have determined for the first time the F₁₆CuPc thin film structure, from the monolayer to the multilayer regime. The findings reveal a low density disordered layer at the interface with the SiO₂, on top of which the nucleation and two-dimensional growth of long and narrow islands of upright standing molecules take place.¹ We have disclosed a thickness-dependent polymorphism (β and β_{bilayer} structures) found in the in-plane crystal structure, which implies large differences in the molecular arrangement within the surface plane.² In contrast to the homologous H₁₆CuPc molecule (often taken as a reference), the F₁₆CuPc films exhibit the same structure independently from the deposition temperature. Given the crucial influence of the crystal structure on the charge transport properties, these findings are of paramount importance for the understanding of the performance of F₁₆CuPc based devices.

A new route to optimize the structure of F₁₆CuPc films has been further demonstrated, consisting in the use of functionalized SiO₂ substrates with a methyl terminated self-assembling monolayer. This surface, with a much lower surface tension, leads to the growth of films with a similar structure but a greatly enhanced

domain size. The higher lateral order results in a reduction of grain boundaries within the F₁₆CuPc films, and thus in a decreased density of traps. In turn, the effective electron field-effect mobility in F₁₆CuPc based devices increases by an order of magnitude.³

The studies on the growth of p-n organic heterostructures consisting in F₁₆CuPc and pentacene reveal the presence of highly anisotropic F₁₆CuPc-pentacene interactions, since the growth presents a strong dependence with the molecular orientation in the underlying film. When F₁₆CuPc is deposited onto pentacene, the molecules on the pentacene terraces arrange into the energetically preferred upright-standing configuration (i.e. similarly as on SiO₂), while the different energetic and electronic environment at the pentacene edges catalyzes the growth of high and narrow crystallites formed by lying-down F₁₆CuPc molecules.^{4,5} For the opposite deposition sequence, pentacene on upright-standing F₁₆CuPc forms excellently ordered, closed films in the well-known thin-film structure. When deposited on lying-down F₁₆CuPc, the pentacene is not subject to any templating effect and grows again in the thin-film structure, though showing in this case an island growth scenario.

Furthermore, the growth of p-n heterostructures consisting on DIP deposited onto F₁₆CuPc has been shown to result either in smooth, layered heterostructures (at RT), or in the formation of organic nanodots by Stranski-Krastanov growth (T=120 °C).⁶ The formation of DIP nanodots has been demonstrated to be related to a novel type of surface reconstruction, affecting the three layers of the underlying F₁₆CuPc film closest to the DIP. Upon deposition in the inverse order, a similar scenario is observed in which F₁₆CuPc grows in the “reconstructed” structure at high substrate temperature, but in the known β -structure for low growth temperatures. In this deposition sequence, however, F₁₆CuPc presents no Stranski-Krastanov growth, regardless of the deposition temperature.

Interestingly, the observed growth scenario differs from the usual growth modes in inorganic heteroepitaxy. Here, the Stranski-Krastanov growth takes place within a relaxed wetting layer, while it is the substrate which is subject to a reconstruction. On the other side, the growth of a “reconstructed” overlayer does not lead to the Stranski-

Krastanov growth of islands. These differences evidence that issues like strain or epitaxy, which are well understood in the context of inorganic growth theories, play a completely different (and still largely unknown) role in the growth of organic materials.

The growth scenarios observed for the heterostructures consisting in F₁₆CuPc combined either with DIP or pentacene are largely different in spite of the similarities between these two molecules. This is a consequence of the specificity of the involved interactions and complexity of the kinetic processes, which hinders the task of establishing a paradigm for the growth of organic heterostructures. However, these results suggest that ultra-thin organic buffer layers can be exploited to tune organic growth to achieve desired morphologies.

Finally, we have shown that DIP-F₁₆CuPc intermolecular interactions drive the self-assembly of highly ordered, two-dimensional supramolecular structures on metal surfaces, when mixed with the appropriate molecular ratio. DIP-F₁₆CuPc ratios of 1:1 and 2:1 lead to the formation of crystalline structures with a better ordering than that of the pure monomolecular layers. These results represent a highly interesting route for the self-assembly of functional structures with an exceptional long-range order (with domain sizes extending above 100 nm), which could as well be used as templates for the synthesis of further nanostructured systems.

Articles related to the thesis, at the time of its defense

¹ D. G. de Oteyza, E. Barrena, S. Sellner, J. O. Ossó, H. Dosch, Structural rearrangements during the initial growth stages of organic thin films of F₁₆CuPc on SiO₂, *J. Phys. Chem. B* **110**, 16618 (2006)

² D. G. de Oteyza, E. Barrena, J. O. Ossó, S. Sellner, H. Dosch, *J. Am. Chem. Soc.* (in print)

³ D. G. de Oteyza, E. Barrena, J. O. Ossó, H. Dosch, S. Meyer, J. Pflaum, Controlled enhancement of the electron field-effect mobility of F₁₆CuPc thin film transistors by use of functionalized SiO₂ substrates, *Appl. Phys. Lett.* **87**, 183504 (2005)

⁴ D. G. de Oteyza, E. Barrena, J. O. Ossó, S. Sellner, H. Dosch, Site-selective molecular arrangement in organic heterostructures, *Chem. Mater.* **18**, 4212 (2006)

⁵ D. G. de Oteyza, E. Barrena, S. Sellner, J. O. Ossó, H. Dosch, submitted

⁶ E. Barrena, D. G. De Oteyza, S. Sellner, H. Dosch, J. O. Ossó, B. Struth, In situ study of the growth of organic nanodots in organic heteroepitaxy, *Phys. Rev. Lett.* **97**, 076102 (2006)

8 Outlook

It is very difficult to consider a thesis complete. In the research performed during more than three years a few questions can be settled and clarified. However, new doors are again opened by the very same research efforts, generating more unsolved questions. This applies to this thesis as it does to many others, in which further work would be expected to lead to interesting results and a more complete outcome. We close this infinite cycle at this point of the thesis.

However, among the most urgent questions related to the presented work and planned to be treated in the future, are the following:

i. Further studies on the self-assembly of two-dimensional supramolecular structures with mixed layers: A similar study to the one presented in the frame of this thesis is planned, combining DIP with $H_{16}CuPc$. Given the similar nature of both systems, we expect to gain insight into the influence of specific interactions as those arising from the H-F proximity of $F_{16}CuPc$ and DIP (absent in the $H_{16}CuPc$ -DIP system), or related to different polarizabilities of $F_{16}CuPc$ and $H_{16}CuPc$ on the metal surfaces. In addition, theoretical studies on these issues are planned in the frame of a collaboration.

ii. The search for a paradigm in the growth of organic-organic heterostructures seems a difficult task and requires further efforts to understand the intermolecular interactions acting as the driving forces in the growth and self-assembly processes, as well as to clarify the role of strain, epitaxial relations or interdiffusion in the growth of these systems. Furthermore, there is also the need of correlating the obtained insight on these subjects with the properties and performance of organic devices.

In a first step, we are planning further studies on the growth of organic heterostructures consisting in $F_{16}CuPc$ deposited on pentacene, with the addition of a buffer layer to inhibit the formation of the $F_{16}CuPc$ *l*-structure. Therewith we plan to avoid polymorphism in the resulting structure, what might favor a better performance of ambipolar transistors based on these heterostructures.

9 Appendix

A. Fit parameters resulting from the study on the first $F_{16}\text{CuPc}$ growth stages on SiO_2

	Layer	d (Å)	ρ (Å ⁻³)	β	σ (Å)
subst.	SiO ₂	13.97	0.642	2.219E-07	4.30
	Si	∞	0.720	1.696E-07	2.16
0.04 ML	second	14.55	0.001	1.150E-07	8.15
	first	15.83	0.067	3.487E-07	6.11
	interfacial	2.2	0.062	2.032E-07	0.2
0.10 ML	second	14.95	0.001	1.150E-07	8.15
	first	13.04	0.116	4.096E-07	4.27
	interfacial	2.74	0.094	2.133E-07	1.11
0.18 ML	second	16.01	0.005	5.907E-08	10
	first	13.07	0.148	5.502E-07	3.57
	interfacial	2.81	0.130	1.580E-07	0.10
0.77 ML	second	13.38	0.101	4.675E-07	3.15
	first	11.76	0.355	5.287E-07	4.05
	interfacial	5.68	0.191	2.905E-08	2.47
1.05 ML	second	14.85	0.215	3.281E-07	3.43
	first	11.39	0.402	1.578E-07	3.04
	interfacial	6.42	0.189	4.047E-09	2.36
1.40 ML	third	21.32	0.008	2.868E-07	2.07
	second	15.66	0.358	3.423E-07	3.59
	first	11.02	0.504	4.217E-08	2.39
	interfacial	7.28	0.225	3.813E-09	2.40
1.68 ML	third	21.63	0.016	3.478E-07	2.48
	second	14.61	0.460	8.144E-07	3.59
	first	12.01	0.599	2.165E-07	1.97
	interfacial	6.62	0.232	9.021E-09	2.69

B. Absorption effect of the $F_{16}\text{CuPc}$ thin films.

Here, we report on the influence of X-ray absorption in the diffraction measurements performed in this thesis. The absorption coefficient μ has been determined from direct experimental measurements as well as from fits to reflectivity data, leading to similar values of $3.1 \pm 1.6 \text{ \AA}^{-1}$ and $2.5 \pm 1.6 \text{ \AA}^{-1}$, respectively.

In the growth of organic heterostructures consisting in $F_{16}\text{CuPc}$ on DIP or pentacene, the intensity of DIP or pentacene in-plane reflections was plotted vs. $F_{16}\text{CuPc}$ nominal film thickness. The distance “ l ” traveled by the X-ray beam through the phthalocyanine film of thickness “ d ” is $l=d/\sin\theta$, which is large enough to have a noticeably effect, given the grazing angle conditions. As an example, the integrated intensity of the pentacene (110) reflection of a 202 \AA thick film vs. nominal $F_{16}\text{CuPc}$ thickness is shown in Figure A.1. The estimated intensity taking into account an absorption coefficient of 3.1×10^{-6} and the grazing angle of 0.1° is given by the dashed line.

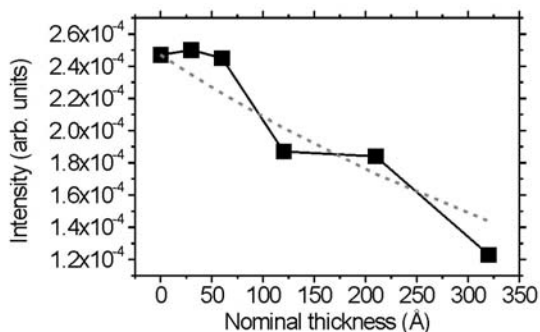


Figure A.1. Integrated intensity of the (110) pentacene reflection of a 202 \AA thick film vs. nominal thickness of the $F_{16}\text{CuPc}$ deposited on top.

Acknowledgement

For those who are not going to read anything but this, I want to take the chance to remind you that I was studying for the last three and half years the growth and structure of organic semiconducting thin films. In other words, I was throwing “interesting” molecules on “interesting” substrates and checking how they arrange by X-ray diffraction and scanning probe microscopies. And now that this is settled, I can start with the acknowledgements to those who have contributed in one way or another to the completion of this thesis.

The two persons without whom the accomplishment of this thesis would have been absolutely impossible are Esther Barrena and Helmut Dosch. I feel so thankful to Esther that it is difficult to resume in few words. I have learnt a lot from her scientific intuition and know-how. Thanks to her good humor (which did not change even after my recidivistic attacks on the lab) the group’s and lab’s spirit have constantly been high, to the level that even a beamtime could seem funny. I owe her many good laughs and I thank her for being such a good friend. To Helmut Dosch I am greatly indebt for providing the financial support and for giving me the opportunity of working under such excellent experimental conditions. In addition, I could savor and learn of his enormous scientific experience. I really appreciate his helpfulness, but also his kindness and the cordial atmosphere in his department.

Wakayama-san needs a very special mention as well. Waka gave me the opportunity to experience Japan. It was terrific from all points of view, personal, cultural and scientific (the whole last chapter has his origin in Japan), with the additional attractiveness of his jovial company. Thanks also to Yumi Hirose for helping so much with all the administrative issues, and to Toyohiro Chikyow, Takahiro Nagata, Kenji Ohmori, Miho Nakayama and all the other department colleagues who made my stay so agreeable.

Thanks a lot to Stefan Sellner for his help in the lab and during the beamtimes, where also Oriol Ossó was often giving us a hand. And coming to beamtimes, the impressive helpfulness of Ralph Weigel with his unlimited ability in solving any technical problem, but also of Nikolei Kasper, were crucial for our measurements in ANKA. I acknowledge the technical support of Bernd Struth and H. Kim when measuring in the ESRF at ID-10B and ID-3, respectively.

Thanks to Jens Pflaum, Stephan Meyer, and Stefan Hirschmann for the agreeable collaborations and fruitful discussions.

Thanks to Xuena Zhang and Tobias Krauss for the good time we have had inside and outside the lab. Thanks to Alejandro Díaz for his didactic explanations about theoretical issues and his “translation” abilities. Thanks to the technicians of the Dosch department, who make our life much easier: Frank Adams, Annette Weisshardt, Stefan Weber, Ernst Günther, Longinus Raschke and Peter Schützendübe. Thanks to Andreas Stierle, always good humored and willing to help us with his accumulated experience. To Harald Reichert for his help with technical and academic questions, and to Hubert Zajonz for interesting discussions. Thanks to Claudia, for proofreading this thesis and reminding me on the differences between British and American English (though I am afraid the thesis is still a mixture). To the rest of the present, past, or transient organic group members: Dipak, Yi, Ayse, Ajay, Arndt, Carmen, Monamie, for always making of this group a merry one. Thanks to all Dosch department members for the good time we have had inside the institute, in Ringberg, or in the periodic Volksfest excursions (or variations thereof).

I am very thankful to Rodolfo Miranda, who was always helping me with the administrative issues in the university, and to Elsa Fuentes, to whom I could always turn to if anything was still unclear.

Thanks to all those friends who made our stay in Stuttgart so enjoyable (I will omit the list out of concern I could forget someone, but you know who...), and to those who came to visit us, bringing high spirits, news and memories from Spain or northern Germany: Juanlu, Carlos, Irene, Iñigo, Valeria, Manu, David, Edu, Ana, Encar, Encarnita (madre), Fanny, Steffi and Adolfo. Four persons that also came but need a very special mention are:

Ajo, she has come for over three and half years. She has been my greatest supporter and we have had an unforgettable time. Tirso (with Wiebke, Till and Daaja), who is a brother as anyone would wish to have one. Ahlke and Luis, who have wholehearted confidence in me and give me unconditional support.

Some pictures
representative
of a PhD thesis.
In particular of...

a "big boss"

a "not-so-big" boss

a department

the same department

6/10/2006

a collaboration

a leak

a team

a beamtime

a summerschool

holidays with
a supporter